

# Remote sensing of chlorophyll-a in small inland waters

by

Amir Masoud Chegoonian

A thesis

presented to the University of Waterloo

in fulfillment of the

thesis requirement for the degree of

Doctor of Philosophy

in

Geography

Waterloo, Ontario, Canada, 2022

© Amir Masoud Chegoonian 2022

## Examining Committee Membership

The following served on the Examining Committee for this thesis. The decision of the Examining Committee is by majority vote.

External Examiner

Simon Bélanger  
Professor,  
Biology, Chemistry and Geography  
Université du Québec à Rimouski.

Supervisor(s)

Claude Duguay  
Professor,  
Geography and Environmental Management  
University of Waterloo.

Kiana Zolfaghari  
Research Scientist,  
Geography and Environmental Management  
University of Waterloo.

Internal Members

Richard Kelly  
Professor,  
Geography and Environmental Management  
University of Waterloo.

Ellsworth LeDrew  
Professor,  
Geography and Environmental Management  
University of Waterloo.

Internal-external Member

Kirsten Müller  
Professor,  
Biology  
University of Waterloo.

## **AUTHOR'S DECLARATION**

This thesis consists of material all of which I authored or co-authored: see Statement of Contributions included in the thesis. This is a true copy of the thesis, including any required final revisions, as accepted by my examiners

I understand that my thesis may be made electronically available to the public.

## Statement of Contributions

This manuscript-style thesis includes four articles either submitted or accepted to scientific journals. I was the lead author with major contributions on the design, development, evaluation and writing of the first three papers. I contributed as a co-author to the last paper (Appendix A) for the remote sensing data analysis. I have not contributed to *in situ* data collection for these manuscripts.

Chegoonian, A., M., Zolfaghari, K., Leavitt, P., R., Baulch, H., M., and Duguay, C., R., (2021, Accepted). “Improvement of field fluorometry estimates of chlorophyll-*a* concentration in a cyanobacteria-rich eutrophic lake”. *Limnology and Oceanography: Methods*.

Chegoonian, A., M., Pahlevan, N., Zolfaghari, K., Leavitt, P., R., Davies, J-M., Baulch, H., M., and Duguay, C., R., (2021, Submitted). “Quantification of chlorophyll-*a* in small eutrophic lakes using Sentinel-2 and Landsat-8 imagery and locally tuned machine learning models”. *ISPRS Journal of Photogrammetry and Remote Sensing*.

Chegoonian, A., M., Leavitt, P., R., Zolfaghari, K., Davies, J-M., Baulch, H., M., and Duguay, C., R., (2021, Submitted). “Regional upscaling of chlorophyll-*a* retrieval from small eutrophic lakes via Sentinel-2: A case study of the Qu’Appelle River drainage basin, Canada”. *Remote Sensing*.

Haig, H., A., Chegoonian, A., M., Davies, J-M., Bateson, D., Leavitt, P., R., (2021). “Marked blue discolouration of late winter ice and water due to autumn blooms of cyanobacteria”. *The Lake and Reservoir Management*.

This thesis was conducted under supervision of Prof. Claude Duguay who aided with the initial proposal of the project and secured funding to carry out the research. Dr. Kiana Zolfaghari, as a co-supervisor, provide guidance and suggestions on the remote sensing aspects. *In situ* data for this research comes from Global Water Futures’ project FORMBLOOM, funded by Canada First Research Excellence Fund, and led by Dr. Helen Baulch from University of Saskatchewan. The Qu’Appelle Long-term Ecological Research program (QU-LTER), supported by grants to Prof. Peter Leavitt from NSERC, the Canada Foundation for Innovation, Canada Research Chairs, and the University of Regina, also provides a part of *in situ* data. Dr. John-Mark Davies from Water Security Agency (WSA) and Buffalo Pound Water Treatment Plant (BPWTP) also contributed to this thesis by providing *in situ* data. Dr. Nima Pahlevan from NASA also supported this research through advice related to the remote sensing aspects of the project. The manuscripts were edited for content and composition by all co-authors.

## Abstract

Small inland waters (SIWs) – waterbodies smaller than 100 km<sup>2</sup> – are the predominant form of lakes globally, yet they are highly subject to water quality degradation, especially due to harmful algae blooms (HABs). Space-borne remote sensing has proven its capability to detect and map HABs in coastal waters as well as large waterbodies mostly through estimating chlorophyll-*a* (Chl*a*). However, remote retrieval of near-surface Chl*a* concentration in SIWs is challenging due to adjacency effects in remotely sensed signals and substantial *in situ* optical interferences of various water constituents. Although various algorithms have been developed or adapted to estimate Chl*a* from moderate-resolution terrestrial missions (~ 10 – 60 m), there remains a need for robust algorithms to retrieve Chl*a* in SIWs. Here, we introduce and evaluate new approaches to retrieve Chl*a* in small lakes in a large lake catchment using Sentinel-2 and Landsat-8 imagery.

*In situ* Chl*a* data used in this study originate from various sources with contrasting measurement methods, ranging from field fluorometry to high-performance liquid chromatography (HPLC). Our analysis revealed that *in vivo* Chl*a* measurements are not consistent with *in vitro* measurements, especially in high Chl*a* amounts, and should be calibrated before being fed into retrieval models. Calibrated models based on phycocyanin (PC) fluorescence and environmental factors, such as turbidity, significantly decreased Chl*a* retrieval error and increased the range of reconstructed Chl*a* values. The proposed calibration models were then employed to build a consistent dataset of *in situ* Chl*a* for Buffalo Pound Lake (BPL) – 30 km length and 1 km width – in the Qu’Appelle River drainage basin, Saskatchewan, Canada. Using this dataset for training and test, support vector regression (SVR) models were developed and reliably retrieved Chl*a* in BPL. SVR models outperformed well-known commonly used retrieval models, namely ocean color (OC3), 2band, 3band, normalized difference chlorophyll index (NDCI), and mixture density networks (MDN) when applied on ~200 matchups extracted from atmospherically-corrected Sentinel-2 data. SVR models also performed well when applied to Landsat-8 data and data processed through various atmospheric correction (AC) processors. The proposed models also suggested good transferability over two optical water types (OWTs) found in BPL.

Based on prior evaluations of the models’ transferability over OWTs in BPL, locally trained machine-learning (ML) models were extrapolated for regional retrieval of Chl*a* in the Qu’Appelle River drainage basin. The regional approach was trained on *in situ* Chl*a* data from BPL and retrieved Chl*a* in

other six lakes in the drainage basin. The proposed regional approach outperformed a recently developed global approach (MDN) in terms of accuracy, and showed more applicability than local models given the scarcity of *in situ* data in most lakes. In addition, ML models, e.g., SVR, performed consistently better than other models when employed in the regional approach.

A rare phenomenon of marked blue discoloration of ice and water in winter 2021 in Pasqua Lake, a small lake in Qu'Appelle Watershed, provided an opportunity to assess the regional approaches in estimating chlorophyll-*a* for waterbodies where enough training data is not available. Therefore, using a developed model based on data from BPL, we produced Chl*a* maps and could successfully relate the discoloration event to a late fall bloom in Pasqua Lake. We included the details of that study in Appendix A.

Altogether, the models and approaches introduced in this thesis can serve as first steps toward developing a remote-sensing-based early warning system for monitoring HABs in small inland waters. Results showed that the development of an early warning system for SIWs based on Chl*a* monitoring is currently possible, thanks to advancements in medium-resolution satellite sensors, *in situ* data collection methods, and machine learning algorithms. However, further steps need to be taken to improve the accuracy and reliability of systems: (a) *in situ* data need to be consistent for being fed into remote sensing models, (b) retrieval models and AC processors should be improved to provide better estimations of Chl*a*, and (c) regional approaches might be developed as alternatives for local and global approaches in the absence of accurate AC processors and scarcity of *in situ* Chl*a* data.

## Acknowledgements

I would like to thank my supervisor Professor Claude Duguay for being a great mentor for me not just academically but also personally. Thank you, Professor Duguay, for allowing me to grow as a researcher under your guidance. I would also like to thank my co-supervisor Dr. Kiana Zolfaghari for helping and encouraging me throughout my Ph.D.

Many thanks to my Ph.D. committee members, Professor Simon Bélanger, Professor Kirsten Müller, Professor Ellsworth LeDrew, and Professor Richard Kelly, for reviewing the thesis and providing their thoughtful comments on this thesis.

I would also like to thank Dr. Helen Baulch, PI of the FORMBLOOM project, for providing me the opportunity to work on such an interesting project during my Ph.D. Thank you also to Prof. Peter Leavitt and Dr. Nima Pahlevan for their great advice and help. I should also thank Dr. John-Mark Davies for providing me with valuable data. Without your help, this study would not have been possible.

A big thank you to those who were involved in fieldworks and lab analyses at University of Saskatchewan, University of Regina, Buffalo Pound Water Treatment Plant, and Saskatchewan Water Security Agency, especially Katy Nugent, David Vandergucht, and Deirdre Bateson. I should also thank my colleagues in the *Duguay Research Group*, including Dr. Nastaran Saberi, Yusof Ghiasi, Michael Dallosch, Marie Hoekstra and others for their ideas and support. I would like to pay my gratitude and respects to my colleague, Dr. Marzieh (Mari) Foroutan for helping me in the first stages of my Ph.D. Dr. Foroutan passed away on flight of PS752. She was a dedicated and passionate researcher and certainly is in my thoughts forever. Rest in peace, Mari!

To my family, particularly my parents and lovely sister, thank you for your love, support, and unwavering belief in me. Without you, I would not be the person I am today. Special thanks to my beloved wife, Parisa, for her love and constant support, for all the late nights and early mornings, and for keeping me sane over the past few months.

## Table of Contents

List of Figures .....	xii
List of Tables .....	xvii
List of Abbreviations .....	xx
Chapter 1 Introduction.....	1
1.1 Motivation .....	1
1.2 Objectives and Contributions .....	3
1.2.1 Structure .....	4
Chapter 2 Background.....	5
2.1 Introduction .....	5
2.2 Algal blooms; physical, chemical, and biological (PCB) aspects .....	5
2.2.1 Phytoplankton, blooms, and HAB definitions.....	5
2.2.2 The relation of algal blooms to PCB parameters.....	6
2.3 Remote sensing of algal blooms.....	11
2.3.1 Principles of HAB remote sensing .....	11
2.3.2 HAB retrieval algorithms .....	14
2.4 Summary .....	22
Chapter 3 Improvement of field fluorometry estimates of chlorophyll- <i>a</i> concentration in a cyanobacteria-rich eutrophic lake.....	23
3.1 Introduction .....	23
3.2 Materials and Procedures .....	26
3.2.1 Study site .....	26

3.2.2 Data .....	29
3.2.3 Data Processing Procedure .....	31
3.3 Assessment .....	35
3.3.1 Models accuracy .....	35
3.3.2 Models reliability .....	39
3.3.3 Models performance in retrieving <i>Chla</i> time-series .....	41
3.3.4 Models importance in retrieving remote <i>Chla</i> .....	42
3.4 Discussion .....	44
3.4.1 Considerations to employ field fluorometers to retrieve <i>Chla</i> .....	44
3.4.2 Effectiveness of PC versus <i>Chla</i> fluorometers in retrieving <i>Chla</i> .....	46
3.4.3 Performance of environmental MLR models .....	49
3.5 Conclusions and recommendations .....	50
<b>Chapter 4 Quantification of chlorophyll-a in small eutrophic lakes using Sentinel-2 and Landsat-8 imagery and locally tuned machine learning models .....</b>	<b>52</b>
4.1 Introduction .....	52
4.2 Materials and Methods .....	55
4.2.1 Study site .....	55
4.2.2 Data .....	59
4.2.3 Methodology .....	62
4.3 Results .....	69
4.3.1 Quantitative assessment of the model on MSI data.....	70
4.3.2 Model sensitivity to AC processors.....	74
4.3.3 Model transferability over water types.....	76
4.3.4 Model sensitivity to sensor type .....	77

4.3.5 Spatial integrity .....	79
4.3.6 Temporal validity .....	83
4.4 Discussion .....	85
4.4.1 Uncertainties in <i>in situ</i> data .....	85
4.4.2 Merits of locally trained ML models.....	86
4.4.3 Atmospheric correction .....	87
4.5 Conclusion.....	88
<b>Chapter 5 Regional upscaling of chlorophyll-<i>a</i> retrieval from small eutrophic lakes via Sentinel-2: A case study of the Qu’Appelle River drainage basin, Canada.....</b>	<b>90</b>
5.1 Introduction .....	90
5.2 Materials and Methods .....	91
5.2.1 Study area .....	91
5.2.2 Data .....	94
5.2.3 Methodology .....	95
5.3 Results .....	97
5.4 Discussion .....	100
5.5 Conclusions .....	101
<b>Chapter 6 Conclusion and Future work .....</b>	<b>102</b>
6.1 Summary of Contributions and Results.....	102
6.2 Limitations and uncertainties .....	104
6.3 Future research directions .....	105
References .....	106
Appendix A Marked blue discolouration of late winter ice and water due to autumn blooms of cyanobacteria.....	128

A.1 Abstract.....	128
A.2 Introduction .....	129
A.3 Methods and Materials .....	131
A.3.1 Study region.....	131
A.3.2 Limnological monitoring.....	134
A.3.3 Laboratory analyses.....	135
A.3.4 Remote sensing.....	136
A.4 Results and Discussion .....	138
A.5 Conclusions .....	148

## List of Figures

Figure 2.1. (a) The relationship between irradiance and phytoplankton growth rate (Gutierrez-Wing et al. 2014). (b) The relationship between irradiance and phytoplankton productivity in different temperatures (Wetzel 2001). .....	8
Figure 3.1. The map and location of the Buffalo Pound Lake (BPL), Saskatchewan, Canada. (a) Position of the Qu'Appelle River watershed within Canada. (b) Location of BPL within Qu'Appelle River watershed. (c) A Landsat-8 image of BPL, overlaid by a bathymetric map. The extent indicator represents the sampling area in the lake (d) A zoom view of the sampling area in BPL overlaid by sampling stations. ....	28
Figure 3.2. A thematic graph of the workflow in this study.....	31
Figure 3.3. Examples of (a) potential biofouling, (b) high impulse values, and (c) NPQ effect on Chl $a$ and PC fluorescence time-series. (a) Very high end-season values of the shallow PC fluorometer that are inconsistent with coincident observations of the same sensor in deep water could be the result of biofouling error. (b) Very high relative values that are occurred in very short periods and are inconsistent with other sensors could be the result of sensor impulse noise. (c) Periodic changes in fluorescence values with an inverse relationship to available PAR could be the result of NPQ.....	32
Figure 3.4. A heatmap showing the Pearson correlation of the selected environmental factors and chl $M$ . .....	34
Figure 3.5. Factory-calibrated Chl $a$ concentration from YSI Chl $a$ fluorometer (chl $^{FC}$ , green line), and <i>in vitro</i> Chl $a$ concentration (chl $M$ , circles), shows that chl $^{FC}$ significantly underestimates Chl $a$ concentration in BPL. Stations are color-coded 1-4.....	36
Figure 3.6. Scatter plots of the fluorescence of (a) Chl $a$ and (b) PC, versus <i>in vitro</i> Chl $a$ concentration (chl $M$ ). $F$ stands for fluorescence. ....	37

Figure 3.7. The results of five-fold cross-validation of the proposed models; (b)  $\text{chl}_p^{\text{chl}}$ , (c)  $\text{chl}_p^{\text{PC}}$ , and (d)  $\text{chl}_p^{\text{ML}}$  versus  $\text{chl}_M$  measurements at stations 1-4. The validation results for  $\text{chl}^{\text{FC}}$ , obtained from YSI Chla fluorometer with a correction for biofouling and NPQ, is also displayed in (a) to compare with the proposed models. The dashed lines correspond to the 1:1 relationship..... 38

Figure 3.8. Visualization of the reliability of  $\text{chl}_p^{\text{ML}}$ , measured as the number of predicted Chla that fall into the confidence zone, computed by the standard deviation of coincident  $\text{chl}_M$ . Values are log-transformed, and the numbers in the legend represent the station from which  $\text{chl}_M$  is acquired..... 40

Figure 3.9. Time-series of  $\text{chl}^{\text{FC}}$ ,  $\text{chl}_p^{\text{ML}}$ , and  $\text{chl}_p^{\text{PC}}$  to retrieve continuous long-term Chla for 2016-2019 in station 1 in BPL. Coincident *in vitro* Chla in stations 1-4 ( $\text{chl}_M$ ) is used to assess the validity of retrieval..... 41

Figure 3.10. Photographs of surface blooms of cyanobacteria on dates when models significantly underestimated *in vitro* estimates of Chla. (a) image from buoy camera on 15 August 2016, (b) image from shore on 10 August 2017. .... 42

Figure 3.11. Different models to retrieve *in vivo* Chla ( $\text{chl}^{\text{FC}}$ ,  $\text{chl}_p^{\text{chl}}$ ,  $\text{chl}_p^{\text{PC}}$ , and  $\text{chl}_p^{\text{ML}}$ ), employed as training data for an SVR algorithm, result in substantial changes in the performance of remote-sensing Chla retrieval. (a-d) Heatmaps of Chla, when an SVR algorithm feed by  $\text{chl}^{\text{FC}}$ ,  $\text{chl}_p^{\text{chl}}$ ,  $\text{chl}_p^{\text{PC}}$ , and  $\text{chl}_p^{\text{ML}}$ , respectively, and is applied on Sentinel-2 image of BPL acquired on 22 July 2019. The insets indicate the validation results for remotely-retrieved Chla, estimated on unseen *in vitro* Chla. .... 43

Figure 3.12. The ratio of cyanobacteria biomass to total phytoplankton biomass in BPL, averaged on three depths (0.8, 2.8, and 3.5 m) in station 1 for 2015-2018. Cyanobacteria tend to be dominant taxa in BPL from day 175 (late June) to day 300 (late October) of a year. .... 47

Figure 3.13. The normalized fluorescence excitation-emission matrices (EEMs) of the most dominant algae and cyanobacteria species in BPL. (a) green algae (*Chlorella vulgaris*) and (b) cyanobacteria (*Anabaena sp.*), modified from (Shin et al. 2018). Regions 1 and 2 are the spectral range of the employed Chla and PC fluorometers, respectively. .... 48

Figure 4.1. Map and location of Buffalo Pound Lake (BPL), Saskatchewan, Canada. (a) Location of the Qu'Appelle River watershed within Canada. (b) Location of BPL within Qu'Appelle River watershed. (c) A Landsat-8 RGB image of BPL overlaid on a bathymetric map on which sampling stations are also shown (solid black triangles numbered 1 to 11). .....56

Figure 4.2. Pair plots of some optically-derived/driven parameters in BPL (averaged on stations 4-11 from late May to early September of 2014-2020). Diagonal elements are the distribution of each parameter, color-coded according to station numbers. Upper-diagonal elements are the scatter plot of paired parameters. Lower-diagonal charts are the contour plots showing the relationship between the parameters in northern and southern stations.  $N$  and  $\rho$  are the number of samples and correlation coefficients, respectively. Units are  $\text{mg m}^{-3}$ ,  $\text{g m}^{-3}$ , NTU, and m for Chla, TSS, turbidity, and SDD, respectively.....58

Figure 4.3. Comparison of MSI bands (red boxes) and OLI bands (blue boxes) in wavelengths < 800 nm. The spectra are from three different samples measured at BPL using an ASD spectrometer and display how water spectra change with changes in Chla content..... 61

Figure 4.4. Overview of workflow developed in this study. .... 62

Figure 4.5. Normalized frequency distributions of MSI-derived  $R_{rs}^{\delta}$  spectra for the matchups processed via ACOLITE and iCOR processors. .... 64

Figure 4.6. Graphical depiction of principles of support vector regression (SVR). (a) Schematic view of regression between Chla and reflectance measurements using SVR. (b) Loss function defined for SVR; while errors less than  $\epsilon$  are not penalized, larger errors are penalized by a linear function. .... 65

Figure 4.7. Matchup analysis of Chla derived from different algorithms applied on MSI-A/B data and near-coincident, co-located *in situ* Chla samples in BPL. The results are from a cross-validation approach in which matchups related to a single year are put aside as unseen test data, and a model is trained with the remaining data. Model performance is finally computed on all matchups (all are predicted once as test data). Year of data acquisition indicated by colored solid circles. .... 71

Figure 4.8. Matchup analysis of measured and predicted Chla from *in situ* Chla and MSI-A/B images for two different regions in BPL, categorized based on optical water type. For each optical water type, a model is trained and tested using a five-fold cross-validation approach. .... 74

Figure 4.9. Median Symmetric Accuracy (MdSA) for Chla retrieval algorithms when applied to MSI-A/B data processed to produce different radiometric products ( $R_{rs}^{\delta}$ ,  $\rho_{rc}$ , and  $\rho_{TOA}$ ) with different AC processors (ACOLITE and iCOR). Note that  $\rho_{rc}$  is generated with ACOLITE and theoretically is not different when using iCOR. N is the total number of matchups. See Table 4.5 for the detailed training/test split process. .... 75

Figure 4.10. Scatter plot of *in situ* Chla versus predicted Chla from MSI-A/B images. Chla values in the northern basin (OWT2, red solid circles) are predicted using a model trained with southern basin matchups (OWT1, blue solid circles) and vice versa. .... 77

Figure 4.11. Matchup analysis of Chla derived from different algorithms applied on OLI data and near-coincident, co-located *in situ* Chla samples in BPL. The results are from a five-fold cross-validation approach. .... 79

Figure 4.12. Chla maps for BPL derived from different retrieval algorithms/AC processors couples applied on MSI-A image acquired on 16 July 2020. The markers in the insets represent examples of the location of *in situ* data, collected on the same date, and employed as unseen test data. The associated numbers beside the markers are Chla concentration in  $\text{mg m}^{-3}$ . 2band was used as the best representative of empirical models. .... 80

Figure 4.13. Spatial profile of normalized Chla along the lake (south to north) for 16 July 2020, derived from *in situ* measurement Chla (solid line) as well as predicted Chla from algorithms applied on MSI image (dashed lines). X-axis denotes station number (see Figure 4.1). .... 82

Figure 4.14. Chla map for BPL derived from different algorithms applied on OLI image acquired on 16 July 2020. The markers in the insets represent examples of *in situ* data, collected on the same date, and employed as unseen test data. The associated numbers beside the markers are Chla in  $\text{mg m}^{-3}$ ... 83

Figure 4.15. Time series of Chla in station 1 in BPL for summer 2020, derived from *in situ* measurement Chla (solid line) as well as predicted Chla from algorithms applied to MSI images. .... 84

Figure 5.1. Map, modified from Haig et al. (2020), showing locations of Qu’Appelle River drainage basin and seven study lakes (Buffalo Pound Lake (BPL), Lake Diefenbaker, Last Mountain Lake, Wascana Lake, Pasqua Lake, Crooked Lake, Katepwa Lake) overlaid by sampling stations (triangles) and major hydrologic boundaries (tan line). Dominant flow direction is noted by arrows along streams. Shading in the top-right inset indicates the Qu’Appelle Valley gross drainage area within the broader context of central Canada. Upper left inset magnifies BPL and its sampling stations. .... 93

Figure 5.2. Overview of workflow developed in this study. .... 95

Figure 5.3. Scatter plots of *in situ* Chla versus predicted Chla from MSI-A/B images. OC3, 2band, LMDN, and SVR were trained with  $R_{rs}^{\delta}$ - Chla matchups from BPL. MDN was trained with global remote-sensing reflectance ( $R_{rs}$ ). The points are color coded based on the lakes (C = Crooked, D = Diefenbaker, K = Katepwa, L = Last Mountain, P = Pasqua, W = Wascana). .... 98

## List of Tables

Table 2.1. Criteria that have been employed as indicators of HABs in different studies on Lake Erie, modified from Ho and Michalak (2015). .....	12
Table 3.1. Buffalo Pound Lake characteristics and water quality parameters in station 1, averaged on late May to early September in 2014-2019. ....	27
Table 3.2. Details of data used in this study. Env. stands for environmental. ....	29
Table 3.3. Multiple linear regression (MLR) model to predict chl <sub>M</sub> , from measured environmental parameters using forward selection. ....	37
Table 3.4. Reliability, estimated as the proportion of retrieved Chl <sub>a</sub> values that within three confidence intervals ( $\pm \sigma$ , $\pm 2\sigma$ , and $\pm 3\sigma$ ) of the mean of <i>in vitro</i> Chl <sub>a</sub> concentration, for each of four fluorescence models. ....	39
Table 4.1. Buffalo Pound Lake characteristics and water quality parameters at station 1 (averaged from late May to early September 2014-2020). P stands for phosphorus, TSS for total suspended solids, and DOC for dissolved organic carbon. a <sub>CDOM</sub> (440) is CDOM absorption measured at 440 nm. ....	57
Table 4.2. Statistics for water constituents associated with two distinct OWTs in BPL (averaged from late May to early September 2017-2020). Units are mg m <sup>-3</sup> and g m <sup>-3</sup> for Chl <sub>a</sub> and TSS, respectively. ....	59
Table 4.3. Details of <i>in situ</i> Chl <sub>a</sub> measurements employed in this study. The unit for depth values is meter. ....	60
Table 4.4. Formulas and coefficients of empirical models employed in this study. b# and w# are the reflectance and wavelength at specified bands, respectively. y (output of the equations) is Chl <sub>a</sub> on a logarithmic scale. ....	66

Table 4.5. Assessment approaches (training-test split) as well as the number of training/test matchups available for each experiment in this study. .... 67

Table 4.6. Annual frequency and statistics of  $R_{rs}^{\delta}$ - Chla matchups derived from MSI sensor. Chla concentration unit is  $\text{mg m}^{-3}$ . .... 68

Table 4.7. Evaluation metrics (general performance) for Chla retrieval models on MSI and *in situ* Chla matchups (N = 193). The Model Win Rate (MWR) is computed relative to SVR as the reference model. Highlighted cells indicate the best score for the corresponding metrics. .... 70

Table 4.8. Evaluation metrics for Chla retrieval models on MSI and *in situ* Chla matchups based on water type. See Figure 4.2 for more details of each water type. The Model Win Rate (MWR) is computed relative to SVR as the reference model. Chla and TSS are the median of Chla and TSS in associated stations. Units are  $\text{mg m}^{-3}$  and  $\text{g m}^{-3}$  for Chla and TSS, respectively. Highlighted cells mark the best score for the corresponding metrics in each OWT. .... 72

Table 4.9. Evaluation metrics for Chla retrieval models on OLI and *in situ* Chla matchups (N = 178). Each model was trained and tested using a five-fold cross-validation approach. The MWR was computed relative to SVR as the reference model. Highlighted cells mark the highest score for the corresponding metrics. .... 77

Table 4.10. Time series correlation of measured and predicted Chla, derived from algorithms applied to MSI images, at station 1 in BPL for summer 2020. .... 84

Table 5.1. Study site locations as well as hydrological, chemical, and biological characteristics from 1993 to 2020. All variable values are represented by mean of 28 yr measurements during May-September. Total dissolved phosphorus (TDP) and dissolved organic carbon (DOC) are measured from depth-integrated samples. Chla and cyanobacterial toxin microcystin are measured from surface samples (~0.5-m depth). .... 93

Table 5.2. Median symmetric accuracy (%) of the models in retrieving Chla in each individual test lake. N is the number of lake-satellite data matches. .... 99

Table 5.3. Bias (unitless) of the models in retrieving *Chl a* for each test lake, separately. N is the number of matchups. Ideal bias equals one as it is computed in log space. .... 99

## List of Abbreviations

$a_{\text{chl}}^*$	Spectral chlorophyll- <i>a</i> -specific absorption coefficient
AC	Atmospheric correction
BPL	Buffalo Pound Lake
CDOM	Colored dissolved organic matter
$C$	Regularization parameter
Chl <i>a</i>	Chlorophyll- <i>a</i>
chl <sup>FC</sup>	Factory-calibrated chlorophyll- <i>a</i>
chl <sub>M</sub>	Measured chlorophyll- <i>a</i>
chl <sub>P</sub> <sup>chl</sup>	Predicted chlorophyll- <i>a</i> using chlorophyll- <i>a</i> fluorescence
chl <sub>P</sub> <sup>ML</sup>	Predicted chlorophyll- <i>a</i> using multiple-linear regression
chl <sub>P</sub> <sup>PC</sup>	Predicted chlorophyll- <i>a</i> using phycocyanin fluorescence
CI	Cyanobacteria Index
CZCS	Coastal Zone Color Scanner
DIC	Dissolved inorganic carbon
DNA	Deoxyribonucleic acid
DO	Dissolved oxygen
DOC	Dissolved organic carbon
DOY	Day of year
$E$	Spectral scalar irradiance
$e$	Error
EEM	Excitation-emission matrices
ESA	European Space Agency
EWS	Early warning system
$F$	Fluorescence intensity
$F_0$	Background fluorescence
$F^{\text{chl}}$	Chlorophyll- <i>a</i> fluorescence
$F^{\text{PC}}$	Phycocyanin fluorescence

FLH	Fluorescence Line Height
GML	Globally trained machine-learning
HAB	Harmful algae blooms
HPLC	High-Performance Liquid Chromatography
$i$	Number of training data
$I_z$	Irradiance at the depth $z$
IOP	Inherent optical properties
$j$	Number of predictors
LANDSAT	Land Remote-Sensing Satellite (System)
LDA	Linear discriminant analysis
LML	Locally trained machine-learning
LSE	Locally trained empirical
MALE	Mean absolute logarithmic error
MAPE	Median percentage error
MCI	Maximum Chlorophyll Index
MDN	Mixture density neural networks
MERIS	Medium Resolution Imaging Spectrometer
ML	Machine-learning
MLP	Multilayer perceptron
MLR	Multiple linear regression
MODIS	Moderate Resolution Imaging Spectroradiometer
MPH	Maximum Peak Height
MSI	Multi-Spectral Instrument
MWR	Model Win Rate
$N$	Number of samples (matchups)
NAP	Non-algal particles
NDCI	Normalized Difference Chlorophyll Index
NIR	Near-infrared
NN	Neural network

nPAR	Normalized photosynthetically active radiation
NPQ	Non-photochemical quenching
NTU	Nephelometric turbidity unit
OCI	Ocean Color Imager
OLCI	Ocean Color and Land Imager
OLI	Operational Land Imager
OWT	Optical water types
PAR	Photosynthetically active radiation
PC	Phycocyanin
PCB	Physical, chemical, and biological
PCR	Polymerase chain reaction
POM	Particulate organic matter
$R^2$	Coefficient of determination
$R_{rs}$	Remote-sensing reflectance
$R_{rs}^{\delta}$	Satellite-derived remote-sensing reflectance
$R_{rs}^{\delta,ACL}$	Satellite-derived remote-sensing reflectance (ACOLITE)
$R_{rs}^{\delta,iCOR}$	Satellite-derived remote-sensing reflectance (iCOR)
RBF	Radial basis function
RFU	Relative fluorescence unit
RMSE	Root mean square error
RMSLE	Root mean square logarithmic error
RTE	Radiative transfer equation
SDD	Secchi disk depth
SIW	Small inland waters
SSPB	Symmetric signed percentage bias
SST	Sea surface temperature
SVM	Support vector machines
SVR	Support vector regressions
TDN	Total dissolved nitrogen

TDP	Total dissolved phosphorus
TDS	Total dissolved solids
TM	Thematic Mapper
TP	Total phosphorus
TSM	Total suspended matter
TSS	Total suspended solid
UAV	Unmanned aerial vehicle
UV	Ultra-violet
VIS	Visible
VNIR	Visible/near infrared
$z$	Depth
$Z_{\max}$	Maximum depth
$\varepsilon$	Threshold
$\phi$	Kernel
$\Phi_F$	Fluorescence quantum yield
$k_d$	diffuse attenuation of downwelling irradiance
$\lambda$	Wavelength
$\rho$	Pearson correlation
$\rho_{rc}$	Rayleigh-corrected reflectance
$\rho_{TOA}$	Top-of-atmosphere reflectance
$\sigma$	Variance
$\omega$	Weights

# Chapter 1

## Introduction

### 1.1 Motivation

Lakes, reservoirs, and rivers contain less than 1% of water on the earth (Wetzel 2001; Likens 2009), yet they are of major importance for their critical role in the maintenance of terrestrial life. According to estimations, 90% of the world's population reside within 10 km of a freshwater body (Kummu et al. 2011). They are the main source of drinking water as well as having recreational, transportation, agricultural and industrial usages. Hence, sustainable water management measures are crucial for ensuring overall environmental stewardship, human health and well-being, as well as continued economic growth.

Small inland waters (SIWs), the matter of this research, are the predominant form of lakes, with 64% of basins  $< 100 \text{ km}^2$  (Downing et al. 2006). They are highly subject to water quality degradation due to urbanization and changes in land use (Carpenter et al. 1998; Cheng and Basu 2017). However, previous studies have mostly focused on large, deep lakes (e.g. Laurentian Great Lakes of North America) (Gons et al. 2008; Wynne et al. 2008; Binding et al. 2012; Binding et al. 2021). This may be related to their greater importance in regional-global interactions, and that they are a critical source of water for many of the large cities surrounding them. Another reason might be limitations in using technologies such as satellite data, which, until recently, did not provide the combined spatial and spectral resolutions needed to retrieve water quality parameters with reasonable accuracies for small lakes (Pahlevan et al. 2020; Smith et al. 2021).

Harmful algal blooms (HABs) are the most pervasive problems in SIWs (Walker 2019); there is evidence that the frequency, magnitude, and persistence of HABs, especially cyanobacteria-HABs, have increased globally (Greb et al. 2018; Huisman et al. 2018; Ho et al. 2019). This increase might be considered as the result of climate warming (Visser et al. 2016), and the excess of nutrients originating from fertilizers (Burkholder et al. 2006; Czerny et al. 2009). Prevention of harmful algal blooms is very difficult due to the broad spectrum of its causes. As a result, early warning systems (EWSs) based on monitoring technologies are being developed and employed to decrease the negative impacts of HABs (Anderson 1994; Stumpf et al. 2009; Jochens et al. 2010; Wynne et al. 2010).

Many EWSs have been developed, but problems remain. For example, although it is known that environmental parameters, such as increasing nutrients (Heisler et al. 2008) and water temperature

(Jaworska and Zdanowski, 2011), effectively contribute in phytoplankton blooms, the accurate spatial and temporal trends of blooms cannot be determined so far due to their dynamic nature and the limitations in monitoring resources and datasets (Ehrlich, 2010). Consequently, although many efforts (Jaworska and Zdanowski, 2011; Anderson et al. 2013; Cyr, 2017; Cameron, 2021), there is lack of information about how blooms form, how they spread over time and space, and how they finally die-off (Huisman et al. 2018). Additionally, although many of the monitoring networks and shipboard sampling systems are suitable for small-scale studies, they are insufficient for operational applications that occur in large scales and change rapidly in time and space (Springer et al. 2005). Instead, satellite or airborne observations are capable of providing huge amounts of data from a large area in a short time (Franz et al. 2005; McCain et al. 2006).

Near-surface concentration of chlorophyll-*a* (Chl*a*) is one of the most important proxies of HABs as Chl*a* is ubiquitous in all phytoplankton types including cyanobacteria (Roesler et al. 2017) and has unique absorption features that can be detected through satellite imaging (Gordon et al. 1980; Gordon et al. 1983; Kutser 2009). Therefore, it can be considered as a key parameter in most EWSs based on remote sensing technologies. To date, remotely-sensed Chl*a* estimates have been applied successfully to large waterbodies, including the open ocean (Gordon et al. 1980; Morel 1980; O'Reilly et al. 1998; Bryan et al. 2005; O'Reilly and Werdell 2019), coastal waters (Werdell et al. 2009; Moses et al. 2012), and large lakes (Gons et al. 2008; Binding et al. 2011b; Schaeffer et al. 2018; Binding et al. 2021), using ocean-color sensors such as the Medium Resolution Imaging Spectrometer (MERIS) and the Sea-viewing Wide Field-of-view Sensor (SeaWiFS). In contrast, Chl*a* retrieval for SIWs has been challenging because the optical properties of inland waters are modulated by particulate organic and inorganic particles, as well as colored dissolved organic matter (CDOM) (Mobley 1994), and there are many sources of uncertainty, such as adjacency effects, in satellite-derived radiometric quantities. In addition, ocean-color sensors with daily revisit temporal resolution lack sufficient high spatial resolution (<100m) to sample SIWs (Philipson et al. 2014; Ansper and Alikas 2019). Given the fact that a significant number of optical satellite observations can be obscured by cloud cover over waterbodies (Li and Roy 2017), the low temporal resolution of terrestrial missions (e.g., Landsat-8 and Sentinel-2) might limit their application in water quality monitoring.

## 1.2 Objectives and Contributions

The overall goal of this thesis is to investigate the possibility of developing early warning systems for harmful algal blooms in small inland waters using remote sensing technologies. Given *Chla* as an ubiquitous HAB indicator retrievable by remote sensing observations, this study specifically seeks new ideas and approaches to map and monitor *Chla* in SIWs using medium-resolution space-borne missions (~ 10 – 60 m).

This thesis introduces new models and approaches to retrieve *Chla* using medium-resolution terrestrial missions, i.e., Landsat-8 and Sentinel-2, in small inland waters. The proposed models are compared with traditional well-known ones to examine their strengths and weaknesses. Model development and assessment are based on extensive *in situ* data collected in several small lakes in Qu'Appelle River drainage basin, Saskatchewan; one of the largest watersheds in Canada. The thesis contains three journal articles that represent a framework for developing EWSs based on *Chla* monitoring in SIWs.

The first article demonstrates that field fluorometry measurements should be calibrated before being fed into remote sensing models. A calibration model using phycocyanin (PC) fluorescence significantly improved *in vivo* *Chla* measurements, thereby decrement of errors in remote *Chla* retrieval by 30% and increment in the range of reconstructed *Chla* values. The results of the first article were then employed to build a consistent dataset of *in situ* *Chla* in Buffalo Pound Lake (BPL), which was used as a training site for developing machine learning models for *Chla* retrieval.

In the second article, we developed a retrieval model based on support vector regressions (SVRs), which outperformed state-of-the-art models when applied to BPL. The robustness and superiority of the proposed models were analyzed in various experiments and their reasonable transferability over two different OWTs was shown.

In the third article, SVR models were employed in regional approaches to retrieve *Chla* in the remaining lakes in the watershed. The accuracy of *Chla* retrieval in these lakes suggests that regional approaches based on machine-learning (ML) models are suitable for developing EWSs based on *Chla* monitoring in SIWs.

### 1.2.1 Structure

This manuscript-based thesis consists of six chapters. The current chapter presents the rationale and objectives of the thesis, outlining the need for monitoring *Chla* concentration in small waterbodies, and coupling the satellite-based observations of *Chla* in early warning systems for harmful algal blooms. Chapter 2 provides a theoretical background of biological/physical aspects of harmful algal blooms, phytoplankton, and *Chla*. It then moves to explain principles of theory of remote sensing of water color, followed by a literature review of remote sensing of HABs and *Chla*. Chapter 3 addresses a solution for a common issue of *in situ* data, i.e., inconsistencies between *in vivo* and *in vitro* measurements. This solution was then used in Chapter 4, where machine-learning models were developed to retrieve *Chla* in a small lake. Chapter 5 introduces a regional approach for extrapolation of locally trained ML models to regional retrieval of *Chla* in a large lake catchment. Finally, Chapter 6 provides a summary of key findings of the research as well as future research directions. Appendix A also demonstrates an application of the methods presented in Chapters 4-5 in mapping and monitoring of marked blue discolouration of late winter ice and water due to autumn blooms of cyanobacteria.

## **Chapter 2**

### **Background**

#### **2.1 Introduction**

This chapter includes two sections, each section covering the pertinent background to the research in this study. Section 2.2 defines some biological/limnological terms and describes important physical, chemical, and biological aspects of algal blooms. Section 2.3 begins with principles of remote sensing of water color and continues with a literature review on remote sensing of HABs and Chl $a$  estimation in waterbodies.

#### **2.2 Algal blooms; physical, chemical, and biological (PCB) aspects**

##### **2.2.1 Phytoplankton, blooms, and HAB definitions**

Phytoplankton, the planktonic organisms that float in the water column or on the surface of water, comprise a group of diverse organisms ranging from unicellular to multicellular and from bacterial to eukaryotic kingdoms (Reynolds, 2006). Although so diverse, they share the same characteristics, giving them the same ecosystem functionality. Most phytoplankton are primary producers; they absorb sunlight, carbon dioxide, water, and nutrients as their food and produce organic compounds and oxygen through photosynthesis (Guschina and Harwood, 2006). Therefore, they are the foundation of marine food chains, making the lives of all marine animals and habitats dependent on them (Reynolds, 2006). In addition, they are a major source of oxygen in the atmosphere (Falkowski, 2012), especially the cyanobacteria, also called blue-green algae, which are considered to be responsible for the creation of the earth's aerobic atmosphere around 2 billion years ago (Demoulin et al. 2019). However, phytoplankton can be harmful when they block the light from reaching other organisms in water, and later when they die-off and deplete water column oxygen (Paerl and Otten, 2013). These harmful blooms, which can be associated with releasing toxins into water (Paerl and Otten, 2013), pose a serious threat to freshwaters and cause public health concerns.

Although no completely acceptable definition of a bloom exists (Smayda 1997a; Smayda 1997b; Ho and Michalak 2015), it is usually defined as an increase of phytoplankton biomass in a waterbody over a relatively short time (between a few days and one or two weeks) in which only one

or a few species have a dominance of more than 80% (Meriluoto et al. 2017). However, in this definition the increase rate has not been determined, and is a variable based on phytoplankton taxonomy, water type, water usage, and so on. For example, whereas a biomass from 30-50  $\mu\text{g L}^{-1}$  in a mesotrophic or less-eutrophic waterbody can be counted as a large bloom, a biomass in the range of 300-400  $\mu\text{g L}^{-1}$  in eutrophic or hypereutrophic lakes can be considered a bloom (Meriluoto et al. 2017). Furthermore, in many studies, especially those focused on the remote sensing of algal blooms, the concept of “rapid growth” is replaced by the concept of “intense accumulation of a singular species of phytoplankton” as this definition makes it easier to identify what a bloom actually is (Wynne et al. 2013). Additionally, for brevity, in this manuscript, the term “algal bloom” is used to refer to phytoplankton blooms.

Among various phytoplankton types, those that release toxins, and in particular microcystin, are considered as harmful algal blooms (WHO 2003; EPA 2015; Health Canada 2020). The mechanisms by which phytoplankton harm ecosystems differ, and Smayda (1997a) counted at least eight mechanisms for doing so. However, according to some studies (Paerl et al. 2001; Ho and Michalak 2015), these mechanisms can be categorized in three distinct categories, based on how they harm ecosystems; (a) a high intensity of any type of phytoplankton in the water column that decreases other organisms’ access to light and oxygen, (b) a high or moderate intensity of specific types of phytoplankton with certain toxicities and functionalities that can harm other organisms, and (c) an expanse of phytoplankton on the water surface, called a scum, is harmful as it blocks sunlight penetration.

### **2.2.2 The relation of algal blooms to PCB parameters**

Even though no unique cause has been identified for algal blooms, scientists have identified two categories: anthropogenic and natural (Iiames et al. 2021). Both cause blooms through making favorable environmental conditions for phytoplankton growth. Among all, light, temperature, nutrients, organic matters, stratification, and buoyancy regulation, as well as ecological competition as the most important environmental parameters that influence phytoplankton growth (Wetzel 2001; Paerl and Otten 2013). Here, we examine the effects of these factors on phytoplankton growth and algal blooms. A more-comprehensive discussion of these factors and their influences can be found elsewhere (Paerl et al. 2001; Wetzel 2001; Reynolds 2006; Paerl and Otten 2013).

### 2.2.2.1 Light and Heat

Although light and heat are two different parameters influencing phytoplankton, their effects are inseparable because sunlight is the main source of heat in waterbodies, and also temperature affects the relationship between phytoplankton metabolisms and light saturation (Reynolds, 2006). Light and heat affect both productivity (photosynthesis rates) and algal growth rate (Gutierrez-Wing et al. 2014; Yang et al. 2017), and are examined in the form of three parameters: light intensity (irradiance), day length, and temperature.

The vertical distribution of phytoplankton in water columns strongly relates to light availability (Mellard et al. 2011). Light intensity in a water column exponentially decreases, as a function of wavelength, with increasing depth. Equation 2.1 computes available irradiance ( $I_z$ ) at the depth  $z$ , where  $I_0$  is downwelling irradiance just below the surface of water, and  $k_d$  is the diffuse attenuation of downwelling irradiance, directly (in the visible range) depending on wavelength. The formula shows that most sunlight is absorbed in the first centimeters of water columns, and as a result, most heat is dedicated to this part. The depth at which the intensity of light (photosynthetically active radiation in 400-700 nm) is enough for photosynthesis is called the euphotic depth or photic zone, where most phytoplankton float.

$$I_z = I_0 e^{-k_d z} \quad (2.1)$$

Light intensity affects both algal-growth and productivity rates (Gutierrez-Wing et al. 2014; Krzemińska et al. 2014). Although phytoplankton's response to light intensity is species-specific, and also after a while many types of adaptations are applied by phytoplankton in high and low light intensities (Carey et al. 2012), the general trends of light-intensity reaction are alike for all phytoplankton types. One can say that productivity and algal growth increase with increasing light intensity until they reach a maximum, above which productivity and growth rates are saturated (Singh and Singh, 2015). Then, productivity and growth rates remain constant for a range of irradiance, only decreasing if light intensity passes a threshold, due to the phenomenon called photo-inhibition in which light intensity denatures the enzymes in phytoplankton (Singh and Singh, 2015). This explains why surface phytoplankton sometimes deteriorate due to UV (ultraviolet) exposure. Figure 2.1 (a) illustrates the trend of algal growth in relation to light intensity.

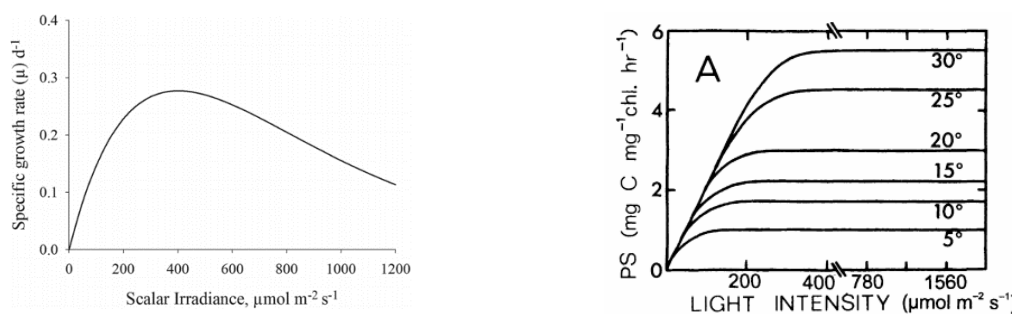


**Figure 2.1. (a) The relationship between irradiance and phytoplankton growth rate computed as biomass change per day (Gutierrez-Wing et al. 2014). (b) The relationship between irradiance and phytoplankton productivity (produced carbon per unit Chla per hour) at different temperatures (Wetzel 2001).**

In addition, as Figure 2.1.b shows, irradiance effect on growth rate and productivity depends on temperature. Figure 2.1.b also proves that as long as the minimum temperature for phytoplankton bioactivity is supplied, and temperature and light intensity remain below the rate of saturation, algal growth and productivity are independent of temperature. The minimum temperature for starting the chemical reactions leading to photosynthesis is about 5°C for most phytoplankton, whereas the temperature for enzymes denaturation and in turn productivity reduction is often about 35°C. The optimum temperature for most phytoplankton types is 20°C to 30°C (Robarts and Zohary 1987; Béchet et al. 2013). However, the reaction to temperature varies greatly between different kinds of phytoplankton (Singh and Singh 2015), and it also changes with adaption abilities. For example, diatoms have productivity in temperatures even below 5°C (Butterwick et al. 2005), and cyanobacteria can tolerate high temperatures, sometimes more than 45°C (Wetzel 2001). Some types of algae can adapt to even 40°C after a short time (~ 5 day) (Béchet et al. 2013), or even manage higher temperatures in hot springs (Nikulina and Kocielek, 2011). Additionally, different types of algae show great diversity in growth (0.3-1.7 divisions  $day^{-1}$ ) at their optimum temperatures (Butterwick et al. 2005). In addition, temperature changes the intensity of light in which phytoplankton productivity and growth rate saturate. Most algae show higher productivity and growth rates with a temperature increase above their saturation point and before their inhibition point (Singh and Singh 2015). It is worth mentioning that indirect temperature effects, such as water mixing or stratification, might have a more significant influence on phytoplankton than direct ones (Robarts and Zohary 1987).

The other important factor for algal growth rate is day length, meaning the time that phytoplankton receive sunlight. Although growth rate has a direct relationship with day length (Bouterfas et al. 2006), studies have proved that continuous irradiance does not necessarily increase growth rate and productivity because of a phenomenon called “flashing-light effect”, meaning that phytoplankton need a minimum time (~100 millisecond) to react to an absorbed photon, and during that time they absorb no other photons (Béchet et al. 2013).

#### 2.2.2.2 Nutrient availability

Basically, phytoplankton absorb nutrients (mostly nitrates and phosphorous), light, and CO<sub>2</sub> to release oxygen and organic components (Reynolds, 2006). All phytoplankton have the capability of carbon fixation by which they absorb carbon directly from atmospheric CO<sub>2</sub> or CO<sub>2</sub> dissolved in the water column (Irion et al. 2021). Thus, carbon is not generally a limiting factor for phytoplankton growth. In contrast, nitrates and phosphorous do limit phytoplankton growth (Bristow et al. 2017). Despite some exceptions, nitrates are limiting factors in marine environments, and phosphorous is one in inland waters (Maberly et al. 2020). Although the absolute amounts of nutrients are important for algal growth, the ratios between different nutrition types in general, and N/P (nitrogen/ phosphorous) specifically, play a more important role in the competition and succession of phytoplankton types (Rhee 1978).

Nitrogen is available in the atmosphere, water and soil. Unlike some types of cyanobacteria that can fix atmospheric nitrogen, most phytoplankton cannot. As a result, most phytoplankton supply their needs for nitrates from soil and water (Paerl and Otten, 2013). In water ecosystems, thanks to bacteria, most nitrates are supplied through decomposed organic matters (Wetzel, 2001). Nitrates are also transported and deposited to water from soil sources and fertilizers (Paerl and Otten, 2013). Unlike nitrates, phosphorous does not exist in the atmosphere and is mostly supplied by soil, rocks, and decomposed organic matter. It is the most limiting factor in inland water blooms (Maberly et al. 2020), especially for the cyanobacteria blooms that are the primary producers of toxins in freshwater (Backer 2002). It has been proven that cyanobacteria tend to bloom in eutrophic waters (phosphorous concentration > 50 mg L<sup>-1</sup>) (Meriluoto et al. 2017). In blooms in which diatoms are the dominant species, silica, the other nutrient, can be a limiting factor. This situation usually happens in fall blooms in temperate lakes (Wetzel 2001). In fact, transition between the states of nitrates, phosphorus and silica

limitations, a very common seasonal phenomenon in lakes, is critical to the succession and dominance of phytoplankton types in an aquatic ecosystem (Andersson et al. 2015).

### 2.2.2.3 Water turbulence and phytoplankton flotation

Water turbulences and phytoplankton flotation are linked factors that must be examined together. Both impact the availability of light and nutrition for phytoplankton as well as predation by zooplankton, thereby impacting the population, growth rate, and productivity of phytoplankton (Smayda, 2002). Flotation is crucial for phytoplankton because sinking out of the photic zone is fatal for most types (Meriluoto et al. 2017). Moreover, movement through a water column, either sinking or floating, can benefit phytoplankton by increasing their exposure to nutrients (Liu et al. 2019). Parameters such as density, particle size, shape, mucilage production, gas vacuoles, accumulation of hydrocarbons, and swimming ability regulate phytoplankton flotation. Most freshwater phytoplankton have a density slightly more than water, leading them to sink in undisturbed water (Wetzel 2001). Nonetheless, gas vesicles give some types of cyanobacteria a density less than water, causing them to float and form scum on water surfaces (Liu et al. 2019). Furthermore, since phytoplankton sinking rates follow Stoke's law, in which larger particles sink faster, small phytoplankton, such as single-cell cyanobacteria, have a lower sinking rate. Shape also affects phytoplankton sinking rates; the greater the surface-to-volume ratio, the slower the sinking velocity (Meriluoto et al. 2017).

Apart from flotation, water turbulence has many impacts on phytoplankton. Since most algae lack gas vacuoles, they depend only on water turbulences to remain in the photic zone (Wetzel 2001). Moreover, water movement due to wind, solar heating, tides, earth's rotation, and water inputs, transport nutrients from depth to surface and concentrate or disperse phytoplankton patches (Reynolds, 2006). In most cases, wind is the most significant contributor to turbulence (Ren et al. 2018). The formed phytoplankton paths move in the direction of wind. Wind concentrates more-buoyant phytoplankton such as *Microsytis* on downwind shores, whereas the return currents from shores accumulate less-buoyant phytoplankton on upwind shores (Smayda, 2002).

As long as no wind is interrupting the water column and no cold air above water is receiving heat from the water, warmer water remains above colder water and prevent any turbulence because of its lower density. This phenomenon, which mostly occurs in small temperate lakes in summer and winter (frozen lakes), is called stratification and provides favorable conditions in which cyanobacteria

proliferate and outperform algae, thanks to the former's vertical motility in the water column, and the latter's tendency to sink (Paerl and Otten, 2013). Furthermore, cyanobacteria can tolerate high temperatures and irradiance, which normally are the results of stratification. They can also bloom under nitrogen-limited conditions, a result of stratification, thanks to their N<sub>2</sub>-fixing capability (Reynolds, 2006). Further, thermal stratification leads sediments to release phosphorus (Meriluoto et al. 2017), the limiting factor for cyano-blooms in most freshwaters, thereby indirectly making conditions favorable for cyanobacterial, which can move through entire water column in shallow waterbodies.

Due to the many influential environmental parameters and the variety of phytoplankton types, one cannot say that turbulence or stratification processes are totally favorable for phytoplankton or not (Paerl and Otten, 2013). In fact, the results of turbulence-stratification processes totally depends on other environmental factors as well as phytoplankton types (Smayda 2002). For example, if limited light-conditions exist in a temperate lake in mid-winter, stratification might help phytoplankton to fix their positions in a stable environment and make some adaptations for this low light and temperature environment. In contrast, for a tropical lake in summer, vertical turbulence reduces the duration of phytoplankton's sun exposure, thereby leading to less photo-inhibition (Wetzel, 2001). As another example, unlike in deep lakes in which vertical turbulence sink algae to below to photic zone, in shallow lakes, turbulence can cause more proliferation as the entire column is in the photic zone.

Moreover, algae types vary in their tolerance of the shear stress resulting from turbulence (Thomas and Gibson 1990; Hondzo and Lyn 1999). Both low and high turbulence rates have been proved to decrease cell division and algal growth rates for some types of phytoplankton. In general, a sufficient turbulence depth and rate is needed to provide phytoplankton with new sources of nutrients, more flotation, and resultant light/dark cycles of medium frequency (Talling 1966; Grobbelaar 1994). Meanwhile, it should be not so much that phytoplankton sinks below the photic zone, preventing them from obtaining sufficient light, and damaging their structures.

## **2.3 Remote sensing of algal blooms**

### **2.3.1 Principles of HAB remote sensing**

The color of water, or normalized water-leaving radiance ( $nL_w$ ), which is the radiance that would exit the water with the sun at the zenith and with mean earth-sun distance, is determined by the properties

of various colored constituents of water, namely water molecules, phytoplankton, colored dissolved organic matter (CDOM), detritus, suspended sediments, and bottom reflectance (if the water is optically shallow) (Gordon and Clark, 1981; Werdell et al. 2018). The ultimate aim of ocean (water) color remote sensing is solving an inverse problem: retrieving these water constituents, which are among the water quality parameters, from sensed radiance. A list of water quality parameters that can be directly or indirectly retrieved from remote sensing has been provided in Platt et al. (2008). HABs should be quantified with criteria that are good indicators of phytoplankton and can be accurately retrieved from  $L_w$ . Table 2.1 lists the criteria that have been employed as indicators of HABs in different studies on Lake Erie.

Type	Criterion	References
Abundance	Cell counts	(Wynne et al. 2010)
	Biomass	(Conroy et al. 2005)
	Biovolume	(Bridgeman et al. 2013)
	Chlorophyll- <i>a</i> concentration	(Davis et al. 2012)
Species-specific	PCR DNA presence	(Dyble et al. 2008)
	Percent cyanobacteria or <i>Microcystis</i>	(Vincent et al. 2004)
Toxicity	Microcystin concentration	(Rinta-Kanto et al. 2009)
	Toxigenic <i>Microcystis</i> presence	(Rinta-Kanto et al. 2009)
Qualitative	Surface scum presence	(Vincent et al. 2004)

**Table 2.1. Criteria that have been employed as indicators of HABs in different studies on Lake Erie, modified from Ho and Michalak (2015).**

In visible wavelengths, assuming phytoplankton as the only constituents in water and ignoring the effects of pure water's inherent optical properties (IOPs) and illumination conditions,  $L_w$  is determined by phytoplankton absorption ( $a_\phi$ ) and phytoplankton backscattering ( $bb_\phi$ ). The former is mostly determined by light absorption by phytoplankton pigments, while the latter is mostly characterized by the abundance, size, and shape of phytoplankton. Thus, under ideal conditions,

pigment concentration, cell abundance, and even phytoplankton type can be retrieved in an inversion process; however, this is not the case under real conditions.

Water color sensors measure the spectral radiance emerging from the top of the atmosphere,  $L_{TOA}$  at discrete wavelengths. Overall, there are many approaches to retrieve IOPs from satellite measurements. Most of these approaches use atmospheric processors to remove the effect of the atmosphere from  $L_{TOA}$  and retrieve remote sensing reflectances ( $R_{rs}$ ).  $R_{rs}$  is calculated as the ratio of water-leaving radiance ( $L_w$ ) to downwelling irradiance ( $E_s$ ), just above the air-water interface. Satellite-derived  $R_{rs}$  values can also be corrected for dependency to solar zenith angle and viewing direction to obtain exact reflectance just above the water surface ( $\rho_w^N$ ) (Mobley, 1994). Algorithms are then applied to reflectance values to produce estimates of water constituents.

Top-of-atmosphere radiometric quantities should be corrected for atmospheric effects before being used in retrieval models. When a sensor views waterbodies from space, it measures upwelling radiances that can include the water surface, the atmosphere, and the water column contributions. The atmospheric contribution, which can be up to 90% of total radiance (Werdell et al. 2018), is the result of solar radiance, scattered by atmospheric gases and aerosols. Radiance at the sensor contains information about the atmosphere; however, only the water-leaving radiance carries information about the water column (Mobley et al. 2016). A sensor cannot separate the various contributions, so atmospheric correction (AC) process is the process of removing the contributions by atmospheric scattering from the measured top-of-atmosphere radiance to obtain the water-leaving radiance. Robust Atmospheric correction is essential for the accurate retrieval of aquatic reflectance and water constituents from remote sensing observations. Models for atmospheric correction over the open ocean is have been developed for decades, but over inland and coastal waters inaccurate AC still leads to large uncertainties in satellite data products and limits the accuracy of water constituents retrieval.

Since early works in the 1980s (Morel and Prieur 1977; Gordon et al. 1980; Morel 1980; Gordon et al. 1983), it has been demonstrated that pigment concentration, especially Chl $a$ , which exists in all phytoplankton types, has a good correlation with  $L_w$ , so it is easier to remotely retrieve than other criteria. Furthermore, field and laboratory measurements of Chl $a$  concentration are less time- and cost-consuming in comparison to other criteria such as cell abundance and toxin concentration. As a result, there is a historical tendency to use Chl $a$  in algal bloom detection and monitoring, and many efforts

have been carried out to develop algorithms to retrieve this parameter from remote sensing images (Gordon et al. 1983; O'Reilly et al. 1998; Kutser 2009; Matthews 2011; Odermatt et al. 2012).

Based on the above-mentioned criteria, some remote sensing algorithms have been developed and employed to detect, identify, and map blooms around the world (Ruddick et al. 2003; Shen et al. 2012; Blondeau-Patissier et al. 2014). Whereas some algorithms have been implemented in operational EWSs (Stumpf et al. 2003; Wynne et al. 2013), most are in preliminary development stages and need to be further investigated. In addition, some algorithms are only used to detect phytoplankton blooms, whereas some are employed in identification of bloom species, as well. Furthermore, most of these algorithms are usable only in ecosystems where phytoplankton are the primary water constituent (Morel and Prieur 1977; Morel 1980), while some are suitable for more turbid waters, discussed in section 4.1.

### **2.3.2 HAB retrieval algorithms**

#### **2.3.2.1 Reflectance-classification algorithms**

These algorithms use supervised and unsupervised classification approaches to assign the reflectance spectra of pixels to a specific spectral categories, either HAB or non-HAB. They usually detect and identify HABs simultaneously. Previous studies demonstrated that different species-specific pigments might lead to distinguishable spectra for four major phytoplankton types, namely *haptophytes*, *Prochlorococcus*, *Synechococcus*-like cyanobacteria and diatoms (Alvain et al. 2005; Alvain et al. 2008). Their method, called PHYSAT, detected and distinguished these major types in SeaWiFS images at the global scale. Adding spectral reflectance for coccolithophore blooms in North Atlantic to a previously-developed spectral library, included eight spectra from different non-bloom types of waters around the world (Moore et al. 2009), led to a probability map for coccolithophore blooms using a fuzzy c-means algorithm (Moore et al. 2012). The method was tested on SeaWiFS, MODIS-Aqua, the Coastal Zone Color Scanner (CZCS), as well as MERIS, and showed reasonable results. In addition, a classification approach based on linear discriminant analysis (LDA) was applied on SeaWiFS data of the Baltic Sea and southwest coast of the UK and distinguished *Karenia mikimotoi*, *Chattonella verruculosa*, and cyanobacteria from non-bloom and harmless-bloom classes (Miller et al. 2006). They also used a *Chla*-median subtraction technique (i.e. subtracting the

median of Chla from estimated Chla) to reduce the false positives of the classifier caused by non-harmful blooms and by high level of sediment in water.

Due to their weak physical basis, if any, reflectance-classification algorithms are totally region-based and should be tuned for each new study site. Although the tuning might be justifiable in big waterbodies, this is not the case in small lakes, due to their abundance. However, these algorithms are promising for water-type classification and also for detecting scum. In addition, their results are often qualitative; however, some methods have been developed to assign intensities to detected blooms. For instance, a classification approach in which imported features are normalized water-leaving radiances in six bands of MODIS and MERIS, as well as some ratios applied on water-leaving radiances and absorption and backscattering coefficients resulted in an identification accuracy of 89% for *Phaeocystis globosa* in the southern North Sea and 88% for *Karenia mikimotoi* in the Western English Channel (Kurekin et al. 2014). They also proposed a formula to compute a HAB density based on feature vectors. Their HAB density criterion showed a better correlation with algal cell counts than Chla derived from MODIS standard algorithms. Even though they argued that their proposed method outperforms Chla-based methods (discussed later) in terms of bloom intensity estimation, and also is robust to different sensor bands and calibration errors, it needs more investigation.

#### 2.3.2.2 Band-ratio algorithms

Band ratios have been the most-used remote sensing algorithms to estimate Chla as a proxy for phytoplankton (Kutser 2009; Matthews 2011; Odermatt et al. 2012). Almost all standard Chla retrieval algorithms for EWSs are based on the reflectance or radiance of blue to green bands, based on Chla absorption in ~430 nm. The most well-documented EWS, developed for monitoring harmful *Karenia brevis* blooms in the Gulf of Mexico, is based on a modified blue-green band-ratio algorithm for SeaWiFS (Tomlinson et al. 2004). Subtracting estimated Chla from a mean Chla over previous two months obtained a Chla anomaly map (Stumpf et al. 2003). Then, applying a  $1 \mu\text{g L}^{-1}$  threshold equal to 100000 cells  $\text{L}^{-1}$ , they detected phytoplankton blooms and then recognized the late spring and early summer ones as harmful *Karenia brevis* blooms, which was the dominant species at the region in late spring and early summer. Further evaluation showed an accuracy of  $> 83\%$  for this approach (Tomlinson et al. 2004). In later studies, they attempted to reduce the false positive rate of the approach by introducing certain environmental factors (Stumpf et al. 2009), using an ensemble strategy

(Tomlinson et al. 2009), and applying an algorithm to reduce the effects of sediment interference (Wynne et al. 2005).

Although they are widely applicable, blue-green algorithms have some problems. They usually overestimate  $Chla < 0.2 \mu\text{g L}^{-1}$  (Volpe et al. 2007), a range that is not the case in inland and coastal waters. The most important problem is that CDOM significantly absorb light in the blue region and consequently have a too-great impact on water-leaving radiance, causing these algorithms fail in case 2 waters. Another blue-green band ratio, called RI, reasonably detected red-tide blooms and estimated  $Chla$  in the optically complex waters of Korean and Chinese coasts (Ahn and Shanmugam 2006); however, results might be regional and not generable.

Other band-ratio algorithms rely on red and NIR bands, where CDOM and total suspended matter (TSM) make much less contribution to light absorption in another  $Chla$  absorption band at  $\sim 665$  nm (Bernard et al. 2005). Studies show that these band ratios can estimate  $Chla$  up to  $100 \mu\text{g L}^{-1}$  (Blondeau-Patissier et al. 2014). Red-NIR band ratios can also use the scattering characteristics of phytoplankton, and by doing so identify phytoplankton types based on their size and shape. However, TSM backscattering and pure water absorption still interfere with phytoplankton backscattering in the red-NIR region. There is also the phycocyanin (PC) absorption peak ( $\sim 620$  nm) in this region, which can be used to estimate cyanobacterial biomass. However some research has shown that current multispectral technologies cannot accurately retrieve PC (Kutser 2009; Matthews 2011) probably due to lack of a specific band at PC absorption wavelength ( $\sim 620$  nm). It should be noted that every band-ratio algorithm, no matter what bands it uses, is very sensitive to incomplete atmospheric correction (AC) (Philpot 1991), which is a critical and challenging issue in water-color remote sensing (Mobley et al. 2016). The problem becomes worse in blue-green band ratios because of the greater sensitivity of blue and green bands to imperfect AC. Another disadvantage of these empirical methods is that they are region-based and should be tuned for other regions, due to their weak physical basis.

### 2.3.2.3 Band-difference algorithms

The second-order derivative of a spectral reflectance can be less sensitive to an inaccurate AC (Philpot 1991). In a discrete spectral reflectance, acquired from satellite images, the second-order derivative can be simplified to a band difference algorithm based on three bands. Therefore, many studies have proposed various difference algorithms mostly place in the red-NIR region to capture the different

characteristics of water-leaving radiance. For example, fluorescence line height (FLH) (Letelier and Abbott 1996) was designed to capture Chl $a$  fluorescence peak height in 681 nm, with forming a baseline using two bands, one shorter and one longer than the fluorescence band. FLH is less sensitive to interference by other absorbing suspended matters and does not saturate at high chlorophyll- $a$  compared to the algorithms that rely on radiance measurements at 443 nm (Letelier and Abbott 1996). Superior results of FLH in relative and absolute Chl $a$  estimation as well as detecting dinoflagellate *Karenia brevis* in coastal waters of SW Florida were shown (Hu et al. 2005). It was also indicated that coupling bloom detection algorithms with an FLH criterion can improve their performance (Soto et al. 2015). However, in Lake of the Woods, FLH could not provide a reasonable Chl $a$  estimation during an intense cyanobacterial bloom (Binding et al. 2011a), which was expectable due to the different fluorescence mechanisms of cyanobacteria compared to algae (Simis et al. 2012; Tomlinson et al. 2016).

In addition, maximum chlorophyll index (MCI) (Gower et al. 2003) was mainly developed to capture the high concentration of phytoplankton via their strong backscattering after 700 nm and before the high absorption of water (~709 nm). Thus, this index has a potential to have a stronger correlation with phytoplankton cell counts, disregarding Chl $a$ . Although MCI has been used to monitor algal blooms around the globe (Gower et al. 2008; Alikas et al. 2010; Binding et al. 2013; Matsushita et al. 2015), it did not show good results for Chl $a$  of less than 30  $\mu\text{g L}^{-1}$  (Gower et al. 2005) or with sensors that lack a spectral band in 709 nm. MCI reasonably retrieved Chl $a$  during an intense cyanobacterial bloom in Lake of the Woods (Binding et al. 2011a). However, their study only included bloom detection, and did not discriminate between bloom types. FAI (Hu 2009), another band-difference algorithm, has been developed to detect floating phytoplankton and plants on water surfaces. Hence, it can be applied to detect cyanobacterial scum. For instance, it was used to detect and identify surface mats of *Trichodesmium* (an ocean cyanobacteria) in MODIS imagery (Hu et al. 2010).

Cyanobacteria Index (CI) (Wynne et al. 2008) is based on the theory that, unlike algae, cyanobacteria have much less fluorescence in 681 nm. In addition, cyanobacteria backscattering is more than that of algae in >700 nm because of their smaller size (Ahn et al. 1992; Matthews et al. 2012). As a result, the  $R_{rs}(681)$  (remote sensing reflectance) of water that contains cyanobacteria is expected to fall below the baseline that is defined as a straight line drawn between  $R_{rs}(665)$  and  $R_{rs}(709)$ . A

strong relationship between CI and cell counts of cyanobacteria in Lake Erie was also reported elsewhere (Wynne et al. 2010). The relationship was later approved for the estimation of cyanobacterium *Microcystis aeruginosa* concentrations over a large number of disparate lakes in the eastern US (Lunetta et al. 2015). Their results suggest that MERIS provides robust estimates (~90% and ~83%) for low (10,000–109,000 cells/mL) and very high (> 1,000,000 cells/mL) cyanobacteria concentrations, respectively. Furthermore, good agreement between CI and *Chla* for a wide range of *Chla* (16 to 115  $\mu\text{g L}^{-1}$ ) in six cyanobacteria-rich, stratified lakes in Florida was reported elsewhere (Tomlinson et al. 2016). Similar results have been seen in other lakes around the world (Moradi 2014; Palmer et al. 2015). CI was also employed in an operational EWS to detect, identify, and map cyanobacterial blooms in Lake Erie (Wynne et al. 2013). It can distinguish harmful cyanobacteria *Microcystis* blooms from non-bloom and non-harmful blooms. It should be mentioned here that before launching Sentinel-3A (S3A) and Sentinel-3B (S3B) in 2016 and 2018, respectively, MERIS was the only sensor that had a spectral band centered at 681 nm, used in the CI. Employing S3A and CI index, (Clark et al. 2017; Schaeffer et al. 2018) took steps towards developing EWSs for small inland waters based on satellite monitoring.

Another algorithm, called maximum peak height (MPH) (Matthews et al. 2012), has been designed to estimate *Chla* in eutrophic lakes and to detect cyanobacteria blooms as well as surface scum. To apply the index, a sensor needs to have five well-located spectral bands in the red edge-NIR region. The advantage of the algorithm is that atmospheric aerosol correction is unnecessary, as it is very challenging over turbid inland waters. The algorithm was also applied to MERIS dataset to provide 10-year time series of cyanobacterial blooms for the 50 largest standing waterbodies in South Africa, most of which were hypertrophic ( $\text{Chla} > 30 \text{ mg m}^{-3}$ ) (Matthews 2014). Further analysis and improvements indicated the superiority of MPH over MCI and FLH and also its capability to be employed for monitoring cyanobacteria over a great range of inland waters at the global scale (Matthews and Odermatt 2015).

#### 2.3.2.4 Machine-learning models

Among statistical algorithms, machine-learning (ML) algorithms, such as neural networks (NN), are commonly used in *Chla* retrieval. For example, the European Space Agency (ESA) estimates *Chla* from MERIS benefiting NN models (Doerffer and Schiller 2007; Schroeder et al. 2007). Likewise,

Multilayer Perceptron (MLP) was applied on MERIS data to retrieve Chla in coastal waters with root mean square errors (RMSE) of  $\sim 0.8 \text{ mg m}^{-3}$  for a Chla range of  $0.03\text{-}8 \text{ mg m}^{-3}$  (Vilas et al. 2011). Support Vector Machines/Regressions (SVM/SVR) (Vapnik 2013) have been also applied to oceanic waters (Haigang et al. 2003; Kwiatkowska and Fargion 2003; Camps-Valls et al. 2006; Martinez et al. 2020; Hu et al. 2021) with various reported performance. SVR uses an  $\varepsilon$ -insensitive (a threshold) cost function in which errors ( $e_i$ ) up to  $\varepsilon$  are not penalized, whereas further deviations are penalized using a linear function, i.e.,  $L(e_i) = \max(|e_i| - \varepsilon, 0)$ . Thus, SVR is more robust to small errors and inherent uncertainties of training data (Zhan et al. 2003), compared to traditional linear regressions or neural networks.

In addition, applying Mixture Density neural Networks (MDN) to a large dataset of *in situ* radiometry and Chla measurements allowed development of a model which outperformed other state-of-the-art algorithms for a wide range of Chla concentration ( $0.1\text{-}100 \text{ mg m}^{-3}$ ) using MSI and OLCI data (Pahlevan et al. 2020), as well as OLI data (Smith et al. 2021). Additionally, Cao et al. (2020) developed BST, a model based on the Gradient Boosting Tree algorithm (XGBoost) (Chen and Guestrin 2016), and successfully tested it on OLI data taken from lakes in eastern China; the model, however, was outperformed by MDN when applied to a global dataset (Smith et al. 2021). Machine learning models (e.g., MDN) can leverage the full visible and near-infrared spectrum (VNIR) and may handle non-linear and ill-posed problems. However, they can be susceptible to uncertainties in AC that could reduce their suitability under sub-optimal atmospheric or aquatic conditions (Pahlevan et al. 2020; Smith et al. 2021).

Machine learning models have also been used in estimating other water parameters, including apparent optical parameters (AOPs) (Jamet et al. 2012) and water constituents (Balasubramanian et al. 2020; Pahlevan et al. 2022), or even performing atmospheric corrections (Doerffer and Schiller, 2007). In addition, applying deep learning models has been very promising in quantifying water quality parameters (Niu et al. 2021; Ye et al. 2021). However, those models usually need thousands of samples for training, which are not currently available for inland waters. Overall, machine learning models are region-based and should be trained by data from target waterbodies. This can substantially limit their usage for small waterbodies (Kutser, 2009).

### 2.3.2.5 Semi-analytical models

Semi-analytical models attempt to model the relationship between  $L_w$  and inherent optical parameters (IOPs) of water. Because water IOPs (absorption and scattering) are the total of water constituents (phytoplankton, CDOM, detritus, suspended sediments, and pure water) IOPs, an inversion equation that relates  $L_w$  to constituents IOPs and concentrations, can lead to an estimate of phytoplankton concentration. Here, for brevity, we ignore mentioning the radiative transfer equation (RTE) and its solutions and refer a reader to (Morel 1980; Gordon et al. 1988; Morel and Gentili 1991; Mobley 1994; Miller et al. 2005; Mishra et al. 2017; Werdell et al. 2018) for more information.

Among parameters in a Semi-analytical model, certain ones can lead to bloom detection and identification. Some studies attempt to detect and distinguish blooms based on retrieving abundance factors such as *Chl a* and [PC] (abundance-based models). For example, differences in phytoplankton absorption was utilized to distinguish diatom blooms from other bloom types in the North West Atlantic zone (Sathyendranath et al. 2004). The results indicated good agreement with *in situ* data; however, the region was case 1 water. The method was also employed in the first step of an approach to identify harmful *Alexandrium fundyense* blooms in the Bay of Fundy, Canada (Devred et al. 2018). Their approach also uses sea surface temperature (SST) as another discrimination criterion. In another study, a relationship between *Chl a* and phytoplankton cell size (micro-, nano- and, picoplankton) was established in the near surface of oceans (Uitz et al. 2006). The same approach but with additional parameters, such as water-leaving radiance as well as absorption and backscattering coefficients in specific bands, was applied elsewhere (Aiken et al. 2007; Hirata et al. 2008).

On the other hand, some other methods attempt to detect and distinguish blooms based on the phytoplankton-related part of total absorption and backscattering spectra (spectrum-based models). In one of the first attempts, only 0.5% of the variability in the total particulate absorption ( $a_p$ ) spectrum can be attributed to the absorption features of accessory pigments (Bricaud et al. 1995; Garver et al. 1994), and as a result, this parameter cannot be used for distinguishing between particular phytoplankton groups. Additionally, chlorophyll-specific absorption spectrum of dinoflagellate ( $a_\phi^*$ ) is not sufficiently different from that of other blooms to allow identification by remote sensing (Millie et al. 1997). Conversely, other studies (Ciotti et al. 2002) attributed more than 80% of  $a_\phi$  to the size of dominant species, because of strong co-variation between phytoplankton size and the factors that

control  $a_\phi$ , such as pigment packaging and the concentration of accessory pigments, such as Chlb, Chlc, and carotenoids. Similar analyses were applied on  $a_\phi^*$  to retrieve phytoplankton size elsewhere (Goela et al. 2013). It was demonstrated that the greatest decrease in water-leaving radiance for waters that contains large amounts of *Karenia brevis* occurs not because of the absorption due to cellular pigmentation, but because of the small amount of particular backscattering (Cannizzaro et al. 2008). They suggested that adding this information, acquired by gliders or UAVs, to the traditional EWS operated in the Gulf of Mexico might significantly decrease false positives caused by diatom blooms (Cannizzaro et al. 2009).

Comparing various Semi-analytical models based on their abilities to detect dominant phytoplankton size, it was concluded that micro- and picoplankton are more accurately detected than nanoplankton (Brewin et al. 2011). The ability to retrieve phytoplankton size can be used to distinguish between phytoplankton types with different sizes such as dinoflagellates vs. cyanobacteria. The spectrum-based models also showed an advantage in retrieving phytoplankton size, independently from Chla. However, these types of models show problems when species have a similar spectral absorption or backscattering. Also, it has been shown that absorption and backscattering spectra vary with phytoplankton growth stages, nutrient availability, and light regimes (Nair et al. 2008). In general, it has been proved that Semi-analytical models have more generality than statistics- and empirical-based models, thanks to their strong physics basis. However, Semi-analytical models need more spectral information (sometimes from hyperspectral sensors) to be employed in inversion models, and also a more-accurate AC, which is very hard to achieve in aquatic environments. Many studies have attempted to compare the above-mentioned algorithms, and most have conducted their comparisons in oligotrophic/mesotrophic waters (Hu et al. 2005; Hu et al. 2008; Tomlinson et al. 2009; Carvalho et al. 2011; Soto et al. 2015). Hybrid approaches of above-mentioned models also showed better results than single algorithms (de Araujo Carvalho 2008; Hu et al. 2008; Carvalho et al. 2010). There are also indices that are region-based and have not yet been evaluated over other regions. For example, coupling certain ratios and difference indices, discriminated the harmful blooms of dinoflagellate *Prorocentrum donghaiense* from non-blooms and diatoms in MODIS images of the coastal waters of China (Tao et al. 2015).

## 2.4 Summary

According to above-mentioned studies, most algorithms and methods have been developed for oceans and large waterbodies and often are not applicable to small waterbodies due to differences in optical water type and employing technologies (sensors). As a result, it is essential to adapt or develop algorithms to use for monitoring of *Chla* and HABs in small waterbodies. This seems more promising given the new improvements in available technologies (*in situ* and space-borne sensors) and machine-learning models. In the next chapters, we elaborate new approaches to monitor *Chla* in small waterbodies using remote sensing technologies.

## Chapter 3

# Improvement of field fluorometry estimates of chlorophyll-a concentration in a cyanobacteria-rich eutrophic lake

### 3.1 Introduction

Chlorophyll-*a* concentration (Chl<sub>a</sub>) is a key indicator of harmful algal blooms (HABs), especially in studies using floating instrument arrays (buoys) or remote-sensing technologies (Bittig et al. 2019; Pahlevan et al. 2020). A broad spectrum of methods exists to measure Chl<sub>a</sub>, including accurate laboratory methods (*in vitro*,  $chl_M$  hereafter) such as High-Performance Liquid Chromatography (HPLC), spectrophotometry, and fluorometry (Pinckney et al. 1994), to very fast field methods, such as *in vivo* fluorometry (Bittig et al. 2019), *in vivo* spectrophotometry (Davis et al. 1997; Roesler and Barnard 2013), and remote sensing (Pahlevan et al. 2020). Although accurate, laboratory methods are less suitable for real-time monitoring or long-term observations due to logistic and economic constraints (Gregor and Maršálek 2004). Given this, as well as the current absence of daily high-spatial-resolution satellite observations for small inland waters (Cao et al. 2019), *in vivo* fluorometry and spectrophotometry have been promoted as important options for real-time monitoring of algal blooms in small water bodies (Richardson et al. 2010; Poxleitner et al. 2016; Silva et al. 2016; Wang et al. 2016; Karpowicz and Ejsmont-Karabin 2017). Here, *in vivo* fluorometry is usually preferred over *in vivo* spectrophotometry due to its ease of use (Roesler and Barnard 2013). However, to date, few studies have critically evaluated the capabilities or limitations of buoy-based instrument platforms in estimating changes in freshwater Chl<sub>a</sub> concentrations (Bertone et al. 2018; Boss et al. 2018; Chaffin et al. 2018)

*In vivo* fluorometric Chl<sub>a</sub> measurements are obtained by sensors that are usually mounted on buoys and illuminate a known volume of water with an excitation irradiance, usually blue wavelengths. This light stimulates the Chl<sub>a</sub> within phytoplankton to fluoresce at red wavelengths, which is quantified as a relative fluorescence unit (RFU) before being converted to Chl<sub>a</sub> concentration as;

$$Chl = (F - F_0) / \Phi_F \int_{400}^{750} E(\lambda) \times a_{chl}^*(\lambda) d\lambda. \quad (3.1)$$

Here  $F$  is the intensity of measured fluorescence (*in vivo* fluorescence hereafter),  $F_0$  is background fluorescence due to humic and other non-chlorophyllous constituents that fluoresce 400-

750 nm,  $E$  is available spectral scalar irradiance [ $\mu\text{mol photons } m^{-2}s^{-1}nm^{-1}$ ],  $a_{chl}^*$  is spectral Chla-specific absorption coefficient [ $m^2mg^{-1}$ ], and  $\Phi_F$  is fluorescence quantum yield (photons fluoresced / photons absorbed). Assuming all fluoresced light is detected and  $E$  is known, only  $a_{chl}^*$  and  $\Phi_F$  need to be known to estimate Chla levels (Roesler et al. 2017). While  $a_{chl}^*$  and  $\Phi_F$  are known and constant for extracted Chla, values may vary for different phytoplankton, depending on factors such as cell packaging, pigment quota, accessory pigment composition, light history, growth phase, and phytoplankton species composition (Morel and Bricaud 1981; Falkowski and Kolber 1995). Assuming  $a_{chl}^*$  and  $\Phi_F$  are constant and that the relationship between  $F$  and Chla is linear, fluorometer manufacturers calibrate  $F$  with solutions with known pigment content to estimate Chla levels. We refer to this *in vivo* Chla concentration as factory-calibrated Chla ( $chl^{FC}$ ), hereafter.

Estimates of  $chl^{FC}$  are most likely to be accurate when used in spatially- and temporally-limited applications (Ferreira et al. 2012; Chaffin et al. 2018) where  $a_{chl}^*$  and  $\Phi_F$  can be assumed constant and similar to pre-defined manufacturer gains (Roesler et al. 2017). In addition,  $chl^{FC}$  is potentially useful for time series of relative Chla content, assuming that the deviation from true values of  $a_{chl}^*$  and  $\Phi_F$  are similar for all Chla predictions (Richardson et al. 2010). For example, a study using a five-band fluorescence probe report a high correlation ( $r = 0.97$ ,  $p < 0.05$ ) between  $chl^{FC}$  and spectrophotometric estimates ( $chl_M$ ) when compared in six productive rivers and reservoirs (Gregor and Maršálek 2004). However, in this case, analyses spanned small regions, and phytoplankton were composed mainly of low-diversity assemblages of cyanobacteria and chlorophytes. Despite strong linear relations between Chla estimators,  $chl^{FC}$  underestimated  $chl_M$  by up to  $50 \mu\text{g L}^{-1}$  (slope = 0.83) and could not retrieve Chla values above  $50 \mu\text{g L}^{-1}$ , especially when colonial cyanobacteria were present. Similarly, a high relative accuracy ( $r = 0.97$ ) and a significant underestimation of Chla (slope = 0.55) were reported in a study comparing  $chl^{FC}$  and spectrophotometric  $chl_M$  in 50 lakes in France (Catherine et al. 2012). Research employing different fluorometers (Kaylor et al. 2018), analytical methods (e.g., HPLC vs. fluorometry), and phytoplankton assemblages have produced evidence of similar biases (Ostrowska et al. 2015; Wang et al. 2016).

Variations in phytoplankton type and growth phase, community composition, and water characteristics can also cause substantial deviation of factory  $a_{chl}^*$  and  $\Phi_F$  values from those independently measured, resulting in poor Chla retrieval (Choo et al. 2018; Bertone et al. 2019; Garrido

et al. 2019). For instance, although *in vivo* fluorometry accurately assessed relative taxonomic composition in marine assemblages, phytoplankton biomass was overestimated by ~1.2– to 3.4-fold (Richardson et al. 2010). Such overestimation becomes crucial when *Chla* data are used to train and test models using remotely-sensed reflectance to estimate bloom abundance and cyanobacterial prevalence. As a result, many studies calibrate fluorescence measurements with coeval spectrophotometric or chromatographic measures of *in situ* *Chla*, instead of using factory-calibrated *Chla* (Mueller et al. 2003; Escoffier et al. 2014; Roesler et al. 2017; Bertone et al. 2018).

*Chla* estimates based on *in vivo* fluorometry are often less accurate than those derived from *in vitro* methods. Apart from biofouling, which can be reduced by regular sensor maintenance (Davis et al. 1997; Manov et al. 2004), *in vivo* fluorescence can be reduced by non-photochemical quenching (NPQ) at high irradiance (Huot and Babin 2010). Although various approaches have been proposed to compensate this signal contamination (Xing et al. 2018; Carberry et al. 2019; Scott et al. 2020), none of them completely remove the NPQ effect (Bittig et al. 2019) even when additional coeval water parameters are measured (Boss and Haëntjens 2016; Wojtasiewicz et al. 2018). Additionally, the fluorescence of colored dissolved organic matter (CDOM) may interfere with that of *Chla*, resulting in the overestimation of *Chla* (Gregor and Maršálek 2004; Xing et al. 2017). Finally, water-column turbidity due to abundant phytoplankton and inorganic particles can interfere with *in vivo* fluorometry (Choo et al. 2019). In contrast, fluorometric estimates of phytoplankton abundance may be improved through the use of *in vivo* phycocyanin (PC) fluorometers that use an orange excitation wavelength instead of blue light to quantify pigment concentrations. For example, Seppälä et al. (2007) found that PC fluorescence has correlated well with spectrophotometrically-derived *Chla* concentration when cyanobacteria were common in the Baltic Sea, and in the Charles River, USA, when used in conjunction with *Chla* fluorescence and turbidity observations ( $R^2 = 0.87$ ) (Rome et al. 2021). Despite its promise, most studies of field fluorometry are limited to laboratory-cultured populations (Escoffier et al. 2014) or oligotrophic/mesotrophic waters with relatively low *Chla* content, such as open oceans and coastal marine areas (Roesler 2016; Roesler et al. 2017; Wojtasiewicz et al. 2018).

Continued environmental degradation by eutrophication (Ho et al. 2019), combined with the formation of international research consortia using instrumented buoys (Hamilton et al. 2015; Boss et al. 2018), has increased demand for real-time monitoring systems, especially for use in eutrophic

waters. However, to fully exploit the *in vivo* fluorescence technology, research is needed to evaluate and improve the reliability and accuracy of such measurements, especially under severely eutrophic conditions. In addition, the lack of standardization and protocols in performing automated quality control, data formatting, and rapid delivery of validated observations is a major challenge in developing reliable water quality databases (Boss et al. 2018). Further, to the best of our knowledge, no study has evaluated the performance of both Chla- and PC-based fluorometers for Chla retrieval at annual time scales and with high resolution *in vitro* measurements.

In this chapter, estimate of *in vivo* Chla are compared to *in vitro* pigment measures in a shallow eutrophic polymictic lake subject to long-term monitoring by limnological sampling and remote-sensing technologies. Here we take advantage of the rich dataset of lake parameters to apply machine-learning (ML) protocols that use environmental conditions to improve Chla estimates. By assessing field measurements of Chla, we seek to improve estimates of planktonic Chla concentration needed to train and test remote-sensing algorithms. This study aims to: (i) identify potential flaws and issues associated with the use of factory-calibrated Chla ( $chl^{FC}$ ); (ii) develop and assess three locally tuned models, namely  $chl_p^{chl}$ ,  $chl_p^{PC}$ , and  $chl_p^{ML}$ , based on Chla fluorescence ( $F^{chl}$ ), PC fluorescence ( $F^{PC}$ ), and multiple linear regression (MLR) of environmental algae-derived factors, to approximate Chla concentration, and; (iii) evaluate the performance of newly proposed models in recovering accurate Chla estimates in two real-world applications; monitoring Chla time series and mapping Chla by remote sensing. We show that, at least for a cyanobacteria-dominated eutrophic lake, Chla was most accurately estimated when based on models using PC fluorescence or environmental predictors.

## 3.2 Materials and Procedures

### 3.2.1 Study site

Buffalo Pound Lake (BPL) is a long (~30 km), narrow (< 1 km), shallow (< 6 m) lake located in the Qu'Appelle River watershed, Saskatchewan, Canada (Figure 3.1, Table 3.1). Currently, the basin exhibits highly eutrophic waters, with summer blooms during June-September and peak surface populations of phytoplankton during July-August (Kehoe et al. 2019). Continuous monitoring for over 25 years shows that cyanobacteria are the predominant taxon during summer; however, other

phytoplankton species may be abundant at the same time (Hammer 1983) (Vogt et al. 2018; Hayes et al. 2019; Swarbrick et al. 2019).

**Table 3.1. Buffalo Pound Lake characteristics and water quality parameters in station 1, averaged on late May to early September in 2014-2019.**

<b>Characteristics</b>	<b>values</b>
Altitude (m)	501
Mean depth (m)	3.8
Maximal depth (m)	5.8
Length (km)	35
Average Width (km)	0.9
Surface (km <sup>2</sup> )	30
Volume (m <sup>3</sup> )	92 × 10 <sup>6</sup>
<b>Water Quality</b>	<b>Mean values</b>
Water temperature (°C)	19
conductivity (µs/cm)	730
DO (µg L <sup>-1</sup> )	9.5
pH	8.5
Turbidity (NTU)	9.1
Total P (µg L <sup>-1</sup> )	86
Chl <sub>a</sub> (µg L <sup>-1</sup> )	31

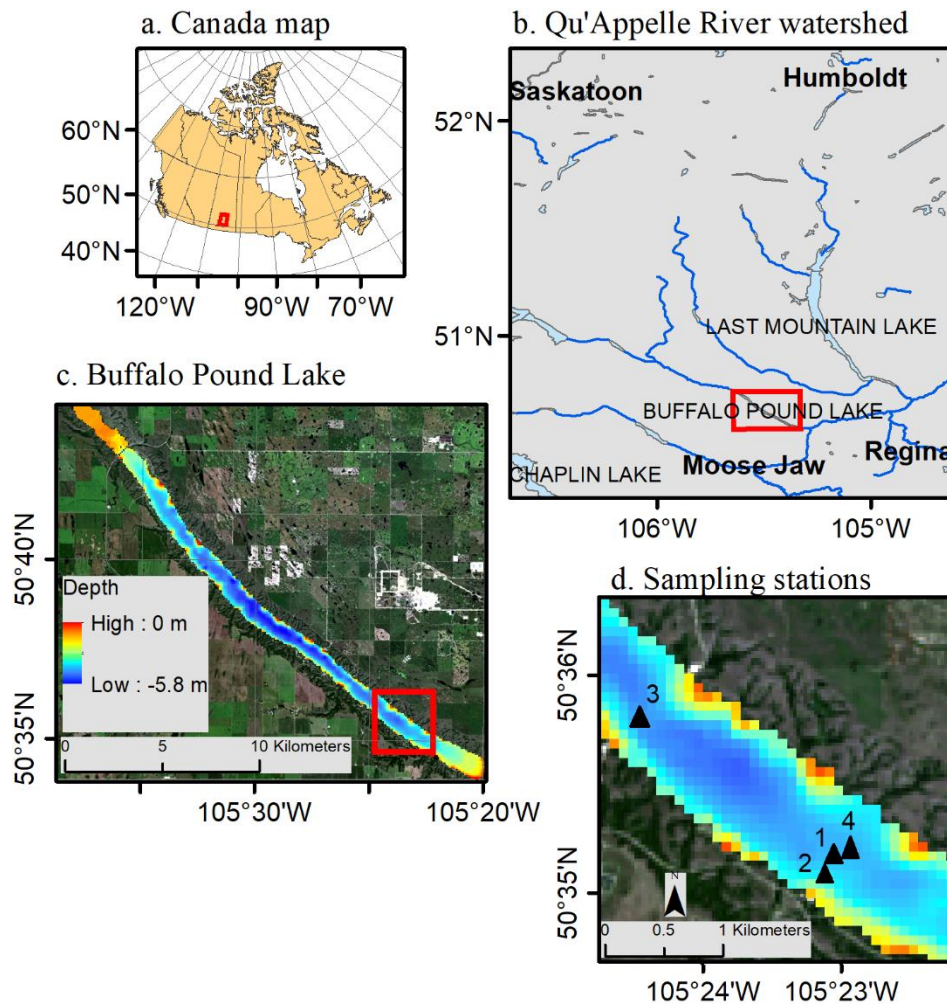


**Figure 3.1. The map and location of the Buffalo Pound Lake (BPL), Saskatchewan, Canada. (a) Position of the Qu'Appelle River watershed within Canada. (b) Location of BPL within Qu'Appelle River watershed. (c) A Landsat-8 image of BPL, overlaid by a bathymetric map. The extent indicator represents the sampling area in the lake (d) A zoom view of the sampling area in BPL overlaid by sampling stations.**

Several attributes make BPL suitable for the comparison of fluorometric, optical, and remotely-sensed estimates of *Chla*. First, the lake is an important freshwater resource, as it serves as drinking water reservoir for one-quarter of the provincial population, including nearby cities of Regina and

Moose Jaw. Second, the lake has multi-decadal records of monitoring, including *Chla* measurement and estimates of HAB abundance (Kehoe et al. 2015). Third, lake size, elongate shape, and landscape orientation parallel to the direction of prevailing winds mean the water column is polymictic, experiencing frequent mixing periods and limited vertical stratification (Dröscher et al. 2008). Finally, the lake has had an instrumented buoy present at a standard location annually from May-September (starting in 2014) that is equipped with *in vivo* sensors for both *Chla* and PC.

### 3.2.2 Data

Pigment data originated from different sources collected concomitantly during 2014-2019.  $F^{chl}$ ,  $F^{PC}$ , and  $chl^{FC}$  were collected from an instrument platform buoyed in the center of BPL (Station 1 in Figure 3.1). In contrast, *in vitro* *Chla* concentration was measured from samples at four stations obtained at regular intervals. Moreover, environmental parameters were recorded by buoy sensors and were supplemented by sampling the water column adjacent to the buoy (see below). Table 3.2 lists the details of *in-situ* measurements.

**Table 3.2. Details of data used in this study. Env. stands for environmental.**

Parameter	Name	Station	Measurement method	Available years	Sampling cycle	Depth (m)
<i>Chla</i> fluorescence	$F^{chl}$	1	field fluorometry	2014-2019	10 min	0.8
PC fluorescence	$F^{PC}$	1	field fluorometry	2014-2019	10 min	0.8
PC fluorescence	$F_{deep}^{PC}$	1	field fluorometry	2014-2018	10 min	2.8
<i>Chla</i> concentration	$chl^{FC}$	1	field fluorometry	2014-2019	10 min	0.8
<i>Chla</i> concentration	$chl_M$	1	lab spectrophotometry	2017-2019	Once/week	0.8
Env. parameters	-	1	field sensors	2014-2019	10 min	0.8, 2.8
RGB photos	-	1	deployed camera	2014-2019	30 min	0
Phytoplankton biomass	-	1	Visual microscopy	2017-2018	~Once/week	0.1

Chla concentration	$chl_M$	2	lab spectrophotometry	2014-2018	Once/week	3
Phytoplankton taxonomy	-	2	Visual microscopy	2014-2018	~Once/week	3
Chla concentration	$chl_M$	3	lab HPLC	2014-2019	twice/month	0-1
Chla concentration	$chl_M$	4	lab spectrophotometry	2015-2019	once/month	1

Two YSI-6600 multi-probes (YSI, Yellow Springs, Ohio, USA) were deployed on the buoy at 0.8 and 2.8 m depth to measure fluorescence at station 1. The shallow multi-probe recorded  $F^{chl}$  and  $F^{PC}$  via YSI 6025 and YSI 6131 sensors, respectively, while the deep probe gauged only PC fluorescence ( $F_{deep}^{PC}$ ). At both depths, the PC fluorometers used an excitation wavelength of  $590\pm 20$  nm and measured fluorescence at  $640\pm 40$  nm, whereas the Chla fluorometer used excitation and emission wavelength ranges of  $470\pm 20$  nm and  $640\pm 40$  nm, respectively. To eliminate fluorometer drift and convert relative fluorescence outputs to units of Chla concentration ( $\mu\text{g L}^{-1}$ ), a two-point calibration process was used at regular intervals (the beginning and middle of observation seasons) for the Chla fluorometer using a standard solution of rhodamine provided by the sensor manufacturer. As a result, buoy multi-probes provide *in vivo* estimates of Chla ( $chl^{FC}$ ), in addition to Chla fluorescence ( $F^{chl}$ ).

Samples for estimation of *in vitro* Chla were collected from four locations; at the exact location of the buoy (station 1), at ~100 m adjacent to the buoy (Stations 2 and 4) and the site of a 28-yr monitoring program (Haig et al. 2020) ~ 2 km distant (Station 3). Samples from station 1 and 4 were collected with a Niskin bottle from 0.8 – 1 m depth on Whatman GF/F frozen, and later extracted following Wintermans and DeMots (1965) in cold 95% ethanol for 24h, and analyzed using a UV-visible spectrophotometer (Shimadzu UV-1601-PC). Station 2 samples are from the water treatment plant intake which is at approximately 3m depth (but pulls water from the water column as a whole). Samples from the intake were filtered onto a 0.45 $\mu\text{m}$  filter, extracted in 90% acetone and analyzed via spectrophotometry (Eaton et al. 2017). At station 3, phytoplankton were collected on GF/C glass-fibre filters (nominal pore size 1.2  $\mu\text{m}$ ) following Swarbrick et al. (2019). Briefly, surface water (~0.5-m depth) and depth-integrated samples were filtered through GF/C filters and frozen ( $-10^\circ\text{C}$ ) until analysis for Chla ( $\mu\text{g L}^{-1}$ ) by standard trichromatic assays (Jeffrey and Humphrey 1975) and biomarker pigments

(nmoles pigment L<sup>-1</sup>) by HPLC (Leavitt and Hodgson 2001). Carotenoids, chlorophylls, and their derivatives were isolated and quantified using a Hewlett Packard model 1100 HPLC system calibrated with authentic standards. The samples in different stations were treated differently as they were collected by different researchers, not necessarily for this study.

Environmental data included estimates of phytoplankton species density (cells or colonies mL<sup>-1</sup>) and biomass (µg ml<sup>-1</sup>) collected in stations 1 and 2 and enumerated following (Findlay and Kasian 1987). In addition, turbidity, temperature profiles, wind speed and direction, flux of photosynthetically active radiation (PAR) in the surface layer and water column, and dissolved CO<sub>2</sub> and O<sub>2</sub> concentrations were recorded by the buoy sensors at Station 1. Further, two cameras, one mounted on the buoy and the other on the shore facing toward the buoy, regularly took RGB photographs of the water surface to detect surface-bloom events.

### 3.2.3 Data Processing Procedure

Coeval estimates of *in vivo* and *in vitro* Chl<sub>a</sub> were processed separately (Figure 3.2). Samples from all stations were paired by collection date. We then developed and validated Chl<sub>a</sub> retrieval models based on paired measurements.

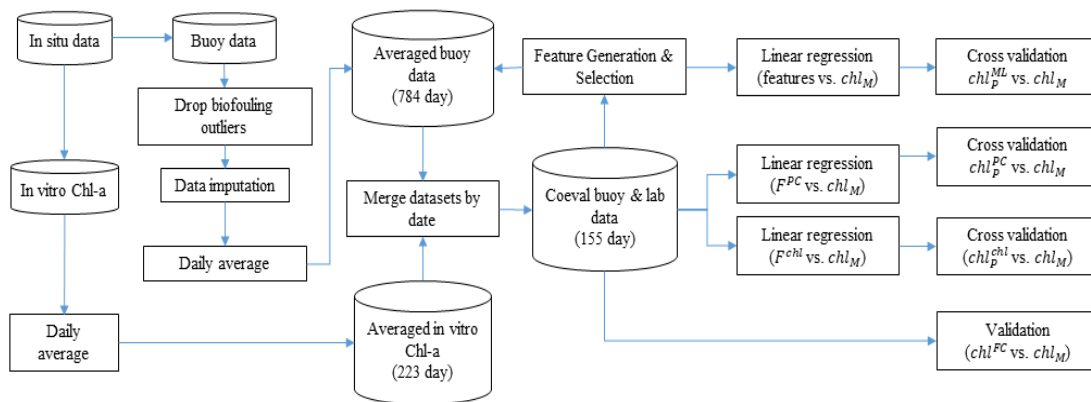


**Figure 3.2. A thematic graph of the workflow in this study.**

#### 3.2.3.1 Data inspection and correction of fluorescence data

Raw fluorescence data were adjusted for effects of biofouling, sensor input noise (high impulse values), and non-photochemical quenching (NPQ) before fluorescence measurements were converted to Chl<sub>a</sub>

concentrations (Figure 3.3). Potential biofouling was identified by comparing surface- and deep-sensor values with estimates of phytoplankton density and photographic evidence of surface blooms. Affected values were removed from further analysis, but accounted for only ~1% of  $F^{chl}$  and  $F^{PC}$  observations, usually towards the end of the sampling season. As seen elsewhere (Sackmann et al. 2008; Wojtasiewicz et al. 2018), fluorescence of both PC and Chla declined ~10% during most days as PAR increased (Figure 3.3). However, as such a pattern may also reflect diel vertical movements of phytoplankton, no correction was made for the decline. Instead, NPQ effects were reduced by averaging fluorescence data over 24 h (Carberry et al. 2019). This procedure produced similar values to a second protocol, in which daytime extremes were replaced by nighttime values (Sackmann et al. 2008; Roesler 2016), while also preserving daily variation in water-column Chla. Finally, high impulse values were defined by fluorescence observations that surpass  $3\sigma$  of daily-averaged fluorescence (observations fall  $3\sigma$  away from mean) and were removed from the data set.

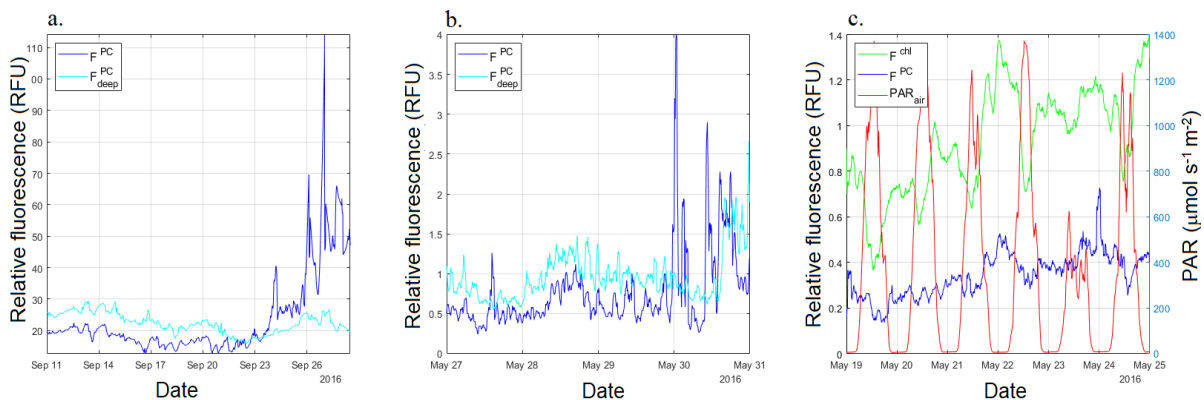


**Figure 3.3. Examples of (a) potential biofouling, (b) high impulse values, and (c) NPQ effect on Chla and PC fluorescence time-series. (a) Very high end-season values of the shallow PC fluorometer that are inconsistent with coincident observations of the same sensor in deep water could be the result of biofouling error. (b) Very high relative values that are occurred in very short periods and are inconsistent with other sensors could be the result of sensor impulse noise. (c) Periodic changes in fluorescence values with an inverse relationship to available PAR could be the result of NPQ.**

### 3.2.3.2 Model development

For data training, we paired  $F^{chl}$  and  $F^{PC}$  observations with concomitant  $chl_M$  measurements from Stations 1-4. The comparison of coeval  $chl_M$  measurements at the four sites revealed few significant differences. Consequently, *Chla* values from all stations were used for model development, with the exception of periods in which surface scum were recorded by the buoy. For these periods, we only used the samples in station 1 (the exact location of the fluorometers). To compensate for differences in sampling depth, location, and methods between  $chl_M$  measurements, all *in vitro* values were averaged by day to produce 155 pairs of coeval  $F^{chl}/F^{PC}$  and  $chl_M$  measurements over six years of observations. We also extracted and tested pairs of  $F^{chl}/F^{PC}$  and  $chl_M$  sampled using other strategies (only one location; only adjacent; unaveraged); however, those protocols reduced the number of paired samples to one-half to two-thirds (to 56 - 77) and did not improve the accuracy of models, so were discontinued.

Model calibration and validation were carried out using a five-fold cross-validation approach (Hawkins et al. 2003), using 80% of pairs ( $n = 124$ ) as training set and the remaining 20% ( $n = 31$ ) as a test set. Moreover, because  $F^{chl}$ ,  $F^{PC}$ , and  $chl_M$  measurements exhibited log-normal distributions, all data were subject to a  $\log_{10}$ -transformation to achieve normal distribution of residuals. Finally, linear regression models were developed to predict  $chl_p^{chl}$  and  $chl_p^{PC}$  from  $F^{chl}$  and  $F^{PC}$ , respectively.

Multiple linear regression models were developed to retrieve *Chla* from environmental parameters independent of those inferred from fluorometric measurements. Predictors included turbidity, dissolved CO<sub>2</sub> concentration, and normalized PAR at 0.8-m depth, parameters which were all correlated individually with *Chla* (Figure 3.4). We defined normalized PAR ( $nPAR_{water}$ ) (Equation 3.2), as the fraction of incident PAR at the lake surface that was not absorbed or scattered when transmitted through the water column. For CO<sub>2</sub>, we used raw signal data, assuming it to have a good correlation with actual CO<sub>2</sub> concentration due to negligible atmosphere variation. We also input the month of observation to account for seasonality and excluded other environmental parameters that did not have a significant individual correlations with *Chla*.

$$nPAR_{water} = PAR_{water} / PAR_{air} \quad (3.2)$$

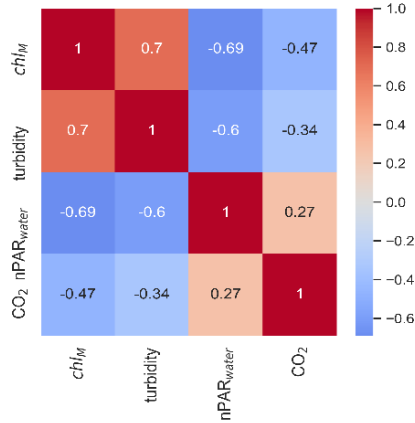


**Figure 3.4. A heatmap showing the Pearson correlation of the selected environmental factors and  $chl_M$ .**

### 3.2.3.3 Model assessment

Predicted Chla ( $chl_p$ ) was assessed on the basis on accuracy and reliability. Accuracy was defined as agreement between  $chl_p$  and  $chl_M$  (closeness of fit), while reliability measured the probability that  $chl_p$  fell into a confidence interval around  $chl_M$ . Reliability also took into account variation in *in vitro* estimates of Chla concentration arising from differences in laboratory protocols.

For estimation of prediction accuracy, we examine both linear and  $\log_{10}$ -transformed metrics following Seegers et al. (2018). Performance metrics included root mean square error (RMSE), root mean square logarithmic error (RMSLE), median percentage error (MAPE), bias (as  $\log_{10}$ -transformed residuals), and mean absolute error in  $\log_{10}$ -space (MALE):

$$RMSE = \left[ \frac{\sum_{i=1}^N (P_i - M_i)^2}{n} \right]^{1/2} \quad (3)$$

$$RMSLE = \left[ \frac{\sum_{i=1}^N (\log_{10}(P_i) - \log_{10}(M_i))^2}{n} \right]^{1/2} \quad (4)$$

$$MAPE = 100 \times \text{median}(|P_i - M_i|/M_i) \quad (5)$$

$$\text{Bias} = 10^z, z = [\sum_{i=1}^n (\log_{10}(P_i) - \log_{10}(M_i))/n] \text{ and,} \quad (6)$$

$$MALE = 10^y, y = [\sum_{i=1}^n |\log_{10}(P_i) - \log_{10}(M_i)|/n] \quad (7)$$

where  $P_i$  and  $M_i$  stand for predicted and *in vitro* measured Chla, respectively. Using these metrics, a Bias of 1.5 implies that predicted Chla are, on average, 50% larger than those measured (Bias = 1 is ideal), whereas a MALE of 1.5 indicates a relative measurement error of 50% (Seegers et al. 2018).

Reliability was computed as the percentage of predicted Chla that fit into a confidence interval derived from *in vitro* measurements. Given considerable variability in coeval Chla values from different laboratories, and that the true value of Chla was unknown, we assumed that  $\log_{10}$ -transformed Chla was a random variable with a normal distribution whose mean and variance are estimated by coeval *in vitro* Chla measurements. Given these assumptions, the reliability of predicted Chla was measured as the probability that predicted values fell into the range of  $c = \mu \pm k\sigma$ , where  $\mu$  and  $\sigma$  are mean and standard deviation, respectively;  $k = 1, 2, 3$  and  $c$  is a confidence interval. Again, all calculations for reliability were conducted using  $\log_{10}$ -transformed Chla data.

Finally, to assess the effect of model selection on the ability of remote-sensing techniques to estimate Chla, we downloaded and processed Sentinel-2 images of BPL corresponding to sampling dates during 2017-2019, the years following Sentinel-2 insertion into orbit. We then paired coeval, co-located Chla and reflectance observations for training and testing a Support Vector Regression (SVR) model to estimate Chla. Details of remote sensing data and processing are provided by Chegoonian et al., (submitted).

### 3.3 Assessment

#### 3.3.1 Models accuracy

Comparison of factory-calibrated Chla ( $chl^{FC}$ ) with *in vitro*  $chl_M$  measurements showed that fluorometric estimates of Chla from the buoy substantially underestimated values derived from laboratory analyses in all years (Figure 3.5). The degree of underestimation was not affected by correction for biofouling or NPQ effects, even though both are distinguishable from effects of inherent model inaccuracy due to their unique temporal patterns (Figure 3.3). In general, agreement between

$chl^{FC}$  and *in vitro* measurements was best early in each year and became markedly worse after June in each year through the period of high summer biomass, often improving again in early fall.

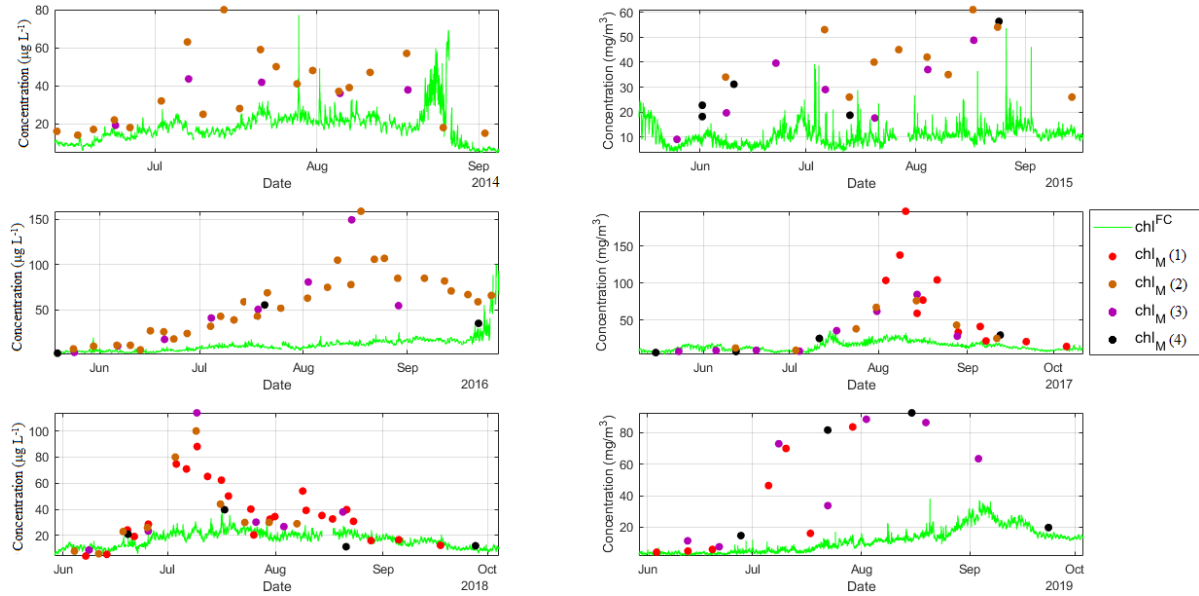


**Figure 3.5. Factory-calibrated  $Chla$  concentration from YSI  $Chla$  fluorometer ( $chl^{FC}$ , green line), and *in vitro*  $Chla$  concentration ( $chl_M$ , circles), shows that  $chl^{FC}$  significantly underestimates  $Chla$  concentration in BPL. Stations are color-coded 1-4.**

Although both  $F^{chl}$  and  $F^{PC}$  measurements were correlated ( $p < 0.01$ ) to *in vitro*  $Chla$ , predictions based on PC fluorescence explained a much greater proportion of variation in  $chl_M$  than did those based in  $F^{chl}$  (Figure 3.6). Specifically,  $F^{PC}$  models were highly correlated with variability in  $chl_M$  ( $R^2 = 0.87$ ), whereas models with sensor-derived  $Chla$  fluorescence values explained only ~34% of variance in  $chl_M$  over a nearly  $200 \mu\text{g L}^{-1}$  range. In contrast, MLR models using forward selection explained 82% of variance in measured  $chl_M$  values. Significant predictors included turbidity, normalized PAR, dissolved  $\text{CO}_2$ , and sampling month (Table 3.3), with about half of sums of squares related to turbidity alone.

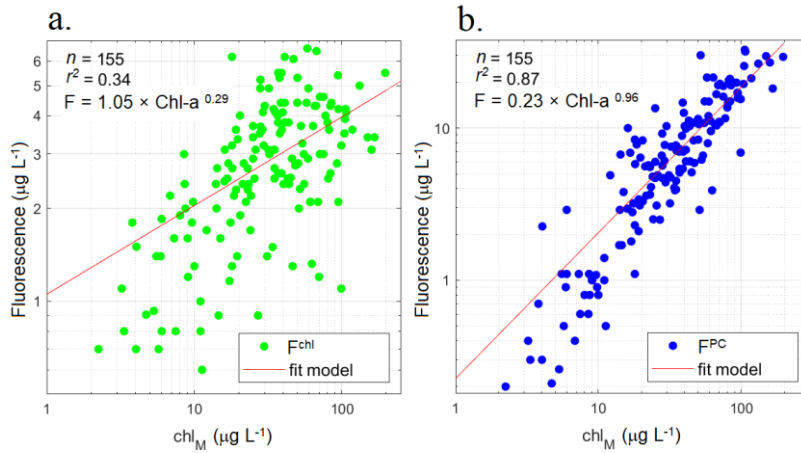


**Figure 3.6. Scatter plots of the fluorescence of (a) Chla and (b) PC, versus *in vitro* Chla concentration ( $chl_M$ ). *F* stands for fluorescence.**

**Table 3.3. Multiple linear regression (MLR) model to predict  $chl_M$ , from measured environmental parameters using forward selection.**

Parameters	Coefficient	Sum of squares	F-test	P-value
turbidity	0.36	12.08	262.14	$9 \times 10^{-35}$
nPAR <sub>water</sub>	-0.38	2.99	64.94	$2 \times 10^{-13}$
CO <sub>2</sub>	-0.26	1.18	25.65	$10^{-6}$
month	1.74	1.82	39.44	$3 \times 10^{-9}$
Residual	-	3.9	-	-

Comparison of modeled ( $chl^{FC}$ ,  $chl_P^{chl}$ ,  $chl_P^{PC}$ ,  $chl_P^{ML}$ ) and measured  $chl_M$  showed predictions using  $chl^{FC}$  were more biased than were values derived from other fluorometric models (Figure 3.7). On average,  $chl^{FC}$  was ~2.5-fold lower than  $chl_M$  resulting in a biased estimator (Bias = 0.42), particularly at  $Chla < 20 \mu\text{g L}^{-1}$  (Bias = 0.74). Further, the relationship between variables was non-linear above  $20 \mu\text{g L}^{-1}$  (Bias = 0.33), similar to patterns previously reported for a FluoroProbe fluorometer for  $Chla$  values  $> 60 \mu\text{g L}^{-1}$  (Gregor and Maršálek 2004). Moreover, only a weak positive

correlation ( $r = 0.55$ ,  $n = 155$ ) was found between  $\log_{10}$ -transformed  $chl^{FC}$  and  $chl_M$ , suggesting that  $chl^{FC}$  values should be treated with caution even in analysis of relative proportions. The remaining models were unbiased (Bias  $\simeq 1$ ), although they differed in terms of prediction accuracy.

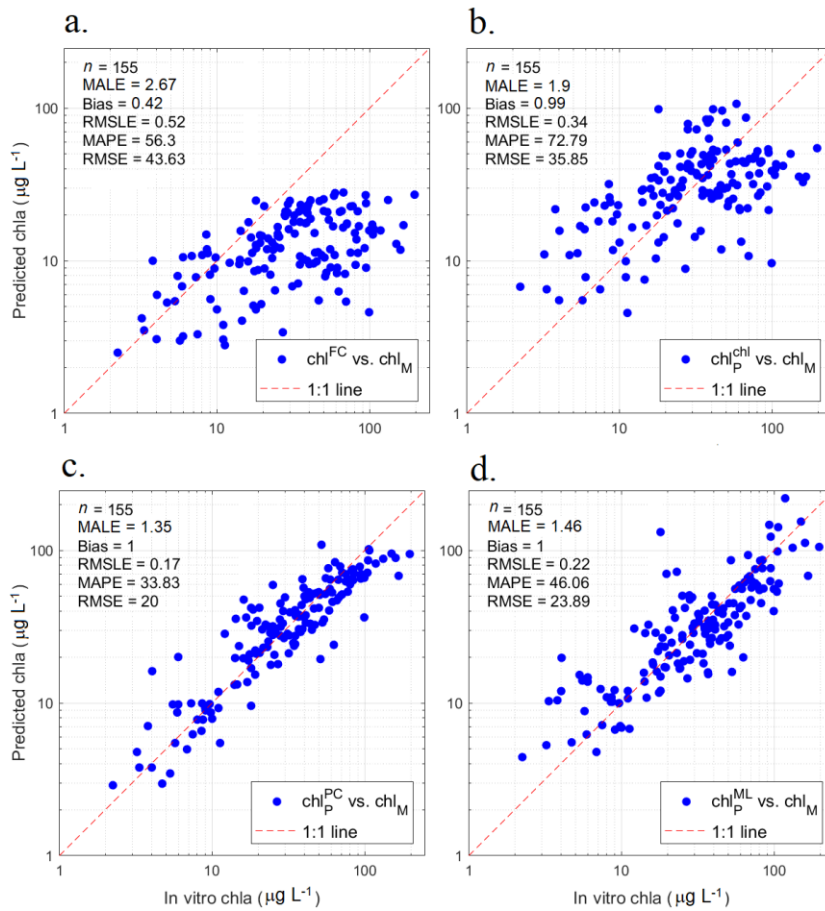


**Figure 3.7.** The results of five-fold cross-validation of the proposed models; (b)  $chl_P^{chl}$ , (c)  $chl_P^{PC}$ , and (d)  $chl_P^{ML}$  versus  $chl_M$  measurements at stations 1-4. The validation results for  $chl^{FC}$ , obtained from YSI Chla fluorometer with a correction for biofouling and NPQ, is also displayed in (a) to compare with the proposed models. The dashed lines correspond to the 1:1 relationship.

Although  $chl_p^{chl}$  improved Chla retrieval compared to the  $chl^{FC}$  model, it still predicted *in situ* Chla with only an average relative error of ~90% of true values (MALE = 1.9). Instead, errors declined ~55% when models employed the PC fluorometer to estimate water-column Chla (Figure 3.7). For example, all error metrics were reduced by ~50% for the  $chl_p^{PC}$  model compared to that based on  $chl_p^{chl}$ , with improvement evident throughout the range of observed values even though  $chl_p^{PC}$  underestimated Chla when concentrations exceeded 120  $\mu\text{g L}^{-1}$  (Figures 3.7.b, 3.7.c). Similarly, the  $chl_p^{ML}$  model (Figure 3.7.d) significantly ( $p < 0.01$ ) outperformed both Chla-based fluorescence models ( $chl^{FC}$ ,  $chl_p^{chl}$ ) in all metrics. In fact, a model with turbidity as the sole predictor (not shown) still outperformed  $chl_p^{chl}$  (MALE = 1.66 vs. MALE = 1.9). In general,  $chl_p^{ML}$  exhibited similar performance relative to that of  $chl_p^{PC}$  (MALE = 1.46 vs. MALE = 1.35) and did not underestimate extremely high Chla values. Instead, the  $chl_p^{ML}$  model tended to overestimate Chla when  $chl_M$  was  $< 10 \mu\text{g L}^{-1}$ .

### 3.3.2 Models reliability

Analysis of model reliability revealed that predictions from the  $chl_p^{ML}$  model fell within  $\pm 2\sigma$  distance (95% confidence interval) of mean  $chl_M$  on 66% (23 out of 35) of observations with ~46% and ~89% falling within  $\pm\sigma$  and  $\pm 3\sigma$ , respectively (Table 3.4). Overall, reliability of  $chl_p^{PC}$  and  $chl_p^{ML}$  models outperformed those based on Chla fluorescence ( $chl^{FC}$ ,  $chl_p^{chl}$ ) irrespective of the confidence interval selected (Table 3.4). Compared to other models,  $chl_p^{PC}$  exhibited the highest accuracy (Figure 3.7), whereas  $chl_p^{ML}$  outperforms it in terms of reliability with 89% of observations within  $\pm 3\sigma$ . For demonstration purposes, a visual presentation of reliability for  $chl_p^{ML}$  with associated  $chl_M$  measurements is depicted in Figure 3.8. Figure 3.8 also can serve as an estimation of consistency among all measurements methods used in this study (fluorometry, spectrophotometry, and HPLC). For example, an individual can see that HPLC observations of Chla (measurements at station 3) are usually lower compared to coincident measurements by the other methods, probably due to differentiate between Chla, Chlb, and Chlc. However, a comprehensive comparison between the methods needs more data collected at the same location and time.

**Table 3.4. Reliability, estimated as the proportion of retrieved Chla values that within three confidence intervals ( $\pm \sigma$ ,  $\pm 2\sigma$ , and  $\pm 3\sigma$ ) of the mean of *in vitro* Chla concentration, for each of four fluorescence models.**

	$chl_P^{FC}$	$chl_P^{chl}$	$chl_P^{PC}$	$chl_P^{ML}$
$\pm\sigma$	0.11	0.2	0.54	0.46
$\pm 2\sigma$	0.11	0.49	0.68	0.66
$\pm 3\sigma$	0.14	0.6	0.77	0.89

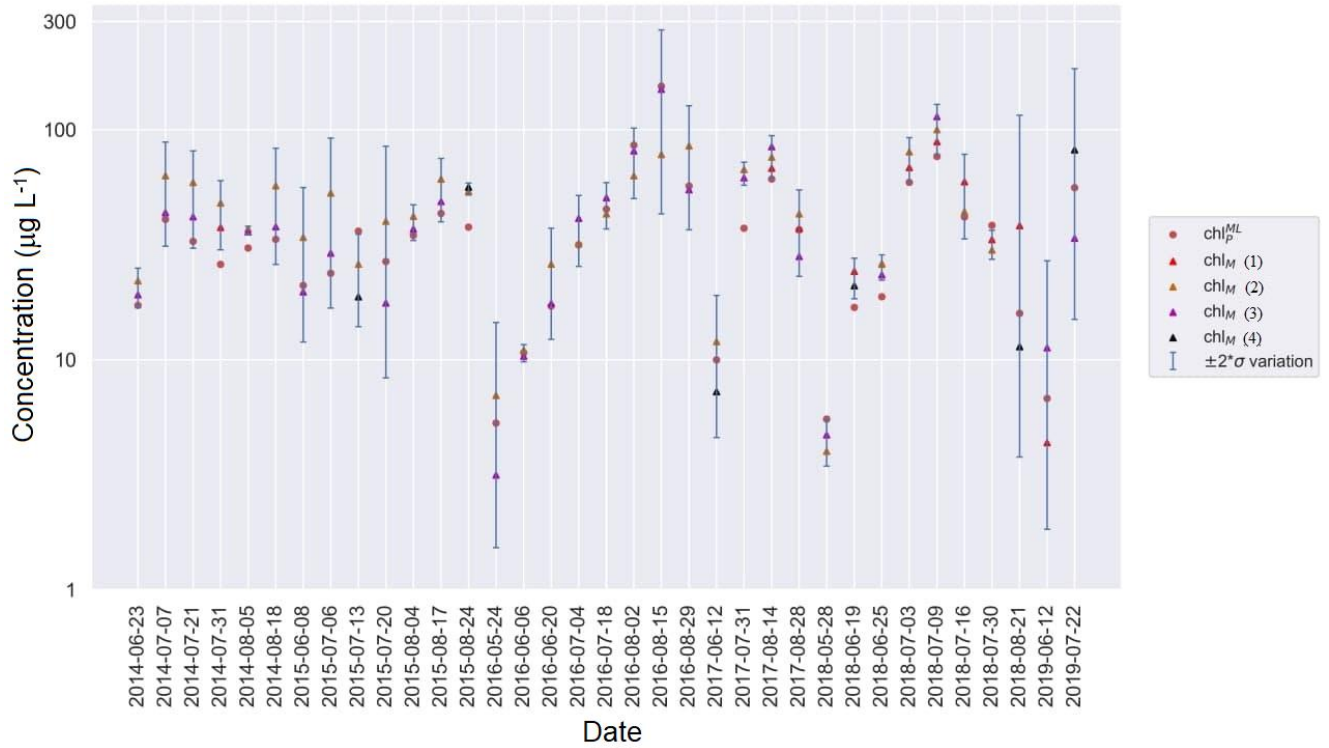


**Figure 3.8. Visualization of the reliability of  $chl_P^{ML}$ , measured as the number of predicted Chl a that fall into the confidence zone, computed by the standard deviation of coincident  $chl_M$ . Values are log-transformed, and the numbers in the legend represent the station from which  $chl_M$  is acquired.**

### 3.3.3 Models performance in retrieving Chla time-series

Estimation of *in situ* Chla using continuous buoy measurements at Station 1 and the proposed models revealed common seasonal patterns of Chla concentration, but high variability in absolute concentrations among years during 2016-2019 (Figure 3.9). Overall, phytoplankton phenology was marked by the onset of elevated concentrations around mid-July, with more intense blooms ( $100 \mu\text{g Chla L}^{-1}$ ) in mid-August, and a slow decline in Chla during September and October. For most models, peak water-column Chla occurred earlier and was lower in 2018, whereas other summers were similar to each other. Visual inspection suggested that peak *in vitro* Chla values were more poorly approximated by models during 2017 than in other years.

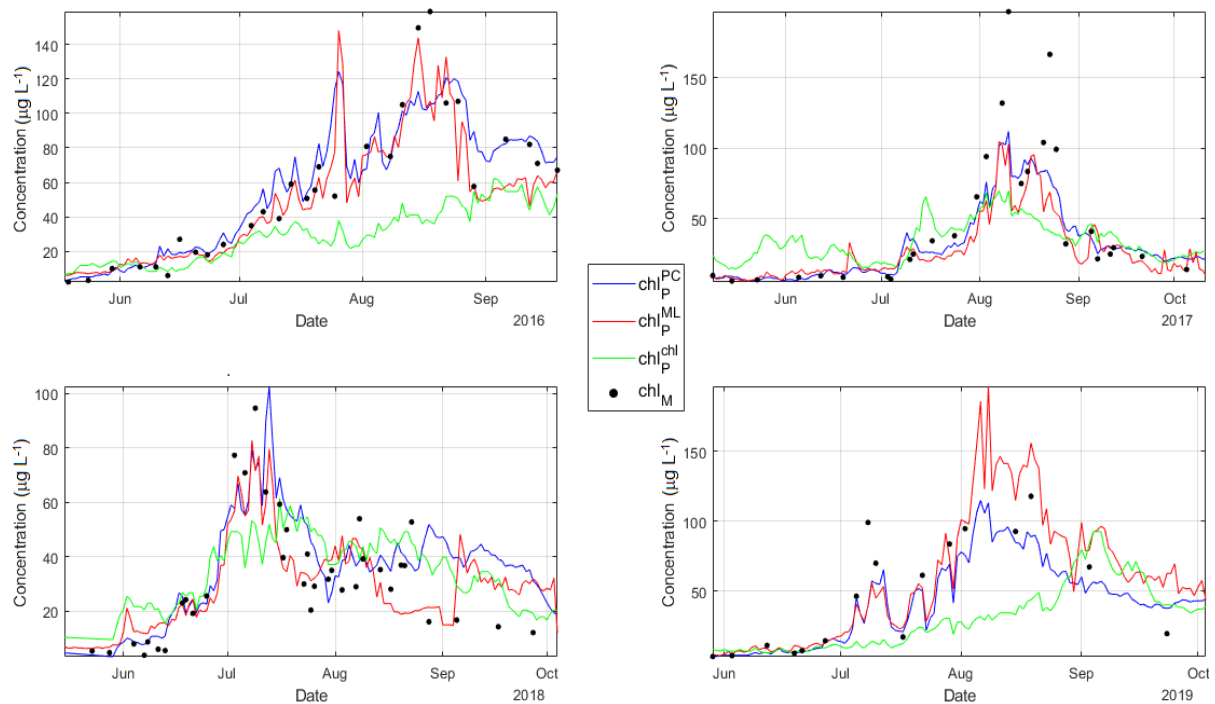


**Figure 3.9. Time-series of  $chl_P^{FC}$ ,  $chl_P^{ML}$ , and  $chl_P^{PC}$  to retrieve continuous long-term Chla for 2016-2019 in station 1 in BPL. Coincident *in vitro* Chla in stations 1-4 ( $chl_M$ ) is used to assess the validity of retrieval.**

Agreement with *in vitro* Chla concentrations was much better for models based on PC fluorescence ( $chl_P^{PC}$ ) and MLR ( $chl_P^{ML}$ ) than for those based on Chla fluorescence ( $chl_P^{chl}$ ) (Figure 3.9). For example,  $chl_P^{chl}$  did not accurately capture values above  $\sim 70 \mu\text{g Chla L}^{-1}$ , whereas  $chl_P^{PC}$  estimated

Chla well to about  $120 \mu\text{g L}^{-1}$  and  $chl_p^{ML}$  retrieved values up to  $150 \mu\text{g L}^{-1}$ . Although  $chl_p^{PC}$  and  $chl_p^{ML}$  often performed equally well in long-term monitoring of Chla, *in vivo* Chla tended to underestimate *in vitro* values in some late-summer instances (e.g., mid-August of 2016 and 2017). Visual analysis of photographs from those dates showed that fluorometric models underestimated Chla when severe surface blooms were evident (Figure 3.10).

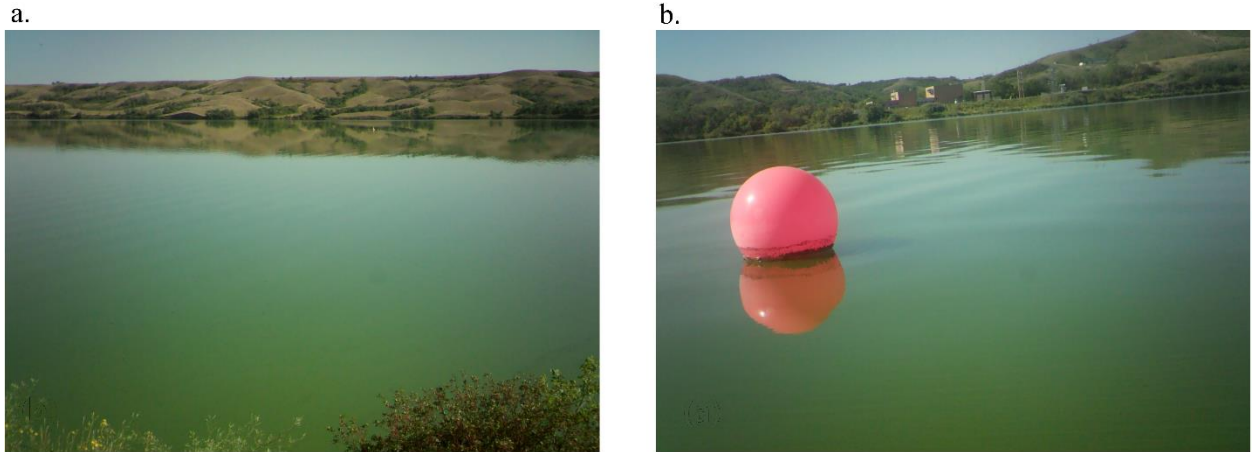


**Figure 3.10. Photographs of surface blooms of cyanobacteria on dates when models significantly underestimated *in vitro* estimates of Chla. (a) image from buoy camera on 15 August 2016, (b) image from shore on 10 August 2017.**

### 3.3.4 Models importance in retrieving remote Chla

To examine the effect of the proposed models on estimation of remote sensing Chla concentration, we populated a recently-developed remote sensing Chla algorithm, SVR (Chegoonian et al., 2021), with 137 reflectance-Chla matchups derived from chlorophyll values estimated from  $chl^{FC}$ ,  $chl_p^{chl}$ ,  $chl_p^{PC}$ , and  $chl_p^{ML}$  models. These trained SVR models were then validated using unseen *in vitro* Chla. When SVR models were applied to a common Sentinel-2 image of BPL, substantial differences were noted in the ability of remote sensing to capture spatial variation in Chla concentrations (Figure 3.11). In particular, the model trained by  $chl^{FC}$  values showed poor relative and absolute performance (Slope = 0.1, MALE = 2.01), whereas use of  $chl_p^{chl}$  increases model strength (Slope = 0.83) but not accuracy (MALE = 2.12). In contrast, both  $chl_p^{PC}$  and  $chl_p^{ML}$  significantly improved estimates of remotely-sensed Chla by increasing accuracy 30% (lowering MALE) compared to  $chl_p^{chl}$ . Furthermore, compared to

$chl^{FC}$ , heatmaps of Chla based on other models detected consistent spatial patterns, although they differed in the maximum Chla returned (Figure 3.11).

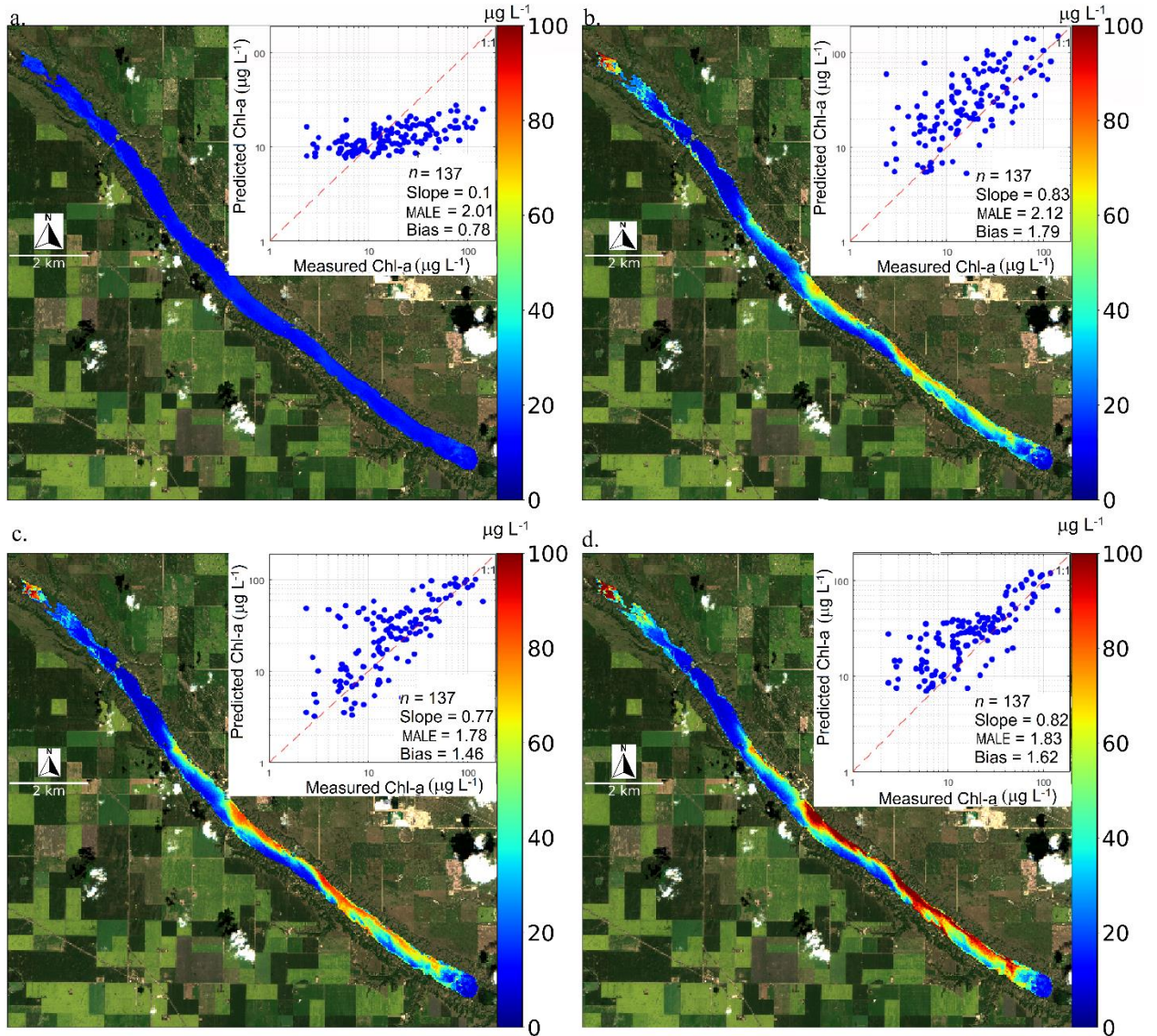


**Figure 3.11. Different models to retrieve *in vivo* Chla ( $chl^{FC}$ ,  $chl_p^{chl}$ ,  $chl_p^{PC}$ , and  $chl_p^{ML}$ ), employed as training data for an SVR algorithm, result in substantial changes in the performance of remote-sensing Chla retrieval. (a-d) Heatmaps of Chla, when an SVR algorithm feed by  $chl^{FC}$ ,  $chl_p^{chl}$ ,  $chl_p^{PC}$ , and  $chl_p^{ML}$ , respectively, and is applied on Sentinel-2 image of BPL**

**acquired on 22 July 2019. The insets indicate the validation results for remotely-retrieved Chla, estimated on unseen *in vitro* Chla.**

### **3.4 Discussion**

Fluorescence estimates of Chla concentrations from instrumented buoys have been used widely to study the characteristics of surface blooms (Seppälä et al. 2007; Groetsch et al. 2014), changes in temporal variability in water productivity (Serôdio et al. 2001; Frankenbach et al. 2020), importance of cyanobacteria to phytoplankton assemblages (Catherine et al. 2012; Zamyadi et al. 2016), and develop networks of limnological buoys to investigate landscape patterns of water quality change (Hamilton et al. 2015; Boss et al. 2018). Often it is assumed that factory-presets of buoy fluorometers allow accurate estimation of absolute Chla concentrations or relative changes over a wide range of lake production. Here we find that on-board fluorometry lacks both accuracy and reliability to estimate *in situ* Chla relative to predictions based on models calibrated with six years of *in vitro* monitoring (Figure 3.7 and Table 3.4), similar to patterns seen elsewhere (Gregor and Maršálek 2004; Catherine et al. 2012; Escoffier et al. 2014; Roesler et al. 2017). Unexpectedly, models based on fluorescence of PC were more accurate than those derived from Chla fluorescence, or MLR models based on non-pigmented parameters (turbidity, CO<sub>2</sub> concentration, transparency, and month). Although all models improved the capability of buoys to recover peak Chla values, PC and MLR models were more reliable than those based on Chla fluorescence. When applied to remotely-sensed reflectance, PC and MLR models also captured a wider range of spatial variability than did other approaches (Figure 3.11), suggesting that these models were more suitable to map transient blooms of cyanobacteria in highly-eutrophic lakes.

#### **3.4.1 Considerations to employ field fluorometers to retrieve Chla**

Weak correspondence between factory-calibrated fluorometric Chla ( $chl^{FC}$ ) and ground-truthed *in situ* values ( $chl_M$ ) have been reported in other studies and by instrument manufacturers (Gregor and Maršálek 2004; Catherine et al. 2012; Escoffier et al. 2014; Roesler et al. 2017). While *in vivo* fluorometric methods are not expected to replace *in vitro* methods in terms of absolute accuracy, they should maintain a reasonable relative accuracy to be useful in ecosystem monitoring applications. Instead, our analyses in a eutrophic lake demonstrated that  $chl^{FC}$  does not even capture the relative changes in laboratory-determined Chla time series (Figures 3.5, 3.7.a), in contrast to investigators who

report a high correlation between  $chl^{FC}$  and  $chl_M$  (Catherine et al. 2012; Escoffier et al. 2014). This difference may relate to the type of fluorometer employed (Roesler et al. 2017), their excitation and emission characteristics (Catherine et al. 2012), or the composition of phytoplankton in the lake (Escoffier et al. 2015). Regardless of the source of disagreement, the low relative accuracy of  $chl^{FC}$  suggests that this metric cannot be used routinely to evaluate spatial or temporal variation in phytoplankton abundance of ultra-eutrophic lakes.

Our findings suggest that the single-excitation-wavelength field fluorometers common to many aquatic instrument platforms (Zamyadi et al. 2016; Piermattei et al. 2018) are neither accurate nor reliable and cannot be used to estimate *in situ* Chla without further correction and site-specific calibration. In particular, accuracy of  $chl^{FC}$  estimations declined at higher Chla values, making this parameter particularly unsuitable for early warning detection of cyanobacterial blooms without correction and calibration (Roesler et al. 2017). We suggest that  $chl^{FC}$  values must be increased by at least 150% to achieve comparable means to those derived from modeled and *in vitro* determinations of Chla. Similar conclusions were reached by Roesler et al. (2017) who proposed a two-fold modification for all fluorometric Chla observations for different sensors (excitation 470 nm, emission 695 nm) in the ocean.

Unlike models using  $chl^{FC}$  and  $chl_p^{chl}$ , those based on fluorescence of PC ( $chl_p^{PC}$ ) were capable of accurately estimating *in situ* Chla concentrations, both in terms of absolute amount and relative variation during series trends or spatial patterns. Although the superior performance of the PC sensor is partly dependent on both the instrument type and lake parameters, we expect that this conclusion may be generalized to other mesotrophic or eutrophic lakes with abundant colonial cyanobacteria, given the wide range of Chla values observed in BPL (2 - 200  $\mu\text{g L}^{-1}$ ). However, these results should be treated by caution in systems dominated by CDOM or non-algal particles as CDOM fluorescence may largely interfere with that of Chl-a and PC, thereby leading to overestimation of phytoplankton (Stedmon and Markager 2005; Goldman et al. 2013; Xiaoling et al. 2019), while non-algal particles can cause underestimation of phytoplankton by absorbing both excitation and emission lights (Brient et al. 2008). The importance of phytoplankton composition to the performance of the PC-based analysis has also been recognized in other cyanobacteria-rich waterbodies (Bowling et al. 2016), including the Baltic Sea (Seppälä et al. 2007) where differences between the accuracy of Chl- and PC-based

fluorometric sensors ( $R^2 = 39\%$  and  $76\%$ , respectively) were similar to those recorded in the present study ( $R^2 = 34\%$  and  $87\%$ ).

Improved information on the mechanisms regulating site-specific variation in the relation between *in vivo* and *in vitro* Chla concentrations is essential for the upscaling of lake analyses to broader geographic landscapes using satellite imagery. Presently, Chla retrieval using remote sensing technologies relies mostly on ML algorithms that are trained and tested using *in situ* Chla measurements. The competency of these algorithms is highly dependent on the quality of *in situ* Chla estimates and is often limited by the low data availability or temporal coherence of observations. We note herein that *in vivo* Chla measures were usually improved after our correction and calibration process; however, there remained some circumstances in which corrected Chla still underestimated *in situ* concentrations (Figure 3.9). Specifically, corrected Chla values underestimated *in vitro* Chla when concentrations were  $> 100 \mu\text{g L}^{-1}$  and positively-buoyant colonial cyanobacteria (e.g., *Microcystis*, *Anabaena*, *Aphanizomenon* spp.) are abundant in the surface waters (Hayes et al. 2019; Swarbrick et al. 2019). Such extreme surface blooms tend to occur in hypereutrophic waters, particularly during calm intervals which follow prolonged periods of strong winds and turbulent mixing (Paerl 2009). Under these conditions, transmission of photons is reduced by high densities of cyanobacteria, leading to underestimates of fluorescence by *in vivo* methods, while *in vitro* estimates of pigment concentration based on chemical extraction do not change. When possible, training of remote sensing algorithms should not use *in vivo* Chla estimates from buoys collected during these surface bloom intervals to avoid bias in analysis of temporal and spatial variability.

#### **3.4.2 Effectiveness of PC versus Chla fluorometers in retrieving Chla**

Phycocyanin-based fluorescence models were more accurate and more reliable than those developed using Chla fluorometry with both extended range (up to  $120 \mu\text{g Chla L}^{-1}$ ) and more linear relationships with *in vitro* Chla at lower concentrations (Figure 3.7). These findings were unexpected because Chla fluorometers are designed to be sensitive to the total biomass of Chla from phytoplankton, including both algae and cyanobacteria, whereas PC-based fluorometers are expected to be sensitive mainly to cyanobacteria and secondarily cryptophytes. Several characteristics of our study may have predisposed PC models to outperform those based on Chla.

First, cyanobacteria are the predominant taxon in BPL after June through the end of summer in all years (Vogt et al. 2018; Hayes et al. 2019; Swarbrick et al. 2019). As seen in Seppälä et al. (2007), a strong linear relationship between PC fluorescence and Chl $a$  concentration (Figure 3.6.b) is expected in instances where cyanobacteria compose over 50% of community biomass. In BPL, cyanobacteria usually comprise 40-100% of total phytoplankton biomass after late June based on both direct taxonomic counts 2015-2018 (Figure 3.12) and 25 yr of HPLC analysis of *in situ* biomarker carotenoid pigments (Vogt et al. 2018; Swarbrick et al. 2019). Given that phytoplankton biomass is generally low during June due to invertebrate grazing (Dröscher et al. 2009), and that cyanobacteria are rare at this time relative to cryptophytes and green algae (McGowan et al. 2005), we anticipate that correspondence between modeled Chl $a$  (based on PC fluorescence) and *in situ* Chl $a$  may be weaker in spring and early summer.

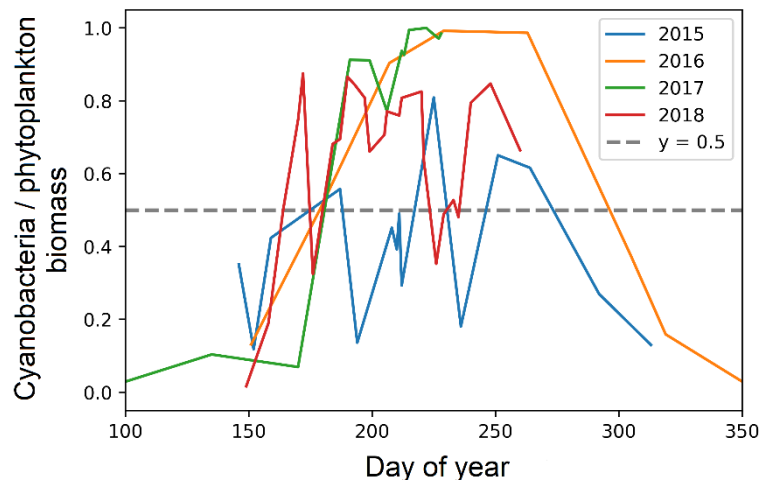


**Figure 3.12. The ratio of cyanobacteria biomass to total phytoplankton biomass in BPL, averaged on three depths (0.8, 2.8, and 3.5 m) in station 1 for 2015-2018. Cyanobacteria tend to be dominant taxa in BPL from day 175 (late June) to day 300 (late October) of a year.**

Second, cyanobacteria fluorescence originates in both Chl $a$  and PC due to the role of the latter as an accessory pigment in these prokaryotes. Phycocyanin plays a major role in harvesting light, but transfers most of energy to Chl $a$  and fluoresces residual energy at ~650 nm (Simis et al. 2012). The transferred light stimulates Chl $a$  to fluoresce in around 680 nm in direct proportion to Chl $a$  concentration (Johnsen and Sakshaug 2007). Therefore, the PC fluorometer, whose emission filter is

wide enough to pass both Chla and PC fluorescence ( $640 \pm 40$  nm), senses both PC and Chla fluorescence of cyanobacteria.

Third, *in vivo* Chla fluorometer commonly used in freshwater instrument buoys can be insensitive to the presence of cyanobacteria if the prokaryotes do not possess short-wavelength forms of phycoerythrin (Raateoja et al. 2004; Suggett et al. 2004; Johnsen and Sakshaug 2007). As cyanobacteria predominate at very high Chla levels (Vogt et al. 2018; Hayes et al. 2019), such insensitivity may disproportionately underestimate high Chla values (Figure 3.7.b). In support of this hypothesis, we note that *Dolichospermum* and *Chlorella vulgaris* were the most abundant cyanobacteria and algae, respectively, based on cell enumerations at station 2 during 2014-2018, and that the excitation-emission matrices (EEMs) of these taxa show that only Chla from eukaryotes contributes strongly to Chla fluorescence in the range of detection (region 1 in Figure 3.13). These sensors are often insensitive to the fluorescence of the cyanobacteria (Figure 3.13.b) relative to that from other phytoplankton (Figure 3.13.a).

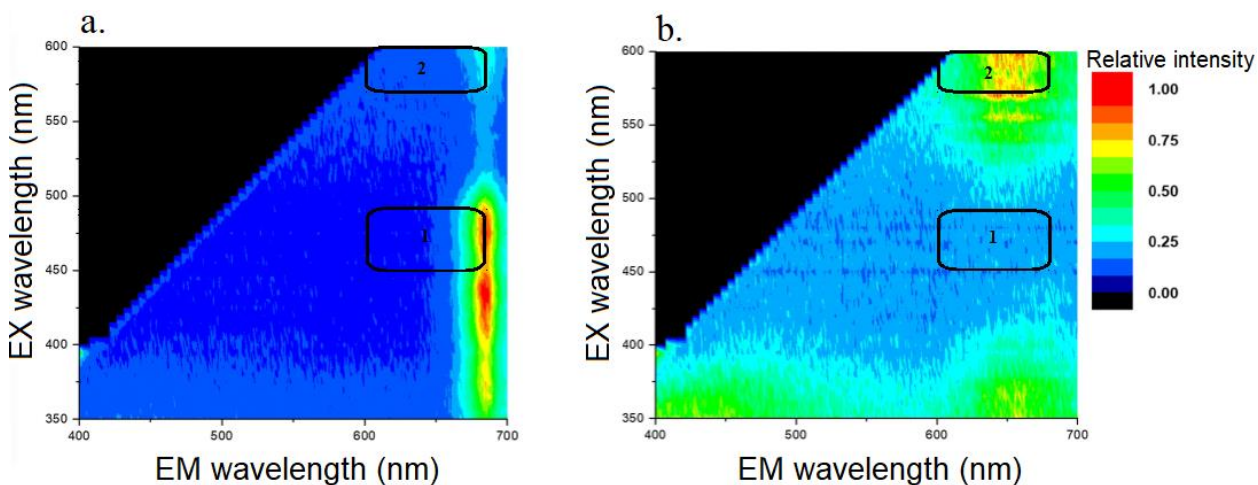


**Figure 3.13. The normalized fluorescence excitation-emission matrices (EEMs) of the most dominant algae and cyanobacteria species in BPL. (a) green algae (*Chlorella vulgaris*) and (b) cyanobacteria (*Dolichospermum*), modified from (Shin et al. 2018). Regions 1 and 2 are the spectral range of the employed Chla and PC fluorometers, respectively.**

Fourth, the PC fluorometer stimulates fluorescence from algae which lack PC, possibly by initiating energy transfer from accessory pigments to Chla (e.g., Chlb, carotenoids). Region 2 in Figure

3.13 confirms that there is fluorescence from *Chlorella vulgaris* in the spectral range of the PC fluorometer. It has been shown that fluorometers with an emission band above 660 nm are affected by overlapping fluorescence signals of Chl $a$  fluorescence (Simis et al. 2012). Given this sensitivity of the PC fluorometer to detect Chl $a$  fluorescence, this system appears also capable of estimating lower Chl $a$  values during intervals when cyanobacteria are normally rare (May to early June) (McGowan et al. 2005; Hayes et al. 2019; Swarbrick et al. 2019).

Fifth, wide variation in the Chl $a$  content and fluorescence characteristics among different algal taxa or growth phases may have contributed to the poor performance of the Chl $a$  fluorometer even during intervals when eukaryotes are abundant. According to Equation 3.1, different algal taxa yield different  $\alpha_{chl}^*$  and  $\Phi_F$  values, causing non-linearity in the relationship of fluorescence and Chl $a$ . While a calibration slope varies as a function of growth irradiance or growth phase, the largest source of slope variability is due to variations in accessory pigmentation (Proctor and Roesler 2010). In the case of BPL, there are at least eight common accessory pigments present in the water column at any given time, with substantial seasonal variation in the predominant compound (McGowan et al. 2005; Swarbrick et al. 2019).

### 3.4.3 Performance of environmental MLR models

Here, we showed the reasonable performance of MLR based on environmental factors to retrieve *in vitro* Chl $a$ . Although turbidity occasionally enters predictive models elsewhere (Rome et al. 2021), to the best of our knowledge, ours is the first model with turbidity as the main parameter that exhibits performance comparable to that of fluorescence-based models. As turbidity probes are inexpensive, robust, and easy to calibrate, relative to fluorometric sensors (Rome et al. 2021), the strong performance should be compared to other locations to evaluate the suitability in monitoring phytoplankton blooms. If validated, this approach for the calibration of previous long records of turbidity measurements may be useful in expanding the spatial extent of Chl $a$  retrieval for time series development in similar eutrophic lakes where turbidity is dominated by phytoplankton. This might be negated in case of sediment resuspension under strong wind mixing events.

Our MLR model includes several *in situ* factors as *in vitro* Chl $a$  predictors. Apart from statistical justifications for these parameters (strong correlation and significant improvement of the model performance; Figure 3.4 and Table 3.3), inclusion of the predictors was consistent with

relationships with Chla known from previous studies. For example, turbidity may have been included because it is mainly biological in nature in BPL and is known to increase with cyanobacterial density. Similarly, the negative correlation between light transmission (normalized PAR) and Chla is consistent with the effects of light attenuation by Chla, as well as physical shading by phytoplankton biomass. Inclusion of sampling month as a predictor is consistent with the strong seasonal succession of phytoplankton seen in these lakes (McGowan et al. 2005; Dröscher et al. 2008; Baulch et al. 2009; Vogt et al. 2018; Swarbrick et al. 2019). Finally, a negative relationship between Chla and CO<sub>2</sub> concentration is expected as the diel cycles of CO<sub>2</sub> concentration are controlled in part by changes in pH and photosynthesis, both of which are strongly affected by the abundance of cyanobacteria (Wiik et al. 2018). We also tested incorporating fluorescence measurements into the MLR model; however, an ANOVA test showed that, for such a model, almost all chlorophyll variance can be explained with fluorescence parameter, making other environmental factors insignificant.

### 3.5 Conclusions and recommendations

Analysis of long-term, coeval *in vivo* and *in vitro* Chla measurements in a eutrophic lake demonstrated that factory-calibrated *in vivo* Chla ( $chl^{FC}$ ) of a single-excitation-band fluorometer should be corrected and tuned in a site-specific manner to provide more accurate and reliable estimates of phytoplankton abundance. Here we introduced three different models to predict Chla from *in vivo* measurements in an eutrophic lake dominated by cyanobacteria; two single-linear models based on raw fluorescence from Chla and phycocyanin (PC) fluorometers (called  $chl_p^{chl}$  and  $chl_p^{PC}$ , respectively) and one MLR model (called  $chl_p^{ML}$ ), trained by environmental factors, such as turbidity and CO<sub>2</sub> concentration. These models were assessed and compared based on both individual metrics and their performance in real applications.

In terms of the ability to recover *in vitro* Chla concentrations (‘accuracy’), the model based on PC-fluorescence ( $chl_p^{PC}$ ) compensated the high bias in factory-calibrated Chla ( $chl^{FC}$ ) and reduced average relative error from ~150% to ~35% when gauged by mean absolute logarithmic error (MALE) among other metrics. In terms of reliability of recovered values (ability to capture range of variation),  $chl_p^{ML}$  model maintained ~90% reliability to return Chla values within  $\pm 3\sigma$  of mean *in vitro* Chla ( $chl_M$ ), whereas  $chl_p^{PC}$  and  $chl_p^{chl}$  returned ~77% and ~60%.

Application of *in vivo* estimates of Chla concentration to train algorithms used in remote sensing showed that only fluorescence-corrected models were capable of delineating the spatial variation in Chla within BPL. Specifically, models based on PC fluorescence and environmental factors significantly improved lake monitoring by increasing the range of Chla retrieval to up to 150  $\mu\text{g L}^{-1}$ , whereas  $chl_p^{chl}$  could not retrieve values  $> 70 \text{ Chla } \mu\text{g L}^{-1}$ . Further use of  $chl_p^{PC}$  instead of  $chl_p^{chl}$  also decreased the error of Chla retrieval using Sentinel-2 images by  $\sim 35\%$ . For a system that is designed to monitor HABs in a highly eutrophic lake, system saturation at only moderate Chla levels is problematic.

We conclude that several features of the PC fluorometer make it more suitable to develop remote sensing protocols for lakes subject to intense surface blooms of cyanobacteria. Given that a source of inaccuracy in remote retrieval of Chla is uncertainties in Chla training data, especially when different *in vivo* and *in vitro* approaches are involved in collecting *in situ* data, the models proposed here may be considered as a preprocess step to improve consistency between *in vivo* and *in vitro* measurements of Chla before feeding into a remote-sensing model.

## Chapter 4

# Quantification of chlorophyll-a in small eutrophic lakes using Sentinel-2 and Landsat-8 imagery and locally tuned machine learning models

### 4.1 Introduction

Small inland waters (SIWs) are the predominant form of lakes globally (Downing et al. 2006), yet they are highly subject to water quality degradation due to urbanization and changes in land use (Carpenter et al. 1998). Despite recognition of the problem for decades, water quality of SIWs continues to degrade rapidly, resulting in harmful algal blooms (HABs) (Walker 2019) whose frequency, magnitude, and persistence have increased globally due to climate warming (Ho et al. 2019). Changes in near-surface concentration of chlorophyll-*a* (Chl*a*) is one of the most reliable proxies retrievable of HAB intensification, as Chl*a* is present in all phytoplankton, including cyanobacteria (Roesler et al. 2017), and has unique absorption features that can be detected through space-borne imaging (Kutser 2009).

Accurate Chl*a* retrieval from optical radiometry is affected by the interplay between solar photons in water-leaving radiance ( $L_w$ ) and the inherent optical properties (absorption, scattering) of pure water and its dissolved or suspended constituents. In particular, reflectance is affected strongly by phytoplankton density, colored dissolved organic matter (CDOM), and non-algal particles (NAP) (Babin et al. 2003), while  $L_w$  is further attenuated by atmospheric characteristics within the path to satellite sensors. To retrieve Chl*a*, atmospheric correction (AC) processors are used to convert top-of-atmosphere reflectance ( $\rho_{TOA}$ ) to satellite-derived remote sensing reflectance ( $R_{rs}^\delta$ ).  $R_{rs}^\delta$  includes uncertainties in the AC and sensor radiometric measurements and approximates remote sensing reflectance ( $R_{rs}$ ), defined as the ratio of water-leaving radiance to the total downwelling irradiance just above water. Afterwards, a wide range of algorithms, including semi-analytical, empirical, and machine-learning (ML) models, can be applied to retrieve Chl*a* from reflectance measurements (Morel 1980; Carder et al. 1999; Odermatt et al. 2012).

Empirical models based on blue-green wavelengths (e.g., NASA's OCx models) tend to perform well when phytoplankton governs  $R_{rs}$  (Morel 1988; O'Reilly et al. 1998; Morel and

Maritorena 2001; O'Reilly and Werdell 2019), but can be inaccurate when CDOM or NAP control optical properties (Novoa et al. 2012; Le et al. 2013; Freitas and Dierssen 2019). In such cases and when Chl $a$  concentration is high (mostly in freshwaters with severe blooms), studies suggest using red and near-infrared (NIR) wavelengths, where Chl $a$  absorption (~667 nm) and fluorescence (683 nm) peaks are located, while CDOM and NAP absorption, as well as NAP backscattering may be negligible or spectrally-invariant (Gitelson 1992; Gitelson et al. 2007).

Various red-NIR indices have been developed and validated for ocean color sensors, including the 2band, 3band, and Normalized Difference Chlorophyll Index (NDCI) (Dall'Olmo and Gitelson 2005; Moses et al. 2009; Mishra and Mishra 2012) for use with data from the Medium Resolution Imaging Spectrometer (MERIS). Similarly, the Maximum Chlorophyll Index (MCI) (Gower et al. 2005), the Fluorescence Line Height (FLH) (Letelier and Abbott 1996), and the Maximum Peak Height (MPH) (Matthews et al. 2012) are based on absorption and fluorescence features of Chl $a$ . Models based upon red or NIR bands may be less sensitive to uncertainties in AC, especially when closely spaced (Moses et al. 2009); nonetheless, models performance depends on the range of Chl $a$  variation, the amount of interference from other constituents (e.g., NAP backscattering), and the band configuration of sensors.

Machine-learning (ML) algorithms, especially neural networks (NN), are widely used to retrieve Chl $a$  over geographically-extensive regions using extensive synthetic or *in situ* radiometric measurements from diverse optical water types (OWTs). For example, the European Space Agency (ESA) provides a Chl $a$  product from MERIS using a processing scheme based on NN (Doerffer and Schiller 2007; Schroeder et al. 2007). Similarly, Vilas et al. (2011) applied Multilayer Perceptron (MLP) on MERIS data to retrieve Chl $a$  in coastal waters with root mean square errors (RMSE) of ~0.8 mg m<sup>-3</sup> for a Chl $a$  range of 0.03-8 mg m<sup>-3</sup>, while Support Vector Machines/Regressions (SVM/SVR) (Vapnik 2013) have been applied to oceanic waters (Haigang et al. 2003; Kwiatkowska and Fargion 2003; Camps-Valls et al. 2006; Martinez et al. 2020; Hu et al. 2021).

To date, remotely-sensed Chl $a$  estimates have been applied successfully to large waterbodies, including the open ocean (Bryan et al. 2005; O'Reilly and Werdell 2019), coastal waters (Werdell et al. 2009; Moses et al. 2012), and large lakes (Gons et al. 2008; Binding et al. 2011b; Schaeffer et al. 2018; Binding et al. 2021), using ocean-color sensors such as MERIS, MODIS, and the Sea-viewing Wide

Field-of-view Sensor (SeaWiFS). In contrast, *Chl<sub>a</sub>* retrieval for SIWs has been challenging because of uncertainties in atmospheric correction, especially adjacency effects (Pahlevan et al. 2020), and that optics of inland waters is further modulated by particulate organic and inorganic particles, as well as CDOM (Mobley 1994). Generally, ocean-color sensors lack sufficient high spatial resolution (<100m) to sample SIWs (Philipson et al. 2014; Ansper and Alikas 2019). Thus, while the Ocean Color and Land Imager (OLCI) onboard Sentinel-3 provides a 300-m spatial resolution and diverse spectral bands that can capture water *Chl<sub>a</sub>* content in large lakes (Smith et al. 2018; Pahlevan et al. 2020), there have been few applications to freshwaters with width or length less than a few km (Philipson et al. 2014).

Hence, for small inland waters, recent research focuses on the Multi-Spectral Instrument (MSI) and Operational Land Imager (OLI) sensors onboard Sentinel-2 (S2) and Landsat-8 (L8) satellites, platforms providing excellent global coverage and spatial resolutions of 10 to 60 m. Although designed for land observations, these sensors are also applicable to small aquatic ecosystems (Pahlevan et al. 2014; Cao et al. 2019; Xu et al. 2020) because images are available at sub-weekly temporal resolution at higher latitudes (Li and Roy 2017), proven to be consistent (Wulder et al. 2015; Claverie et al. 2018; Helder et al. 2018; Pahlevan et al. 2019), and readily accessible (Zhu et al. 2019), while radiometric quality (absolute and relative calibration, signal-to-noise ratio) is sufficient for remote sensing of aquatic environments (Helder et al. 2018; Pahlevan et al. 2019).

Diverse computational models have been used with MSI and OLI sensors, including 2band, 3band, and NDCI (Anspers and Alikas 2019). While MSI has been utilized for detecting cyanobacterial blooms and retrieval of *Chl<sub>a</sub>* concentration in subalpine lakes (Bresciani et al. 2018), studies suggest that current approaches have limitations at the extremes of the observed *Chl<sub>a</sub>* range (Dörnhöfer et al. 2016; Toming et al. 2016). Furthermore, the accuracy of these approaches has usually been assessed using only the coefficient of determination ( $R^2$ ), a parameter with limited degrees of freedom (Kvålseth 1985). Instead, application of Mixture Density neural Networks (MDN) to a large dataset of *in situ* radiometry and *Chl<sub>a</sub>* measurements allowed development of a model which outperformed other state-of-the-art algorithms for a wide range of *Chl<sub>a</sub>* concentration (0.1-100 mg m<sup>-3</sup>) using MSI and OLCI data (Pahlevan et al. 2020), as well as OLI data (Smith et al. 2021). Additionally, Cao et al. (2020) developed boosting tree (BST), a model based on the Gradient Boosting Tree algorithm (XGBoost)

(Chen and Guestrin 2016), and successfully tested it on OLI data taken from lakes in eastern China; the model, however, was outperformed by MDN when applied to a global dataset (Smith et al. 2021).

Despite recent developments, retrieving reliable Chl $a$  in SIWs using moderate-resolution satellite data remains challenging. Empirical models (differential/ratio-based indices) leverage only a limited range of the spectrum and may not optimally solve ill-posed conditions (O'Sullivan 1986) that are common in inverse problems such as Chl $a$  retrieval (Sydor et al. 2004; Defoin-Platel and Chami 2007; Werdell et al. 2018; Pahlevan et al. 2020). Similarly, while globally trained ML (GML) models (e.g., MDN) can leverage the full visible and near-infrared spectrum (VNIR) and may handle non-linear and ill-posed problems, they can be susceptible to uncertainties in AC that could reduce their suitability under sub-optimal atmospheric or aquatic conditions (Pahlevan et al. 2020; Smith et al. 2021). Taken together, these observations suggest that development of locally trained ML (LML) models using  $R_{rs}^{\delta}$  measurements might be a suitable option for local monitoring of Chl $a$  in SIWs.

Here, we introduce a machine learning approach based on SVR to retrieve robust and reliable Chl $a$  time series and spatial maps in Buffalo Pound Lake, Saskatchewan, Canada, using MSI and OLI imagery. Our SVR model was trained and validated with  $\sim 200$  co-located *in situ* Chl $a$  measurements with corresponding  $R_{rs}^{\delta}$  observations. We compared model performance against several state-of-the-art algorithms, including OC3, MDN, 2band, BST, and LMDN – a locally trained MDN – in terms of its quantitative (general and stratified) performance as well as its spatial and temporal consistency. Then, we assessed the robustness of the model in the presence of uncertainties from two AC processors (i.e., iCOR and ACOLITE) and different two broadly-defined OWTs, to assess its potential utility for other small eutrophic lakes.

## 4.2 Materials and Methods

### 4.2.1 Study site

Buffalo Pound Lake (BPL) is a long ( $\sim 30$  km), narrow ( $< 1$  km), and shallow ( $< 6$  m) lake located in the Qu'Appelle River watershed, Saskatchewan, Canada (Figure 4.1, Table 4.1). Currently, the basin exhibits eutrophic waters, with summer blooms occurring during June-September and peak surface populations of phytoplankton often during July-August which might be accompanied by scum on the water surface (Kehoe et al. 2019). Continuous monitoring for over 25 years shows that

cyanobacteria are the predominant phytoplankton phylum during July-September (Vogt et al. 2018; Swarbrick et al. 2019). The lake landscape orientation parallel to the direction of prevailing winds means that the water column is polymictic, experiencing frequent mixing periods with intermittent vertical stratification (Dröscher et al. 2008).

Several attributes make BPL suitable for the development of remote sensing models of *Chla*. First, the lake is an important freshwater resource as it supplies drinking water to one-quarter of the provincial population, including the nearby cities of Regina and Moose Jaw (Hosseini et al. 2018). Second, multi-decadal records of field data exist for the lake, including *Chla* measurements, and the waterbody experiences severe HAB events (Kehoe et al. 2015). Third, the lake size and its elongated shape allow use of sensors with relatively high spatial resolution, such as MSI and OLI.

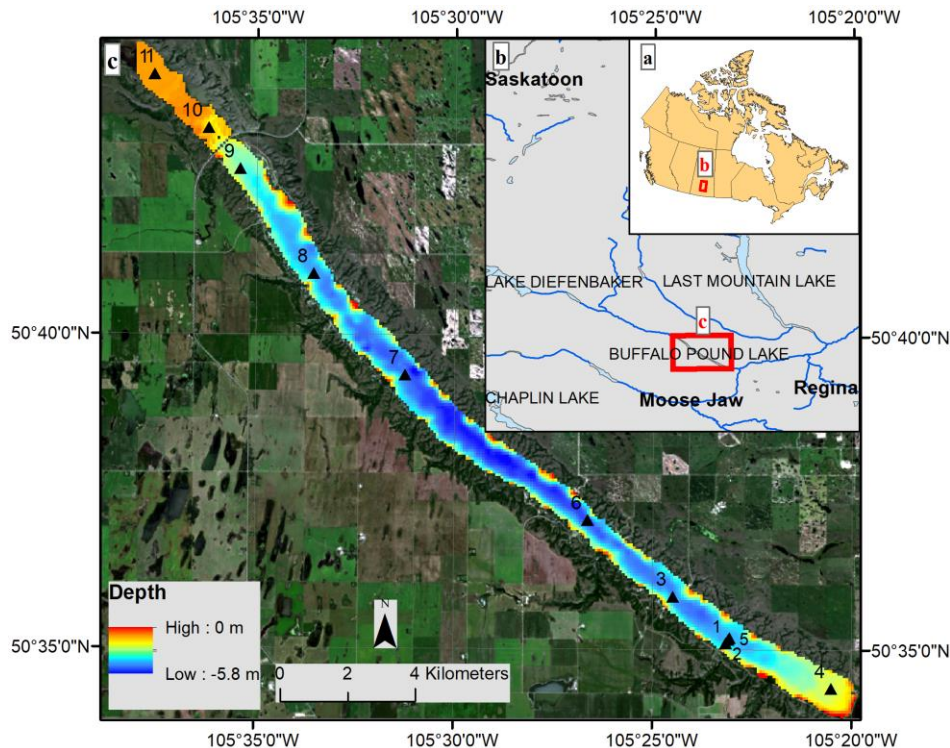


**Figure 4.1.** Map and location of Buffalo Pound Lake (BPL), Saskatchewan, Canada. (a) Location of the Qu'Appelle River watershed within Canada. (b) Location of BPL within Qu'Appelle River watershed. (c) A Landsat-8 RGB image of BPL overlaid on a bathymetric map on which sampling stations are also shown (solid black triangles numbered 1 to 11).

**Table 4.1. Buffalo Pound Lake characteristics and water quality parameters at station 1 (averaged from late May to early September 2014-2020). P stands for phosphorus, TSS for total suspended solids, and DOC for dissolved organic carbon.  $a_{CDOM}(440)$  is CDOM absorption measured at 440 nm.**

Physical Characteristic	Value	Water Quality Parameter	Mean Value
Altitude (m)	501	Water temperature (°C)	19
Mean depth (m)	3.8	Total P (mg m <sup>-3</sup> )	88
Maximum depth (m)	5.8	Chl $a$ (mg m <sup>-3</sup> )	31
Length (km)	30	TSS (g m <sup>-3</sup> )	11.8
Average width (km)	0.9	$a_{CDOM}(440)$ (m <sup>-1</sup> )	0.28
Surface (km <sup>2</sup> )	30	DOC (g m <sup>-3</sup> )	6.7
Volume (m <sup>3</sup> )	92 × 10 <sup>6</sup>	Turbidity (NTU)	9.2

Chl $a$  in BPL is higher than the average for freshwaters (Filazzola et al. 2020), as opposed to Dissolved Organic Carbon (DOC) which is in a low/medium amount for freshwaters (Toming et al. 2020). It can be claimed that particles, especially algal particles, mostly control the optical characteristics of water in BPL. This hypothesis can be confirmed by Figure 4.2 (upper diagonal) where the optical characteristics of water samples e.g., turbidity and Secchi Disk Depth (SDD) are highly correlated with Total Suspended Solids (TSS) and Chl $a$ . However, Figure 4.2 (lower diagonal) also reveals that the relationship depends on the station location as southern stations (1-8) show a stronger relationship between Chl $a$  and optical characteristics. This can be justified based on the distribution of water constituents, plotted in Figure 4.2 (diagonal), where northern stations (9-11) contain more sediments, as opposed to the southern stations which are more dominated by Chl $a$ .

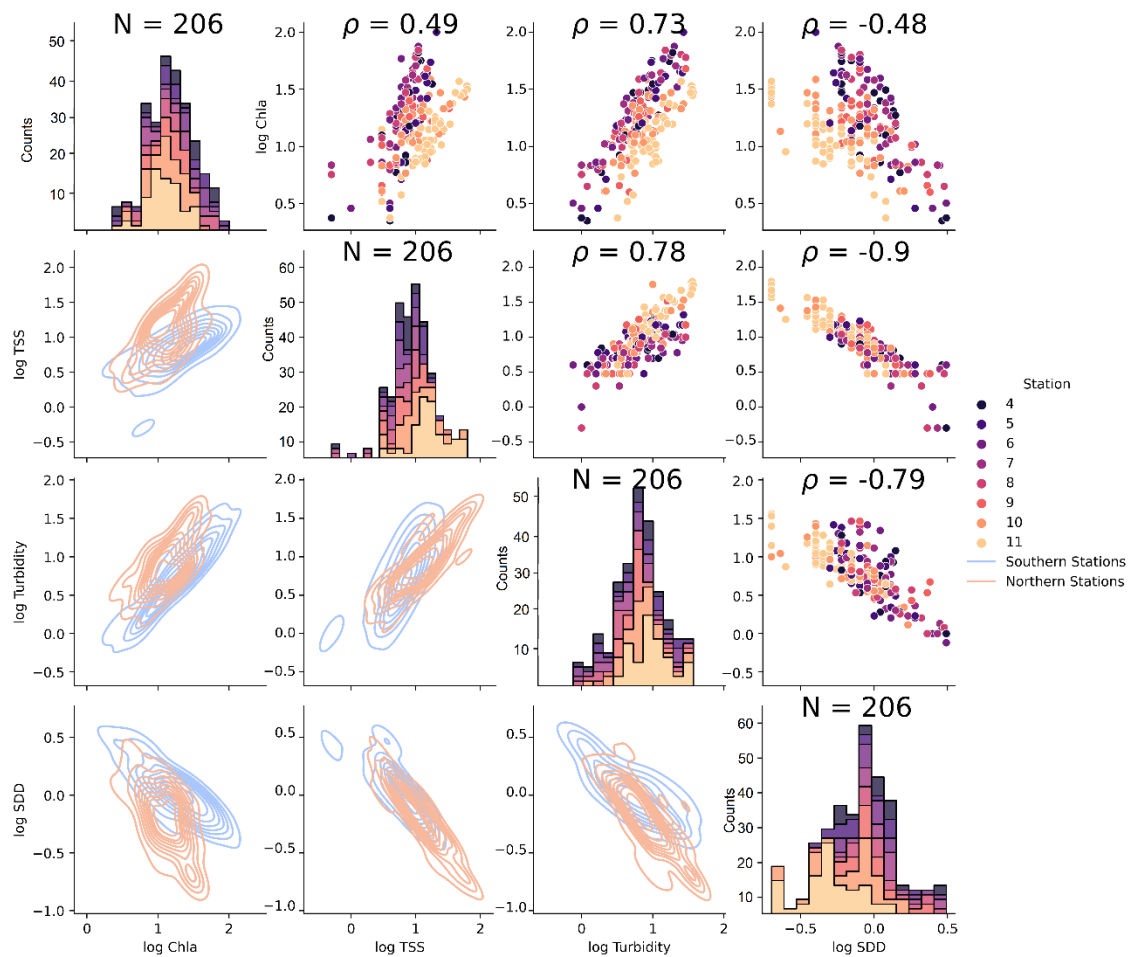


**Figure 4.2.** Pair plots of some optically-derived/driven parameters in BPL (averaged on stations 4-11 from late May to early September of 2014-2020). Diagonal elements are the distribution of each parameter, color-coded according to station numbers. Upper-diagonal elements are the scatter plot of paired parameters. Lower-diagonal charts are the contour plots showing the relationship between the parameters in northern and southern stations.  $N$  and  $\rho$  are the number of samples and correlation coefficients, respectively. Units are  $\text{mg m}^{-3}$ ,  $\text{g m}^{-3}$ , NTU, and m for Chla, TSS, turbidity, and SDD, respectively.

We categorized BPL into two distinct OWTs based on the concentration of optical water constituents (Table 4.2) and their relationship with water optical parameters (Figure 4.2). OWT1 characterizes the southern basin (stations 1-8), where *Chla* concentrations are elevated and optical characteristics are similar to those recorded in plankton-rich systems elsewhere (OWT4 in Pahlevan et al. (2021) or OWT8 in Spyrakos et al. (2018)). In contrast, the northern basin (stations 9-11) exhibits a considerable concentration of suspended sediments and lower *Chla* values (Table 4.2), similar to OWT5 in Pahlevan et al. (2021) or OWT4 in Spyrakos et al. (2018).

**Table 4.2. Statistics used to distinguish two distinct OWTs in BPL (averaged from late May to early September 2017-2020). Units are  $\text{mg m}^{-3}$  and  $\text{g m}^{-3}$  for *Chla* and TSS, respectively.**

	OWT1 (stations 1-8)		OWT2 (stations 9-11)	
	<i>Chla</i>	TSS	<i>Chla</i>	TSS
Median	17.1	6.5	11.4	11
Mean	25.9	7.2	14.9	14.8
Standard deviation	24.7	4.1	12.2	13.1
N	159	104	201	125

#### 4.2.2 Data

Although there is a long history of recorded *in situ* data in BPL (Swarbrick et al. 2019), we selected the period of 2014-2020 to match Landsat-8 and Sentinel-2 mission lifetimes.

##### 4.2.2.1 *In situ* *Chla* data

*In situ* *Chla* data originated from multiple datasets (Table 4.3). At station 1, autonomous, on-site fluorescence probes were available through deployment on a buoy. These fluorometric measurements were then calibrated using a method described in Chapter 3. In addition, discrete water samples were collected from the lake surface and 0.8 m depth, with *Chla* collected on Whatman GF/F frozen and later extracted following Winternans and DeMots (1965) and analyzed using a UV-visible spectrophotometer (Shimadzu UV-1601-PC). Samples from station 2 were obtained from the water treatment plant intake at a depth of approximately 3 m in this polymictic lake. Samples from the intake were filtered onto a 0.45  $\mu\text{m}$  filter, extracted in 90% acetone and analyzed via spectrophotometry following standard methods (Eaton et al. 2017).

Phytoplankton from station 3 were collected on GF/C glass-fibre filters (nominal pore size 1.2  $\mu\text{m}$ ) following Swarbrick et al. (2019). Briefly, surface water ( $\sim 0.5\text{-m}$  depth) and depth-integrated samples were filtered through GF/C filters and frozen ( $-10^\circ\text{C}$ ) until analysis for Chl*a* ( $\text{mg m}^{-3}$ ) through standard trichromatic assays (Jeffrey and Humphrey 1975) and biomarker pigments ( $\text{nmoles pigment L}^{-1}$ ) by HPLC (Leavitt and Hodgson 2001). Carotenoids, chlorophylls, and their derivatives were isolated and quantified using a Hewlett Packard model 1100 HPLC system calibrated with authentic standards.

Finally, samples from stations 4-11 were collected during monthly field visits at a 1-m depth using a Niskin bottle. Samples for Chl*a* analysis were subsampled from the Niskin into laboratory bottles, stored in dark coolers with blue ice, and analyzed using method 10200H from Standard Methods (Eaton et al. 2017). Briefly, samples were filtered at low vacuum through  $0.45 \mu\text{m}$  nitrocellulose filters. Pigments were extracted from filters using a 90% acetone solution followed by vortexing. The resulting samples were steeped for between 2 and 24 hours and then absorbance was read at 630, 647, 664, and 750 nm using a Hack DR/4000 UV-VIS spectrophotometer. Chl*a* values were calculated using Jeffrey and Humphrey's trichromatic equation (Jeffrey and Humphrey 1975). Different methods of Chl*a* measurements result in discrepancy in estimations. Section 3.3.2 provides an estimation of such discrepancy in our case. However, more analyses are needed using co-location coincident observations.

**Table 4.3. Details of *in situ* Chl*a* measurements employed in this study. The unit for depth values is meter.**

Station	Measurement method	Available years	Sampling interval	Sampling time	Depth	Number of matchups
1	field fluorometry (Bittig et al. 2019)	2014-2020	10 min	all-day	0.8	37
1	lab spectrophotometry (Eaton et al. 2017)	2017-2020	$\sim$ once/week	daytime	0, 0.8	20
2	lab spectrophotometry (Eaton et al. 2017)	2014-2020	once/week	$\sim$ 5 a.m.	2.8	25

3	lab	HPLC (Leavitt and Hodgson 2001)	2014-2019	twice/month	~ 11 a.m.	0-1*	11
---	-----	---------------------------------	-----------	-------------	-----------	------	----

4-11	lab	spectrophotometry (Eaton et al. 2017)	2015-2020	once/month	daytime	1	100
------	-----	---------------------------------------	-----------	------------	---------	---	-----

\* depth-integrated sampling

#### 4.2.2.2 Satellite images

Cloud-free level-1C MSI images acquired by the Sentinel-2A/B satellites during the open water season were downloaded for the period 2017-2020 with a 2-3 days revisit time. The MSI sensor collects data in 13 spectral bands from 443 to 2190 nm at spatial resolutions of 10, 20, and 60 m, and with a 12-bit radiometric resolution (Li et al. 2017). In addition, cloud-free OLI level-1 images from NASA's Landsat-8 satellite (launched 2013) were downloaded for the period 2014-2020. The spatial resolution of the optical channels of OLI is 30 m, and the satellite overpasses the study site every ~8 days. In the case of eutrophic waters, the MSI band configuration is more suitable for Chla retrievals than that of OLI (Ansper and Alikas 2019) due to the availability of a red-edge band at 709 nm. Figure 4.3 compares the configuration of sensors with Chla spectral reflectance, including reflectance spectra for samples with different Chla concentration measured in BPL using an ASD spectrometer (Analytical Spectral Devices, ASD Inc., Boulder, CO, USA), measured using a white reference Spectralon and averaged over 10 observations.

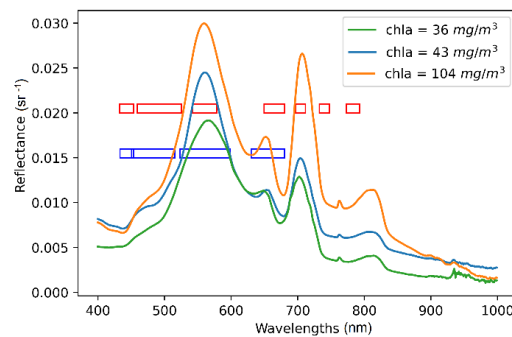


**Figure 4.3. Comparison of MSI bands (red boxes) and OLI bands (blue boxes) in wavelengths < 800 nm. The spectra are from three different samples measured at BPL using an ASD spectrometer and display how water spectra change with changes in Chla content.**

### 4.2.3 Methodology

The data analysis workflow developed in this study was similar for all analyses (Figure 4.4) although algorithms (e.g., AC processors and Chla retrieval models) and train-test split approaches differed between experiments (Table 4.4).

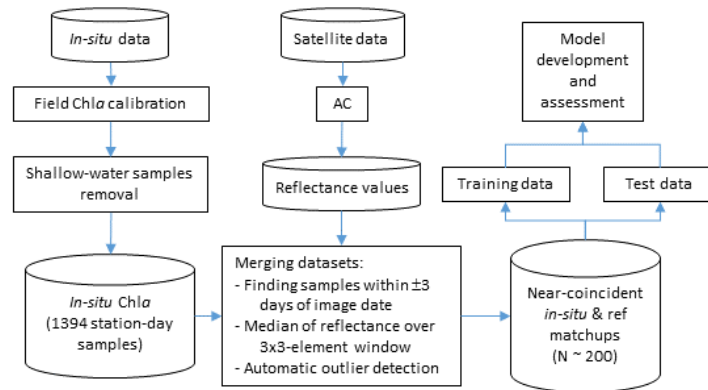


**Figure 4.4. Overview of workflow developed in this study.**

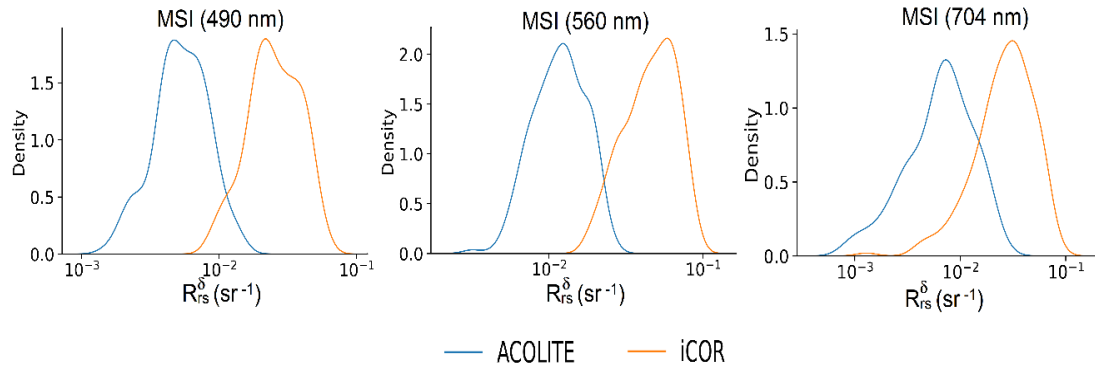
#### 4.2.3.1 Data preprocessing

All images were corrected for atmospheric effects to produce two different reflectance quantities, namely  $R_{rs}^{\delta}$  (satellite-derived remote sensing reflectance) and  $\rho_{rc}$  (Rayleigh-corrected reflectance). We selected ACOLITE (v20210114.0) (Vanhellemont and Ruddick 2014; Vanhellemont 2019) and iCOR (version 3) (De Keukelaere et al. 2018) as AC processors since they outperform other processors in inland waters with OWTs similar to BPL (Pahlevan et al. 2021), especially when red-NIR wavelengths are used (Ilori et al. 2019). Visual inspection of images showed no significant sunglint effect in BPL. iCOR applies the SIMilarity Environment Correction (SIMEC) algorithm (Sterckx et al. 2015) to reduce the adjacency effect that may be an issue for BPL due to its narrow width. Regardless of AC processors, all MSI spectral bands were then resampled to a 60-m grid to be consistent for further steps.

Optically-deep waters are the focus of this study; hence, Chla samples for which Secchi Disk Depth (SDD) measurements equal to bottom depth were excluded. This way we ensure that no signal comes from lake bottom reflection. *In situ* samples (1394 station-day samples) were then collated with the closest matching satellite-derived  $R_{rs}^{\delta}$  products to create co-located  $R_{rs}^{\delta}$  – Chla matchups. The

maximum time span between field sampling and image acquisition was set to  $\pm 3$  days. Although this time span is much longer than  $\pm 3$  hours, which has been suggested for oceanic waters (Werdell and Bailey 2005), many studies extend the time window even up to  $\pm 7$  days for inland waters without any significant decrease in accuracy (Tang et al. 2003; Lunetta et al. 2015; Dörnhöfer et al. 2018; Anspér and Alikas 2019). To correct for potential mismatches, we used continuous Chla measurements from the buoy to exclude matchups for which Chla at the time of satellite overpass differed from *in situ* values by  $> 20\%$ . Representative  $R_{rs}^{\delta}$  spectra for matchups were chosen to be the median of  $3 \times 3$ -element windows centered around the matchup locations.

Both AC processors mask land and clouds automatically; however, we manually deleted matchups that were contaminated by thin clouds/haze and cloud shadow through a visual assessment of images. Both processors also sometimes overcorrect for atmospheric effects, resulting in negative reflectance, especially in the 443 and 490 nm bands. In our case, there were few instances of negative reflectance values ( $\sim 5\%$ ) and these were excluded after inspection. Finally, we implemented an outlier detection algorithm to remove samples whose  $R_{rs}^{\delta}$  deviated from mean values by more than  $\pm 3\sigma$ . Approximately 200 matchups (depending on sensor type and AC processor) were selected for algorithm development and evaluation. The  $R_{rs}^{\delta}$  plots and the distribution of  $R_{rs}^{\delta}$  derived from ACOLITE and iCOR ( $R_{rs}^{\delta,ACL}$  and  $R_{rs}^{\delta,iCOR}$ , respectively) are shown in Figure 4.5.



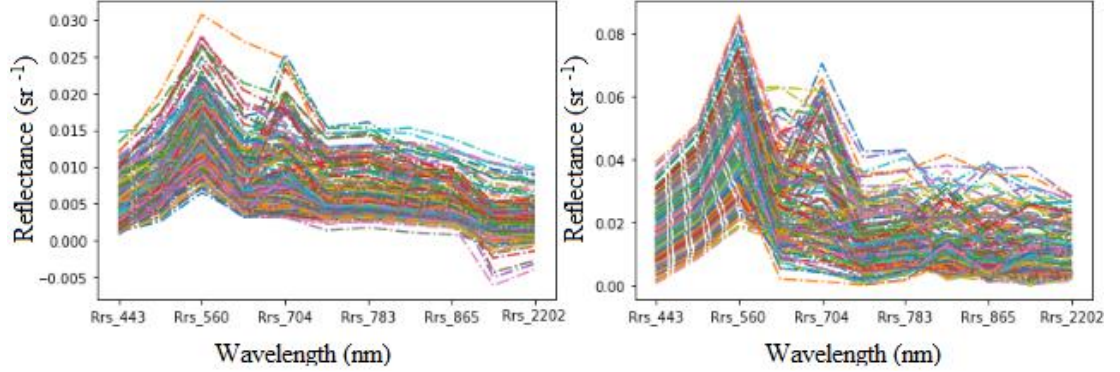


**Figure 4.5. Normalized frequency distributions of MSI-derived  $R_{rs}^{\delta}$  spectra for the matchups processed via ACOLITE and iCOR processors (top).  $R_{rs}^{\delta}$  spectra for the matchups processed via ACOLITE and iCOR processors (bottom). Colors in the bottom plot is only for a better visualization.**

#### 4.2.3.2 Model development

Assuming  $\varepsilon$  to be a threshold, SVR uses an  $\varepsilon$ -insensitive cost function in which errors ( $e_i$ ) up to  $\varepsilon$  are not penalized, whereas further deviations are penalized using a linear function, i.e.,  $L(e_i) = \max(|e_i| - \varepsilon, 0)$ . Thus, compared to traditional linear regressions or neural networks, SVR is more robust to small errors and inherent uncertainties of training data (Zhan et al. 2003). Weights ( $\omega$ ) are estimated in the linear regression problem (Equation 4.1), where  $i$  is the number of training data,  $j$  is the number of predictors (spectral bands), and  $\phi$  is a kernel (a non-linear mapping function). SVR minimizes Equation 4.2, where  $\xi_i$  (Figure 4.6.a) are  $|e_i| > \varepsilon$  and  $C$  is the regularization parameter, balancing the minimization of errors and generalization capabilities (Smola and Schölkopf 2004; Camps-Valls et al. 2006). Figure 4.6 depicts a schematic view of the regression between Chl $a$  and reflectance measurements using SVR.

$$Chla_i = \sum_{j=1}^M \omega^T \phi(R_{rsj}) \quad (4.1)$$

$$Cost = \frac{1}{2} \|\omega\|^2 + C \sum_i L(e_i) \quad (4.2)$$

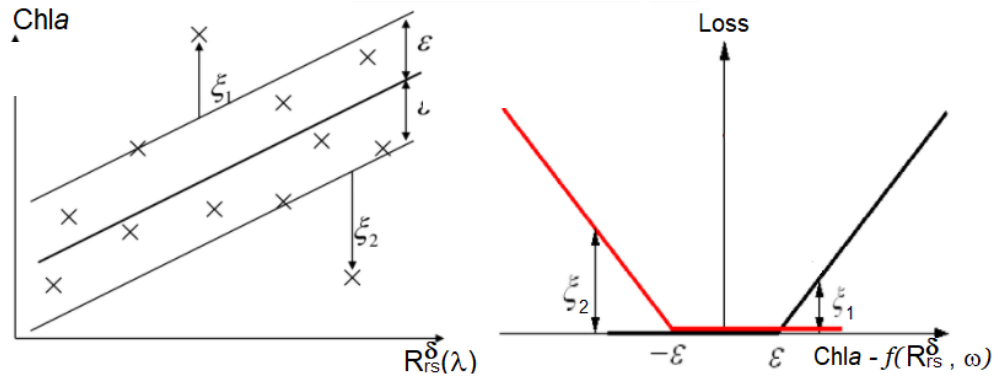


**Figure 4.6. Graphical depiction of principles of support vector regression (SVR). (a) Schematic view of regression between  $Chla$  and reflectance measurements using SVR. (b) Loss function defined for SVR; while errors less than  $\epsilon$  are not penalized, larger errors are penalized by a linear function.**

Input and output  $Chla$  values were  $\log_{10}$ -transformed in the model. We allowed some outliers (larger residuals than  $\epsilon$ ) using a  $C = 2.5$  parameter (regularization term) to decrease the chance of overfitting. We also employed a Radial Basis Function kernel (RBF), rather than other tested kernels, with  $\gamma = 0.14$  and  $0.25$  for MSI and OLI data, respectively, to handle non-linearity in the feature space.  $\gamma$  determines the radius of influence of samples selected as support vectors. These hyperparameters ( $C$ ,  $\gamma$ , and kernel type) were tuned using a grid-search cross-validation process that minimizes model errors on a validation set. Here, the validation set was one-fifth of the training data that was periodically set apart for hyperparameter tuning. After identifying optimized hyperparameters, the validation set was merged with the whole training data and fed into the model for a final training process.

Using  $R_{rs}^{\delta} - Chla$  matchups, we re-trained several state-of-the-art empirical  $Chla$  retrieval algorithms for use with MSI and OLI spectral bands, namely OC3 (O'Reilly et al. 1998; O'Reilly and Werdell 2019), 2band (Moses et al. 2009), 3band (Dall'Olmo and Gitelson 2005), and NDCI (Mishra and Mishra 2012) for MSI, and OC3 as well as FLH-blue (Beck et al. 2016), for OLI. After logarithmic transformation, these differential/ratio-based indices implied a linear relationship with logarithmic-

transformed  $Chla$ . The exceptions were 2band and 3band for which we added a power-of-two term to better fit the data. The tuned formula and coefficients for empirical models are presented in Table 4.4.

**Table 4.4. Formulas and coefficients of empirical models employed in this study.  $b\#$  and  $\lambda \#$  are the reflectance and wavelength at specified bands, respectively.  $y$  (output of the equations) is  $Chla$  on a logarithmic scale.**

Sensor	Algorithm	Formula
MSI	OC3 (O'Reilly et al. 1998)	$y = 2.198 - 2.404x, x = \log[\max(b1, b2)/b3]$
	2band (Moses et al. 2009)	$y = -1.165 + 4.146x - 1.337x^2, x = \log[b5/b4]$
	3band (Dall'Olmo and Gitelson 2005)	$y = 1.094 + 1.631x - 0.65x^2, x = \log[(b4^{-1} - b5^{-1}) * b6]$
	NDCI (Mishra and Mishra 2012)	$y = 1.082 + 2.283x, x = \log[(b5 - b4)/(b5 + b4)]$
OLI	OC3 (O'Reilly et al. 1998)	$y = 0.807 - 1.886x, x = \log[\max(b1, b2)/b3]$
	FLH-blue (Beck et al. 2016)	$y = 0.799 + 98.256x, x = b3 - (b2 + (b4 - b2) * \left(\frac{\lambda3 - \lambda2}{\lambda4 - \lambda2}\right))$

We also applied MDN and BST models as representatives of state-of-the-art ML models developed for MSI and OLI. MDN was implemented using the STREAM package (<https://github.com/STREAM-RS/STREAM-RS>) (Pahlevan et al. 2020; Smith et al. 2021). In addition, we implemented a locally trained MDN (LMDN) using local  $R_{rs}^\delta - Chla$  matchups. A similar process was conducted for the BST model (Cao et al. 2020) using the BST-OLI package ([https://github.com/zgcao/bst\\_oli](https://github.com/zgcao/bst_oli)) and a locally trained XGBoost model, LBST. The reflectance spectra imported into these LML models (LMDN and LBST) were identical to our SVR model; i.e.,  $R_{rs}^\delta$  derived from the first seven and four spectral bands (400-800 nm) for MSI and OLI, respectively.

#### 4.2.3.3 Model assessment

MSI was selected as the main sensor for quantitative assessments, due to its greater potential for quantifying *Chla* compared to OLI (Cao et al. 2019; Smith et al. 2021). For the following experiments, select matchups were split into training and test datasets; however, the approach to do so was different among the experiments to assure a complete assessment of our model. Table 4.5 summarizes the evaluation approaches (training-test splitting) as well as the number of training/test matchups available for each experiment.

**Table 4.5. Assessment approaches (training-test split) as well as the number of training/test matchups available for each experiment in this study.**

Experiment	Evaluation approach	$N_{Total}$	$N_{Training}$	$N_{Test}$
General performance	Cross-validation on yearly-grouped matchups	193	~150	~50
Stratified performance	Five-fold cross-validation	137*	110*	27*
		56**	45**	11**
Model sensitivity to AC processors	Five-fold cross-validation	193 <sup>†</sup>	154 <sup>†</sup>	39 <sup>†</sup>
		208 <sup>‡</sup>	166 <sup>‡</sup>	42 <sup>‡</sup>
Model transferability over water type	Cross-validation on OWT-grouped matchups	193	137* 56**	56** 137*
Model robustness for each sensor	Five-fold cross-validation	178	142	36
Spatial integrity	Matchups for a specific date are set apart as test data	193	184	9
Temporal validity	Station 1 matchups collected in 2020 are set apart as test data	193	173	20

\* matchups for OWT1 - \*\* matchups for OWT2 - <sup>†</sup> matchups for ACOLITE - <sup>‡</sup> matchups for iCOR

Assessment of general performance (section 4.3.1.1) and model transferability (section 4.3.3) was based on a cross-validation approach in which the matchups were categorized either annually (Table 4.6) or geographically (southern/northern basins). In each run,  $R_{rs}^{\delta}$  – *Chla* matchups related to

a single year (or basin) were put aside as test data before the model was trained with the remaining data and used to predict the validation test data. Model performance was computed using all matchups, which were predicted once as test data.

**Table 4.6. Annual frequency and statistics of  $R_{rs}^{\delta}$ - Chla matchups derived from MSI sensor. Chla concentration unit is  $\text{mg m}^{-3}$ .**

	2017	2018	2019	2020
<b>N</b>	33	51	48	61
<b>Mean Chla</b>	17.3	19.6	18.4	20
<b>Median Chla</b>	15.4	26	18.8	19.3
<b>Standard deviation Chla</b>	2.8	2.6	4.3	2.3

To gain insight into the model performance in two eutrophic conditions (OWTs; stratified performance hereafter; section 4.3.1.2), model sensitivity to the two AC processors (section 4.3.2), and its robustness for each sensor (section 4.3.4), we used a five-fold cross-validation approach to randomly select among  $R_{rs}^{\delta}$  – Chla matchups. This approach ensures sufficient, equal training/test data for each run.

Assessment of model capability in generating Chla maps (section 4.3.5) using both MSI and OLI images were based on images from a single date (16 July 2020) when we had both cloud-free images from both sensors (~10 minutes apart) and the maximum number of coincident (within 2 h) *in situ* Chla samples (9 total), spanning a broad range of Chla (~10-100  $\text{mg m}^{-3}$ ). The corresponding matchups were considered equivalent to unseen test data, and the models were trained with the remaining matchups (184 matchups for MSI and 169 for OLI) (Table 4.5). In addition, to assess the stability of Chla retrieval over time (section 4.3.6), MSI-derived  $R_{rs}^{\delta}$  – Chla matchups corresponding to the continuous measurements of the buoy in 2020 were considered as unseen test data, and the remaining matchups were used to train the models.

#### 4.2.3.4 Accuracy metrics

Both linear and log10-transformed metrics are examined for accuracy assessment of the models. In general, metrics calculated in log-transformed space (i.e. RMSLE, SSPB, and MdSA) are

believed to provide a better assessment due to the log-normal distribution of Chla (Seegers et al. 2018; O'Reilly and Werdell 2019). The performance metrics for accuracy assessment were estimated as follows:

$$RMSE = [\sum_{i=1}^N (P_i - M_i)^2 / n]^{1/2} \text{ (mg m}^{-3}\text{)} \quad (4.3)$$

$$RMSLE = [\sum_{i=1}^N (\log_{10}(P_i) - \log_{10}(M_i))^2 / n]^{1/2} \quad (4.4)$$

$$MAPE = 100 \times \text{median}(|P_i - M_i| / M_i) \quad (4.5)$$

$$SSPB = 100 \times \text{sign}(z)(10^{|z|} - 1), z = \text{median}(\log_{10}(P_i / M_i)) \text{ (\%)} \quad (4.6)$$

$$MdSA = 100 \times (10^y - 1), y = \text{median}|\log_{10}(P_i / M_i)| \text{ (\%)} \quad (4.7)$$

where  $P_i$  and  $M_i$  stand for predicted and measured Chla, respectively. RMSLE is the root mean squared log-error, MAPE is the median absolute percentage error, SSPB represents symmetric signed percentage bias, and MdSA is the median symmetric accuracy, computed in log-space (Morley et al. 2018).

SSPB and MdSA were expressed as percent (%), expected to be resistant to outliers, zero-centered, and easily interpretable (Pahlevan et al. 2020). While SSPB measures the bias of a model, MdSA is believed to be an indicator for its precision. Because SSPB and MdSA are relatively new indices, we also estimated RMSE, RMSLE, and MAPE to facilitate the comparison with earlier studies. Finally, models were evaluated using Slope and Model Win Rate (MWR) criteria, wherein Slope is used to compare the results with earlier studies, while MWR, expressed in %, is used to determine which model performs better in pair-wise comparison of the residuals (Seegers et al. 2018).

### 4.3 Results

Chla retrieval was assessed from three different aspects: quantitative performance, spatial integrity, and temporal validity. This approach allows us to assess whether models show superiority in a quantitative assessment while performing poorly in retrieving Chla time series, a common problem during periods of intense cyanobacterial blooms. We also examined the robustness of the proposed model under various scenarios, including changes in water type, AC processors and radiometric products, and remote sensing data types.

### 4.3.1 Quantitative assessment of the model on MSI data

Quantitative assessments were conducted using both general and stratified performance. Here, general performance analysis employed all matchups, whereas stratified analysis was conducted separately on two OWTs common in BPL and provides insights into the use of SVR models in eutrophic conditions. We present  $R_{rs}^{\delta,ACL}$  for performance analysis, although no significant difference in results was observed when using  $R_{rs}^{\delta,iCOR}$  (data not shown).

#### 4.3.1.1 General performance

Overall accuracy of models in retrieving Chla was computed over all stations and the whole Chla range (~ 1-125 mg m<sup>-3</sup>; Table 4.7, Figure 4.7). Results show that LML models significantly outperform all other models for most metrics, with an error decrement of > 15% when considering MdSA. In particular, SVR outperformed all empirical models as reported via MWR, representing > 60% of retrievals. Compared to LMDN, SVR performed marginally better (~3% improvement relative to MdSA) but returned equal estimates of bias (as SSPB). The slope for SVR (0.78) demonstrates reasonable performance through the whole range of Chla in BPL. Among other models, OC3 performance was poor, as expected because of its dependency on blue-green band ratios, while other empirical models for eutrophic waters (2band, 3band, and NDCI) performed better and similarly in BPL, with the 2band algorithm generally outperforming other empirical models.

**Table 4.7. Evaluation metrics (general performance) for Chla retrieval models on MSI and *in situ* Chla matchups (N = 193). The Model Win Rate (MWR) is computed relative to SVR as the reference model; i.e., OC3 = 74% implies that SVR leads to smaller residuals 74% of the times.**

**Highlighted cells indicate the best score for the corresponding metrics.**

	MdSA (%)	SSPB (%)	RMSLE	MAPE (%)	RMSE (mg m <sup>-3</sup> )	Slope	MWR (%)
<b>OC3</b>	99.1	-6.2	0.43	55.71	29.53	0.11	73.6
<b>2band</b>	50.3	-12.9	0.31	36.39	18.95	0.7	60.1
<b>3band</b>	54.2	-10.2	0.36	38.33	355.5	1.06	61.1
<b>NDCI</b>	52.3	-14.3	0.32	37.63	27.13	0.66	61.1
<b>MDN</b>	55.9	28.2	0.35	48.32	36.81	1.23	62.2

<b>LMDN</b>	38.9	3	0.29	33.22	17.51	0.83	52.9
<b>SVR</b>	35.6	3.4	0.27	31.5	13.96	0.78	N/A

Furthermore, the MDN model trained on global  $R_{rs}$  data exhibited comparable precision to empirical models (~56% error), albeit with a high bias (SSPB = 28%) and a tendency to overestimate Chla (Slope = 1.23) characteristic of its sensitivity to  $R_{rs}^\delta$ . Surprisingly, LMDN showed high performance, implying the ability of MDN to be trained even with only ~200 matchups (~10% of the number of matchups in Pahlevan et al. (2020)).

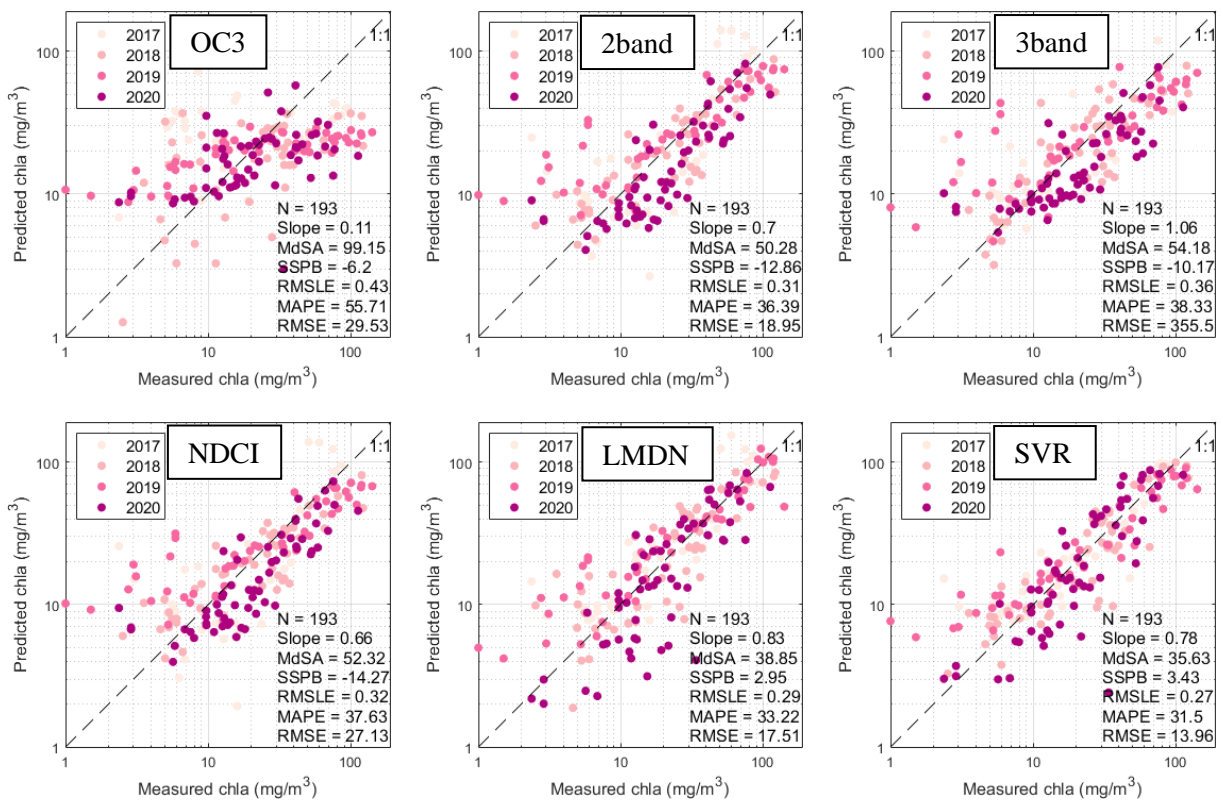


**Figure 4.7. Matchup analysis of Chla derived from different algorithms applied on MSI-A/B data and near-coincident, co-located *in situ* Chla samples in BPL. The results are from a cross-validation approach in which matchups related to a single year are put aside as unseen test data, and a model is trained with the remaining data. Model performance is finally computed**

**on all matchups (all are predicted once as test data). Year of data acquisition indicated by colored solid circles.**

Visual inspection of scatter plots reveals that SVR (and LMDN) predictions are less biased according to the annual sampling, as opposed to the empirical models. Scatter plots of *Chla* retrievals also illustrate a reasonable overall performance of all models (except OC3) for *Chla* > 10 mg m<sup>-3</sup> ( $\overline{MdSA} = 39.9 \pm 10.32\%$ ). However, retrieving *Chla* < 10 mg m<sup>-3</sup> was challenging ( $\overline{MdSA} = 57.8 \pm 6.95\%$ ), with most models overestimating *Chla* in this range ( $\overline{SSPB} = 46.8 \pm 12.1\%$ ). Nonetheless, SVR and LMDN models exhibited a substantially better performance ( $\overline{Slope} = 0.47 \pm 0.04$ ) compared to the other models ( $\overline{Slope} = -0.19 \pm 0.09$ ). While all models failed to retrieve *Chla* less than 2 mg m<sup>-3</sup>, the absence of data in this range (2 matchups) prevents detailed evaluation of performance. We infer from Figure 4.7 that empirical models underestimated *Chla* > 30 mg m<sup>-3</sup> ( $\overline{SSPB} = -43.4 \pm 7.1\%$ ) especially values > 100 mg m<sup>-3</sup>, while ML models (SVR and LMDN) did not ( $\overline{SSPB} = -7.2 \pm 5.2\%$ ), possibly because the latter uses at least four additional MSI spectral bands.

#### 4.3.1.2 Stratified performance

Analysis of stratified performance (OWT1 vs. OWT2) suggests that SVR significantly outperforms all other algorithms in the southern basin, which is almost 80% of the lake area (Table 4.8). SVR also excelled relative to other algorithms in the northern basin, when considering most performance metrics including MdSA and MWR. However, LMDN performance was comparable to that of SVR in the northern basin and even surpassed it in terms of SSPB and Slope. The reasonable performance of LMDN with few data (e.g., in the northern basin with only 45 samples for training) was unexpected; however, results should be treated with caution due to the availability of test data (11 samples in each run; Table 4.6). Scatter plots in Figure 4.8 further demonstrate that empirical models failed to estimate *Chla* in the northern basin (Slope < 0.1), while LML models provide better estimates of *Chla* in turbid water (Slope = 0.3).

**Table 4.8. Evaluation metrics for *Chla* retrieval models on MSI and *in situ* *Chla* matchups based on water type. See Table 4.2 for more details of each water type. The Model Win Rate (MWR) is computed relative to SVR as the reference model.  $\overline{Chla}$  and  $\overline{TSS}$  are the median of**

**Chla and TSS in associated stations. Units are mg m<sup>-3</sup> and g m<sup>-3</sup> for Chla and TSS, respectively.**

**Highlighted cells mark the best score for the corresponding metrics in each OWT.**

		MdSA %	SSPB %	RMSLE	MAPE %	RMSE mg m <sup>-3</sup>	Slope	MWR %
<b>OWT1</b>  <b>N=137</b>  <b><math>\overline{Chla}=26</math></b>  <b><math>\overline{TSS}=7</math></b>	<b>OC3</b>	108.7	-14.4	0.46	64.55	34.99	0.04	80.3
	<b>2band</b>	36.84	-4.27	0.25	29.55	16.49	0.72	54.7
	<b>3band</b>	46.93	-5.84	0.31	33.28	30.19	0.64	56.9
	<b>NDCI</b>	37.7	-5.6	0.26	30.69	22.19	0.76	56.2
	<b>MDN</b>	50.4	29.9	0.28	39.6	29.04	1.19	59.1
	<b>LMDN</b>	38.8	6.4	0.25	29.91	15.34	0.81	52.1
	<b>SVR</b>	32.7	4.2	0.24	29.57	15.43	0.82	N/A
<b>OWT2</b>  <b>N=56</b>  <b><math>\overline{Chla}=15</math></b>  <b><math>\overline{TSS}=15</math></b>	<b>OC3</b>	59.3	-10.5	0.39	39.86	10.75	0.01	60.7
	<b>2band</b>	84.3	-22.4	0.81	48.02	12.33	-0.16	66.1
	<b>3band</b>	69.2	-20.3	1.95	46.16	12.27	-0.15	66.1
	<b>NDCI</b>	74.6	-16.6	0.4	47.45	10.51	0.04	60.7
	<b>MDN</b>	87.8	10.9	0.48	55.02	51.04	2.6	66.1
	<b>LMDN</b>	53.1	3.2	0.34	39.9	8.94	0.34	51.6
	<b>SVR</b>	51.4	-6.9	0.33	38.04	8.85	0.29	N/A

Most metrics suggest that Chla retrieval was more accurate in the southern basin compared to the northern one. For instance, MdSA indicated a 15% - 50% decrement for all models, except OC3. The higher concentration of suspended sediments and NAP in the northern basin, which leads to a higher Chla interference by NAP backscattering particularly at longer wavelengths (red-NIR), might justify the higher accuracy of Chla retrieval in the southern basin. This pattern may also explain the higher accuracy of OC3 in the northern basin; given that it was the only model that did not use red-NIR bands.

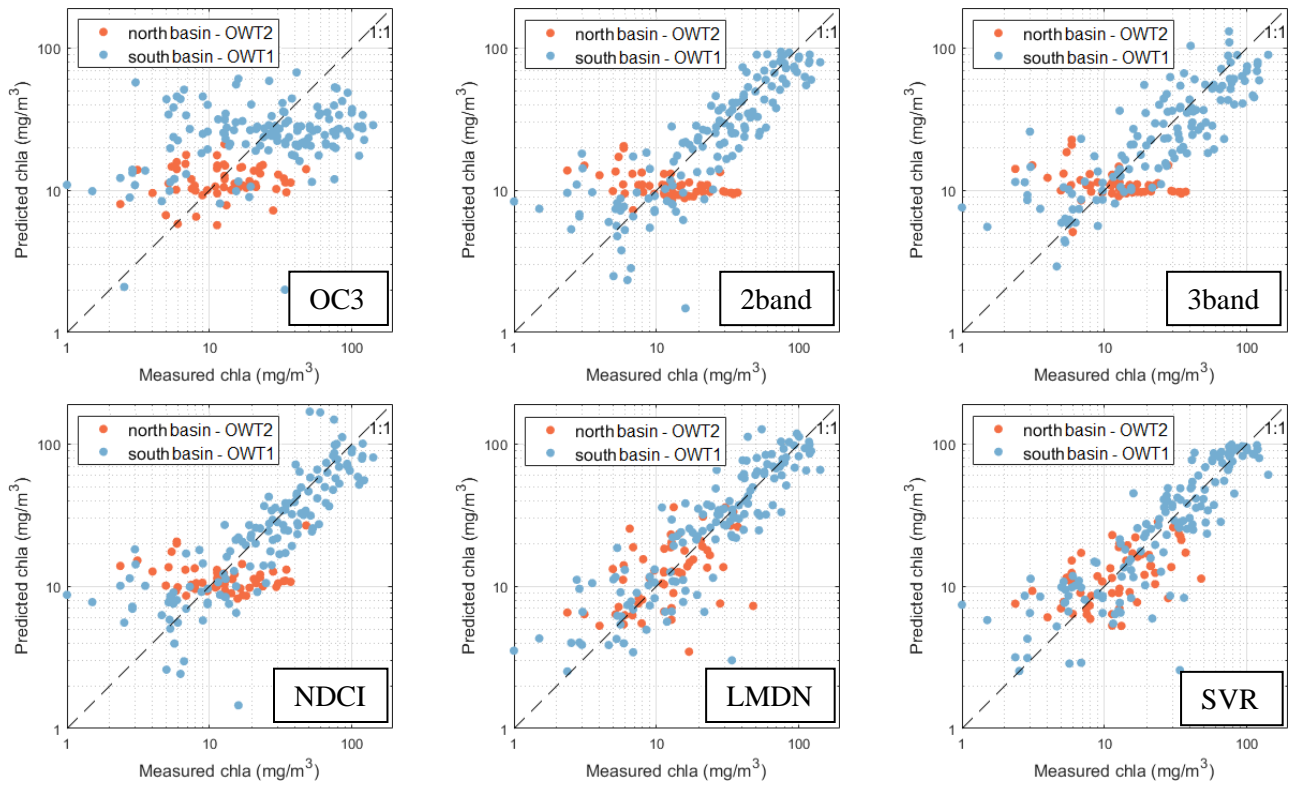


**Figure 4.8. Matchup analysis of measured and predicted Chla from *in situ* Chla and MSI-A/B images for two different regions in BPL, categorized based on optical water type. For each optical water type, a model is trained and tested using a five-fold cross-validation approach.**

#### 4.3.2 Model sensitivity to AC processors

Model performance was assessed over two different AC processors (ACOLITE, iCOR) and three radiometric products ( $R_{rs}^{\delta}$ ,  $\rho_{rc}$ , and  $\rho_{TOA}$ ) applied to MSI data (Figure 4.9). While ACOLITE provided all three products, iCOR only returns  $R_{rs}^{\delta}$ . Overall, SVR and LMDN manifested robust outputs for both AC processors and all the radiometric products ( $\overline{MdsA} = 43.7 \pm 3.7\%$ ). In contrast, the mean of variability for empirical models is almost two fold greater ( $\pm 7.8\%$ ), with a maximum for OC3 ( $\pm 14.8\%$ ) and a minimum for 2band ( $\pm 3.5\%$ ). SVR- $R_{rs}^{\delta,ACL}$  exhibited the best performance among different combinations of retrieval models and AC processors. SVR's superiority was also evident when

employing  $R_{rs}^{\delta, iCOR}$  or  $\rho_{rc}$ , with only  $\rho_{TOA}$  showing comparable results to those obtained with LMDN (< 2% difference).

No single AC processor or radiometric product performed best in all Chla retrieval models. For example, OC3 and 3band worked better with iCOR as the AC processor, while the others (2band, NDCI, LMDN, SVR) all presented better results with ACOLITE. For these latter models,  $R_{rs}^{\delta}$  displays the highest accuracy compared to the other products ( $\rho_{rc}$ ,  $\rho_{TOA}$ ), suggesting that ACOLITE outperformed iCOR whenever it successfully carried out aerosol correction ( $\rho_{rc} \rightarrow R_{rs}^{\delta}$ ). Our results also show that Rayleigh correction ( $\rho_{TOA} \rightarrow \rho_{rc}$ ) as implemented in ACOLITE reduced Chla retrieval accuracy except for OC3, confirming that this correction over-corrects reflectance in red-NIR wavelengths while remaining beneficial for use with blue-green bands. On the other hand, declining accuracy after aerosol correction in OC3 applications indicates that the AC processors failed to accurately remove aerosol effects in blue-green bands, a task that has proven to be challenging elsewhere (Pahlevan et al. 2021).

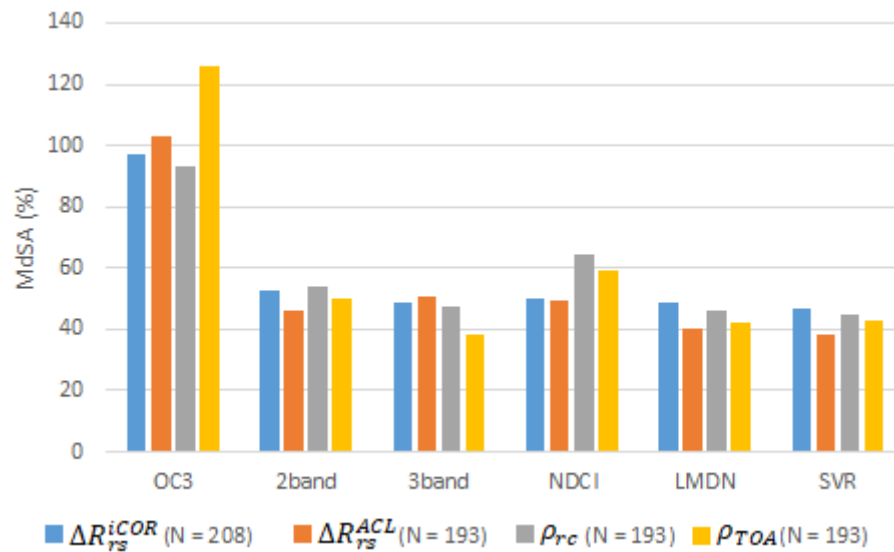
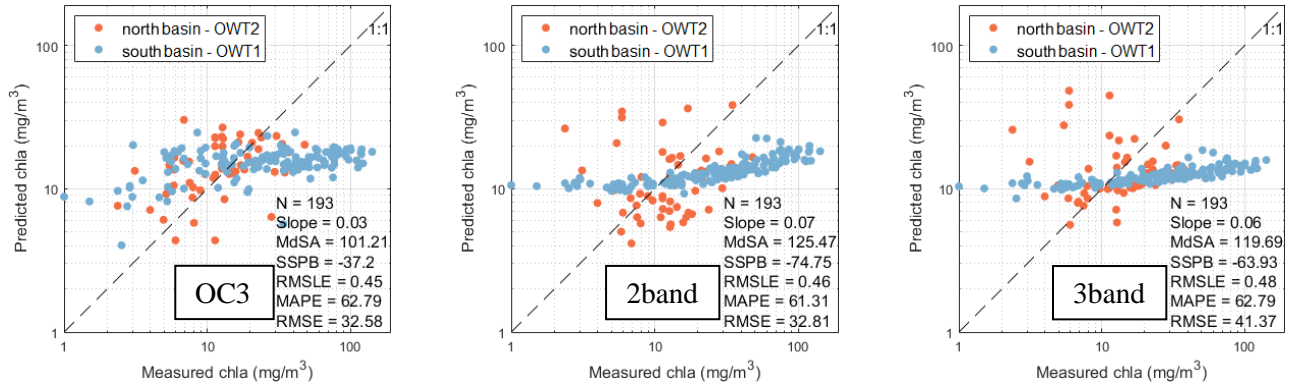


**Figure 4.9. Median Symmetric Accuracy (MdSA) for Chla retrieval algorithms when applied to MSI-A/B data processed to produce different radiometric products ( $R_{rs}^{\delta}$ ,  $\rho_{rc}$ , and  $\rho_{TOA}$ ) with different AC processors (ACOLITE and iCOR). Note that  $\rho_{rc}$  is generated with ACOLITE and**

theoretically is not different when using iCOR. N is the total number of matchups. See Table 4.5 for the detailed training/test split process.

### 4.3.3 Model transferability over water types

Model transferability over two OWTs in BPL was assessed using  $R_{rs}^{\delta,ACL}$  - Chla matchups derived from MSI images (see section 4.2.3.3) (Figure 4.10). All empirical algorithms (OC3, NDCI, 2band, and 3band) failed to retrieve Chla when they were trained by matchups from a different, but similar, OWT (MdSA > 100%, Slope < 0.2). Additionally, LMDN showed poor transferability over both water types (MdSA > 200%, Slope < 0.2). In contrast, SVR maintained a reasonable transferability over two OWTs (MdSA = 61%, Slope = 0.35) compared to rivals. Although the error and bias increased ~two to four times compared to instances where both OWTs were used to train the SVR model (MdSA = 61% vs. 36% and SSPB = 15.8% vs. 3.4%) (see section 4.3.1.1), they remained within an acceptable range for many applications. SVR's high transferability might be related to its proven resistance to overfitting, thanks to the regularization parameter C.



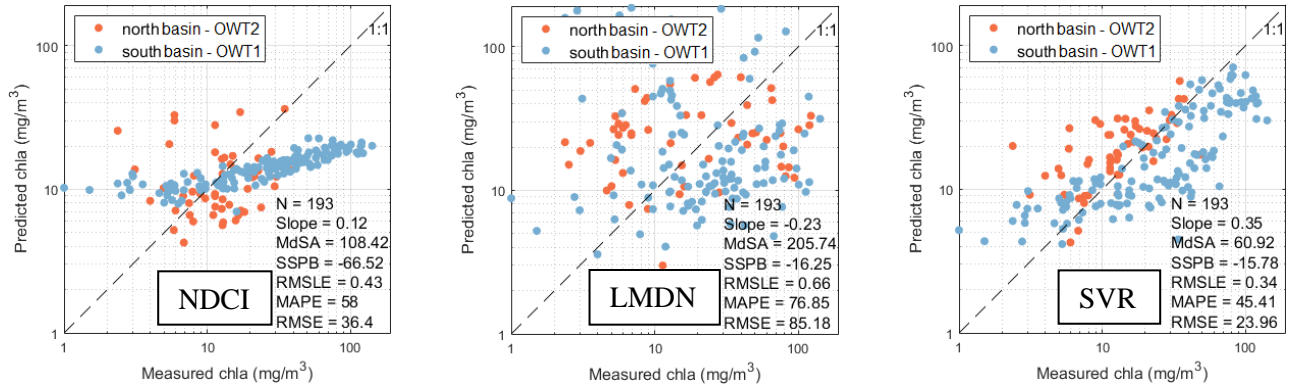


**Figure 4.10. Scatter plot of *in situ* Chla versus predicted Chla from MSI-A/B images. Chla values in the northern basin (OWT2, red solid circles) are predicted using a model trained with southern basin matchups (OWT1, blue solid circles) and vice versa.**

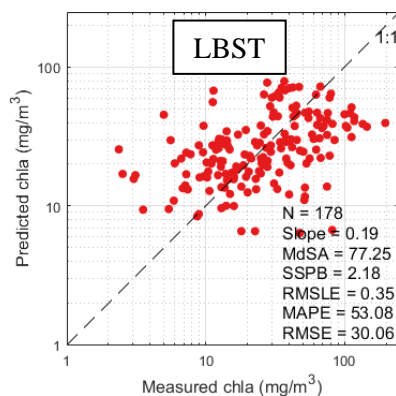
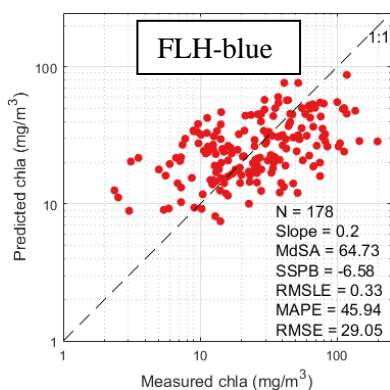
#### 4.3.4 Model sensitivity to sensor type

$R_{rs}^{\delta,ACL}$  - Chla matchups derived from OLI images were employed to retrieve Chla in BPL. LMDN outperformed SVR in most metrics when using OLI data, by ~5% in MdSA and with a two-fold greater Slope (Table 4.9). MDN displayed an overall error of 95% and a bias of ~50% reflecting the training of this global model with *in situ*  $R_{rs}$  rather than  $R_{rs}^{\delta}$ . Additionally, even though OLI lacks spectral bands at red-edge wavelengths, a red-NIR empirical model (FLH-blue) outperformed the blue-green-based index of OC3 by ~10%. A global BST model (Cao et al. 2020) failed to estimate Chla in BPL (results not provided here), similar to what has been observed elsewhere (Smith et al. 2021), likely due to much lower CDOM absorption in BPL compared to the waterbodies that were used to train BST ( $\overline{a_{CDOM}^{(440)}} = 0.28 \text{ m}^{-1}$  vs.  $\overline{a_{CDOM}^{(440)}} = 0.8\text{-}1 \text{ m}^{-1}$ ). Finally, the LBST model exhibited poor performance (MdSA = 77%), possibly because the boosting algorithms degrade in the presence of outliers and errors in training data (Li and Bradic 2018).

**Table 4.9. Evaluation metrics for Chla retrieval models on OLI and *in situ* Chla matchups (N = 178). Each model was trained and tested using a five-fold cross-validation approach. The MWR was computed relative to SVR as the reference model. Highlighted cells mark the highest score for the corresponding metrics.**

	MdSA (%)	SSPB (%)	RMSLE	MAPE (%)	RMSE (mg m <sup>-3</sup> )	Slope	MWR (%)
OC3	75.7	3	0.35	56.41	31.65	0.08	0.57
FLH-b	64.7	-6.6	0.33	45.94	29.05	0.2	0.6
LBST	77.2	2.2	0.35	53.08	30.06	0.19	0.59
MDN	94.98	48.9	0.42	64.7	38.4	0.14	0.65
LMDN	55.02	8.1	0.32	40.23	27.43	0.45	0.47
SVR	60.27	2.8	0.32	43.78	27.83	0.23	N/A

Overall, Ch<sub>l</sub>a retrieval using OLI data (Table 4.9) appeared less accurate than that based on MSI summarized in Table 4.7 ( $\overline{MdSA} = 71.3 \pm 13.2\%$  vs.  $\overline{MdSA} = 55.2 \pm 19.3\%$ ). OLI's poor performance was also inferred from low Slope (< 0.5), likely due to the absence of a red-edge band. Similar to MSI, LML models (LMDN and SVR) corroborated a better performance than empirical and GML models when applied to OLI data. The analysis of scatter plots (Figure 4.11) also revealed that all models failed to estimate Ch<sub>l</sub>a values < 10 mg m<sup>-3</sup> and concentrations > 100 mg m<sup>-3</sup>. Although the former limitation was also observed when using MSI data (see section 4.3.1.1), the latter might be intensified because OLI does not possess a spectral band in the domain of Ch<sub>l</sub>a fluorescence (680-710 nm).



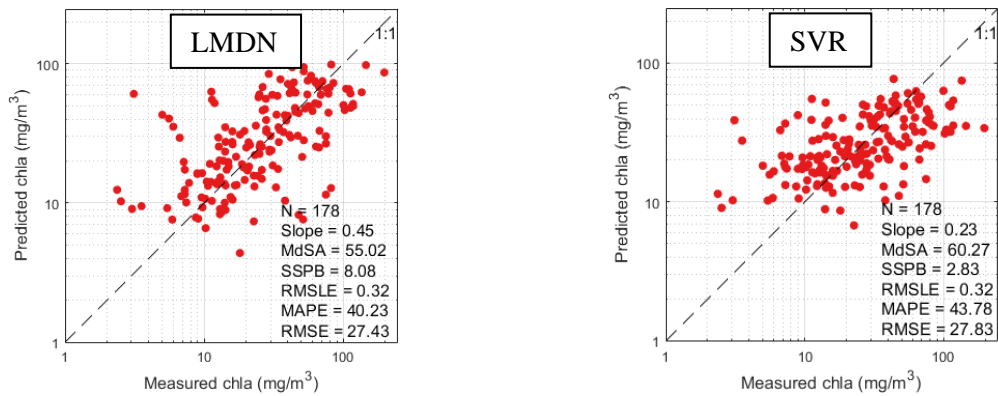


**Figure 4.11. Matchup analysis of Chla derived from different algorithms applied on OLI data and near-coincident, co-located *in situ* Chla samples in BPL. The results are from a five-fold cross-validation approach.**

#### 4.3.5 Spatial integrity

Chla maps for BPL were generated from an MSI image taken on 16 July 2020 (Figure 4.12). All model-processor combinations suggested Chla as low as  $\sim 10 \text{ mg m}^{-3}$  in the north basin, whereas some models/processors (e.g., SVR-iCOR) predicted Chla values up to  $\sim 100 \text{ mg m}^{-3}$  in the south basin. Regardless of the AC processor used, ML models (SVR and LMDN) seem to deliver overall smoother maps (less noise) compared to the 2band output, probably due to leveraging all spectral bands.

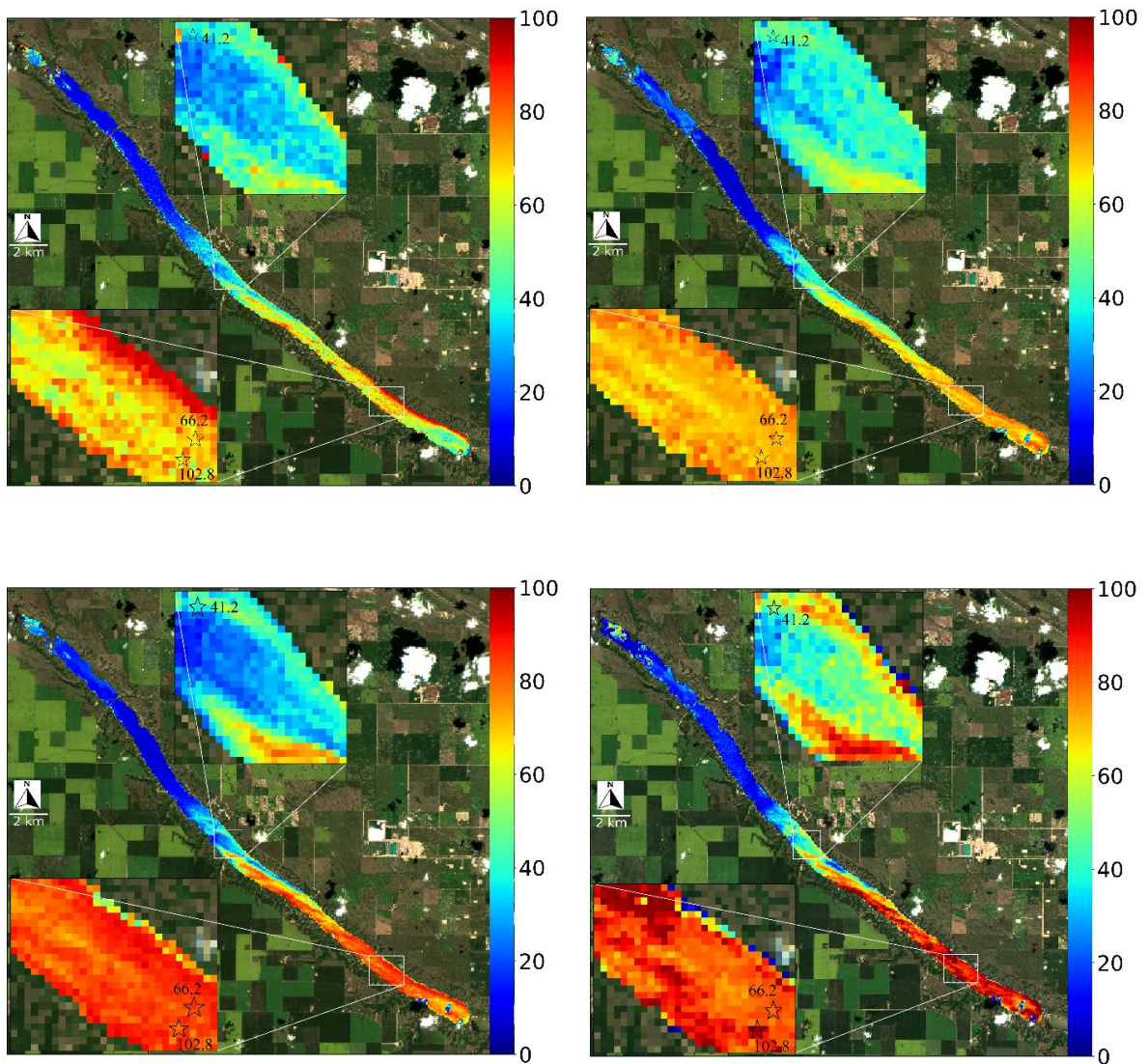


**Figure 4.12. Chl<sub>a</sub> maps for BPL derived from different retrieval algorithms/AC processors couples applied on MSI-A image acquired on 16 July 2020. The markers in the insets represent examples of the location of *in situ* data, collected on the same date, and employed as unseen test data. The associated numbers beside the markers are Chl<sub>a</sub> concentration in mg m<sup>-3</sup>. 2band was used as the best representative of empirical models.**

Visual comparison of Chla maps based on near-coincident *in situ* measurements revealed that the SVR model, coupled with iCOR processor, had the highest consistency with *in situ* measurements (Figure 4.12). Although all models/processors showed a reasonable and similar performance in mapping moderate Chla concentrations (Figure 4.12, upper insets), they differed more substantially in estimating high Chla values at the south of the lake. SVR tended to estimate higher Chla concentrations than did LMDN and 2band models, regardless of AC processors, (lower insets in Figure 4.12). SVR-iCOR also seemed to be more capable of detecting high spatial gradients in Chla, as it is the only combination to capture large gradients of Chla at two nearby stations (Chla = 66.2 to Chla = 102.8; lower insets Figure 4.12). Such high-frequency changes in Chla may be related to the surface patchiness of cyanobacteria.

SVR results appeared prone to adjacency effects compared to LMDN and 2band models. This issue should be treated with caution especially when producing maps of nearshore Chla. Similarly, the elevated Chla estimates produced for the shore and northern basin by models probably arise from very shallow depths (< 2 m) and high density of rooted aquatic macrophytes. While maps were produced using MDN and empirical models, none outperformed the above-mentioned models. For instance, MDN returned some unrealistically high Chla values, and OC3 routinely and significantly underestimated Chla.

As it is sometimes more important to reconstruct spatial patterns of Chla than accurately estimate absolute concentrations, we normalized the predicted Chla vector of unseen matchups for stations 4-11 (a profile along the lake), by dividing by the vector norm to better evaluate which algorithms recorded spatial patterns of Chla in BPL (Figure 4.13). Overall, normalization did not reveal a single superior model/processor in terms of retrieving spatial gradients of Chla. While SVR-iCOR provided the most similar pattern to measured Chla gradients in the northern basin (#station > 8), SVR-ACOLITE demonstrated good performance in retrieving Chla changes in the southern stations 5-8. In contrast, the 2band model performed well at stations 4-5 whereas LMDN performed poorly at stations 4-6 and 10-11. Together, these patterns suggest that SVR showed the highest overall capability in retrieving the Chla gradient along the lake.

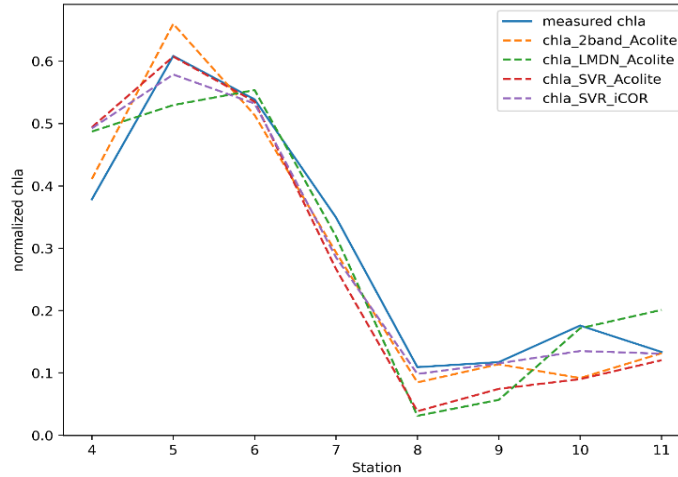


**Figure 4.13. Spatial profile of normalized Chla along the lake (south to north) for 16 July 2020, derived from *in situ* measurement Chla (solid line) as well as predicted Chla from algorithms applied on MSI image (dashed lines). X-axis denotes station number (see Figure 4.1).**

We also mapped Chla over the lake using OLI data for the same date (16 July 2020) using FLH-Blue, LBST, LMDN, and SVR models (Figure 4.14). Maps from LBST and LMDN were markedly noisy, whereas LMDN showed reasonable quantitative performance for OLI data (Table 4.9), and FLH-Blue and SVR generated smooth maps. The SVR model exhibited more consistency with *in situ* data (marked points in Figure 4.14), while LMDN retrieved Chla values higher ( $120 \text{ mg m}^{-3}$ ) than observed *in situ*, and the other algorithms underestimated Chla. In terms of reconstructing the spatial pattern of Chla, LMDN seems to provide the best performance, consistent with its higher Slope (Slope = 0.45) (Table 4.9).

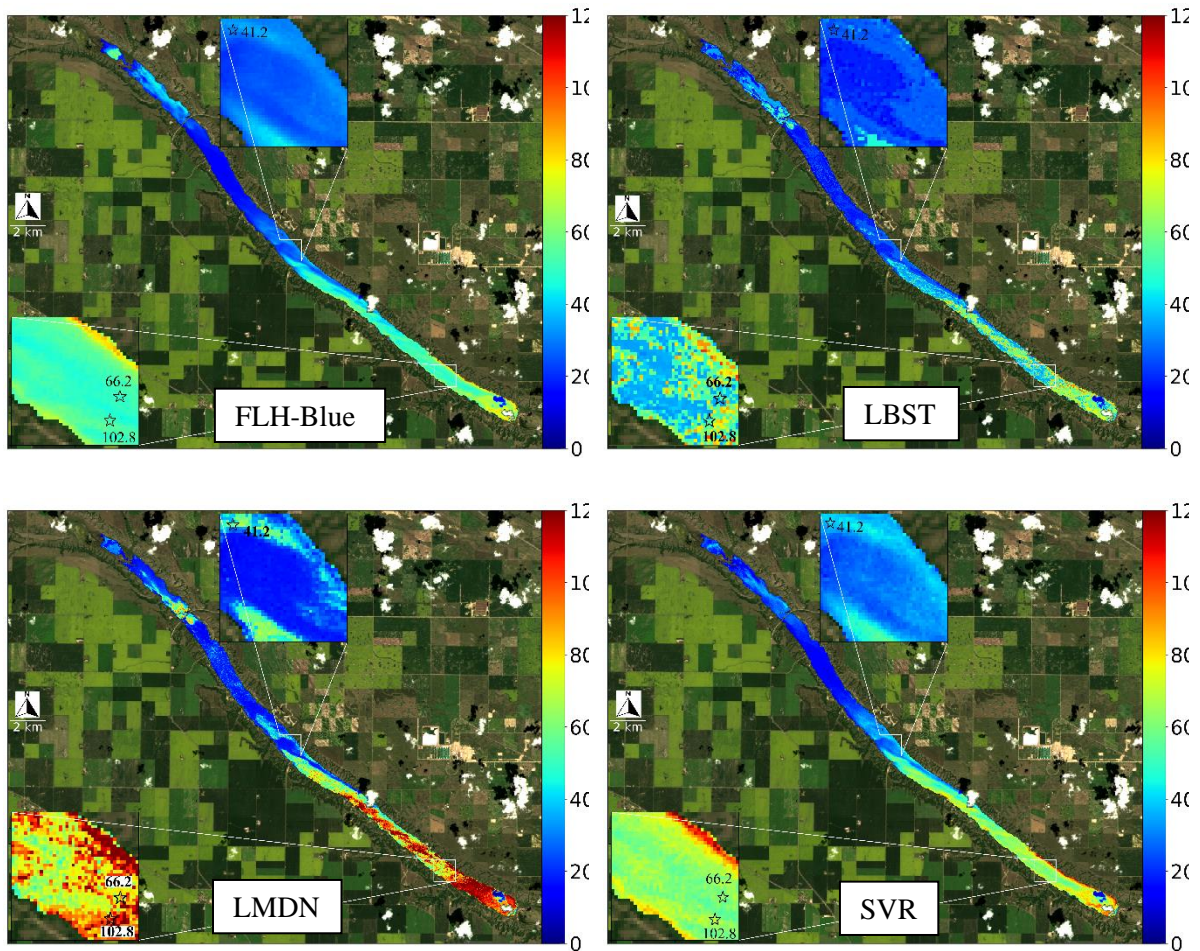


**Figure 4.14.** Chla map for BPL derived from different algorithms applied on OLI image acquired on 16 July 2020. The markers in the insets represent examples of *in situ* data, collected on the same date, and employed as unseen test data. The associated numbers beside the markers are Chla in  $\text{mg m}^{-3}$ .

#### 4.3.6 Temporal validity

Robust retrieval of Chla over time is a daunting task in a eutrophic waterbody due to high variations in surface bloom densities and resultant freshwater optics and temporal variation in atmospheric conditions. Comparison of SVR-iCOR, SVR-ACOLITE, LMDN-ACOLITE, and 2band-ACOLITE processing couples at station 1 in BPL revealed that SVR-iCOR tracked *in situ* Chla measurements

better than the other model/processor combinations (Figure 4.15), with particularly good capture of intense summer blooms in mid-July and early September. In both cases, SVR-iCOR followed the shape and magnitude of the measured time series, despite a ~15% underestimation of peak Chla values. In contrast, ACOLITE failed to mask cloud shadow contaminated pixels on 7<sup>th</sup> August 2020, led to significantly underestimation of Chla and inconsistencies in time series retrieval. For more moderate Chla concentrations (20-60 mg m<sup>-3</sup>), SVR-ACOLITE displayed better performance than SVR-iCOR. Overall, a correlation analysis between the time series of measured and predicted Chla showed that SVR-iCOR outperformed other models in retrieving Chla time series by ~ 10% (Table 4.10).

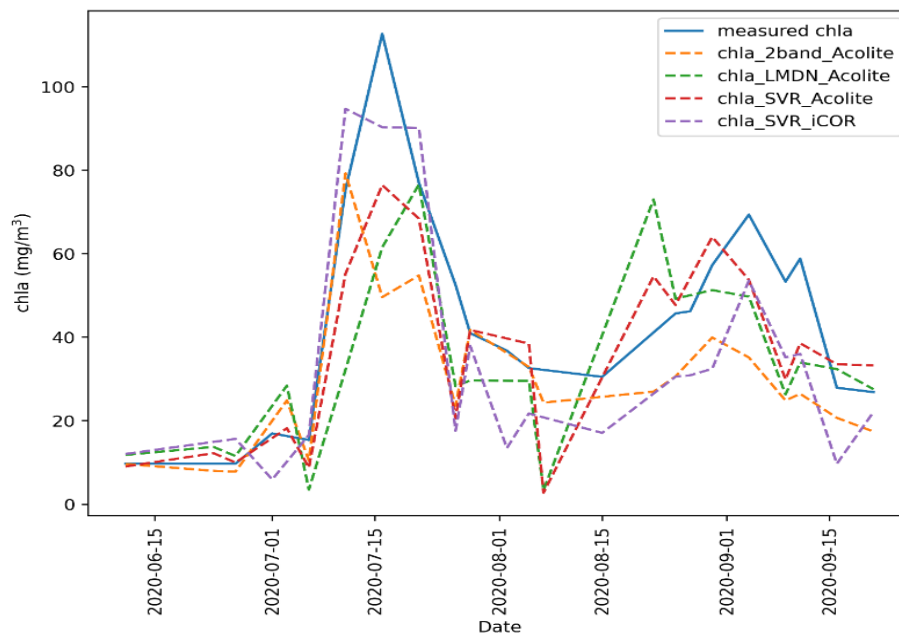


**Figure 4.15. Time series of Chla in station 1 in BPL for summer 2020, derived from *in situ* measurement Chla (solid line) as well as predicted Chla from algorithms applied to MSI images.**

**Table 4.10. Time series correlation of measured and predicted Chla, derived from algorithms applied to MSI images, at station 1 in BPL for summer 2020. Number of matchups was 21 for ACOLITE processor and 20 for iCOR.**

	<b>2band-ACOLITE</b>	<b>LMDN- ACOLITE</b>	<b>SVR- ACOLITE</b>	<b>SVR-iCOR</b>
<b>Correlation (<math>\rho</math>)</b>	0.728	0.684	0.705	0.798

## 4.4 Discussion

Locally trained machine-learning models, particularly those based on SVR, provided the best retrieval of Chla for a small eutrophic lake using MSI and OLI images. These models also generated realistic time series and spatial gradients of Chla. Overall, these models were robust to variations in AC processors (ACOLITE vs. iCOR) and sensor types (MSI vs. OLI). Together, our analysis suggests that pre-trained SVR models may be useful for Chla estimation on regional waterbodies, provided that optical water types and atmospheric conditions are similar (see Chapter 5).

### 4.4.1 Uncertainties in *in situ* data

Although we attempted to reduce the uncertainties associated with *in situ* Chla data, any comparison of remotely sensed images and spatially-limited lake measurements can be complicated due to high variations in *in situ* data (Clay et al. 2019; Qiu et al. 2021). Here, we tried to reduce noise in Chla measurements by conducting each measurement several times and averaging values. However, our *in situ* data originated from different laboratories using contrasting measurement techniques (field fluorometry, laboratory spectrophotometry, and HPLC), instrumentation, calibration, and field sampling (surface 1 m vs. depth-integrated) (see Section 3.3.2 for an intercomparison between these methods). While these factors may affect model performance, they also suggest that our algorithms exhibit minimal overfitting and systematic errors in performance assessment, and may be generalizable to other lakes in the region of study. It also should be acknowledged that even with *in situ* measurements at same depths, it is still likely that different laboratory methods (HPLC and spectrophotometry) lead to different Chla values as it has been shown that HPLC tends to estimate lower Chla values because of its ability to separate Chlb and Chlc (Meyns et al. 1994). However, we could not measure the potential uncertainty due to these differences due to lack of co-located measurements by different methods.

Several lines of evidence suggest that uncertainties in Chla measurements did not alter results of comparative assessment of retrieval models. First, we used the median symmetric accuracy (MdSA)

as the main metric to compare the models, as it is highly robust to potential outliers in *in situ* Chla measurements. Second, we conducted various experiments with different numbers and combinations of matchups, and in all cases, SVR showed robust and similar results, meaning that uncertainties in lake production do not substantially alter results. Moreover, given that BPL is well mixed vertically (Dröscher et al. 2008), we expect that differences in sampling protocols may not greatly affect our findings. Finally, earlier studies suggest that SVMs can handle diverse, highly uncertain datasets, because they use only a part of data (support vectors) for learning (Foody and Mathur 2006; Chegoonian et al. 2017). Handling uncertainties of *in situ* data becomes crucial when input data to observatory systems often originate from various field and laboratory sources.

#### 4.4.2 Merits of locally trained ML models

When compared with traditional empirical models (e.g., OC3, 2band), LML models exhibit several clear advantages, particularly with regards to SVR models. First, their ability to leverage all spectral bands and the capability to learn and model diverse uncertainties (*in situ* data, non-linearity, non-Chla constituents) is an advantage over traditional empirical/physical models and led to 15% - 65% error reduction. Such performance might be improved further when using models such as LMDN that can deal with ill-posed problems (Pahlevan et al. 2020).

Currently, the uncertainties in AC processors are the major hurdle for employing GML models in inland waterbodies (Pahlevan et al. 2020). These models are often trained with *in situ* radiometric measurements and can be degraded when fed by satellite-derived measurements. LML models that can learn AC uncertainties ( $R_{rs}^{\delta}$ ) specific to a lake of interest may be an important solution for application to local and regional resource management issues, such as blooms of toxic cyanobacteria near recreational areas or drinking water inlets. Meanwhile, development of global models based on satellite-derived reflectance or including ancillary data may provide an opportunity to expand the geographic range of applications of ML models (Smith et al. 2021).

Presently, the need for substantial training data is a major obstacle to development of local ML models. Fortunately, here we demonstrate that LML models (SVR and LMDN) were trainable with ~200 matchups (section 4.3.1.1), while stability of the results even with only ~50 matchups was encouraging (section 4.3.1.2), as many regional agencies in Europe and North America conduct routine monitoring (e.g., Soranno et al. 2017). Ideally, such locally trained models should possess reasonable

generalization to retrieve reliable Chla in nearby lakes where optical conditions, water type, and atmospheric conditions differ only slightly. Our results suggest that SVR models exhibit adequate transferability when trained and tested with two different (but similar) water types in BPL (section 4.3.3). Although this capability is in agreement with SVR resistance to overfitting (Kwiatkowska and Fargion 2003; Zhan et al. 2003; Mountrakis et al. 2011), it is still essential to further validate our results using a more consistent and systematically collected/calibrated *in situ* Chla dataset.

This study was also the first independent assessment of the global MDN model in a small eutrophic lake. Although MDN is not expected to outperform locally trained models, it showed reasonable precision in estimating Chla (error within ~60% of *in situ* measurements). Nonetheless, it tended to significantly overestimate Chla (high bias) relative to locally trained,  $R_{rs}^{\delta}$ -fed models. Substantial uncertainties in AC process, especially adjacency effects, which can be seen in drastically different  $R_{rs}^{\delta}$  distributions from ACOLITE and iCOR (Figure 4.4), may explain MDN overestimation.

#### 4.4.3 Atmospheric correction

Algorithms developed to retrieve downstream products such as Chla, always should exhibit consistent performance with different intermediate processors, specifically AC processors. Here, we demonstrate the robustness of the SVR model when data is processed using ACOLITE and iCOR, and three different radiometric products, that is  $R_{rs}^{\delta}$ ,  $\rho_{rc}$ , and  $\rho_{TOA}$ . The fact that  $\rho_{rc}$  and  $\rho_{TOA}$  exhibit reasonable results – especially when using red-NIR bands – is in agreement with findings from previous studies (Wynne et al. 2010; Matthews et al. 2012; Matthews and Odermatt 2015). Furthermore, our results show that the accuracy of estimates increased when using  $R_{rs}^{\delta}$  for retrieval models, other than those based on OC3 and 3band for which  $\rho_{rc}$  generated more accurate products. We also note that empirical algorithms using blue-green bands (e.g., OC3) significantly benefited from Rayleigh correction for blue light scattering. While Rayleigh correction did not appear to increase the accuracy of the models based on red-NIR bands, further evaluations are needed to evaluate this finding.

Modeling results were consistent with those of Pahlevan et al. (2021), who recently conducted a comprehensive comparison between AC processors in retrieving  $R_{rs}$  using an extensive global dataset. For example, we observed that 2band and NDCI – two algorithms that use only 665 and 704 nm bands – performed better when they are coupled with ACOLITE than with iCOR. Similarly, OC3

and 3band models that use blue (443 or 492 nm) and 740 nm bands showed better performance with iCOR when compared to ACOLITE (Pahlevan et al. 2021). We interpret the high consistency between the assessments of downstream products (Chla concentration) and satellite-derived reflectance as an indicator of the effectiveness of AC process on the accuracy of downstream products. However, we also recognize that further examination of the effectiveness of AC will require a separate estimate of retrieval uncertainty from the AC process; an assessment that needs field radiometric measurements which were not sufficiently available in our study.

Comparisons among experiments in this study, as well as drastically different  $R_{rs}^{\delta}$  distributions derived from ACOLITE and iCOR (Figure 4.5), suggest that different AC processors may lead to significant differences in retrieval performance. Thus, the algorithms for retrieval of downstream products should be examined as retrieval models/AC processors. For instance, the SVR model shows greater accuracy when used in conjunction with ACOLITE (Figure 4.9), and more temporal stability when using iCOR as the AC processor (Figure 4.15). However, the comparison between ACOLITE and iCOR is not entirely equivalent due to differences in the number of matchups (15 more for iCOR when masked by ACOLITE); thus, other studies (Ilori et al. 2019; Warren et al. 2019; Xu et al. 2020; Pahlevan et al. 2021) could serve better for a more comprehensive comparison of AC processors.

## 4.5 Conclusion

This paper presents a machine-learning model based on support vector regression (SVR) to retrieve Chla concentration from satellite-derived reflectance measurements ( $R_{rs}^{\delta}$ ) of Sentinel-2 (MSI) and Landsat-8 (OLI). The proposed model was trained and evaluated using a dataset of near-coincident, co-located *in situ* Chla and  $R_{rs}^{\delta}$  observations (N ~ 200), collected in a mid-latitude eutrophic lake from 2014-2020. Comparison of the SVR model against state-of-the-art, commonly used alternates revealed that SVR outperformed all other algorithms when using MSI data. This superiority is seen in both general (entire samples, Chla = 1-125 mg m<sup>-3</sup>) and stratified levels (two distinct optical water types).

The proposed model also showed superiority in retrieving time series of Chla and producing Chla maps, two important applications of remote sensing in monitoring and mapping of harmful algal blooms. The superiority of SVR was also demonstrated by return of robust and similar results following alteration of AC processors (ACOLITE vs. iCOR). The model was also stable when fed with different

radiometric products ( $R_{rs}^{\delta}$ ,  $\rho_{rc}$ , and  $\rho_{TOA}$ ). Quantitative evaluation of SVR also showed a promising transferability among two optical water types common to this study region, particularly in comparison to standard models.

Together, these findings reveal the high potential of SVR models to retrieve Chl $a$  in small waterbodies, even using data from multi-spectral terrestrial missions such as MSI and OLI. Although results presented herein are for only one small lake, we believe that they can be generalized to other eutrophic mid-latitude waterbodies of similar optical water types. Development of such models for consistent retrievals from long-term observational records of satellite missions such as Landsat and Sentinel increases the potential for monitoring and mapping the extent and intensity of harmful algal blooms in an era of global warming.

## Chapter 5

# Regional upscaling of chlorophyll-*a* retrieval from small eutrophic lakes via Sentinel-2: A case study of the Qu'Appelle River drainage basin, Canada

### 5.1 Introduction

Small inland waters (SIWs) are biogeochemical and ecological hotspots that respond quickly to changes in the landscape (Cheng and Basu 2017). The water quality of SIWs continues to degrade rapidly, mostly due to harmful algal blooms (HABs) (Walker 2014), and near-surface concentration of chlorophyll-*a* (Chl*a*) is one of the most reliable indicators of HAB outbreaks as it has unique absorption features that can be detected through satellite imaging (Kutser 2009). Although satellite-based retrieval of Chl*a* is a common task in oceans and large waterbodies where Chl*a* primarily governs water optical characteristics (O'Reilly and Werdell 2019), it remains challenging in SIWs due to substantial optical interferences from various water constituents and uncertainties in the atmospheric correction (AC) process (Pahlevan et al. 2020; Pahlevan et al. 2021).

Various models, ranging from semi-analytical and empirical to machine-learning (ML), have been developed to retrieve Chl*a* in SIWs from moderate-resolution terrestrial missions (~ 10 – 60 m) (Ansper and Alikas 2019; Cao et al. 2020; Pahlevan et al. 2020; Smith et al. 2021). Overall, these models can be categorized into two broad groups; local and global approaches. Depending on lake data availability, analysts either employ globally trained models without local training using Chl*a* data or train local models using *in situ* Chl*a* when enough lake-satellite sampling matchups are available. Global models are developed mostly using globally distributed, extensive datasets of synthetic or *in situ* remote-sensing reflectance ( $R_{rs}$ ) (Doerffer and Schiller 2007; Schroeder et al. 2007; Pahlevan et al. 2020) and often outperformed by local models that are fed by satellite-derived remote-sensing reflectance ( $R_{rs}^{\delta}$ ) (Chapter 4) due to AC uncertainties (Smith et al. 2021). Developing global models using satellite-derived measurements (e.g., Rayleigh-corrected reflectance ( $\rho_{rc}$ )) may increase Chl*a*

retrieval accuracy (Smith et al. 2021), but such models are often not available for specific sensors, such as the Multi-Spectral Instrument (MSI), nor are they used for local applications due to a high diversity of regional atmospheric conditions.

Local approaches to retrieve *Chla* from SIWs are also limited by the abundance and diversity of lakes as well as the limited availability of *in situ* data. In principle, a model trained on one (or few) SIWs with available *in situ* *Chla* can be applied to waterbodies with no *in situ* data provided that the model is generalizable and SIWs share similar optical water types (OWTs) and atmospheric conditions. In case of SIWs, these conditions might be extended to sharing similar size/shape as well as similarity in adjacent land cover, due to substantial adjacency effects. Such models were not available until recently when new ML models were introduced to retrieve *Chla* in SIWs. These models outperform traditional empirical models thanks to leveraging all visible and near-infrared (VNIR) spectral bands. Potential advantages of ML models include mixture density network's (MDN) ability to mitigate the ill-posed issue (Pahlevan et al. 2020) and include ancillary data (Smith et al. 2021), reasonable Support Vector Regression (SVR) generalizability over water types and AC processors (Chapter 4), and BST stability to overfitting (Cao et al. 2020). For example, recent studies (Chapter 4) show that SVR performs reasonably well (error  $\approx 60\%$ ) when it is trained by matchups of one OWT and retrieves *Chla* for a slightly different OWT within a single lake; however, this approach has not been tested by comparison of model output to other regional SIWs.

Here we take advantage of a four-year dataset of bi-weekly *Chla* measurements in seven interconnected lakes in Saskatchewan, Canada, to: (i) introduce the concept of regional approaches as a means to mitigate current limitations of global and local approaches in SIWs, and; (ii) assess and contrast the performance of various ML and empirical models in application to regional extrapolations. Based on prior *in situ* evaluations within an optically-diverse lake (Chapter 4), we hypothesized that ML models would provide the most reliable means of estimating *Chla* in regional lakes.

## **5.2 Materials and Methods**

### **5.2.1 Study area**

The Qu'Appelle River Watershed (50°00' N-51°30'N, 101°30'W-107°10'W) covers an area of  $\sim 52,000$  km<sup>2</sup> of sub-humid agricultural cropland and grasslands and provides water to  $\sim 30\%$  of the population

of Saskatchewan, Canada. This study examined seven lakes in the watershed; five of the lakes (Diefenbaker (D), Buffalo Pound Lake (BPL), Pasqua (P), Katepwa (K), Crooked (C)) form a central chain along the river course, while two lakes (Last Mountain (L) and Wascana (W)) drain into mid-reaches of the Qu'Appelle River (Figure 5.1, Table 5.1). Morphometric parameters vary between the lakes by up to 100-fold including surface area ( $2\text{--}371 \times 10^6 \text{ m}^2$ ), volume ( $3\text{--}7487 \times 10^6 \text{ m}^3$ ), and max depth (5.5–62.0 m). However, they are all elongated with almost similar width and adjacent land cover, making the assumption of similar adjacency effects valid. Agricultural cropland (75%), grasslands (12%), surface waters (5%), and the urban centers of Moose Jaw and Regina compose most of the land cover in the Qu'Appelle catchment (Vogt et al. 2011; Haig et al. 2020).

Source waters for the Qu'Appelle River originate from both local inputs (groundwater, precipitation) and meltwaters from the Canadian Rocky Mountains. Most lakes are eutrophic to hypereutrophic, except for mesotrophic Lake Diefenbaker and meso-eutrophic Last Mountain Lake (Finlay et al. 2015). Additionally, lakes are all polymictic, although Katepwa Lake occasionally experiences thermal stratification in late summer (Hayes et al. 2020). All lakes experience HAB events (Swarbrick et al. 2019) with *Chla* and total suspended solids (TSS) (Table 5.1) suggesting that most lakes, except relatively transparent Lake Diefenbaker, can be categorized in optical water types (OWTs) 4-6 (Pahlevan et al. 2021) based on the concentration of optical water constituents.

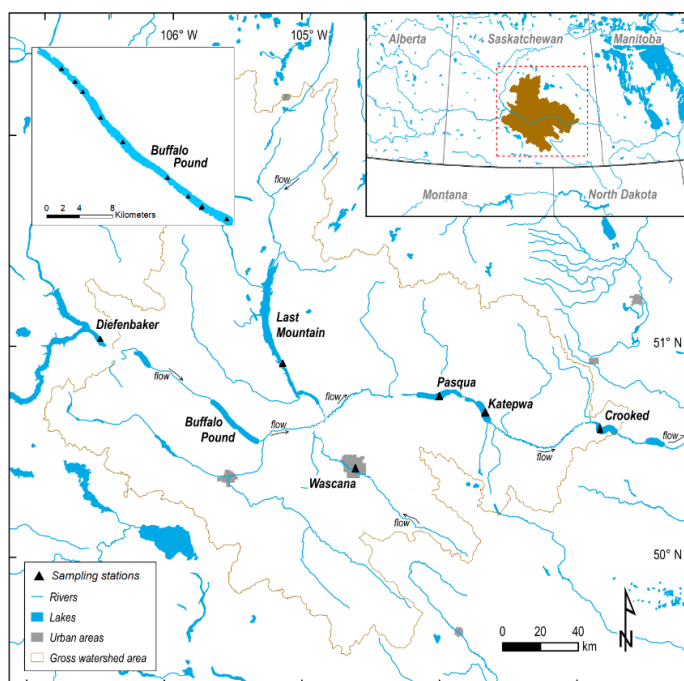


**Figure 5.1. Map, modified from Haig et al. (2020), showing locations of Qu’Appelle River drainage basin and seven study lakes (Buffalo Pound Lake (BPL), Lake Diefenbaker, Last Mountain Lake, Wascana Lake, Pasqua Lake, Crooked Lake, Katopwa Lake) overlaid by sampling stations (triangles) and major hydrologic boundaries (tan line). Dominant flow direction is noted by arrows along streams. Shading in the top-right inset indicates the Qu’Appelle Valley gross drainage area within the broader context of central Canada. Upper left inset magnifies BPL and its sampling stations.**

**Table 5.1. Study site locations as well as hydrological, chemical, and biological characteristics from 1993 to 2020. For each variable, values are represented by the mean of 28 years of measurements during May-September. Total dissolved phosphorus (TDP) and dissolved organic carbon (DOC) are measured from depth-integrated samples. Chla and cyanobacterial toxin microcystin are measured from surface samples (~0.5-m depth).**

	<b>BPL</b>	<b>Crooked</b>	<b>Diefenbaker</b>	<b>Katopwa</b>	<b>Last Mountain</b>	<b>Pasqua</b>	<b>Wascana</b>
<b>Latitude</b>	50.60	50.60	51.02	50.70	50.99	50.78	50.44

<b>Longitude</b>	-105.41	-102.68	-106.50	-103.64	-105.18	-103.95	-104.61
<b>Surface Area (m<sup>2</sup> x10<sup>6</sup>)</b>	30	14	371	16	186	19	2
<b>Volume (m<sup>3</sup> x10<sup>6</sup>)</b>	93	114	7487	232	1863	117	3
<b>Length (km)</b>	30	10	225	10	93	16	2
<b>Width (km)</b>	1	1.6	6	1.7	3	1.5	1
<b>Mean depth (m)</b>	3	7.9	21.6	14.3	7.9	6	1.5
<b>TDP (µg P L<sup>-1</sup>)</b>	32.2	157.4	-	173.8	54.3	165	374
<b>DOC (mg L<sup>-1</sup>)</b>	7.7	14.9	6.2	16.1	14	14.3	17.3
<b>Secchi depth (m)</b>	1.1	1.6	3.5	1.4	1.9	1.4	0.7
<b>Chla (µg L<sup>-1</sup>)</b>	47.9	62.4	4.9	49.4	46	67.9	62.1
<b>Microcystin (µg L<sup>-1</sup>)</b>	1.5	0.5	-	1.1	0.7	1.7	0.4
<b>TSS (mg L<sup>-1</sup>)</b>	11.8	6.7	5	11.1	-	7.7	-

## 5.2.2 Data

*In situ* data were collected using standard techniques of a 28-year long-term monitoring program in all lakes (Haig and Leavitt 2019); however, we selected the period of 2017-2020 to match the Sentinel-2 mission lifetime, as the input for our model development are derived from atmospherically corrected imagery (i.e.,  $R_{rs}^{\delta}$ ).

### 5.2.2.1 *In situ* Chla data

In BPL, Chla data originates from multiple datasets, as elaborated in (Chapter 4). Briefly, fluorometers deployed on a buoy regularly measured near-surface Chla in one station. Fluorometric Chla were then calibrated using the method described in (Chapter 3). Additionally, samples collected weekly by a water treatment plant and monthly by field visits across the lake were analyzed via spectrophotometry. Moreover, bi-weekly near-surface Chla samples from one station were analyzed by HPLC (Leavitt and Hodgson 2001).

In the other six lakes (test lakes), phytoplankton were collected on GF/C glass-fibre filters (nominal pore size 1.2 µm) following Swarbrick et al. (2019). Surface water (~0.5-m depth) and depth-integrated samples were filtered through GF/C filters and frozen (-10°C) until analysis for Chla (mg m<sup>-3</sup>) by standard trichromatic assays (Jeffrey and Humphrey 1975) and biomarker pigments (nmoles

pigment  $L^{-1}$ ) by HPLC (Leavitt and Hodgson 2001). Carotenoids, chlorophylls, and their derivatives were isolated and quantified using a Hewlett Packard model 1100 HPLC system calibrated with authentic standards.

### 5.2.2.2 Satellite imagery

Cloud-free level-1C Multi-Spectral Instrument (MSI) images acquired by the Sentinel-2A/B satellites during the open water season over the lakes (~May - October) were downloaded for the period 2017-2020. The Sentinel-2 constellation provides image acquisitions every ~ 2-3 days over the area of interest. The MSI sensor samples in 13 spectral bands from 443 to 2190 nm with spatial resolutions of 10, 20, 60 m and with a 12-bit radiometric resolution (Li et al. 2017), making it suitable for aquatic applications (Pahlevan et al. 2019).

### 5.2.3 Methodology

The methodology adopted in this study is illustrated in Figure 5.2 and is further explained in the subsections below.

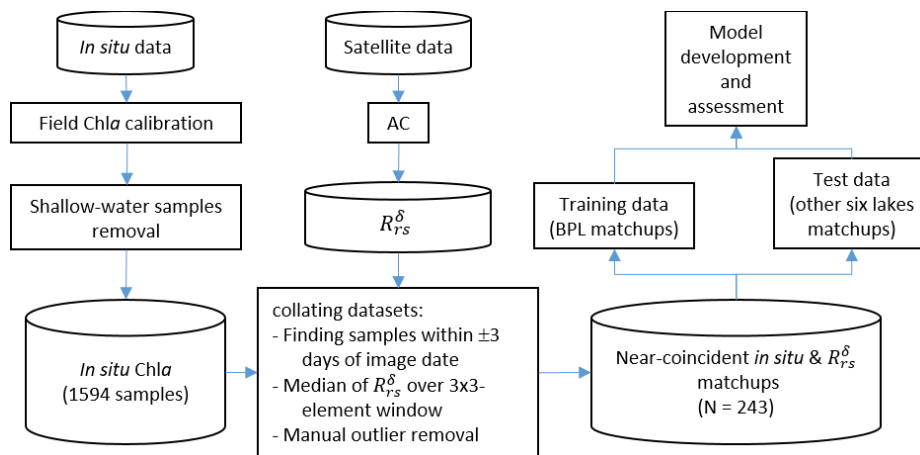


**Figure 5.2. Overview of workflow developed in this study.**

### 5.2.3.1 Data preparation

MSI images were fully corrected for atmospheric effects to produce  $R_{rs}^{\delta}$ . We used ACOLITE (v20210114.0) (Vanhellemont 2019) as the AC processor due to its good performance in inland waters with OWT 4-6 (Pahlevan et al. 2021). Visual inspection of images showed no significant sunglint effect in the study lakes. All MSI spectral bands were then resampled to 60-m grid to be consistent for further steps.

Chla samples of the test lakes (C, D, K, L, P, W) followed a process similar to that of BPL (Chapter 3). Briefly, the process ensures that samples are from optically-deep waters. The remaining *in situ* samples (1594 samples) were then collated with closest matching  $R_{rs}^{\delta}$  to create co-located  $R_{rs}^{\delta}$ –Chla matchups. Maximum time span between field sampling and image acquisition was set to  $\pm 3$  days for training data in BPL and  $\pm 1$  days for test data in the other lakes. Representative  $R_{rs}^{\delta}$  spectra for matchups were chosen to be the median of  $3 \times 3$ -element windows centered around the matchup locations.

ACOLITE masks land and clouds automatically. In addition, we manually deleted matchups that were contaminated by thin clouds/haze and cloud shadow through a visual assessment. Moreover, matchups with negative reflectance ( $\sim 5\%$  of total) were excluded from further processes. We also excluded 6 matchups with  $\text{Chla} > 100 \text{ mg/m}^3$  as they were suspected of scum presence. Eventually, 243 matchups (193 in BPL and 50 in the test lakes) were selected for algorithm development and evaluation.

### 5.2.3.2 Model development and assessment

Three types of retrieval models were adopted; locally trained empirical models (LE), globally trained ML models (GML), and locally trained ML (LML) models. Locally trained models, namely OC3 (O'Reilly et al. 1998), 2band (Moses et al. 2009), LMDN (Pahlevan et al. 2020), and SVR (Chapter 4) were trained using 193  $R_{rs}^{\delta}$ –Chla matchups in BPL, as described in (Chapter 4). OC3 represents blue-green indices which often perform well in ecosystems where water color is governed by Chla (O'Reilly and Werdell 2019). 2band was selected as it showed the best performance among other red-NIR indices in retrieving Chla in BPL (Chapter 4). Similarly, LMDN and SVR outperformed other algorithms in

BPL (Chapter 4). Furthermore, a GML model – MDN (Smith et al. 2021), which has been trained with  $R_{rs}$ , was assessed in this study.

All models were tested using  $R_{rs}^{\delta}$ – Chla matchups from the test lakes (N = 50). Both linear and log10-transformed metrics were examined for accuracy assessment of the models; however, the metrics calculated in log-transformed space, e.g. MdSA (Morley et al. 2018) and Bias (Seegers et al. 2018) are believed to provide a better assessment due to the log-normal distribution of Chla (Seegers et al. 2018). The accuracy metrics are as follows;

$$RMSE = [\sum_{i=1}^N (P_i - M_i)^2 / n]^{1/2} \text{ (mg m}^{-3}\text{)} \quad (5.1)$$

$$RMSLE = [\sum_{i=1}^N (\log_{10}(P_i) - \log_{10}(M_i))^2 / n]^{1/2} \quad (5.2)$$

$$MAPE = 100 \times \text{median}(|P_i - M_i| / M_i) \quad (5.3)$$

$$\text{Bias} = 10^z, z = [\sum_{i=1}^n (\log_{10}(P_i) - \log_{10}(M_i)) / n] \quad (5.4)$$

$$\text{MdSA} = 100 \times (10^y - 1), y = \text{median}|\log_{10}(P_i / M_i)| \text{ (\%)} \quad (5.5)$$

where  $P_i$  and  $M_i$  stand for predicted and measured Chla, respectively. RMSLE is the root mean squared log-error, MAPE is the median absolute percentage error, and MdSA is the median symmetric accuracy, computed in log-space. Bias of 1.5 implies that predicted Chla values are, on average, 50% larger than those measured (Bias = 1 is ideal) (Seegers et al. 2018). MdSA (Morley et al. 2018), is expressed in % and expected to be resistant to outliers to a great extent, zero centered, and interpretable (Pahlevan et al. 2020). As opposed to Bias, MdSA is believed to be an indicator for precision.

### 5.3 Results

SVR and LMDN showed similar performance in retrieving Chla in the test lakes ( $\text{MdSA} \approx 61\%$ ,  $\text{Bias} \approx 1$ ) (Figure 5.3). 2band estimations also displayed a high correlation with *in situ* Chla through the whole range of Chla (Slope = 0.72). MDN showed an overestimation of Chla in almost all lakes ( $\text{Bias} = 2.15$ ), likely due to uncertainties in  $R_{rs}^{\delta}$ . OC3 exhibited poor performance ( $\text{MdSA} = 73\%$ ) as it is more suitable for oligotrophic waters (O'Reilly and Werdell 2019). LML models (SVR, LMDN) significantly outperformed both LE (OC3, 2band) and the GML model (MDN) ( $\overline{\text{MdSA}} 62 \pm 1\%$  vs.  $83 \pm 21\%$ ;  $\overline{\text{Bias}} 1.02 \pm 0.02$  vs.  $1.51 \pm 0.57$ ). Overall, LML models maintained a reasonable performance

given the wide range of Chla (1-100 mg/m<sup>3</sup>). However, they substantially overestimated Chla < 3 mg/m<sup>3</sup>, which is a well-known challenge for retrieving Chla in inland waters.

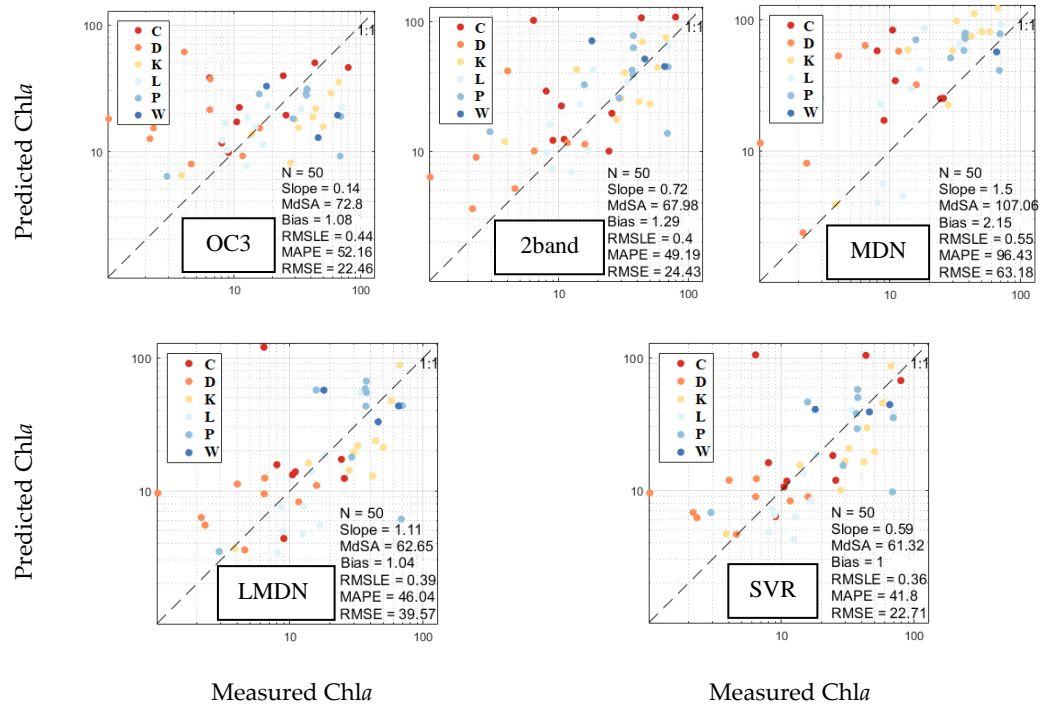


**Figure 5.3. Scatter plots of *in situ* Chla versus predicted Chla from MSI-A/B images. OC3, 2band, LMDN, and SVR were trained with  $R_{rs}^{\delta}$ - Chla matchups from BPL. MDN was trained with global remote-sensing reflectance ( $R_{rs}$ ). The points are color coded based on the lakes (C = Crooked, D = Diefenbaker, K = Katepwa, L = Last Mountain, P = Pasqua, W = Wascana).**

An inter-comparison of accuracy between lakes (Table 5.2) reveals that SVR shows the least variability in accuracy among lakes ( $\sigma_{MdSA} = 21.4\%$ ), followed by LMDN and 2band (23.1% and 23.5%, respectively). On average, the models performed best on Katepwa, Last Mountain, and Pasqua lakes ( $\overline{MdSA} \approx 70\%$ ), moderately for Crooked and Wascana lakes ( $\overline{MdSA} \approx 120\%$ ), and poorest for Lake Diefenbaker ( $\overline{MdSA} \approx 200\%$ ), the least eutrophic of the basins. Overall, Crooked and Wascana are the most eutrophic sites, while Last Mountain and Katepwa share a similar range of Chla values to those in Buffalo Pound Lake (Table 5.1). 2band outperformed other models in Lake Diefenbaker. For Crooked and Last Mountain lakes, SVR maintained the best results, whereas LMDN exhibited the best

performance for estimates in Katepwa and Pasqua lakes. In general, OC3 and MDNs were inferior in most of the lakes, although OC3 performed reasonably in Crooked, Last Mountain, and Pasqua sites.

**Table 5.2. Median symmetric accuracy (%) of the models in retrieving Chla in each individual test lake. N is the number of lake-satellite data matchups.**

	<b>OC3</b>	<b>2band</b>	<b>LMDN</b>	<b>SVR</b>	<b>MDN</b>
<b>C (N = 9, Chla = 24.1±23.9)</b>	62.9	113.8	105.5	42.04	286
<b>D (N = 9, Chla = 6±4.9)</b>	478	67.1	92.3	88.8	248.2
<b>K (N = 10, Chla = 36.8±19.3)</b>	101.6	57.8	50.6	52.6	81.1
<b>L (N = 10, Chla = 20.4±19.1)</b>	50.3	60.5	64	50.2	123.9
<b>P (N = 9, Chla = 37.2±21.6)</b>	60.4	67.3	59.6	89.3	90.9
<b>W (N = 3, Chla = 43.1±23.8)</b>	237.9	45.5	50.4	47.6	193.6

Analysis of observed model bias in each lake (Table 5.3) suggests that MDN overestimated Chla in all lakes, by up to a factor of 3-4 fold for Diefenbaker and Crooked lakes. 2band also overestimated Chla except in Last Mountain. SVR and LMDN overestimated Chla in Crooked, Diefenbaker, and Wascana, while underestimating Chla in Katepwa, Last Mountain, and Pasqua. SVR showed a low bias in all lakes ( $< 1\pm 0.4$ ), except for Diefenbaker lake ( $Bias = 1.85$ ). Overall, all models overestimated Chla in Crooked and Diefenbaker lakes, while they mostly underestimated Chla in Katepwa, Last Mountain, and Pasqua lakes. Estimates of Chla in Pasqua lake showed the least Bias ( $Bias = 1\pm 0.15$ ) (just in case of locally trained models), which is 120% less than that for D lake ( $Bias = 1\pm 1.35$ ).

**Table 5.3. Bias (unitless) of the models in retrieving Chla for each test lake, separately. N is the number of matchups. Ideal bias equals one as it is computed in log space.**

	<b>OC3</b>	<b>2band</b>	<b>LMDN</b>	<b>SVR</b>	<b>MDN</b>
<b>C (N = 9, Chla = 24.1±23.9)</b>	1.44	1.8	1.71	1.38	3.91
<b>D (N = 9, Chla = 6±4.9)</b>	4	1.77	1.8	1.85	2.81
<b>K (N = 10, Chla = 36.8±19.3)</b>	0.55	1.09	0.67	0.67	1.81
<b>L (N = 10, Chla = 20.4±19.1)</b>	0.94	0.88	0.66	0.67	1.13

<b>P (N = 9, Chla = 37.2±21.6)</b>	0.69	1.19	0.96	0.91	2.02
<b>W (N = 3, Chla = 43.1±23.8)</b>	0.53	1.45	1.15	1.09	2.81

## 5.4 Discussion

In this study, we introduced a regional approach in which models were trained with *in situ* data from one waterbody (BPL) and applied to retrieve Chla in other lakes within a 52,000 km<sup>2</sup> drainage area. This regional approach significantly outperformed a recently-developed global approach, MDN (Pahlevan et al. 2020), in terms of both precision and bias, probably due to uncertainties in AC processors (Pahlevan et al. 2021). We suggest that the regional approach proposed here appears to have value as an alternative to global models until a more accurate AC processor emerges.

When employed in regional approaches, ML models (LMDN, SVR) showed better performance relative to traditional empirical models, likely because ML models leverage all VNIR spectral bands of MSI and use a regularization parameter, leading to less overfitting (Chegoonian et al. 2017). This finding is consistent with earlier (Chapter 4) where SVR was found to have good generalizability over two distinct OWTs in BPL. In the present study, the 2band algorithm showed reasonable generalizability as red-NIR indices have strong physical basis and are believed to have good generalizability as long as ecosystems remain similar.

Comparison of the proposed regional approach in test lakes (MdSA<sub>SVR</sub> ≈ 60%) with the locally-trained analyses in BPL (MdSA<sub>SVR</sub> ≈ 35%) (Chapter 4) demonstrated that regional approaches can provide Chla estimations in lakes with no *in situ* data, but only at the cost of reduced retrieval accuracy (e.g., ~ 70% in Qu'Appelle drainage basin). Regardless, we suggest that regional approaches are still suitable for remote sensing of water quality in small inland waters given the scarcity of *in situ* data in most lakes, the widespread nature of HAB outbreaks (Finlay et al. 2015; Ho et al. 2019), and the > 5-10-fold changes in ecosystem production in many eutrophied lakes (Ho et al. 2019).

Global models trained with satellite-derived radiometric products (e.g., MDN<sub>B</sub> trained by  $\rho_{rc}$ ) have been suggested to be suitable for retrieve Chla in waterbodies without *in situ* data (Smith et al. 2021). However, we infer that such models still show substantial bias because of variable atmospheric conditions and uncertainties in AC processing due to aerosol scattering/absorption which is not

corrected by  $\rho_{rc}$ . While we are not aware of such models for MSI data, future studies might evaluate their performance in comparison with the regional approach outlined here.

Several sources of uncertainties may have impacted the accuracy of regional Chl $a$  retrieval. Use of Chl $a$  from multiple sources with different sampling and measurement methods can affect model performance despite decreasing the probability of overfitting (Chapter 4). In addition, satellite radiometric observations of lake pixels might include signals from nearby land pixels (adjacency effect) as the lakes were small and this might affect our results, thereby showing better performance of the regional models in lakes with land cover more similar to BPL. Future studies should be applied in other lake districts, particularly those with more variable lake production. Finally, a more comprehensive study is needed to quantify the effect of variability in water/atmosphere conditions on the performance of regional approaches.

## 5.5 Conclusions

The extrapolation of locally trained ML models to regional retrieval of Chl $a$  in a large lake catchment suggested that the approach is promising especially for small inland waters with similar productivity and optical characteristics, particularly where *in situ* data may not be available. For instance, Appendix A in this thesis presents an application of a regional model developed based on SVR with BPL data for Pasqua Lake in the Qu'Appelle Watershed. Application of global models resulted in high bias in Chl $a$  estimations, a problem which is likely to continue until more accurate AC processors are developed. In the interim, we suggest that regional approaches, coupled with ML models (SVR, LMDN) of known capability in retrieving Chl $a$ , can be employed in early warning systems for HABs in small inland waters. More sophisticated ML models, based on more *in situ* data, and next generation medium-resolution space-borne missions with better spectral/radiometric configuration (e.g., PACE), may further improve performance of regional models.

## Chapter 6

### Conclusion and Future work

#### 6.1 Summary of Contributions and Results

This thesis examined new approaches and methods to retrieve chlorophyll-*a* (Chl*a*) in small inland waters (SIWs) using medium-resolution terrestrial missions such as Landsat-8 and Sentinel-2. We assessed the applicability of current methods, introduced new approaches, and compared them with current methods to evaluate the accuracy of Chl*a* retrieval in SIWs. The results of this research can be used in developing early warning systems for SIWs based on remote sensing technologies.

We demonstrated that a substantial part of errors in remotely retrieved Chl*a* may originate in inconsistencies between *in situ* measurements (Chapter 3). Analysis revealed that fluorometric and *in vitro* estimates of Chl*a* differed both in terms of absolute concentration and patterns of relative change through time. Therefore, three models were developed to improve agreement between metrics of Chl*a* concentration, including two based on Chl*a* and phycocyanin (PC) fluorescence and one based on multiple linear regressions with measured environmental conditions. The model that is based on PC fluorescence was most accurate (error = 35%), whereas that using environmental factors was most reliable (89% within  $3\sigma$  of mean). Models were also evaluated on their ability to produce spatial maps of Chl*a* using remotely-sensed imagery. Here newly-developed models significantly improved system performance with a 30% decrease in Chl*a* errors and a two-fold increase in the range of reconstructed Chl*a* values. Superiority of the PC model likely reflected high cyanobacterial abundance, as well as the excitation-emission wavelength configuration of fluorometers. Our findings suggest that a PC fluorometer, used alone or in combination with environmental measurements, performs better than a single-excitation-band Chl*a* fluorometer in estimating Chl*a* content in highly eutrophic waters.

Using a consistent dataset of *in situ* Chl*a*, we trained and tested a support vector regression (SVR) model, which takes in satellite-derived remote-sensing reflectance spectra ( $R_{rs}^{\delta}$ ) as input for Chl*a* retrieval in a small eutrophic lake, Buffalo Pound Lake (BPL) in Qu'Appelle Watershed. The proposed model leverages the visible and near-infrared bands of Sentinel-2 and Landsat-8 images (400 – 800 nm) and relies on a multi-year dataset of *in situ* Chl*a* ( $N < 200$ ) for training. Following validation against *in situ* Chl*a* measurements over seven ice-free seasons (2014-2020), the SVR model retrieved

*Chla* with a 35% error, outperforming both locally tuned,  $R_{rs}^{\delta}$ -fed empirical models (Normalized Difference Chlorophyll Index, 2- and 3-band models, and OC3) and a recently-developed Mixture Density Network (MDN) by 15% – 65%, while exhibiting comparable performance to a locally trained MDN (LMDN). Moreover, a stratified analysis revealed the superiority of SVR in two distinct optical water types (OWTs) across BPL. SVR also showed robust performance relative to different atmospheric correction (AC) processors (iCOR and ACOLITE) and radiometric products (Rayleigh-corrected reflectance, and top-of-atmosphere reflectance). *Chla* maps for BPL using different combinations of *Chla* retrieval models and AC processors showed minimal noise and best reconstructions of *Chla* profile for a coupled SVR-iCOR processing. However, we observed the highest overall accuracy for SVR-ACOLITE. In addition, this coupled-processing method satisfactorily retrieved time series of *Chla* measurements, particularly for *Chla* values > 100 mg m<sup>-3</sup>, unlike other approaches. Superior transferability of SVR models among the two different OWTs in BPL suggests that these models may perform well in other prairie eutrophic lakes. In the absence of accurate atmospheric corrections, such locally trained machine-learning models (SVR, LMDN) may provide more reliable *Chla* estimations in small waterbodies, particularly when used to monitor harmful algal bloom events.

Currently, remote retrieval of near-surface *Chla* concentration from small inland waters adopts two different approaches; development of local models using in situ *Chla* measurements in target waterbodies or application of globally trained models with no need of local in situ measurements. While the abundance and diversity of small lakes undermine the former approach, application of global models often biases estimations due to uncertainties in atmospheric correction processors. Here, we introduce a regional approach wherein local in situ data from select waterbodies is used to retrieve *Chla* in nearby lakes. We trained state-of-the-art empirical and machine-learning (ML) algorithms, namely OC3, 2band, LMDN, and SVR, over four ice-free seasons (2017-2020) using 193 pairs of near-surface *Chla* in Buffalo Pound Lake, Canada, and near-coincident satellite reflectance from Sentinel-2. Ability of locally trained models and a globally trained mixture density network (MDN) to retrieve *Chla* for unseen data (N = 50) was evaluated for six other catchment lakes. Regional approaches based on locally trained ML models (SVR, LMDN) unbiasedly estimated *Chla* in test sites (overall error  $\approx$  60%) and outperformed locally trained empirical models and globally trained ML models (reduced error by 20%,

bias by 50%). These findings suggest that ML-based regional models are capable of expanding regional *Chla* retrieval from optically-similar waterbodies.

Altogether, results of this study show that current space-borne remote sensing technologies, especially medium-resolution sensors onboard of terrestrial missions, such as Sentinel-2 and Landsat-8 may provide essential information needed for developing early warning systems for harmful algal blooms in small waterbodies. Such an application might be of interest to many stakeholders and organizations, considering the fact that harmful algal blooms continues to degrade water quality in many lakes around the globe, mostly due to climate warming and excess of nutrients. The procedure to develop the methods and assess our results might be considered as simple essential steps to take for developing early warning systems in small inland waters. For example, we showed that a successful employment of remote sensing technologies need consistent *in situ* data to be used as training data. Besides, we introduced a machine learning model to deal with highly uncertain datasets in retrieving *Chla*. The application of regional approaches developed here might be extended to many small waterbodies with no enough training data, where application of remote sensing technologies is currently very limited.

## **6.2 Limitations and uncertainties**

This study has certain limitations and uncertainties. First, our results and conclusions are based on a limited dataset collected in one watershed. Although both *in situ* and radiometric observations span a relatively long period (~ 7 years) and many satellite imagery, previous studies have shown that the performance of *Chla* retrieval models highly depends on optical properties of waterbodies. In other words, the performance of models presented here may be local and cannot generalize to other regions without further research. The lakes selected for this study were eutrophic, but their optical features are mostly governed by phytoplankton. As a result, our results should be treated with caution in waterbodies where colored dissolved organic matter (CDOM) or non-algal particles (NAP) are dominant.

Moreover, *in situ* data in this study contain uncertainty and they originated from different datasets measured by various methods and protocols. Although this variation decreases the chance of overfitting in model development, this may introduce uncertainties in our assessments. In addition, our results regarding atmospheric correction processors may need further investigations as no *in situ* radiometric

observations were available in this study. Thus, we were not able to separate uncertainties in the AC process from those of retrieval models. Adjacency effects might be a major source of error in the performance of models, which we could not quantify in this thesis.

### **6.3 Future research directions**

Technological and theoretical advancements provide further opportunities to expand the work presented here. The recently launched Landsat-9, with similar spatial/spectral characteristics to Landsat-8, halves the revisit time of the Landsat constellation from 16 to 8 days. This can even decrease to 4 days in high latitudes and provide a suitable time frequency for remote observations when combined with Sentinel-2 data. However, further studies are still needed to develop reliable methods to fuse Landsat and Sentinel data to generate aquatic products.

Although offering a daily revisit time and suitable spectral configuration, the Ocean and Land Colour Instrument (OLCI) sensor aboard the Sentinel-3 constellation (300-m spatial resolution) was not assessed in this study. Further studies are needed to assess the performance of OLCI data in small lakes. Moreover, the Ocean Color Imager (OCI) onboard of the PACE satellite mission, planned for launch in 2022, can bring many opportunities to remotes sensing of water quality with a 2-day global coverage of continuous spectral measurements in visible and near-infrared wavelengths. However, OCI still cannot be applied to small waterbodies similar to the ones we studied here.

Global models showed biased estimations of *Chla* in this study, probably due to uncertainties in atmospheric correction processors. Developing global models based on satellite-derived radiometric products, especially for medium-resolution sensors, may improve the performance of global models in small waterbodies. Developing more accurate retrieval models need larger datasets of *Chla*, which will be available in the near future, given the recent advancements in field and buoy sensors. However, our results showed that uncertainties in *in situ* measurements can substantially degrade *Chla* retrieval performance; then, further research is needed to establish standard protocols to measure *Chla* consistently. Furthermore, theoretical developments in machine-learning models can improve *Chla* retrieval performance. Deep learning models can be used if sufficient training *Chla* data is provided. In addition, combining environmental factors (e.g., temperature, wind) as well as radiometric observations of various sensors and AC processors into ML models may increase the accuracy of retrievals.

## References

- Ahn, Y.-H., A. Bricaud, and A. Morel. 1992. Light backscattering efficiency and related properties of some phytoplankters. *Deep Sea Research Part A. Oceanographic Research Papers* 39: 1835-1855.
- Ahn, Y.-H., and P. Shanmugam. 2006. Detecting the red tide algal blooms from satellite ocean color observations in optically complex Northeast-Asia Coastal waters. *Remote Sensing of Environment* 103: 419-437.
- Aiken, J. and others 2007. Validation of MERIS reflectance and chlorophyll during the BENCAL cruise October 2002: preliminary validation of new demonstration products for phytoplankton functional types and photosynthetic parameters. *International Journal of Remote Sensing* 28: 497-516.
- Alikas, K., Kangro, K., and A. Reinart. 2010. Detecting cyanobacterial blooms in large North European lakes using the Maximum Chlorophyll Index. *Oceanologia* 52: 237-257.
- Alvain, S., C. Moulin, Y. Dandonneau, and F.-M. Bréon. 2005. Remote sensing of phytoplankton groups in case 1 waters from global SeaWiFS imagery. *Deep Sea Research Part I: Oceanographic Research Papers* 52: 1989-2004.
- Alvain, S., C. Moulin, Y. Dandonneau, and H. Loisel. 2008. Seasonal distribution and succession of dominant phytoplankton groups in the global ocean: A satellite view. *Global Biogeochemical Cycles* 22.
- Anderson, D. M. 1994. Red tides. *Scientific American* 271: 62-68.
- Andersen, G. S., Pedersen, M. F., and S. L. Nielsen. 2013. Temperature acclimation and heat tolerance of photosynthesis in Norwegian *Saccharina latissima* (Laminariales, Phaeophyceae). *Journal of phycology*, 49: 689-700.
- Andersson, A., Högländer, H., Karlsson, C., and S. Huseby. 2015. Key role of phosphorus and nitrogen in regulating cyanobacterial community composition in the northern Baltic Sea. *Estuarine, Coastal and Shelf Science*, 164: 161-171.
- Ansper, A., and K. Alikas. 2019. Retrieval of chlorophyll a from Sentinel-2 MSI data for the European Union water framework directive reporting purposes. *Remote Sensing* 11: 64.
- Arii, S., Tsuji K, Tomita K, Hasegawa M, Bober B, Haradaa K-I. 2015. Cyanobacterial blue color formation during lysis under natural conditions. *Appl. Environ. Microbiol.* 81:2667–2675. doi.org/10.1128/AEM.03729-14
- Babin, M. and others 2003. Variations in the light absorption coefficients of phytoplankton, nonalgal particles, and dissolved organic matter in coastal waters around Europe. *Journal of Geophysical Research: Oceans* 108.
- Backer, L. C. 2002. Cyanobacterial harmful algal blooms (CyanoHABs): Developing a public health response. *Lake and reservoir Management* 18: 20-31.
- Balasubramanian, S. V., Pahlevan, N., Smith, B., Binding, C., Schalles, J., Loisel, H., ... and E. Boss. 2020. Robust algorithm for estimating total suspended solids (TSS) in inland and nearshore coastal waters. *Remote sensing of environment* 246: 111768.
- Béchet, Q., A. Shilton, and B. Guieysse. 2013. Modeling the effects of light and temperature on algae growth: state of the art and critical assessment for productivity prediction during outdoor cultivation. *Biotechnology advances* 31: 1648-1663.
- Beck, R. and others 2016. Comparison of satellite reflectance algorithms for estimating chlorophyll-a in a temperate reservoir using coincident hyperspectral aircraft imagery and dense coincident surface observations. *Remote Sensing of Environment* 178: 15-30.

- Bergbusch NT, Hayes NM, Simpson GL, Leavitt PR. 2021. Unexpected shift from phytoplankton to periphyton in eutrophic streams due to wastewater influx. *Limnol. Oceanogr.* 66:2745–2761. doi.org/10.1002/lno.11786
- Bernard, S., C. Balt, G. Pitcher, T. Probyn, A. Fawcett, and A. Du Randt. 2005. The use of MERIS for harmful algal bloom monitoring in the southern Benguela. MERIS (A) ATSR Workshop 2005.
- Bertone, E., M. A. Burford, and D. P. Hamilton. 2018. Fluorescence probes for real-time remote cyanobacteria monitoring: A review of challenges and opportunities. *Water Research* 141: 152-162.
- Bertone, E., A. Chuang, M. A. Burford, and D. P. Hamilton. 2019. In-situ fluorescence monitoring of cyanobacteria: Laboratory-based quantification of species-specific measurement accuracy. *Harmful Algae* 87.
- Binding, C., T. Greenberg, J. Jerome, R. Bukata, and G. Letourneau. 2011a. An assessment of MERIS algal products during an intense bloom in Lake of the Woods. *Journal of Plankton Research* 33: 793-806.
- Binding, C., L. Pizzolato, and C. Zeng. 2021. EOLakeWatch; delivering a comprehensive suite of remote sensing algal bloom indices for enhanced monitoring of Canadian eutrophic lakes. *Ecological Indicators* 121: 106999.
- Binding, C. E., T. A. Greenberg, and R. P. Bukata. 2011b. Time series analysis of algal blooms in Lake of the Woods using the MERIS maximum chlorophyll index. *Journal of Plankton Research* 33: 1847-1852.
- Binding CE, Greenberg TA, Bukata RP, Smith DE, Twiss MR. 2012. The MERIS MCI and its potential for satellite detection of winter diatom blooms on partially ice-covered Lake Erie. *J. Plankton Res.* 34:569–573. doi.org/10.1093/plankt/fbs021
- Binding, C. E., Greenberg, T. A., and R. P. Bukata. 2013. The MERIS maximum chlorophyll index; its merits and limitations for inland water algal bloom monitoring. *Journal of Great Lakes Research* 39: 100-107.
- Birks S, Chapman D, Carvalho L, Spears BM, Andersen EH, Argillier C, Auer S, Baattrup-Pedersen A, Banin L, Beklioglu M, et al. 2020. Impacts of multiple stressors on freshwater biota across spatial scales and ecosystems. *Nature Ecol. Evol.* 4:1060–1068. doi.org/10.1038/s41559-020-1216-4
- Bittig, H. C. and others 2019. A BGC-Argo guide: Planning, deployment, data handling and usage. *Frontiers in Marine Science* 6: 502.
- Blondeau-Patissier, D., J. F. Gower, A. G. Dekker, S. R. Phinn, and V. E. Brando. 2014. A review of ocean color remote sensing methods and statistical techniques for the detection, mapping and analysis of phytoplankton blooms in coastal and open oceans. *Progress in oceanography* 123: 123-144.
- Bogard MJ, Vogt RJ, Hayes NM, Leavitt PR. 2020. Unabated nitrogen pollution favours growth of toxic cyanobacteria over chlorophytes in most hypereutrophic lakes. *Environ. Sci. Technol.* 54:3219–3227. doi.org/10.1021/acs.est.9b06299
- Boss, E., and N. Haëntjens. 2016. Primer regarding measurements of chlorophyll fluorescence and the backscattering coefficient with WETLabs FLBB on profiling floats.
- Boss, E. and others 2018. Beyond chlorophyll fluorescence: the time is right to expand biological measurements in ocean observing programs. Wiley Online Library.

- Bouterfas, R., M. Belkoura, and A. Dauta. 2006. The effects of irradiance and photoperiod on the growth rate of three freshwater green algae isolated from a eutrophic lake. *Limnetica* 25: 647-656.
- Bowling, L. C., A. Zamyadi, and R. K. J. W. r. Henderson. 2016. Assessment of in situ fluorometry to measure cyanobacterial presence in water bodies with diverse cyanobacterial populations. 105: 22-33.
- Bresciani, M. and others 2018. Mapping phytoplankton blooms in deep subalpine lakes from Sentinel-2A and Landsat-8. *Hydrobiologia* 824: 197-214.
- Brewin, R. J. and others 2011. An intercomparison of bio-optical techniques for detecting dominant phytoplankton size class from satellite remote sensing. *Remote Sensing of Environment* 115: 325-339.
- Bricaud, A., Babin, M., Morel, A., and H. Claustre. 1995. Variability in the chlorophyll-specific absorption coefficients of natural phytoplankton: Analysis and parameterization. *Journal of Geophysical Research: Oceans* 100: 13321-13332.
- Bridgeman, T. B., J. D. Chaffin, and J. E. Filbrun. 2013. A novel method for tracking western Lake Erie *Microcystis* blooms, 2002–2011. *Journal of Great Lakes Research* 39: 83-89.
- Brient, L. and others 2008. A phycocyanin probe as a tool for monitoring cyanobacteria in freshwater bodies. *Journal of Environmental Monitoring* 10: 248-255.
- Bristow, L. A., Mohr, W., Ahmerkamp, S., and M. M. Kuypers. 2017. Nutrients that limit growth in the ocean. *Current Biology* 27: R474-R478.
- Bryan, A. F. and others 2005. The continuity of ocean color measurements from SeaWiFS to MODIS. *Proc.SPIE*.
- Burkholder, J. M. and others 2006. Comprehensive trend analysis of nutrients and related variables in a large eutrophic estuary: a decadal study of anthropogenic and climatic influences. *Limnology and Oceanography* 51: 463-487.
- Butterwick, C., S. Heaney, and J. Talling. 2005. Diversity in the influence of temperature on the growth rates of freshwater algae, and its ecological relevance. *Freshwater Biology* 50: 291-300.
- Cameron, E. S. 2021. Spatiotemporal Shifts in Cyanobacterial Communities in a Northern Temperate Watershed—Applications of Next-Generation Sequencing and Implications for Monitoring and Climate Change Adaptation.
- Camps-Valls, G., L. Gómez-Chova, J. Muñoz-Marí, J. Vila-Francés, J. Amorós-López, and J. Calpe-Maravilla. 2006. Retrieval of oceanic chlorophyll concentration with relevance vector machines. *Remote Sensing of Environment* 105: 23-33.
- Cannizzaro, J. P., K. L. Carder, F. R. Chen, C. A. Heil, and G. A. Vargo. 2008. A novel technique for detection of the toxic dinoflagellate, *Karenia brevis*, in the Gulf of Mexico from remotely sensed ocean color data. *Continental Shelf Research* 28: 137-158.
- Cannizzaro, J. P., C. Hu, D. C. English, K. L. Carder, C. A. Heil, and F. E. Müller-Karger. 2009. Detection of *Karenia brevis* blooms on the west Florida shelf using in situ backscattering and fluorescence data. *Harmful Algae* 8: 898-909.
- Cao, Z., R. Ma, H. Duan, and K. Xue. 2019. Effects of broad bandwidth on the remote sensing of inland waters: Implications for high spatial resolution satellite data applications. *ISPRS Journal of Photogrammetry and Remote Sensing* 153: 110-122.
- Cao, Z. and others 2020. A machine learning approach to estimate chlorophyll-a from Landsat-8 measurements in inland lakes. *Remote Sensing of Environment* 248: 111974.

- Carberry, L., C. Roesler, and S. Drapeau. 2019. Correcting in situ chlorophyll fluorescence time-series observations for nonphotochemical quenching and tidal variability reveals nonconservative phytoplankton variability in coastal waters. *Limnology and Oceanography: Methods* 17: 462-473.
- Carder, K. L., F. Chen, Z. Lee, S. Hawes, and D. Kamykowski. 1999. Semianalytic Moderate-Resolution Imaging Spectrometer algorithms for chlorophyll a and absorption with bio-optical domains based on nitrate-depletion temperatures. *Journal of Geophysical Research: Oceans* 104: 5403-5421.
- Carey C. C., Ewing H. A., Cottingham K. L., Weathers K. C., Thomas R. Q., J. F. Haney. 2012. Occurrence and toxicity of the cyanobacterium *Gloeotrichia echinulata* in low-nutrient lakes in the northeastern United States. *Aquat. Ecol.* 46:395–409. doi.org/ 10.1007/s10452-012-9409-9
- Carey, C. C., Ibelings, B. W., Hoffmann, E. P., Hamilton, D. P., and J. D. Brookes. 2012. Eco-physiological adaptations that favour freshwater cyanobacteria in a changing climate. *Water research* 46: 1394-1407.
- Carpenter, S. R., N. F. Caraco, D. L. Correll, R. W. Howarth, A. N. Sharpley, and V. H. Smith. 1998. Nonpoint pollution of surface waters with phosphorus and nitrogen. *Ecological applications* 8: 559-568.
- Carpenter SR. 2003. Regime Shifts in Lake Ecosystems: Pattern and Variation. Excellence in Ecology 15: Oldendorf (Germany): International Ecology Institute.
- Carvalho, G. A., P. J. Minnett, L. E. Fleming, V. F. Banzon, and W. Baringer. 2010. Satellite remote sensing of harmful algal blooms: A new multi-algorithm method for detecting the Florida Red Tide (*Karenia brevis*). *Harmful algae* 9: 440-448.
- Carvalho, G. A., P. J. Minnett, V. F. Banzon, W. Baringer, and C. A. Heil. 2011. Long-term evaluation of three satellite ocean color algorithms for identifying harmful algal blooms (*Karenia brevis*) along the west coast of Florida: A matchup assessment. *Remote sensing of environment* 115: 1-18.
- Catherine, A. and others 2012. On the use of the FluoroProbe®, a phytoplankton quantification method based on fluorescence excitation spectra for large-scale surveys of lakes and reservoirs. *Water Research* 46: 1771-1784.
- Chaffin, J. D., D. D. Kane, K. Stanislawczyk, and E. M. Parker. 2018. Accuracy of data buoys for measurement of cyanobacteria, chlorophyll, and turbidity in a large lake (Lake Erie, North America): implications for estimation of cyanobacterial bloom parameters from water quality sonde measurements. *Environmental science and pollution research* 25: 25175-25189.
- Chegoonian, A., M. Mokhtarzade, and M. Valadan Zoej. 2017. A comprehensive evaluation of classification algorithms for coral reef habitat mapping: challenges related to quantity, quality, and impurity of training samples. *International Journal of Remote Sensing* 38: 4224-4243.
- Chegoonian, A., M., K. Zolfaghari, H. M. Baulch, and C. R. Duguay. 2021. Support Vector Regression for Chlorophyll-A Estimation Using Sentinel-2 Images in Small Waterbodies. *IEEE International Geoscience and Remote Sensing Symposium IGARSS*, pp. 7449-7452, doi: 10.1109/IGARSS47720.2021.9554110.
- Chen, T., and C. Guestrin. 2016. Xgboost: A scalable tree boosting system, p. 785-794. *Proceedings of the 22nd acm sigkdd international conference on knowledge discovery and data mining*.
- Cheng, F. Y., and N. B. Basu. 2017. Biogeochemical hotspots: Role of small water bodies in landscape nutrient processing. *Water Resources Research* 53: 5038-5056.

- Choo, F. and others 2018. Performance evaluation of in situ fluorometers for real-time cyanobacterial monitoring. *H2Open Journal* 1: 26-46.
- Choo, F., A. Zamyadi, R. Stuetz, G. Newcombe, K. Newton, and R. Henderson. 2019. Enhanced real-time cyanobacterial fluorescence monitoring through chlorophyll-a interference compensation corrections. *Water research* 148: 86-96.
- Christensen MR, Graham MD, Vinebrooke RD, Findlay DL, Paterson MJ, Turner MA. 2006. Multiple anthropogenic stressors cause ecological surprises in boreal lakes. *Global Chang. Biol.* 12:2316–2322. doi.org/10.1111/j.1365-2486.2006.01257.x
- Ciotti, A. M., M. R. Lewis, and J. J. Cullen. 2002. Assessment of the relationships between dominant cell size in natural phytoplankton communities and the spectral shape of the absorption coefficient. *Limnology and Oceanography* 47: 404-417.
- Ciotti, A. M., and A. Bricaud. 2006. Retrievals of a size parameter for phytoplankton and spectral light absorption by colored detrital matter from water-leaving radiances at SeaWiFS channels in a continental shelf region off Brazil. *Limnology and Oceanography: Methods* 4: 237-253.
- Clark, J. M. and others 2017. Satellite monitoring of cyanobacterial harmful algal bloom frequency in recreational waters and drinking water sources. *Ecological indicators* 80: 84-95.
- Claverie, M. and others 2018. The Harmonized Landsat and Sentinel-2 surface reflectance data set. *Remote Sensing of Environment* 219: 145-161.
- Clay, S., A. Peña, B. DeTracey, and E. Devred. 2019. Evaluation of satellite-based algorithms to retrieve chlorophyll-a concentration in the Canadian Atlantic and Pacific Oceans. *Remote Sensing* 11: 2609.
- Conroy, J. D., D. D. Kane, D. M. Dolan, W. J. Edwards, M. N. Charlton, and D. A. Culver. 2005. Temporal trends in Lake Erie plankton biomass: roles of external phosphorus loading and dreissenid mussels. *Journal of Great Lakes Research* 31: 89-110.
- Cyr, H. 2017. Winds and the distribution of nearshore phytoplankton in a stratified lake. *Water research* 122: 114-127.
- Czerny, J., J. Barcelos e Ramos, and U. Riebesell. 2009. Influence of elevated CO<sub>2</sub> concentrations on cell division and nitrogen fixation rates in the bloom-forming cyanobacterium *Nodularia spumigena*. *Biogeosciences* 6: 1865-1875.
- Dall’Olmo, G., and A. A. Gitelson. 2005. Effect of bio-optical parameter variability on the remote estimation of chlorophyll-a concentration in turbid productive waters: experimental results. *Applied optics* 44: 412-422.
- Davies J-M. 2004. Linking ecology and management of water quality: The distribution and growth of phytoplankton in coastal lakes of British Columbia. [dissertation]. University of Victoria.
- Davis, R., C. Moore, J. Zaneveld, and J. J. J. o. G. R. O. Napp. 1997. Reducing the effects of fouling on chlorophyll estimates derived from long-term deployments of optical instruments. 102: 5851-5855.
- Davies J-M. 2006. Application of the Canadian Water Quality Index for assessing changes in water quality along the Qu'Appelle River, Saskatchewan, Canada. *Lake Reserv. Manag.* 22:308–320. doi.org/10.1080/07438140609354365
- Davis, T. W., F. Koch, M. A. Marcoval, S. W. Wilhelm, and C. J. Gobler. 2012. Mesozooplankton and microzooplankton grazing during cyanobacterial blooms in the western basin of Lake Erie. *Harmful Algae* 15: 26-35.
- de Araujo Carvalho, G. 2008. The use of satellite-based ocean color measurements for detecting the Florida Red Tide (*Karenia brevis*). Citeseer.

- De Keukelaere, L. and others 2018. Atmospheric correction of Landsat-8/OLI and Sentinel-2/MSI data using iCOR algorithm: validation for coastal and inland waters. *European Journal of Remote Sensing* 51: 525-542.
- Defoin-Platel, M., and M. Chami. 2007. How ambiguous is the inverse problem of ocean color in coastal waters? *Journal of Geophysical Research: Oceans* 112.
- Demoulin, C. F., Lara, Y. J., Cornet, L., François, C., Baurain, D., Wilmotte, A., and E. J. Javaux. 2019. Cyanobacteria evolution: Insight from the fossil record. *Free Radical Biology and Medicine* 140: 206-223.
- Devred, E. and others 2018. Development of a conceptual warning system for toxic levels of *Alexandrium fundyense* in the Bay of Fundy based on remote sensing data. *Remote Sensing of Environment* 211: 413-424.
- Dickey JWE, Coughlan NE, Dick JTA, Médoc V, McCard M, Leavitt PR, Lacroix G, Fiorini S, Millot A, Cuthbert RN. 2021. Breathing space: Deoxygenation of aquatic environments can drive differential ecological impacts across biological invasion stages. *Biol. Invasions* 23:2831–2847. doi.org/10.1007/s10530-021-02542-3
- Dixit AS, Hall RI, Leavitt PR, Smol JP, Quinlan R. 2000. Effects of sequential depositional basins on lake response to urban and agricultural pollution: A paleoecological analysis of the Qu'Appelle Valley, Saskatchewan, Canada. *Freshwat. Biol.* 43:319–338. doi.org/10.1046/j.1365-2427.2000.00516.x
- Doerffer, R., and H. Schiller. 2007. The MERIS Case 2 water algorithm. *International Journal of Remote Sensing* 28: 517-535.
- Donald DB, Bogard MJ, Finlay K, Bunting L, Leavitt PR. 2013. Phytoplankton-specific response to enrichment of phosphorus-rich surface waters with ammonium, nitrate and urea. *PLOS One* 8:e53277. doi.org/10.1371/journal.pone.0053277
- Dörnhöfer, K., A. Göritz, P. Gege, B. Pflug, and N. Oppelt. 2016. Water constituents and water depth retrieval from Sentinel-2A—A first evaluation in an oligotrophic lake. *Remote Sensing* 8: 941.
- Dörnhöfer, K., P. Klinger, T. Heege, and N. Oppelt. 2018. Multi-sensor satellite and in situ monitoring of phytoplankton development in a eutrophic-mesotrophic lake. *Science of The Total Environment* 612: 1200-1214.
- Downing, J. A. and others 2006. The global abundance and size distribution of lakes, ponds, and impoundments. *Limnology and Oceanography* 51: 2388-2397.
- Downing JA, Polasky S, Olmstead SM, Newbold SC. 2021. Protecting local water quality has global benefits. *Nature Comm.* 12:2709. doi.org/10.1038/s41467-021-22836-3
- Dröscher, I., K. Finlay, A. Patoine, and P. R. Leavitt. 2008. *Daphnia* control of the spring clear-water phase in six polymictic lakes of varying productivity and size. *Internationale Vereinigung für theoretische und angewandte Limnologie: Verhandlungen* 30: 186-190.
- Dröscher, I., A. Patoine, K. Finlay, and P. R. Leavitt. 2009. Climate control of the spring clear-water phase through the transfer of energy and mass to lakes. *Limnology and Oceanography* 54: 2469-2480.
- Dyble, J., G. L. Fahnenstiel, R. W. Litaker, D. F. Millie, and P. A. Tester. 2008. Microcystin concentrations and genetic diversity of *Microcystis* in the lower Great Lakes. *Environmental Toxicology: An International Journal* 23: 507-516.
- European Environmental Agency (EEA). 2018. *European Waters: Assessment of Status and Pressures 2018*. (Brussels): European Environment Agency. <https://www.eea.europa.eu/publications/state-of-water/>. Accessed April 2021.

- European Space Agency (ESA). 2021a. Sentinel-2 MSI Technical Guide. <https://sentinel.esa.int/web/sentinel/technical-guides/sentinel-2-msi>. Accessed April 2021.
- European Space Agency (ESA). 2021b. Sentinel-3 OLCI Technical Guide. <https://sentinel.esa.int/web/sentinel/technical-guides/sentinel-3-olci>. Accessed April 2021.
- Ehrlich, L. 2010. Sampling and identification: methods and strategies. *Algae: Source to Treatment*, Am. Water Works Assoc. Denver, 25-69.
- Escoffier, N., C. Bernard, S. Hamlaoui, A. Groleau, and A. Catherine. 2014. Quantifying phytoplankton communities using spectral fluorescence: the effects of species composition and physiological state. *Journal of Plankton Research* 37: 233-247.
- . 2015. Quantifying phytoplankton communities using spectral fluorescence: the effects of species composition and physiological state. *Journal of Plankton Research* 37: 233-247.
- Ewing HA, Weathers KC, Cottingham KL, Leavitt PR, Greer ML, Carey CC, Steele BG, Fiorillo AU, Sowles JP. 2020. “New” cyanobacterial blooms are not new: Two centuries of lake production are related to ice cover and land use. *Ecosphere* 11:e03170. doi.org/10.1002/ecs2.3170
- Falkowski, P., and Z. J. Kolber. 1995. Variations in chlorophyll fluorescence yields in phytoplankton in the world oceans. *22*: 341-355.
- Falkowski, P. 2012. Ocean science: the power of plankton. *Nature*, 483: S17-S20.
- Ferreira, R. D., C. C. F. Barbosa, and E. M. Novo. 2012. Assessment of in vivo fluorescence method for chlorophyll-a estimation in optically complex waters (Curuai floodplain, Pará - Brazil) %J *Acta Limnologica Brasiliensia*. 24: 373-386.
- Filazzola, A. and others 2020. A database of chlorophyll and water chemistry in freshwater lakes. *Scientific Data* 7: 310.
- Filbee-Dexter K, Pittman J, Haig HA, Alexander SM, Symons CC, Burke MJ. 2017. Ecological surprise: Concept, synthesis, and social dimensions. *Ecosphere* 8:e02005. doi.org/10.1002/ecs2.2005.
- Findlay, D., and S. Kasian. 1987. Phytoplankton community responses to nutrient addition in Lake 226, Experimental Lakes Area, northwestern Ontario. *Canadian Journal of Fisheries and Aquatic Sciences* 44: s35-s46.
- Finlay, K. and others 2015. Decrease in CO<sub>2</sub> efflux from northern hardwater lakes with increasing atmospheric warming. *Nature* 519: 215-218.
- Finlay K, Leavitt PR, Patoine A, Wissel B. 2010a. Magnitudes and controls of organic and inorganic carbon flux through a chain of hard-water lakes on the northern Great Plains. *Limnol. Oceanogr.* 55:1551–1564. doi.org/10.4319/lo.2010.55.4.1551
- Finlay K, Patoine A, Donald DB, Bogard MJ, Leavitt PR. 2010b. Experimental evidence that pollution with urea can degrade water quality in phosphorus-rich lakes of the northern Great Plains. *Limnol. Oceanogr.* 55:1213–1230. doi.org/10.4319/lo.2010.55.3.1213
- Finlay K, Vogt RJ, Simpson GL, Leavitt PR. 2019. Seasonal interdependence of pCO<sub>2</sub> and CO<sub>2</sub> flux in a hardwater lake of the northern Great Plains: The legacy effect of climate and limnological conditions during 36 years. *Limnol. Oceanogr.* 64:S118–S129. doi.org/10.1002/lno.11113
- Foody, G. M., and A. Mathur. 2006. The use of small training sets containing mixed pixels for accurate hard image classification: Training on mixed spectral responses for classification by a SVM. *Remote Sensing of Environment* 103: 179-189.

- Frankenbach, S. and others 2020. Synoptic Spatio-Temporal Variability of the Photosynthetic Productivity of Microphytobenthos and Phytoplankton in a Tidal Estuary. *Frontiers in Marine Science* 7.
- Franz, B. A., Werdell, P. J., Meister, G., Bailey, S. W., Eplee Jr, R. E., Feldman, G. C., and D. Thomas. 2005. The continuity of ocean color measurements from SeaWiFS to MODIS. In *Earth Observing Systems X* (Vol. 5882, p. 58820W). International Society for Optics and Photonics.
- Freitas, F. H., and H. M. Dierssen. 2019. Evaluating the seasonal and decadal performance of red band difference algorithms for chlorophyll in an optically complex estuary with winter and summer blooms. *Remote Sensing of Environment* 231: 111228.
- Garrido, M., P. Cecchi, N. Malet, B. Bec, F. Torre, and V. Pasqualini. 2019. Evaluation of FluoroProbe® performance for the phytoplankton-based assessment of the ecological status of Mediterranean coastal lagoons. *Environmental Monitoring and Assessment* 191: 204.
- Garver, S. A., D. A. Siegel, and M. B. Greg. 1994. Variability in near-surface particulate absorption spectra: What can a satellite ocean color imager see? *Limnology and Oceanography* 39: 1349-1367.
- Gitelson, A. 1992. The peak near 700 nm on radiance spectra of algae and water: relationships of its magnitude and position with chlorophyll concentration. *International Journal of Remote Sensing* 13: 3367-3373.
- Gitelson, A. A., J. F. Schalles, and C. M. Hladik. 2007. Remote chlorophyll-a retrieval in turbid, productive estuaries: Chesapeake Bay case study. *Remote Sensing of Environment* 109: 464-472.
- Goela, P. C., J. Icelly, S. Cristina, A. Newton, G. Moore, and C. Cordeiro. 2013. Specific absorption coefficient of phytoplankton off the Southwest coast of the Iberian Peninsula: A contribution to algorithm development for ocean colour remote sensing. *Continental Shelf Research* 52: 119-132.
- Goldman, E. A., E. M. Smith, and T. L. Richardson. 2013. Estimation of chromophoric dissolved organic matter (CDOM) and photosynthetic activity of estuarine phytoplankton using a multiple-fixed-wavelength spectral fluorometer. *Water research* 47: 1616-1630
- Gons, H. J., M. T. Auer, and S. W. Effler. 2008. MERIS satellite chlorophyll mapping of oligotrophic and eutrophic waters in the Laurentian Great Lakes. *Remote Sensing of Environment* 112: 4098-4106.
- Gordon, H. R., D. K. Clark, J. L. Mueller, and W. A. Hovis. 1980. Phytoplankton pigments from the Nimbus-7 Coastal Zone Color Scanner: comparisons with surface measurements. *Science* 210: 63-66.
- Gordon, H. R., and D. K. Clark. 1981. Clear water radiances for atmospheric correction of coastal zone color scanner imagery. *Applied optics* 20: 4175-4180.
- Gordon, H. R., D. K. Clark, J. W. Brown, O. B. Brown, R. H. Evans, and W. W. Broenkow. 1983. Phytoplankton pigment concentrations in the Middle Atlantic Bight: comparison of ship determinations and CZCS estimates. *Applied optics* 22: 20-36.
- Gordon, H. R., Brown, O. B., Evans, R. H., Brown, J. W., Smith, R. C., Baker, K. S., and D. K. Clark. 1988. A semianalytic radiance model of ocean color. *Journal of Geophysical Research: Atmospheres*, 93(D9), 10909-10924.
- Gower, J., S. King, W. Yan, G. Borstad, and L. Brown. 2003. Use of the 709 nm band of MERIS to detect intense plankton blooms and other conditions in coastal waters. *Proc. MERIS User Workshop, Frascati, Italy, 10–13 November 2003*. Citeseer.

- Gower, J., S. King, G. Borstad, and L. Brown. 2005. Detection of intense plankton blooms using the 709 nm band of the MERIS imaging spectrometer. *International Journal of Remote Sensing* 26: 2005-2012.
- Gower, J., S. King, and P. Goncalves. 2008. Global monitoring of plankton blooms using MERIS MCI. *International Journal of Remote Sensing* 29: 6209-6216.
- Greb, S. and others 2018. Earth observations in support of global water quality monitoring. International Ocean-Colour Coordinating Group.
- Gregor, J., and B. Maršálek. 2004. Freshwater phytoplankton quantification by chlorophyll a: a comparative study of in vitro, in vivo and in situ methods. *Water Research* 38: 517-522.
- Grobbelaar, J. U. 1994. Turbulence in mass algal cultures and the role of light/dark fluctuations. *Journal of Applied Phycology* 6: 331-335.
- Groetsch, P. M., S. G. Simis, M. A. Eleveld, and S. W. Peters. 2014. Cyanobacterial bloom detection based on coherence between ferrybox observations. *Journal of Marine Systems* 140: 50-58.
- Guschina, I. A., and J. L. Harwood. 2006. Lipids and lipid metabolism in eukaryotic algae. *Progress in lipid research* 45: 160-186.
- Gutierrez-Wing, M. T., A. Silaban, J. Barnett, and K. A. Rusch. 2014. Light irradiance and spectral distribution effects on microalgal bioreactors. *Engineering in Life Sciences* 14: 574-580.
- Haig, H. and others 2020. Comparison of isotopic mass balance and instrumental techniques as estimates of basin hydrology in seven connected lakes over 12 years. *Journal of Hydrology X* 6: 100046.
- Haig, H. A., and P. R. Leavitt. 2019. The Qu'Appelle Long-Term Ecological Research Program: A 26-Yr Hierarchical Platform to Study Freshwater Ecosystems of the Northern Great Plains. Wiley Online Library.
- Haigang, Z., S. Ping, and C. Chuqun. 2003. Retrieval of oceanic chlorophyll concentration using support vector machines. *IEEE Transactions on Geoscience and Remote Sensing* 41: 2947-2951.
- Hall RI, Leavitt PR, Quinlan R, Dixit AS, Smol JP. 1999. Effects of agriculture, urbanization and climate on water quality in the northern Great Plains. *Limnol. Oceanogr.* 44:739–756. doi.org/10.4319/lo.1999.44.3\_part\_2.0739
- Hamilton, D. P. and others 2015. A Global Lake Ecological Observatory Network (GLEON) for synthesising high-frequency sensor data for validation of deterministic ecological models. *Inland Waters* 5: 49-56.
- Hammer, U. T. J. H. 1983. Limnological studies of the lakes and streams of the upper Qu'Appelle river System, Saskatchewan, Canada. 99: 125-144.
- Hawkins, D. M., S. C. Basak, and D. Mills. 2003. Assessing model fit by cross-validation. *Journal of chemical information and computer sciences* 43: 579-586.
- Hayes, N. M. and others 2019. Spatial and temporal variation in nitrogen fixation and its importance to phytoplankton in phosphorus-rich lakes. *Freshwater Biology* 64: 269-283.
- Hayes, N. M., H. A. Haig, G. L. Simpson, and P. R. Leavitt. 2020. Effects of lake warming on the seasonal risk of toxic cyanobacteria exposure. *Limnology and Oceanography Letters* 5: 393-402.
- Haig, H. A., Chegoonian, A. M., Davies, J. M., Bateson, D., and P. R. Leavitt. 2021. Marked blue discoloration of late winter ice and water due to autumn blooms of cyanobacteria. *Lake and Reservoir Management*, 1-15.

- Health Canada, 2020. Guidelines for Canadian Drinking Water Quality. <https://www.canada.ca/en/health-canada/services/environmental-workplace-health/reports-publications/water-quality/guidelines-canadian-drinking-water-quality-summary-table.html>.
- Heisler, J., Glibert, P. M., Burkholder, J. M., Anderson, D. M., Cochlan, W., Dennison, W. C., and M. Suddleson. 2008. Eutrophication and harmful algal blooms: a scientific consensus. *Harmful algae* 8: 3-13.
- Helder, D. and others 2018. Observations and recommendations for the calibration of Landsat 8 OLI and Sentinel 2 MSI for improved data interoperability. *Remote Sensing* **10**: 1340.
- Hirata, T., J. Aiken, N. Hardman-Mountford, T. Smyth, and R. Barlow. 2008. An absorption model to determine phytoplankton size classes from satellite ocean colour. *Remote Sensing of Environment* **112**: 3153-3159.
- Ho, J. C., and A. M. Michalak. 2015. Challenges in tracking harmful algal blooms: A synthesis of evidence from Lake Erie. *Journal of Great Lakes Research* **41**: 317-325.
- Ho, J. C., A. M. Michalak, and N. Pahlevan. 2019. Widespread global increase in intense lake phytoplankton blooms since the 1980s. *Nature* **574**: 667-670.
- Hondzo, M., and D. Lyn. 1999. Quantified small-scale turbulence inhibits the growth of a green alga. *Freshwater Biology* **41**: 51-61.
- Horváth H, Kovács A, Riddick C, Présing M. 2013. Extraction methods for phycocyanin determination in freshwater filamentous cyanobacteria and their application in a shallow lake. *Eur. J. Phycol.* 48:278–286. doi.org/10.1080/09670262.2013.821525
- Hosseini, N., E. Akomeah, J.-M. Davis, H. Baulch, and K.-E. Lindenschmidt. 2018. Water quality modeling of a prairie river-lake system. *Environmental Science and Pollution Research* **25**: 31190-31204.
- Hu, C. and others 2005. Red tide detection and tracing using MODIS fluorescence data: A regional example in SW Florida coastal waters. *Remote Sensing of Environment* **97**: 311-321.
- Hu, C., R. Luerssen, F. E. Muller-Karger, K. L. Carder, and C. A. Heil. 2008. On the remote monitoring of *Karenia brevis* blooms of the west Florida shelf. *Continental Shelf Research* **28**: 159-176.
- Hu, C. 2009. A novel ocean color index to detect floating algae in the global oceans. *Remote Sensing of Environment* **113**: 2118-2129.
- Hu, C., J. Cannizzaro, K. L. Carder, F. E. Muller-Karger, and R. Hardy. 2010. Remote detection of *Trichodesmium* blooms in optically complex coastal waters: Examples with MODIS full-spectral data. *Remote Sensing of Environment* **114**: 2048-2058.
- Hu, C., L. Feng, and Q. Guan. 2021. A Machine Learning Approach to Estimate Surface Chlorophyll-a Concentrations in Global Oceans From Satellite Measurements. *IEEE Transactions on Geoscience and Remote Sensing* **59**: 4590-4607.
- Huisman J, Codd GA, Paerl HW, Ibelings BW, Verspagen JMH, Visser PM. 2018. Cyanobacterial blooms. *Nature Rev. Microbiol.* 16:471–483. doi.org/ 10.1038/s41579-018-0040-1
- Huot, Y., and M. Babin. 2010. Overview of fluorescence protocols: theory, basic concepts, and practice, p. 31-74. *Chlorophyll a fluorescence in aquatic sciences: Methods and applications*. Springer.
- Iames, J. S., Salls, W. B., Mehaffey, M. H., Nash, M. S., Christensen, J. R., and B. A. Schaeffer. 2021. Modeling Anthropogenic and Environmental Influences on Freshwater Harmful Algal Bloom Development Detected by MERIS Over the Central United States. *Water Resources Research* **57**., e2020WR028946.

- Ilori, C. O., N. Pahlevan, and A. Knudby. 2019. Analyzing performances of different atmospheric correction techniques for Landsat 8: application for coastal remote sensing. *Remote Sensing* **11**: 469.
- Irion, S., Christaki, U., Berthelot, H., L'helguen, S., and L. Jardillier. 2021. Small phytoplankton contribute greatly to CO<sub>2</sub>-fixation after the diatom bloom in the Southern Ocean. *The ISME Journal*, 1-14.
- Jamet, C., Loisel, H., and D. Dessailly. 2012. Retrieval of the spectral diffuse attenuation coefficient  $K_d(\lambda)$  in open and coastal ocean waters using a neural network inversion. *Journal of Geophysical Research: Oceans* 117.
- Jane SF, Hansen GJA, Kraemer BM, Leavitt PR, Mincer JL, North RL, Pilla RM, Stetler JT, Williamson CE, Woolway RI, et al. 2021. Widespread de-oxygenation of temperate lakes. *Nature* 594:66–70. doi.org/10.1038/s41586-021-03550-y
- Jaworska, B., and B. Zdanowski. 2011. Patterns of seasonal phytoplankton dynamics as the element of ecological successional changes proceeding in a lake (Lake Kortowskie, northern Poland). *Limnological Review* **11**: 105.
- Jeffrey, S. W., and G. F. Humphrey. 1975. New spectrophotometric equations for determining chlorophylls a, b, c1 and c2 in higher plants, algae and natural phytoplankton. *Biochemie und Physiologie der Pflanzen* **167**: 191-194.
- Jeppesen E, Søndergaard M, Jensen JP, Havens KE, Anneville O, Carvalho L, Coveney MF, Deneke R, Dokulil MT, Foy B, et al. 2005. Lake responses to reduced nutrient loading—an analysis of contemporary long-term data from 35 case studies. *Freshwat. Biol.* 50:1747–1771. doi.org/10.1111/j.1365-2427.2005.01415.x
- Jochens, A. E. and others 2010. Integrated ocean observing system in support of forecasting harmful algal blooms. *Marine Technology Society Journal* **44**: 99-121.
- Johnsen, G., and E. J. J. o. P. Sakshaug. 2007. Biooptical characteristics of PSII and PSI in 33 species (13 pigment groups) of marine phytoplankton, and the relevance for pulse-amplitude-modulated and fast-repetition-rate fluorometry 1. **43**: 1236-1251.
- Karpowicz, M., and J. Ejsmont-Karabin. 2017. Effect of metalimnetic gradient on phytoplankton and zooplankton (Rotifera, Crustacea) communities in different trophic conditions. *Environmental Monitoring and Assessment* **189**: 367.
- Kaylor, M. J., A. Argerich, S. M. White, B. J. VerWey, and I. Arismendi. 2018. A cautionary tale for *in situ* fluorometric measurement of stream chlorophyll a: influences of light and periphyton biomass. **37**: 287-295.
- Kehoe, M., B. Ingalls, J. Venkiteswaran, and H. Baulch. 2019. Successful forecasting of harmful cyanobacteria blooms with high frequency lake data. *bioRxiv*: 674325.
- Kehoe, M. J., K. P. Chun, and H. M. Baulch. 2015. Who smells? Forecasting taste and odor in a drinking water reservoir. *Environmental science & technology* **49**: 10984-10992.
- Kraemer BM, Pilla RM, Woolway RI, Anneville O, Ban S, Colom-Montero W, Devlin SP, Dokulil MT, Gaiser EE, Hambright KD, et al. 2021. Climate change drives widespread shifts in lake thermal habitat. *Nature Clim. Change* 11:521–529. doi.org/10.1038/s41558-021-01060-3
- Krzemińska, I., Pawlik-Skowrońska, B., Trzcińska, M., and J. Tys. 2014. Influence of photoperiods on the growth rate and biomass productivity of green microalgae, Bioprocess and biosystems engineering **37**: 735-741.
- Kummu, M., H. De Moel, P. J. Ward, and O. Varis. 2011. How close do we live to water? A global analysis of population distance to freshwater bodies. *PloS one* **6**: e20578.

- Kurekin, A., P. Miller, and H. Van der Woerd. 2014. Satellite discrimination of *Karenia mikimotoi* and *Phaeocystis* harmful algal blooms in European coastal waters: Merged classification of ocean colour data. *Harmful Algae* **31**: 163-176.
- Kutser, T. 2009. Passive optical remote sensing of cyanobacteria and other intense phytoplankton blooms in coastal and inland waters. *International Journal of Remote Sensing* **30**: 4401-4425.
- Kvålseth, T. O. 1985. Cautionary Note about R 2. *The American Statistician* **39**: 279-285.
- Kwiatkowska, E. J., and G. S. Fargion. 2003. Application of machine-learning techniques toward the creation of a consistent and calibrated global chlorophyll concentration baseline dataset using remotely sensed ocean color data. *IEEE Transactions on Geoscience and Remote Sensing* **41**: 2844-2860.
- Le, C., C. Hu, J. Cannizzaro, D. English, F. Muller-Karger, and Z. Lee. 2013. Evaluation of chlorophyll-a remote sensing algorithms for an optically complex estuary. *Remote Sensing of Environment* **129**: 75-89.
- Leavitt, P., and D. Hodgson. 2001. *Sedimentary Pigments. Tracking environmental change Using Lake Sediments. Volume 3: Terrestrial, Algal, and Siliceous Indicators.* Kluwer Academic Publishers, Dordrecht, The Netherlands.
- Leavitt PR, Brock CS, Ebel C, Patoine A. 2006. Landscape-scale effects of urban nitrogen on a chain of freshwater lakes in central North America. *Limnol. Oceanogr.* 51:2262–2277. doi.org/10.4319/lo.2006.51.5.2262
- Le Moal M, Gascuel-Oudoux C, Ménesguen A, Souchon Y, Étrillard C, Levain A, Moatar F, Pannard A, Souchu P, Lefebvre A, et al. 2019. Eutrophication: A new wine in an old bottle? *Sci. Tot. Environ.* 651:1–11. doi.org/10.1016/j.scitotenv.2018.09.139
- Letelier, R. M., and M. R. Abbott. 1996. An analysis of chlorophyll fluorescence algorithms for the Moderate Resolution Imaging Spectrometer (MODIS). *Remote Sensing of Environment* **58**: 215-223.
- Li, A. H., and J. Bradic. 2018. Boosting in the presence of outliers: adaptive classification with nonconvex loss functions. *Journal of the American Statistical Association* **113**: 660-674.
- Li, J., and D. P. Roy. 2017. A global analysis of Sentinel-2A, Sentinel-2B and Landsat-8 data revisit intervals and implications for terrestrial monitoring. *Remote Sensing* **9**: 902.
- Li, S., S. Ganguly, J. L. Dungan, W. Wang, and R. R. Nemani. 2017. Sentinel-2 MSI radiometric characterization and cross-calibration with Landsat-8 OLI. *Advances in Remote Sensing* **6**: 147.
- Liu, M., Ma, J., Kang, L., Wei, Y., He, Q., Hu, X., and H. Li. 2019. Strong turbulence benefits toxic and colonial cyanobacteria in water: A potential way of climate change impact on the expansion of Harmful Algal Blooms. *Science of the total environment* **670**: 613-622.
- Likens, G. E. 2009. *Encyclopedia of inland waters.* Elsevier.
- Lu C, Tian H. 2017. Global nitrogen and phosphorus fertilizer use for agriculture production in the past half century: Shifted hot spots and nutrient imbalance. *Earth Syst. Sci. Data*, 9:181–192. doi.org/10.5194/essd-9-181-2017
- Lunetta, R. S., B. A. Schaeffer, R. P. Stumpf, D. Keith, S. A. Jacobs, and M. S. Murphy. 2015. Evaluation of cyanobacteria cell count detection derived from MERIS imagery across the eastern USA. *Remote Sensing of Environment* **157**: 24-34.
- Maberly, S. C., Pitt, J. A., Davies, P. S., and L. Carvalho. 2020. Nitrogen and phosphorus limitation and the management of small productive lakes. *Inland Waters* **10**: 159-172.

- Magnuson JJ. 1990. Long-term ecological research and the invisible present. *BioScience* 40:495–501. doi.org/10.2307/1311317
- Manov, D. V., G. C. Chang, and T. D. Dickey. 2004. Methods for reducing biofouling of moored optical sensors. *Journal of Atmospheric and Oceanic Technology* **21**: 958-968.
- Martinez, E. and others 2020. Reconstructing global chlorophyll-a variations using a non-linear statistical approach. *Frontiers in Marine Science* **7**: 464.
- Matsushita, B., Yang, W., Yu, G., Oyama, Y., Yoshimura, K., and T. Fukushima. 2015. A hybrid algorithm for estimating the chlorophyll-a concentration across different trophic states in Asian inland waters. *ISPRS journal of photogrammetry and remote sensing* **102**: 28-37.
- Matthews, M. W. 2011. A current review of empirical procedures of remote sensing in inland and near-coastal transitional waters. *International Journal of Remote Sensing* **32**: 6855-6899.
- Matthews, M. W., S. Bernard, and L. Robertson. 2012. An algorithm for detecting trophic status (chlorophyll-a), cyanobacterial-dominance, surface scums and floating vegetation in inland and coastal waters. *Remote Sensing of Environment* **124**: 637-652.
- Matthews, M. W. 2014. Eutrophication and cyanobacterial blooms in South African inland waters: 10 years of MERIS observations. *Remote Sensing of Environment* **155**: 161-177.
- Matthews, M. W., and D. Odermatt. 2015. Improved algorithm for routine monitoring of cyanobacteria and eutrophication in inland and near-coastal waters. *Remote Sensing of Environment* **156**: 374-382.
- McCain, C., Hooker, S., Feldman, G., & P. Bontempi. 2006. Satellite data for ocean biology, biogeochemistry, and climate research. *Eos, Transactions American Geophysical Union* **87**: 337-343.
- McGowan, S., P. R. Leavitt, and R. I. Hall. 2005. A whole-lake experiment to determine the effects of winter droughts on shallow lakes. *Ecosystems* **8**: 694-708.
- McGowan S, Patoine A, Graham MD, Leavitt PR. 2005. Intrinsic and extrinsic controls of lake phytoplankton synchrony. *Verh. Internat. Verein. Limnol.* 29:794–798. doi.org/10.1080/03680770.2005.11902787
- Mélin, F., and R. Doerffer. Reports and Monographs of the International Ocean Colour Coordinating Group.
- Mellard, J. P., Yoshiyama, K., Litchman, E., and C. A. Klausmeier. 2011. The vertical distribution of phytoplankton in stratified water columns. *Journal of theoretical biology*, **269**: 16-30.
- Meriluoto, J., L. Spoof, and G. A. Codd. 2017. Handbook of cyanobacterial monitoring and cyanotoxin analysis. John Wiley & Sons.
- Meyns, S., Illi, R., and Ribí, B. 1994. Comparison of chlorophyll-a analysis by HPLC and spectrophotometry: where do the differences come from?. *Archiv für Hydrobiologie*. 129-139.
- Millennium Ecosystem Assessment. 2005. Ecosystems and Human Well-being. Vol. 1. Current State and Trends. Washington (DC): Island Press. ISBN: 781559632287
- Miller, P. I., J. D. Shutler, G. F. Moore, and S. B. Groom. 2006. SeaWiFS discrimination of harmful algal bloom evolution. *International Journal of Remote Sensing* **27**: 2287-2301.
- Miller, R. L., C. E. Del Castillo, and B. A. McKee. 2005. Remote sensing of coastal aquatic environments. Springer.
- Millie, D. F., O. M. Schofield, G. J. Kirkpatrick, G. Johnsen, P. A. Tester, and B. T. Vinyard. 1997. Detection of harmful algal blooms using photopigments and absorption signatures: A case study of the Florida red tide dinoflagellate, *Gymnodinium breve*. *Limnology and oceanography* **42**: 1240-1251.

- Mishra, D. R., I. Ogashawara, and A. A. Gitelson. 2017. Bio-optical modeling and remote sensing of inland waters. Elsevier.
- Mishra, S., and D. R. Mishra. 2012. Normalized difference chlorophyll index: A novel model for remote estimation of chlorophyll-a concentration in turbid productive waters. *Remote Sensing of Environment* **117**: 394-406.
- Mishra S, Stumpf RP, Schaeffer BA, Werdell PJ, Loftin KA, Meredith A. 2019. Measurement of cyanobacterial bloom magnitude using satellite remote sensing. *Sci. Reports* 9:18310. doi.org/10.1038/s41598-019-54453-y
- Mobley, C. D. 1994. Light and water: radiative transfer in natural waters. Academic press.
- Mobley, C. D., J. Werdell, B. Franz, Z. Ahmad, and S. Bailey. 2016. Atmospheric correction for satellite ocean color radiometry.
- Moore, T. S., J. W. Campbell, and M. D. Dowell. 2009. A class-based approach to characterizing and mapping the uncertainty of the MODIS ocean chlorophyll product. *Remote Sensing of Environment* **113**: 2424-2430.
- Moore, T. S., M. D. Dowell, and B. A. Franz. 2012. Detection of coccolithophore blooms in ocean color satellite imagery: A generalized approach for use with multiple sensors. *Remote sensing of environment* **117**: 249-263.
- Moradi, M. 2014. Comparison of the efficacy of MODIS and MERIS data for detecting cyanobacterial blooms in the southern Caspian Sea. *Marine pollution bulletin* **87**: 311-322.
- Morel, A., and L. Prieur. 1977. Analysis of variations in ocean color 1. *Limnology and oceanography* **22**: 709-722.
- Morel, A. 1980. In-water and remote measurements of ocean color. *Boundary-layer meteorology* **18**: 177-201.
- Morel, A., and A. P. Bricaud. 1981. Theoretical results concerning light absorption in a discrete medium, and application to specific absorption of phytoplankton. **28**: 1375-1393.
- Morel, A. 1988. Optical modeling of the upper ocean in relation to its biogenous matter content (case I waters). *Journal of geophysical research: oceans* **93**: 10749-10768.
- Morel, A., and B. Gentili. 1991. Diffuse reflectance of oceanic waters: its dependence on Sun angle as influenced by the molecular scattering contribution. *Applied optics* **30**: 4427-4438.
- Morel, A., and S. Maritorena. 2001. Bio-optical properties of oceanic waters: A reappraisal. *Journal of Geophysical Research: Oceans* **106**: 7163-7180.
- Morley, S. K., T. V. Brito, and D. T. Welling. 2018. Measures of model performance based on the log accuracy ratio. *Space Weather* **16**: 69-88.
- Moses, W. J., A. A. Gitelson, S. Berdnikov, and V. Povazhnyy. 2009. Satellite estimation of chlorophyll-a concentration using the red and NIR bands of MERIS—The Azov sea case study. *IEEE Geoscience and Remote Sensing Letters* **6**: 845-849.
- Moses, W. J., A. A. Gitelson, S. Berdnikov, V. Saprygin, and V. Povazhnyi. 2012. Operational MERIS-based NIR-red algorithms for estimating chlorophyll-a concentrations in coastal waters—The Azov Sea case study. *Remote Sensing of Environment* **121**: 118-124.
- Mountrakis, G., J. Im, and C. Ogole. 2011. Support vector machines in remote sensing: A review. *ISPRS Journal of Photogrammetry and Remote Sensing* **66**: 247-259.
- Mueller, J., R. Bidigare, C. Trees, J. Dore, D. Karl, and L. Van Heukelem. 2003. Biogeochemical and bio-optical measurements and data analysis protocols: ocean optics protocols for satellite ocean color sensor validation. Revision 4, Vol. 2. NASA/TM-2003 **21621**: 39-64.

- Myers RA, Hutchings JA, Barrowman NJ. 1997. Why do fish stocks collapse? The example of cod in Atlantic Canada. *Ecol. Applic.* 7:91–106. doi.org/10.1890/1051-0761(1997)007[0091:WDFSCT]2.0.CO;2
- Nair, A. and others 2008. Remote sensing of phytoplankton functional types. *Remote Sensing of Environment* **112**: 3366-3375.
- Nikulina, T. V., and J. P. Kociolek. 2011. Diatoms from hot springs from Kuril and Sakhalin Islands (Far East, Russia). In *The diatom world* (pp. 333-363). Springer, Dordrecht.
- Niu, C., Tan, K., Jia, X., and X. Wang. 2021. Deep learning based regression for optically inactive inland water quality parameter estimation using airborne hyperspectral imagery. *Environmental Pollution* 117534.
- Novoa, S., G. Chust, Y. Sagarminaga, M. Revilla, A. Borja, and J. Franco. 2012. Water quality assessment using satellite-derived chlorophyll-a within the European directives, in the southeastern Bay of Biscay. *Marine Pollution Bulletin* **64**: 739-750.
- O'Reilly, J. E. and others 1998. Ocean color chlorophyll algorithms for SeaWiFS. *Journal of Geophysical Research: Oceans* **103**: 24937-24953.
- O'Reilly, J. E., and P. J. Werdell. 2019. Chlorophyll algorithms for ocean color sensors-OC4, OC5 & OC6. *Remote sensing of environment* **229**: 32-47.
- O'Sullivan, F. 1986. A statistical perspective on ill-posed inverse problems. *Statistical science*: 502-518.
- Odermatt, D., A. Gitelson, V. E. Brando, and M. Schaepman. 2012. Review of constituent retrieval in optically deep and complex waters from satellite imagery. *Remote Sensing of Environment* **118**: 116-126.
- Ogashawara I. 2019. The use of Sentinel-3 imagery to monitor cyanobacterial blooms. *Environments* 6:60. doi.org/10.3390/environments6060060
- Olivier JGJ, Peters JAHW. 2020. Trends in global CO<sub>2</sub> and total greenhouse gas emissions: 2020 report. The Hague: PBL Netherlands Environmental Assessment Agency.
- Orihel DM, Bird DF, Brylinsky M, Chen H, Donald DB, Huang DY, Giani A, Kinniburgh D, Kling H, Kotak BG, et al. 2012. High microcystin concentrations occur only at low nitrogen-to-phosphorus ratios in nutrient-rich lakes. *Can. J. Fish. Aquat. Sci.* 69:1457–1462. doi.org/10.1139/F2012-088
- Ostrowska, M., J. Stoń-Egiert, and B. J. C. S. R. Woźniak. 2015. Modified methods for defining the chlorophyll concentration in the sea using submersible fluorimeters—Theoretical and quantitative analysis. **109**: 46-54.
- Paerl, H. W., R. S. Fulton, P. H. Moisander, and J. Dyble. 2001. Harmful freshwater algal blooms, with an emphasis on cyanobacteria. *TheScientificWorldJournal* **1**: 76-113.
- Paerl, H. W. 2009. Controlling eutrophication along the freshwater–marine continuum: dual nutrient (N and P) reductions are essential. *Estuaries and Coasts* **32**: 593-601.
- Paerl, H. W., and T. G. Otten. 2013. Harmful cyanobacterial blooms: causes, consequences, and controls. *Microbial ecology* **65**: 995-1010.
- Pahlevan, N., Z. Lee, J. Wei, C. B. Schaaf, J. R. Schott, and A. Berk. 2014. On-orbit radiometric characterization of OLI (Landsat-8) for applications in aquatic remote sensing. *Remote Sensing of Environment* **154**: 272-284.
- Pahlevan, N., S. K. Chittimalli, S. V. Balasubramanian, and V. Vellucci. 2019. Sentinel-2/Landsat-8 product consistency and implications for monitoring aquatic systems. *Remote sensing of Environment* **220**: 19-29.

- Pahlevan, N. and others 2020. Seamless retrievals of chlorophyll-a from Sentinel-2 (MSI) and Sentinel-3 (OLCI) in inland and coastal waters: A machine-learning approach. *Remote Sensing of Environment* **240**: 111604.
- Pahlevan, N. and others 2021. ACIX-Aqua: A global assessment of atmospheric correction methods for Landsat-8 and Sentinel-2 over lakes, rivers, and coastal waters. *Remote Sensing of Environment* **258**: 112366.
- Pahlevan, N., Smith, B., Alikas, K., Anstee, J., Barbosa, C., Binding, C., ... & Ruiz-Verdù, A. (2022). Simultaneous retrieval of selected optical water quality indicators from Landsat-8, Sentinel-2, and Sentinel-3. *Remote Sensing of Environment*, *270*, 112860.
- Palmer, S. C. and others 2015. Validation of Envisat MERIS algorithms for chlorophyll retrieval in a large, turbid and optically-complex shallow lake. *Remote Sensing of Environment* **157**: 158-169.
- Philipson, P., K. Eriksso, and K. Stelzer. 2014. MERIS data for monitoring of small and medium sized humic Swedish lakes, p. 1-4. 2014 IEEE/OES Baltic International Symposium (BALTIC). IEEE.
- Philpot, W. D. 1991. The derivative ratio algorithm: avoiding atmospheric effects in remote sensing. *IEEE Transactions on Geoscience and Remote Sensing* **29**: 350-357.
- Piermattei, V. and others 2018. Cost-effective technologies to study the arctic ocean environment. *Sensors* **18**: 2257.
- Pinckney, J., R. Papa, and R. J. J. o. M. M. Zingmark. 1994. Comparison of high-performance liquid chromatographic, spectrophotometric, and fluorometric methods for determining chlorophyll a concentrations in estuarine sediments. **19**: 59-66.
- Platt, T., Hoepffner, N., Stuart, V., and C. C. Brown. 2008. Why ocean colour? The societal benefits of ocean-colour technology. Reports and Monographs of the International Ocean-Colour Coordinating Group (IOCCG).
- Poxleitner, M., G. Trommer, P. Lorenz, and H. Stibor. 2016. The effect of increased nitrogen load on phytoplankton in a phosphorus-limited lake. *Freshwater Biology* **61**: 1966-1980.
- Proctor, C. W., and C. S. Roesler. 2010. New insights on obtaining phytoplankton concentration and composition from *in situ* multispectral Chlorophyll fluorescence. *Limnology and Oceanography: Methods* **8**: 695-708.
- Qiu, G. and others 2021. Relationships between optical backscattering, particulate organic carbon, and phytoplankton carbon in the oligotrophic South China Sea basin. *Optics Express* **29**: 15159-15176.
- Raateoja, M., J. Seppälä, P. J. L. Ylöstalo, and oceanography. 2004. Fast repetition rate fluorometry is not applicable to studies of filamentous cyanobacteria from the Baltic Sea. **49**: 1006-1012.
- Ren, G., Liu, J., Wan, J., Li, F., Guo, Y., and D. Yu. 2018. The analysis of turbulence intensity based on wind speed data in onshore wind farms. *Renewable energy* **123**: 756-766.
- Reynolds, C. S. 2006. The ecology of phytoplankton. Cambridge University Press.
- Rhee, G. Y. 1978. Effects of N: P atomic ratios and nitrate limitation on algal growth, cell composition, and nitrate uptake 1. *Limnology and oceanography* **23**: 10-25.
- Richardson, T. L. and others 2010. Spectral fluorometric characterization of phytoplankton community composition using the Algae Online Analyser®. *Water Research* **44**: 2461-2472.
- Rinta-Kanto, J. M., E. A. Konopko, J. M. DeBruyn, R. A. Bourbonniere, G. L. Boyer, and S. W. Wilhelm. 2009. Lake Erie Microcystis: relationship between microcystin production, dynamics of genotypes and environmental parameters in a large lake. *Harmful algae* **8**: 665-673.

- Robarts, R. D., and T. Zohary. 1987. Temperature effects on photosynthetic capacity, respiration, and growth rates of bloom-forming cyanobacteria. *New Zealand Journal of Marine and Freshwater Research* **21**: 391-399.
- Roesler, C. and others 2017. Recommendations for obtaining unbiased chlorophyll estimates from *in situ* chlorophyll fluorometers: A global analysis of WET Labs ECO sensors. *Limnology and Oceanography: Methods* **15**: 572-585.
- Roesler, C. S., and A. H. Barnard. 2013. Optical proxy for phytoplankton biomass in the absence of photophysiology: Rethinking the absorption line height. *Methods in Oceanography* **7**: 79-94.
- Roesler, C. S. 2016. *In situ* chlorophyll fluorescence observations on NERACOOS Mooring A01: Revised data flagging and changing phenology. Massachusetts Water Resources Authority.
- Rome, M., R. E. Beighley, and T. Faber. 2021. Sensor-based detection of algal blooms for public health advisories and long-term monitoring. *Science of The Total Environment* **767**: 144984.
- Ruddick, K. and others 2003. Overview of Ocean Colour: theoretical background, sensors and applicability for the detection and monitoring of harmful algae blooms (capabilities and limitations).
- Sackmann, B., M. Perry, and C. J. B. d. Eriksen. 2008. Seaglider observations of variability in daytime fluorescence quenching of chlorophyll-a in Northeastern Pacific coastal waters. **5**.
- Sathyendranath, S., L. Watts, E. Devred, T. Platt, C. Caverhill, and H. Maass. 2004. Discrimination of diatoms from other phytoplankton using ocean-colour data. *Marine ecology progress series* **272**: 59-68.
- Sauchyn DJ, Davidson D, Johnston M. 2020. Prairie Provinces. In *Canada in a Changing Climate: Regional Perspectives Report*. Warren FJ, Lulham N, Lemmen DS, editors. Ottawa (ON): Government of Canada. 72 p.
- Schaeffer, B. A. and others 2018. Mobile device application for monitoring cyanobacteria harmful algal blooms using Sentinel-3 satellite Ocean and Land Colour Instruments. *Environmental modelling & software* **109**: 93-103.
- Scheffer M, Carpenter SR, Foley JA, Folke C, Walker B. 2001. Catastrophic state change in ecosystems. *Nature* 413:591-596. doi.org/ 10.1038/35098000
- Schindler DW. 1977. Evolution of phosphorus limitation in lakes. *Science* 195:260–262. doi.org/10.1126/science.195.4275.260
- Schindler DW, Vallentyne JR. 2008. *The algal bowl: Over-fertilization of the world's freshwaters and estuaries*. New York (NY): Routledge. ISBN 13 978-1844076239.
- Schroeder, T., M. Schaale, and J. Fischer. 2007. Retrieval of atmospheric and oceanic properties from MERIS measurements: A new Case-2 water processor for BEAM. *International Journal of Remote Sensing* **28**: 5627-5632.
- Scott, J. P., S. Croke, I. Cetinić, C. E. Del Castillo, and C. L. Gentemann. 2020. Correcting non-photochemical quenching of Saildrone chlorophyll-a fluorescence for evaluation of satellite ocean color retrievals. *Optics Express* **28**: 4274-4285.
- Sechidis K, Sperrin M, Petherick ES, Luján M, Brown G. 2017. Dealing with under-reported variables: An information theoretic solution. *Internat. J. Approx. Reason.* 85:159–177. doi.org/10.1016/j.ijar.2017.04.002
- Seegers, B. N., R. P. Stumpf, B. A. Schaeffer, K. A. Loftin, and P. J. Werdell. 2018. Performance metrics for the assessment of satellite data products: an ocean color case study. *Optics express* **26**: 7404-7422.

- Seppälä, J., P. Ylöstalo, S. Kaitala, S. Hällfors, M. Raateoja, and P. Maunula. 2007. Ship-of-opportunity based phycocyanin fluorescence monitoring of the filamentous cyanobacteria bloom dynamics in the Baltic Sea. *Estuarine, Coastal and Shelf Science* **73**: 489-500.
- Serôdio, J., J. M. da Silva, and F. Catarino. 2001. Use of *in vivo* chlorophyll a fluorescence to quantify short-term variations in the productive biomass of intertidal microphytobenthos. *Marine Ecology Progress Series* **218**: 45-61.
- Sharma S, Blagrave K, Magnuson JJ, O'Reilly CM, Oliver S, Batt RD, Magee MR, Straile D, Weyhenmeyer GA, Winslow L, et al. 2019. Widespread loss of lake ice around the Northern Hemisphere in a warming world. *Nature Clim. Change* 9:227–231. doi.org/10.1038/s41558-018-0393-5
- Shcherbak VI, Semenyuk NY, Linchuk MI. 2019. Winter under the ice water bloom formed by *Aphanizomenon gracile* Lemmermann. *Hydrobiol. J.* 55:20–34. doi.org/10.1615/HydrobJ.v55.i5.20
- Shen, L., H. Xu, and X. Guo. 2012. Satellite remote sensing of harmful algal blooms (HABs) and a potential synthesized framework. *Sensors* **12**: 7778-7803.
- Shin, Y.-H., M. T. Gutierrez-Wing, and J.-W. Choi. 2018. A field-deployable and handheld fluorometer for environmental water quality monitoring. *Micro and Nano Systems Letters* **6**: 16.
- Silva, T. and others 2016. Comparison of cyanobacteria monitoring methods in a tropical reservoir by *in vivo* and *in situ* spectrofluorometry. *Ecological Engineering* **97**: 79-87.
- Simis, S. G., Y. Huot, M. Babin, J. Seppälä, and L. Metsamaa. 2012. Optimization of variable fluorescence measurements of phytoplankton communities with cyanobacteria. *Photosynthesis research* **112**: 13-30.
- Simis SGH, Peters SWM, Gons HJ. 2005. Remote sensing of the cyanobacterial pigment phycocyanin in turbid inland water. *Limnol. Oceanogr.* 50:237–245. doi.org/10.4319/lo.2005.50.1.0237
- Singh, S., and P. Singh. 2015. Effect of temperature and light on the growth of algae species: a review. *Renewable and sustainable energy reviews* **50**: 431-444.
- Smayda, T. J. 1997a. What is a bloom? A commentary. *Limnology and Oceanography* **42**: 1132-1136.
- . 1997b. Harmful algal blooms: their ecophysiology and general relevance to phytoplankton blooms in the sea. *Limnology and oceanography* **42**: 1137-1153.
- . 2002. Turbulence, watermass stratification and harmful algal blooms: an alternative view and frontal zones as “pelagic seed banks”. *Harmful Algae* **1**: 95-112.
- Smith, B. and others 2021. A chlorophyll-a algorithm for Landsat-8 based on mixture density networks. *Frontiers in Remote Sensing* **1**.
- Smith, M. E., L. R. Lain, and S. Bernard. 2018. An optimized chlorophyll a switching algorithm for MERIS and OLCI in phytoplankton-dominated waters. *Remote Sensing of Environment* **215**: 217-227.
- Smol JP. 2008. Pollution of lakes and rivers: A paleoenvironmental perspective. New York (NY): Wiley. ISBN: 978-1-405-15913-5
- Smola, A. J., and B. Schölkopf. 2004. A tutorial on support vector regression. *Statistics and Computing* **14**: 199-222.
- Sobiechowska-Sasim M, Stoń-Egiert J, Kosakowska A. 2014. Quantitative analysis of extracted phycobilin pigments in cyanobacteria – an assessment of spectrophotometric and spectrofluorometric methods. *J. Appl. Phycol.* 26:2065–2074. doi.org/10.1007/s10811-014-0244-3

- Song W, Bardowell S, O'Shea KE. 2007. Mechanistic study and the influence of oxygen on the photosensitized transformations of microcystins (cyanotoxins). *Environ. Sci. Technol.* 41:5336–5341. doi.org/10.1002/es0630660.
- Soto, I. M., J. Cannizzaro, F. E. Muller-Karger, C. Hu, J. Wolny, and D. Goldgof. 2015. Evaluation and optimization of remote sensing techniques for detection of *Karenia brevis* blooms on the West Florida Shelf. *Remote Sensing of Environment* **170**: 239-254.
- Sourisseau, M., K. Jegou, M. Lunven, J. Quere, F. Gohin, and P. Bryere. 2016. Distribution and dynamics of two species of Dinophyceae producing high biomass blooms over the French Atlantic Shelf. *Harmful algae* **53**: 53-63.
- Springer, J., J. Burkholder, H. Glasgow, P. Glibert, and R. Reed. 2005. Use of a real-time monitoring network (RTRM) and shipboard sampling to characterize a dinoflagellate bloom in the Neuse Estuary, North Carolina, USA. *Harmful Algae* **4**: 553-574.
- Spyrakos, E. and others 2018. Optical types of inland and coastal waters. *Limnology and Oceanography* **63**: 846-870.
- Stainton MP, Capel MJ, Armstrong FAJ. 1977. The chemical analysis of freshwater. Second edition. Miscellaneous Special Publication No. 25. Winnipeg (MB): Fisheries and Environment Canada, Fisheries and Marine Service.
- Stedmon, C. A., and S. Markager. 2005. Tracing the production and degradation of autochthonous fractions of dissolved organic matter by fluorescence analysis. *Limnology and Oceanography* **50**: 1415-1426.
- Sterckx, S., S. Knaeps, S. Kratzer, and K. Ruddick. 2015. SIMilarity Environment Correction (SIMEC) applied to MERIS data over inland and coastal waters. *Remote Sensing of Environment* **157**: 96-110.
- Stumpf, R. and others 2003. Monitoring *Karenia brevis* blooms in the Gulf of Mexico using satellite ocean color imagery and other data. *Harmful Algae* **2**: 147-160.
- Stumpf, R. P. and others 2009. Skill assessment for an operational algal bloom forecast system. *Journal of Marine Systems* **76**: 151-161.
- Stumpf RP, Davis TW, Wynee TT, Graham JL, Loftin KA, Johengen TH, Palladino D, Burtner A. 2016. Challenges for mapping cyanotoxin patterns from remote sensing of cyanobacteria. *Harmful Algae* 54:160–173. doi.org/10.1016/j.hal.2016.01.005
- Su H, Ji B, Wang Y. 2019. Sea ice extent detection in the Bohai Sea using Sentinel-3 OLCI data. *Remote Sens.* 11:2436. doi.org/10.3390/rs11202436
- Suggett, D. J., H. L. MacIntyre, R. J. J. L. Geider, and O. Methods. 2004. Evaluation of biophysical and optical determinations of light absorption by photosystem II in phytoplankton. **2**: 316-332.
- Swarbrick, V. J., G. L. Simpson, P. M. Glibert, and P. R. Leavitt. 2019. Differential stimulation and suppression of phytoplankton growth by ammonium enrichment in eutrophic hardwater lakes over 16 years. *Limnology and Oceanography* **64**: S130-S149.
- Sydor, M., R. W. Gould, R. A. Arnone, V. I. Haltrin, and W. Goode. 2004. Uniqueness in remote sensing of the inherent optical properties of ocean water. *Applied optics* **43**: 2156-2162.
- Talling, J. 1966. The annual cycle of stratification and phytoplankton growth in Lake Victoria (East Africa).
- Tang, D., H. Kawamura, M.-A. Lee, and T. Van Dien. 2003. Seasonal and spatial distribution of chlorophyll-a concentrations and water conditions in the Gulf of Tonkin, South China Sea. *Remote Sensing of Environment* **85**: 475-483.

- Tao, B. and others 2015. A novel method for discriminating *Prorocentrum donghaiense* from diatom blooms in the East China Sea using MODIS measurements. *Remote Sensing of Environment* **158**: 267-280.
- Taranu ZE, Gregory-Eaves I, Leavitt PR, Bunting L, Buchaca T, Catalan J, Domaizon I, Guilizzoni P, Lami A, McGowan S, et al. 2015. Acceleration of cyanobacterial dominance in lakes in north temperate-subarctic lakes during the Anthropocene. *Ecol. Lett.* 18:375–384. doi.org/10.1111/ele.12420
- Thomas, W. H., and C. H. Gibson. 1990. Effects of small-scale turbulence on microalgae. *Journal of Applied Phycology* **2**: 71-77.
- Toming, K., T. Kutser, A. Laas, M. Sepp, B. Paavel, and T. Nõges. 2016. First experiences in mapping lake water quality parameters with Sentinel-2 MSI imagery. *Remote Sensing* **8**: 640.
- Toming, K., J. Kotta, E. Uuema, S. Sobek, T. Kutser, and L. J. Tranvik. 2020. Predicting lake dissolved organic carbon at a global scale. *Scientific Reports* **10**: 8471.
- Tomlinson, M., T. Wynne, and R. Stumpf. 2009. An evaluation of remote sensing techniques for enhanced detection of the toxic dinoflagellate, *Karenia brevis*. *Remote Sensing of Environment* **113**: 598-609.
- Tomlinson, M. C. and others 2004. Evaluation of the use of SeaWiFS imagery for detecting *Karenia brevis* harmful algal blooms in the eastern Gulf of Mexico. *Remote Sensing of Environment* **91**: 293-303.
- Tomlinson, M. C. and others 2016. Relating chlorophyll from cyanobacteria-dominated inland waters to a MERIS bloom index. *Remote Sensing Letters* **7**: 141-149.
- Uitz, J., H. Claustre, A. Morel, and S. B. Hooker. 2006. Vertical distribution of phytoplankton communities in open ocean: An assessment based on surface chlorophyll. *Journal of Geophysical Research: Oceans* **111**.
- United Nations, Department of Economic and Social Affairs, Population Division (UNDESA). 2019. *World Population Prospects 2019: Highlights* (ST/ESA/SER.A/423). <https://population.un.org/wpp/>. Accessed 20 May 2021.
- United States Environmental Protection Agency (EPA). 2015. *Drinking Water Health Advisory for the Cyanobacterial Microcystin Toxins*.
- Utermöhl H. 1958. Zur Vervollkommnung der quantitativen Phytoplankton-methodik. *Mitteilungen International Vererin Limnologie* 9:1–38. doi.org/10.1080/05384680.1958.11904091
- Vanhellemont, Q., and K. Ruddick. 2014. Turbid wakes associated with offshore wind turbines observed with Landsat 8. *Remote Sensing of Environment* **145**: 105-115.
- Vanhellemont, Q. 2019. Adaptation of the dark spectrum fitting atmospheric correction for aquatic applications of the Landsat and Sentinel-2 archives. *Remote Sensing of Environment* **225**: 175-192.
- Vilas, L. G., E. Spyraeos, and J. M. T. Palenzuela. 2011. Neural network estimation of chlorophyll a from MERIS full resolution data for the coastal waters of Galician rias (NW Spain). *Remote Sensing of Environment* **115**: 524-535.
- Vincent, R. K. and others 2004. Phycocyanin detection from LANDSAT TM data for mapping cyanobacterial blooms in Lake Erie. *Remote Sensing of Environment* **89**: 381-392.
- Visser, P. M. and others 2016. How rising CO<sub>2</sub> and global warming may stimulate harmful cyanobacterial blooms. *Harmful Algae* **54**: 145-159.

- Vogt, R. J., J. A. Rusak, A. Patoine, and P. R. Leavitt. 2011. Differential effects of energy and mass influx on the landscape synchrony of lake ecosystems. *Ecology* **92**: 1104-1114.
- Vogt, R. J., S. Sharma, and P. R. Leavitt. 2018. Direct and interactive effects of climate, meteorology, river hydrology, and lake characteristics on water quality in productive lakes of the Canadian Prairies. *Canadian Journal of Fisheries and Aquatic Sciences* **75**: 47-59.
- Volpe, G., R. Santoleri, V. Vellucci, M. R. d'Alcalà, S. Marullo, and F. d'Ortenzio. 2007. The colour of the Mediterranean Sea: Global versus regional bio-optical algorithms evaluation and implication for satellite chlorophyll estimates. *Remote Sensing of Environment* **107**: 625-638.
- Walker, H. W. 2014. Harmful algae blooms in drinking water: removal of cyanobacterial cells and toxins. CRC Press.
- . 2019. Harmful algae blooms in drinking water: removal of cyanobacterial cells and toxins. CRC Press.
- Wang J, Wagner ND, Fulton JM, Scott JT. 2021. Diazotrophs modulate phycobiliproteins and nitrogen stoichiometry differently than other cyanobacteria in response to light and nitrogen availability. *Limnol. Oceanogr.* 66: 2333–2345. doi.org/10.1002/lno.11757
- Wang, Y.-K., P.-Y. Chen, H.-U. Dahms, S.-L. Yeh, and Y.-J. J. A. E. I. Chiu. 2016. Comparing methods for measuring phytoplankton biomass in aquaculture ponds. **8**: 665-673.
- Warren, M. A. and others 2019. Assessment of atmospheric correction algorithms for the Sentinel-2A MultiSpectral Imager over coastal and inland waters. *Remote Sensing of Environment* **225**: 267-289.
- Wejnerowski L, Rzymiski P, Kokociński M, Meriluoto J. 2018. The structure and toxicity of winter cyanobacterial bloom in a eutrophic lake of the temperate zone. *Ecotoxicology* 27:752–760. doi.org/10.1007/s10646-018-1957-x
- Werdell, P. J., and S. W. Bailey. 2005. An improved in-situ bio-optical data set for ocean color algorithm development and satellite data product validation. *Remote sensing of environment* **98**: 122-140.
- Werdell, P. J., S. W. Bailey, B. A. Franz, L. W. Harding, G. C. Feldman, and C. R. McClain. 2009. Regional and seasonal variability of chlorophyll-a in Chesapeake Bay as observed by SeaWiFS and MODIS-Aqua. *Remote Sensing of Environment* **113**: 1319-1330.
- Werdell, P. J. and others 2018. An overview of approaches and challenges for retrieving marine inherent optical properties from ocean color remote sensing. *Progress in oceanography* **160**: 186-212.
- Wetzel, R. G. 2001. *Limnology: lake and river ecosystems*. gulf professional publishing.
- Wiik, E. and others 2018. Generalized Additive Models of Climatic and Metabolic Controls of Subannual Variation in pCO<sub>2</sub> in Productive Hardwater Lakes. *Journal of Geophysical Research: Biogeosciences* **123**: 1940-1959.
- Wojtasiewicz, B., N. J. Hardman-Mountford, D. Antoine, F. Dufois, D. Slawinski, and T. W. Trull. 2018. Use of bio-optical profiling float data in validation of ocean colour satellite products in a remote ocean region. *Remote Sensing of Environment* **209**: 275-290.
- Woolway RI, Jennings E, Shatwell T, Golub M, Pierson DC, Maberly SC. 2021. Lake heatwaves under climate change. *Nature* 589:402–407. doi.org/10.1038/s41586-020-03119-1
- World Health Organization (WHO). 2003. Guidelines for safe recreational water environments: Coastal and fresh waters.

- Woźniak M, Bradtke KM, Darecki M, Krężel A. 2016. Empirical model for phycocyanin concentration estimation as an indicator of cyanobacterial bloom in the optically complex coastal waters of the Baltic Sea. *Remote Sens.* 8:212. doi.org/10.3390/rs8030212
- Wulder, M. A. and others 2015. Virtual constellations for global terrestrial monitoring. *Remote Sensing of Environment* **170**: 62-76.
- Wynne, T. and others 2008. Relating spectral shape to cyanobacterial blooms in the Laurentian Great Lakes. *International Journal of Remote Sensing* **29**: 3665-3672.
- Wynne, T. T., R. P. Stumpf, M. C. Tomlinson, V. Ransibrahmanakul, and T. A. Villareal. 2005. Detecting *Karenia brevis* blooms and algal resuspension in the western Gulf of Mexico with satellite ocean color imagery. *Harmful Algae* **4**: 992-1003.
- Wynne, T. T., R. P. Stumpf, M. C. Tomlinson, and J. Dyble. 2010. Characterizing a cyanobacterial bloom in western Lake Erie using satellite imagery and meteorological data. *Limnology and Oceanography* **55**: 2025-2036.
- Wynne, T. T. and others 2013. Evolution of a cyanobacterial bloom forecast system in western Lake Erie: development and initial evaluation. *Journal of Great Lakes Research* **39**: 90-99.
- Xiaoling, Z., Y .Gaofang, Z. Nanjing, Y. Ruifang, L .Jianguo, and L. Wenqing. 2019. Chromophoric dissolved organic matter influence correction of algal concentration measurements using three-dimensional fluorescence spectra. *Spectrochimica Acta Part A: Molecular and Biomolecular Spectroscopy* **210**: 405-411.
- Xing, X. and others 2017. Correction of profiles of in-situ chlorophyll fluorometry for the contribution of fluorescence originating from non-algal matter. *Limnology and Oceanography: Methods* **15**: 80-93.
- Xing, X., N. Briggs, E. Boss, and H. Claustre. 2018. Improved correction for non-photochemical quenching of *in situ* chlorophyll fluorescence based on a synchronous irradiance profile. *Optics express* **26**: 24734-24751.
- Xu, Y., L. Feng, D. Zhao, and J. Lu. 2020. Assessment of Landsat atmospheric correction methods for water color applications using global AERONET-OC data. *International Journal of Applied Earth Observation and Geoinformation* **93**: 102192.
- Yan Y, Bao Z, Shao J. 2018. Phycocyanin concentration retrieval in inland waters: A comparative review of the remote sensing techniques and algorithms. *J. Great Lakes Res.* 44:748–755. doi.org/10.1016/j.jglr.2018.05.004
- Yang, J., Tang, H., Zhang, X., Zhu, X., Huang, Y., and Z. Yang. 2018. High temperature and pH favor *Microcystis aeruginosa* to outcompete *Scenedesmus obliquus*. *Environmental Science and Pollution Research* **25**: 4794-4802.
- Ye, H., Tang, S., and C. Yang. 2021. Deep Learning for Chlorophyll-a Concentration Retrieval: A Case Study for the Pearl River Estuary. *Remote Sensing* **13**: 3717.
- Zamyadi, A., F. Choo, G. Newcombe, R. Stuetz, and R. K. Henderson. 2016. A review of monitoring technologies for real-time management of cyanobacteria: Recent advances and future direction. *TrAC Trends in Analytical Chemistry* **85**: 83-96.
- Zhan, H., P. Shi, and C. Chen. 2003. Retrieval of oceanic chlorophyll concentration using support vector machines. *IEEE Transactions on Geoscience and Remote Sensing* **41**: 2947-2951.
- Zhu, Z. and others 2019. Benefits of the free and open Landsat data policy. *Remote Sensing of Environment* **224**: 382-385.

## **Appendix A**

### **Marked blue discolouration of late winter ice and water due to autumn blooms of cyanobacteria**

#### **A.1 Abstract**

Continued eutrophication of inland waters by nutrient pollution can combine with ongoing unprecedented atmospheric and lake warming to create emergent environmental surprises. Here we report the first known occurrence of marked blue discolouration of ice and water in highly eutrophic prairie lakes during late winter 2021. Intense blue staining was reported first to governmental agencies by ice fishers in early March 2021, then communicated widely through social media, resulting in First Nations and public concern over potential septic field release, toxic spills, urban pollution, and agricultural mismanagement. Analysis of water from stained and reference sites using UV-visible spectrophotometry and high-performance liquid chromatography demonstrated that the blue colour arose from high concentrations ( $\sim 14 \text{ mg L}^{-1}$ ) of the cyanobacterial pigment C-phycoyanin that was released after an unexpected bloom of *Aphanizomenon flos-aquae* in late October 2020 was frozen in littoral ice. Remote sensing using the Sentinel 3A/B OLCI and Sentinel 2A/B MSI platforms suggested that blue staining compassed  $0.68 \pm 0.24 \text{ km}^2$  ( $4.25 \pm 1.5\%$  of lake surface area), persisted over 4 weeks, and was located within 50 m of the lakeshore in regions where fall blooms of cyanobacteria had been particularly dense. Although toxin levels were low ( $\sim 0.2 \mu\text{g microcystin L}^{-1}$ ), high concentrations of C-phycoyanin raised public concern over eutrophication, pollution, and climate change and mobilized rapid governmental and academic response. Given that global climate change and nutrient pollution are increasing the magnitude and duration of cyanobacterial blooms, blue staining may become widespread in eutrophic lakes subject to substantial ice cover.

## A.2 Introduction

Despite recognition of causes and effects of nutrient pollution, water quality continues to decline in many lakes within inhabited catchments (European Environmental Agency 2018, Le Moal et al. 2019) leading to unanticipated effects (Carpenter 2003). During the 20th century, this degradation was often associated with phosphorus pollution from point sources, such as cities, wastewater treatment plants and intensive livestock operations (Schindler 1977, Jeppesen et al. 2005). However, since that time, long-term monitoring and nutrient budgets demonstrate that diffuse or non-point sources of nutrients are responsible for continued water quality loss in both river and lake ecosystems (Carpenter et al. 1998, Le Moal et al. 2019, Birks et al. 2020). Human augmentation of both nitrogen (N) and phosphorus (P) fluxes favours nutrient accumulation in standing waters, leading to outbreaks of harmful algal blooms (HABs), deoxygenation of both surface and deepwater habitats, biodiversity declines, diminished ecosystem services, and substantial economic hardship (Schindler and Vallentyne 2008, Downing et al. 2021, Jane et al. 2021). In particular, continuing influx of P is creating non-linear changes in freshwater ecosystems, including shifts to other forms of regulation (N, light, microelements) (Bogard et al. 2020), outbreaks of toxic cyanobacteria on continental scales (Taranu et al. 2015), and sudden ecosystem state changes (Scheffer et al. 2001, Carpenter 2003). Given that global human population growth remains rapid (UNDESA 2019), fluxes of nutrients are currently at historical maxima (Lu and Tian 2017), and both factors are likely to increase by 30-50% during the next 50 years (Millennium Ecosystem Assessment 2005), unexpected changes in freshwater production, structure, and function should become more prevalent.

Climate warming is also pushing freshwater ecosystems into unprecedented states. For example, as surface waters warm, they can favour the disproportionate growth of cyanobacteria in both unproductive (Carey et al. 2012, Ewing et al. 2019) and highly eutrophic ecosystems (Huisman et al. 2018). The high specific heat of water allows lakes in particular to accumulate energy, leading to more pronounced aquatic 'heat waves', reduced ice cover, and extended duration of growing seasons (Sharma et al. 2019, Woolway et al. 2021). These conditions increase the magnitude and duration of toxic cyanobacterial blooms (Hayes et al. 2019), and may contribute to unexpected blooms of phytoplankton during formerly cooler and less productive seasons (Wejnerowski et al. 2018, Shcherbak et al. 2019). Temperature increases are also depleting oxygen from lakes at unequalled rates (Jane et

al. 2021), leading to habitat loss in lakes worldwide (Kraemer et al. 2021). These conditions can favour invasive species, further reducing the biodiversity of stressed freshwaters (Dickey et al. 2021). Given the ineffective control of global greenhouse gas emissions (Olivier and Peters 2020), atmospheric and lake temperatures will continue to rise resulting in regional ecosystem stresses that have no historical precedent (Woolway et al. 2021).

Ecological surprises are likely to occur more frequently as the magnitude of lake fertilization and warming increase into uncharted waters (Christensen et al. 2006, Fibee-Dexter et al. 2017). Historically, such deviations from experiential expectations or mechanistic forecasts often arose because of an incomplete understanding of the natural range of ecosystem conditions, a form of temporal myopia known as the “invisible present” to neo-ecologists (Magnuson et al. 1990) but which is familiar to paleolimnologists (Smol 2008). However, unabated human population growth and resource utilization has the potential to push some freshwater ecosystems into trajectories that cannot be forecast easily from current process-oriented studies. On-going examples of such ecological surprises include hysteretic state change in shallow lakes (Scheffer et al. 2001, Carpenter 2003), sudden collapse of freshwater and marine fish stocks (Myers et al. 1997), under-ice blooms of diazotrophic cyanobacteria (Wejnerowski et al. 2018, Shcherbak et al. 2019), and sudden establishment of invasive species outside their apparent biological limits (Dickey et al. 2021), as well as smaller-scale examples that are likely under-reported (Sechidis et al. 2017).

Here we file the first known report of one such lake-scale ecological surprise – a marked blue discolouration of ice and water in a series of highly eutrophic prairie lakes during spring 2021. First reported to governmental agencies by ice fishers in early March 2021, communication of the blue water phenomenon spread within days to social media (Facebook, Twitter), traditional news coverage (print, radio, television), and public outreach to government agencies (Ministry of Environment, Water Security Agency). Analysis of water and lipid-solute biomarker pigments demonstrated that the blue colour resulted from high concentrations of the cyanobacterial pigment C-phycoerythrin derived from a late-fall bloom of *Aphanizomenon flos-aquae* that had frozen into nearshore ice late in 2020. Such events may become more frequent, as temperate waters continue to warm, eutrophy, and interact with other novel environmental changes (Birks et al. 2020).

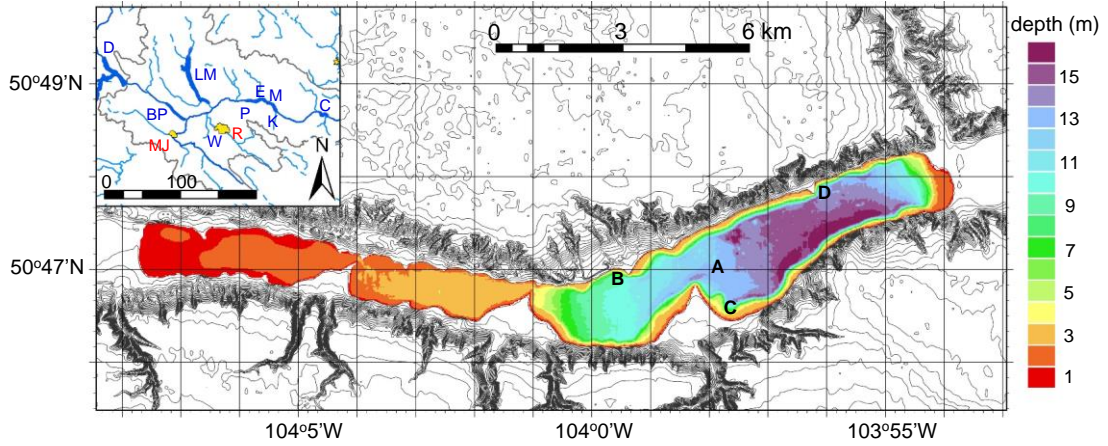
## **A.3 Methods and Materials**

### **A.3.1 Study region**

Intense blue staining of ice and water was reported first to the Saskatchewan Water Security Agency (WSA) on 11 March 2021 for Pasqua Lake, with subsequent social media reports for downstream Echo Lake (Figure A.1). These two sites are part of the 58,775 km<sup>2</sup> Qu'Appelle River drainage basin located in the prairie grassland ecoregion of southern Saskatchewan, Canada (Vogt et al. 2011, Haig and Leavitt 2019). The Qu'Appelle River arises naturally west of Buffalo Pound Lake and flows eastward through a series of seven productive lakes (Buffalo Pound, Pasqua, Echo, Mission, Katepwa, Crooked, Round) to its confluence with the Assiniboine River in Manitoba (Figure A.1.a). River flow is augmented by discharge from the mesotrophic Lake Diefenbaker reservoir to the west, whereas hypereutrophic Wascana Lake and eutrophic Last Mountain Lake drain into the Qu'Appelle River mid-reach, north of the City of Regina (Figure A.1.a).

Regional climate (Köppen *Dfb* classification) exhibits short summers (mean 19°C in July), cold winters (mean -16°C in January), high evaporation (~60 cm yr<sup>-1</sup>) relative to precipitation (~30 cm yr<sup>-1</sup>), and ~75% of annual runoff during a short snowmelt period after mid-March (Leavitt et al. 2006, Haig et al. 2020). Land use within the Qu'Appelle watershed is comprised mainly of agriculture (75%; wheat, canola), along with natural grasslands (12%), the urban centres (5%) of Moose Jaw and Regina, and surface waters (8%) (Hall et al. 1999, Leavitt et al. 2006). Nutrient-rich urban effluent from upstream Regina (tertiary and biologically treated) and Moose Jaw (modified tertiary) first enters Pasqua Lake via the Qu'Appelle River before being conveyed downstream to eastern basins (Davies 2006, Bergbusch et al. 2021).

a. Pasqua Lake morphometry



b. Pasqua Lake discolouration site B



c. Pasqua Lake discolouration Site C

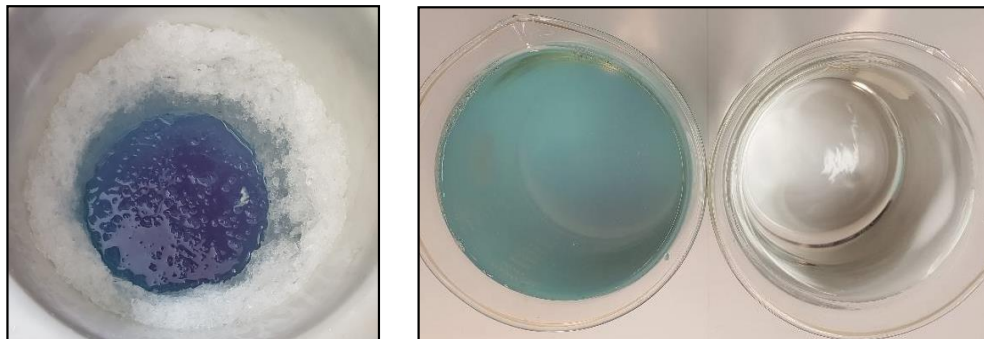


**Figure A.1. Pasqua Lake, Saskatchewan, Canada. (a) Lake morphology and drainage basin (inset). Regional Qu’Appelle lakes (inset, blue) include Diefenbaker (D), Buffalo Pound (BPL), Last Mountain (L), Wascana (W), Pasqua (P), Echo (E), Mission (M), Katepwa (K) and Crooked (C). Cities (inset, red) include Regina (R) and Moose Jaw (MJ). Reference site (A), and three blue-water sampling sites (B, C, D) indicated on main morphometric map. (b) Blue staining of ice and water along north shore of Pasqua Lake (Site B). Photo courtesy of Larry Bedel. (c) Discoloration of water in ice-fishing hole at Site B on the south shore of Pasqua Lake (left; photo courtesy of Tracey Kleim) and comparison of a 15-cm deep sample of 0.45 µm pore filtered lake water from Site B and deionized water (right).**

Pasqua Lake is composed of a series of four progressively deeper basins (Figure A.1.a), each with alkaline and eutrophic waters that together exhibit a relatively short water residence time (~0.65 year) (Table A.1). Dissolved inorganic (DIC) and organic carbon (DOC) content is elevated, resulting in late summer pH > 9 (Finlay et al. 2010a). Like other Qu’Appelle lakes, Pasqua Lake is polymictic, although pronounced deepwater anoxia occurs in the eastern basin during late summer when Chl a > 100 µg L<sup>-1</sup>, as well as under ice during winter (Hall et al. 1999, Vogt et al. 2011). Phytoplankton communities are diverse and include surface blooms of N<sub>2</sub>-fixing and non-N<sub>2</sub>-fixing cyanobacteria (*Aphanizomenon*, *Dolichospermum*, *Microcystis*, *Planktothrix*, *Limnothrix*) during July-September when irradiance (~ 300 cloudless days year<sup>-1</sup>) and dissolved P concentrations are elevated (> 50 µg P L<sup>-1</sup>), and mass ratios of dissolved N:P can be < 5:1 (Vogt et al. 2011, Hayes et al. 2019) (Table A.1).

**Table A.1 Physical and chemical features of Pasqua Lake, Saskatchewan, Canada, 2014–2020.**

**Samples were taken either biweekly (n = 62) or monthly (n = 33) during the ice-free season (May–Sep) from 1-m depth, except dissolved organic and inorganic carbon which were from depth-integrated samples, and microcystin which was from 0.25-m depth. ND = no detect at detection limit of 0.016 µg/L for microcystin and 0.009 mg N/L for nitrate.**

<i>Variable</i>	<b>n</b>	<b>Mean</b>	<b>SD</b>	<b>Range (min, max)</b>
<i>Total Phosphorus, TP (mg P/L)</i>	33	0.17	0.08	0.06, 0.41
<i>Ortho Phosphorus, SRP (mg P/L)</i>	33	0.12	0.08	0.02, 0.37
<i>Total Nitrogen, TN calculated (mg N/L)</i>	33	1.95	0.43	1.31, 3.41
<i>Ammonia (mg N/L)</i>	33	0.28	0.23	0.02, 0.81

<i>Nitrate (mg N/L)</i>	33	0.030	0.047	ND, 0.18
<i>TN : TP (by mass)</i>	33	13.5	6.3	4.7, 31.6
<i>Specific Conductance (<math>\mu\text{S}/\text{cm}</math>)</i>	33	1574	142	1200, 1770
<i>Dissolved Inorganic Carbon, DIC (mg/L)</i>	62	54.94	3.13	45.46, 62.86
<i>Dissolved Organic Carbon, DOC (mg/L)</i>	62	13.57	1.80	10.18, 17.90
<i>Chlorophyll a, Chl-a (<math>\mu\text{g}/\text{L}</math>)</i>	33	44.64	31.3	0.1, 110
<i>Microcystin LR equivalents (<math>\mu\text{g}/\text{L}</math>)</i>	62	1.28	3.63	ND, 20.06
<i>Secchi disk transparency (m)</i>	62	1.37	0.94	0.17, 3.40

### A.3.2 Limnological monitoring

Pasqua Lake was sampled biweekly between early May and late September 2020 by the University of Regina following standard protocols of the 28-year Qu'Appelle Long Term Ecological Research Program (Vogt et al. 2011, Haig and Leavitt 2020). Additional monthly samples were collected and analyzed by the WSA using similar protocols (Davies 2006). The lake was also sampled by the WSA through ~30 cm of ice at two near-shore locations and a central reference site on 12 March 2021, as well as two additional locations three days later (Figure A.1.a). At all stations, water and air temperature ( $^{\circ}\text{C}$ ), dissolved oxygen ( $\text{mg O}_2 \text{ L}^{-1}$ ), specific conductance ( $\mu\text{S cm}^{-1}$ ), salinity ( $\text{g total dissolved solids [TDS] L}^{-1}$ ), and pH were measured using either a YSI model 85 or model EXOI meter. Depth-integrated water samples were collected by pooling samples from a 2.2-L Van Dorn water bottle deployed at 1.0-m intervals, while surface samples were collected at ~0.5-m depth (Vogt et al. 2011). Depth-integrated water (surface to  $Z_{\text{max}} - 1 \text{ m}$ ) was screened through a 243- $\mu\text{m}$  mesh net to remove zooplankton and stored at  $4^{\circ}\text{C}$  in a dark bottle until processed.

Samples for analysis of Chl a, particulate organic matter (POM), phytoplankton pigments, and stable isotopes of C and N were filtered onto Whatman GF/C glass fiber filters (nominal pore size 1.2- $\mu\text{m}$ ) and stored frozen in the dark. Surface and depth-integrated water samples were filtered through 0.45- $\mu\text{m}$  pore membrane filter and the filtrate was stored until nutrient analysis (Vogt et al. 2011). As well, unfiltered surface samples were preserved with Lugol's IKI solution for microscopic analysis of phytoplankton community composition (Findlay and Kasian 1987, Donald et al. 2013).

### A.3.3 Laboratory analyses

Nutrient concentrations were estimated using standard QU-LTER protocols at the Biogeochemical Analytical Service Laboratory, University of Alberta, Edmonton, Alberta, Canada (Vogt et al. 2011), while governmental samples were analyzed using similar protocols at either the Saskatchewan Research Council or the Romanow Provincial Laboratory (Davies 2006). Depth-integrated water was screened (243- $\mu\text{m}$  mesh) then filtered through an 0.45- $\mu\text{m}$  pore membrane filter within three hours of collection before analysis for total dissolved phosphorus (TDP) and orthophosphate (SRP), both as  $\mu\text{g P L}^{-1}$ , as well as  $\text{NO}_3^-$ ,  $\text{NH}_4^+$ , dissolved Kjeldahl N, and total dissolved nitrogen (TDN) (all  $\text{mg N L}^{-1}$ ) using standard analytical procedures (Stainton et al. 1977). WSA samples included total N and P derived from unfiltered water.

Chl a samples were analyzed using standard trichromatic methods (Jeffrey and Humphrey 1975), while high performance liquid chromatography (HPLC) was used to quantify changes in phytoplankton community composition (Leavitt and Hodgson 2001, Donald et al. 2013). Briefly, chlorophyll, carotenoid and derivative pigments were extracted from POM on GF/C filters, dried under inert  $\text{N}_2$  gas, and re-dissolved into an injection solution before introduction into a fully-calibrated Agilent Model 1100 HPLC fitted with photodiode array and fluorescence detectors. Lipid-soluble biomarker pigments ( $\text{nmoles pigment L}^{-1}$ ) were quantified for total phytoplankton abundance (Chl a, pheophytin a,  $\beta$ -carotene), siliceous algae (fucoxanthin), mainly diatoms (diatoxanthin, diadinoxanthin), cryptophytes (alloxanthin), dinoflagellates (peridinin), chlorophytes and cyanobacteria (lutein-zeaxanthin), chlorophytes alone (Chl b), total cyanobacteria (echinenone), colonial cyanobacteria (myxoxanthophyll), Nostocales cyanobacteria (canthaxanthin), and potentially  $\text{N}_2$ -fixing cyanobacteria (aphanizophyll) following Leavitt and Hodgson (2001). Ratios of concentrations of undegraded Chl a to pheophytin a (Chl a: Pheo a) were used to estimate phytoplankton vitality, as the latter compound is a Chl degradation product that is normally rare in live cells (Leavitt and Hodgson 2001).

Concentrations of C-phycoyanin were estimated for winter samples collected in March 2021. This pigment is used by cyanobacteria to regulate cellular N content (Wang et al. 2021). Briefly, water was filtered through 0.45- $\mu\text{m}$  pore filters and absorbance measured 400-900 nm using an Agilent model 8453 UV-Visible spectrophotometer fitted with a 10-cm quartz cuvette. Absolute pigment

concentrations *in situ* were estimated from the difference in absorbance of filtered water from blue ice and reference sites and by applying a 15-point calibration curve relating absorbance to known concentrations of authentic C-phycoerythrin from *Spirulina* (Sigma-Aldrich, Oakville). We assumed all *in situ* absorbance at 620 nm was due to C-phycoerythrin, but recognize this procedure might overestimate concentrations if phycoerythrin (from cyanobacteria and cryptophytes) is also present (Sobiechoowska-Sasim et al. 2014).

Phytoplankton communities in the uppermost 1 m of the water column were enumerated to species and quantified using standard Utermöhl (1958) techniques by David Findlay of Plankton-R-Us Inc. (Winnipeg, Manitoba). Briefly, whole samples of ~ 25 mL were deposited onto depression slides using a sedimentation chamber and cells or colonies were identified at 100-1000 x magnification using a light microscope with reference to relevant taxonomic keys (Findlay and Kasian 1987). Densities of taxa were estimated as cells mL<sup>-1</sup> and were converted to biovolume using estimates of greatest axial linear dimensions and application of species-specific formula for cell shape.

#### **A.3.4 Remote sensing**

Temporal changes in the estimated abundance of Chl a and C-phycoerythrin were derived from remote sensing of Pasqua Lake during August – November 2020 (Chl a) and March – April 2021 (C-phycoerythrin). Briefly, we employed the MultiSpectral Instrument (MSI) and Ocean and Land Colour Instrument (OLCI) sensors on-board of Sentinel-2 A/B and Sentinel-3 A/B satellites to estimate Chl a and C-phycoerythrin, respectively. Images from MSI have finer spatial resolution (10 - 60 m) and a Chl a-suitable spectral band configuration (664 nm, 709 nm), but only 2-3 day temporal resolution at this latitude (European Space Agency 2021a), whereas OLCI has a daily revisit time and 16 spectral bands within 400-800 nm, but only 300-m resolution (European Space Agency 2021b). The MSI sensor can estimate lake-surface Chl a concentrations in small inland waters (Pahlevan et al. 2020) and its high spatial resolution provides us with detailed maps of seasonal changes in Chl distribution during ice-free conditions. Similarly, the Sentinel 3 OLCI sensor has been used to estimate phycoerythrin and infer cyanobacterial blooms in lakes (Mishra et al. 2019, Ogashawara 2019), as it has a spectral band centred on 620 nm, as well as additional wavelengths that allow correction for scattering by particles (e.g., 709 nm). Here we used the OLCI for the first time to approximate levels of phycoerythrin captured in lake

ice. For both sensors, we downloaded all clear-sky images of Top-of-Atmosphere-radiance ( $\rho_{\text{TOA}}$ ) (level 1 data) provided by the European Space Agency (ESA).

All images were corrected for atmospheric effect that may interfere with estimates of surface reflectance. As up to ~90% of signal that a sensor receives is from atmosphere, not the waterbody, we corrected  $\rho_{\text{TOA}}$  data from both sensors using two atmospheric models, iCOR (De Keukelaere et al. 2018) and Acolite (Valhellefont 2019), both suitable for water quality applications (Pahlevan et al. 2021). All high-resolution MSI images were corrected using Acolite model, whereas OLCI images were processed using the iCOR model because the latter also includes the SIMEC algorithm to reduce the adjacency effect on nearshore pixels (Sterckx et al. 2015). This correction was required because of the relatively coarse spatial-resolution of OLCI images (300 m), the peripheral location of the reported blue-ice phenomenon, and the relatively narrow width of Pasqua Lake (~2 km). Resultant processed images approximate remote sensing reflectance ( $R_{\text{rs}}$ ) at the lake surface.

Chl a concentrations were estimated using a support vector regression (SVR) that used all MSI bands (Chegoonian et al. 2021) and that had been trained previously with seven years of biweekly measurements of Chl a during May – September from upstream Buffalo Pound Lake (Finlay et al. 2019). Because of proximity and similarity of the two lakes (Vogt et al. 2011, Hayes et al. 2020), inferred Chl a concentrations were expected agreed to within ~35% of *in situ* measured values. Because C-phycoyanin absorbs strongly at 620 nm, but not at the nearby OLCI band centred on 709 nm (Figure A.2.b), we used the index ratio  $R_{\text{rs}620 \text{ nm}}/R_{\text{rs}709 \text{ nm}}$  to map potential phycocyanin distribution, while also correcting for absorbance of longer wavelengths by water and other substances (Simis et al. 2005, Yan et al. 2018). This way, a lower ratio of reflectance should be related to high concentrations of C-phycoyanin. However, because there were too few *in situ* measurements to calibrate the OLCI sensor in the present study, the computed ratio is presented as an index of relative reflectance and used to map potential phycocyanin distribution (Woźniak et al. 2016). Further, all maps were overlaid by original satellite true colour (RGB) images for pixels that had been masked; we masked land pixels using a waterbody layer in Sentinel-3 products, while a mask for OLCI pixels with thick snow on lake ice was applied following (Su et al. 2019). Finally, OLCI images were compared visually with those from the less productive Last Mountain Lake, where the blue-ice phenomenon had not yet been reported.

#### A.4 Results and Discussion

The presence of blue ice and underlying blue water was reported for multiple sites in Pasqua Lake during the second week of March 2021 (sites B-D; Figure A.1.a). Subsequently, blue ice and water were reported on social media for the western end of Echo Lake. In these instances, intense staining was observed within 100 m of lakeshore, often where snow cover was limited, or had been compressed due to vehicular traffic of ice fishers and other recreational users (Figure A.1.b). Sampling holes revealed interbedded layers of blue and white ice. Visual inspection of water samples by WSA personnel suggested that the darkest discolouration occurred in the uppermost waters rather than in samples 1 - 2 m below the ice sheet. Ice-fishing holes were filled with blue water whose colour was stable for several weeks in the laboratory at 10°C in the dark after filtration through GF/C filters (Figure A.1.c). Neither blue ice nor water was reported by the public or WSA for central stations on Pasqua Lake (e.g., site A), although it is unknown whether that reflected the absence of discolouration or lower human traffic and reporting. Subsequent interviews with individual scientists and members of the public suggested that the blue ice phenomenon had not been recorded during at least the past 25 years (Haig and Leavitt 2019) nor in living memory of members of Pasqua First Nations, whose reserve is located on the southern shore of Pasqua Lake (Figure A.1.a).

Spectrophotometric analysis revealed strong absorbance by GF/C-filtered water between 500 and 650 nm at blue-water nearshore locations but not at the central reference station (Figure A.2.a). For example, the absorbance maximum at site C occurred 608-620 nm, with a slight shoulder 545-575 nm. This aqueous spectrum was similar to that of technical-grade C-phycoerythrin purified from *Spirulina* in deionized water (Figure A.2.b). Application of the calibration curve relating absorbance to dissolved mass of C-phycoerythrin (Figure A.2.c) to the blue-water samples (Figures A.1.a, A.2.a) suggested that nearshore concentrations of pigment were up to 14 mg C-phycoerythrin L<sup>-1</sup>.

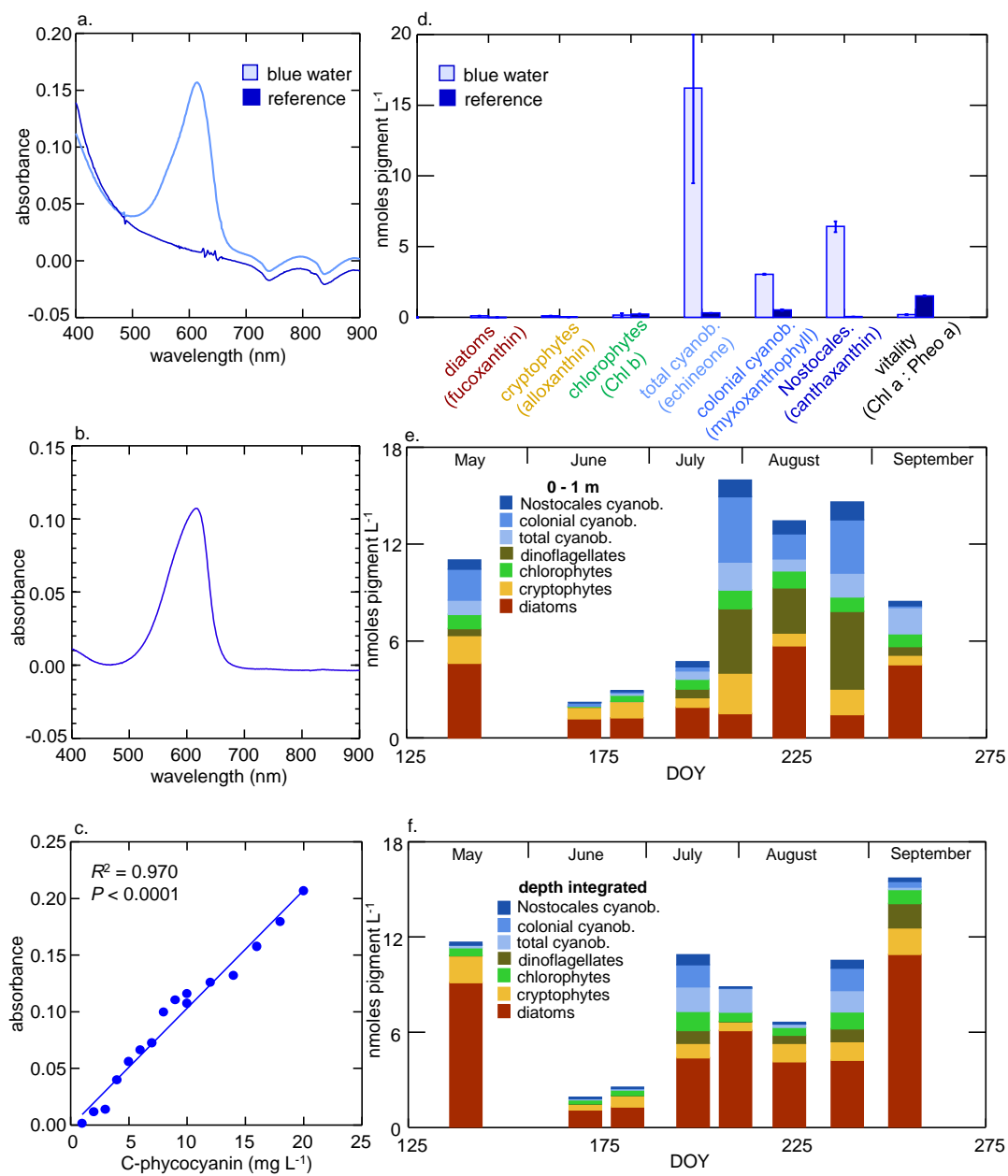


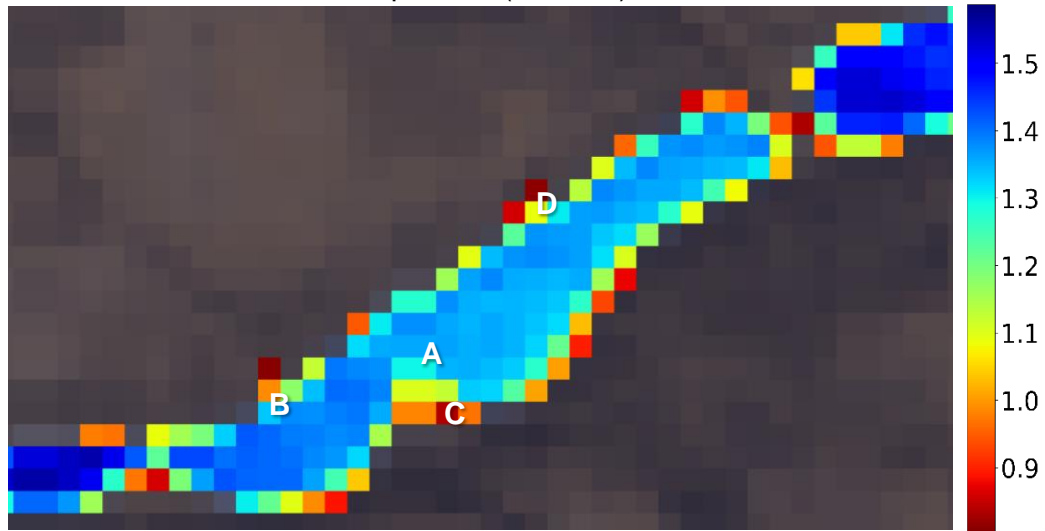
**Figure A.2. Pigment properties of water from Pasqua Lake and reference samples. (a) Absorbance spectrum of filtered water (0.45-µm pore) from nearshore site C (light blue) and mid-lake reference site A (dark line) between 400 and 900 nm. (b) Absorbance spectrum of laboratory grade C-phycoerythrin from *Spirulina*, 400-900 nm. (c) Calibration curve relating**

**absorbance at 620 nm to the mass of C-phycoyanin from *Spirulina*; Absorbance = 0.010 x (mg C-phycoyanin L<sup>-1</sup>) – 0.001. (d) Biomarker pigment composition of particulate organic matter (POM) collected from blue water site C (light blue) and mid-lake reference site A (dark blue), as well as ratio of undegraded Chl a to its main degradation product pheophytin a (Chl a: Pheo a). Changes in carotenoid composition (nmoles pigment L<sup>-1</sup>) in Pasqua Lake May-Sept 2020 for (e) 1 m depth surface samples, and (f) depth-integrated water samples. In both cases, concentrations (nmoles pigment L<sup>-1</sup>) include pigments from total cyanobacteria (echinenone), colonial cyanobacteria (myxoxanthophyll), Nostocales cyanobacteria (canthaxanthin), dinoflagellates (peridinin), chlorophytes (Chl b), cryptophytes (alloxanthin) and diatoms (diatoxanthin).**

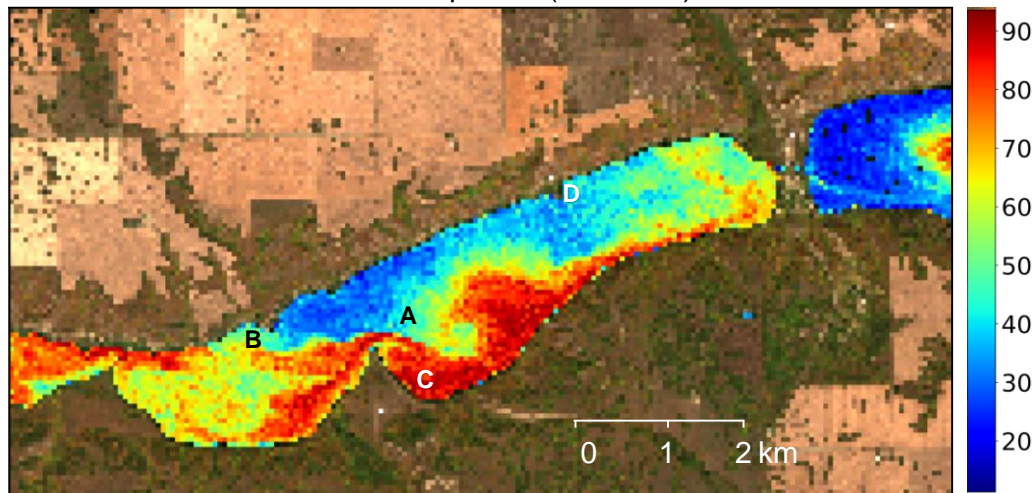
Analysis of POM on the GF/C filters using HPLC (Figure A.2.d) revealed that late-winter blue-water samples from nearshore sites had elevated concentrations of biomarker pigments from colonial cyanobacteria, including echinenone (all cyanobacteria), myxoxanthophyll (colonial cyanobacteria) and canthaxanthin (Nostocales cyanobacteria) but not those from other phytoplankton, including diatoms (fucoxanthin), cryptophytes (alloxanthin), chlorophytes (Chl b) or dinoflagellates (peridinin). At site C, concentrations of cyanobacterial pigments in March 2021 were up to 10-fold greater than values observed at any point in the preceding 2020 ice-free season, either in samples collected from the surface 1 m (Figure A.2.e) or in depth-integrated waters (Figure A.2.f), despite surface blooms of cyanobacteria being abundant in Pasqua Lake after mid-July. Based on carotenoid concentrations, Chl a in blue water samples should have exceeded 500 µg L<sup>-1</sup> had live cyanobacteria been present. In contrast, HPLC pigment concentrations were several orders of magnitude lower at the central reference location (site A) than either winter nearshore or previous summer stations, although winter samples at site A also included mainly biomarkers from colonial cyanobacteria (echinenone, myxoxanthophyll, canthaxanthin) and chlorophytes (Chl b) (Figure A.2.d). Analysis of Chl a: Pheo a ratios suggested that particulate matter was largely detrital, particularly in the blue-water region where ratios ( $0.19 \pm 0.4$ ) were 10-fold lower than mid-lake values ( $1.51 \pm 0.03$ ), and 100-fold less than expected ratio in regional live phytoplankton assemblages (~15; Bergbusch et al. 2021). Together, these observations suggest that blue staining of ice and water arose because exceptionally high densities of colonial cyanobacteria were trapped in nearshore ice and released their water-soluble pigment C-phycoyanin,

possibly due to repeated freezing and thawing, a process known to extract that pigment (Horváth et al. 2013).

a. Sentinel 3 OLCI scan 05 Apr 2021 (DOY 95)



b. Sentinel 2 MSI scan Chl 19 Sep 2020 (DOY 263)



c. Nearshore bloom  
19 Oct 2020 (DOY 295)



d. Phytoplankton biomass (% total) for  
nearshore bloom 19 Oct 2020 (DOY 295)

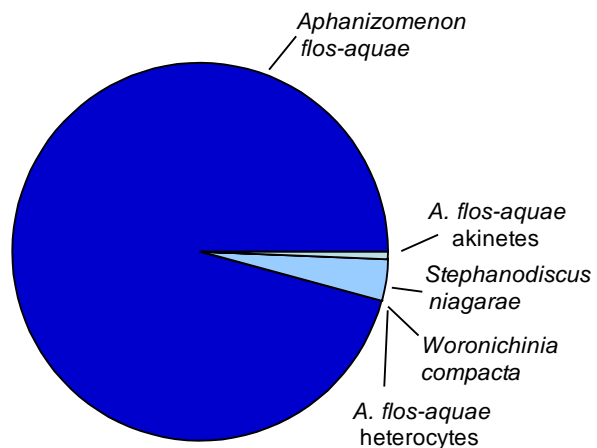


**Figure A.3. Satellite maps of cyanobacterial bloom occurrence on Pasqua Lake (central, eastern basins) and Echo Lake (western basin) in Saskatchewan, Canada. (a) Heat map of reflectance ratio  $R_{rs620\text{ nm}}/R_{rs709\text{ nm}}$  on 05 April 2021 as detected by Sentinel-3A/B OLCI sensor, corrected for cloud cover and adjacency effect. Hot (red) colours indicate maximal relative absorbance at 620 nm and potentially high concentrations of C-phycoyanin (e.g., Sites B, C, D), whereas cool (blue-green) colours show minimal absorbance at 620 nm and infer limited blue discolouration (Site A). The inset shows the spectral response of sampling points (A, B, C, and D), acquired from OLCI image on 05 April 2021. (b) Heat map of surface water Chl concentrations in Pasqua Lake 19 Sept 2020 as detected by Sentinel-2A/2B sensor. Hot (red) colours indicate elevated concentrations of Chl a, whereas cool (blue, green) colours indicated low chlorophyll content (as  $\mu\text{g L}^{-1}$ ). (c) Nearshore accumulation of decaying *Aphanizomenon flos-aquae* at outlet of Pasqua and Echo Lake, 19 October 2020. Photo courtesy of Aura Lee MacPherson. (d) Relative (%) total biomass of cells in surface 1-m sample from outlet of Pasqua and Echo Lake, 19 October 2020. DOY = calendar day of year.**

Maps of  $R_{rs620\text{ nm}}/R_{rs709\text{ nm}}$  ratios suggested that C-phycoyanin-like signals were strongly concentrated at the margins of Pasqua Lake from the date of initial detection during the first week of March until at least early April 2021 (Figure A.3.a; Figure A.4). On all dates of satellite reconnaissance, reflectance ratios were usually much lower at blue-water sites than at the central reference site (Figure A.4), consistent with observed patterns of discolouration within the lake. Analysis of spatial and temporal patterns in  $R_{rs620\text{ nm}}/R_{rs709\text{ nm}}$  ratios showed no obvious trend in nearshore pixels, but provided evidence that overall reflectance ratios declined during March, likely due to a loss of fresh snow cover from the lake surface (Figures A.4, A.5). Given that all blue-water sites (B-D) exhibited  $R_{rs620\text{ nm}}/R_{rs709\text{ nm}}$  ratios of  $\sim 0.9$  (Figure A.3.a), we used that threshold to estimate that  $0.68 \pm 0.24\text{ km}^2$  ( $4.25 \pm 1.5\%$ ) of Pasqua Lake area ( $16.02\text{ km}^2$ ) could have exhibited marked blue discolouration (Figure A.5). Using these data, we further estimated that staining occurred mainly within 50 m of lakeshore by assuming the area of blue water was evenly distributed around the lake margin (see Figure A.5). Finally, comparison of OLCI maps from nearby eutrophic Last Mountain Lake (Figure A.4) suggested that intense episodes of blue ice were more common in Pasqua Lake than at Last Mountain Lake, consistent with regional reports from the public.

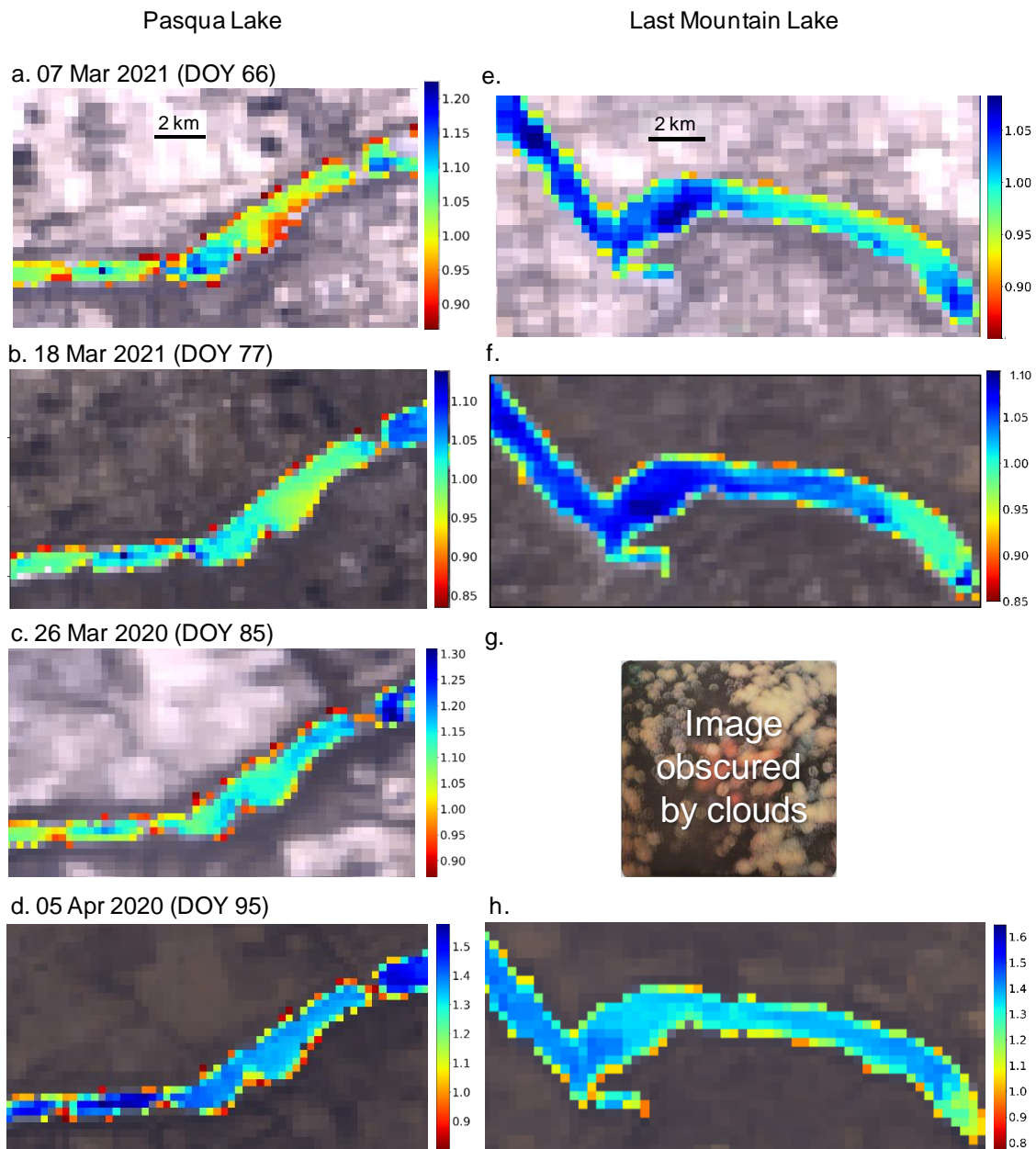


**Figure A.4.** Heat maps of reflectance ratio  $Ref_{620\text{ nm}}/Ref_{709\text{ nm}}$  for late winter 2021 (07 March – 05 April) as detected by Sentinel-3A/B OLCI sensor, corrected for cloud cover and adjacency effect. See Methods for details. Hot (red) colors indicate maximal relative absorbance at 620 nm and potentially high concentrations of C-phycoyanin, whereas cool (blue) colors show minimal

**absorbance at 620 nm and limited blue discoloration. Left column images of hypereutrophic Pasqua Lake, right column images of the south end of eutrophic Last Mountain Lake (except panel g). Scale bar represents 2 km. Color bar on each figure represents  $\text{Ref}_{620 \text{ nm}}/\text{Ref}_{709 \text{ nm}}$ .**

Surface blooms of *Aphanizomenon flos-aquae* during late October 2020 may have concentrated cyanobacteria to the margins of Pasqua Lake and favoured their entrapment in rapidly-forming nearshore ice sheets (Figure A.3.c). In particular, rafts of senescent cyanobacteria were observed on the shorelines of Pasqua, Echo, and downstream Crooked lakes during late October 2020. Microscopic analysis of one such bloom at the outflow of Pasqua and Echo lakes (Figure A.3.d) revealed high concentrations of cells, heterocytes, and akinetes from *A. flos-aquae*, as well as other cyanobacteria and eutrophic diatoms (*Stephanodiscus niagarae*) typical of these lakes (Hall et al 1999, Dixit et al. 2000, Donald et al. 2013). The presence of surface blooms of diazotrophic cyanobacteria in October has not been recorded previously for regional lakes, as non- $\text{N}_2$ -fixing taxa such as *Planktothrix* and *Limnithrix* spp. typically predominate by mid-September due to rapidly-diminishing irradiance and water temperature (Leavitt et al. 2006, Donald et al. 2013, Hayes et al. 2019). However, under-ice blooms of *Aphanizomenon* have been reported recently from eutrophic lakes in agricultural areas of Poland and the Ukraine (Wejnerowski et al. 2018, Shcherbak et al. 2019), possibly reflecting increased lake heating during late fall in the northern hemisphere (Woolway et al. 2021), and are known in winter from some ice-free maritime lakes (Davies et al. 2004).

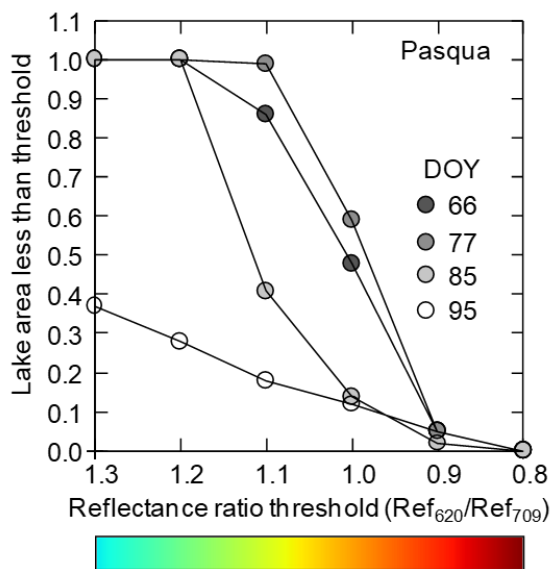
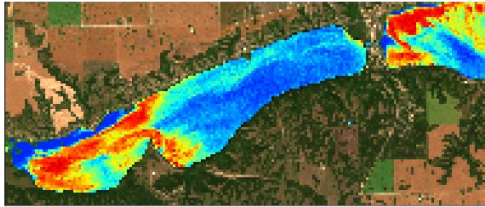


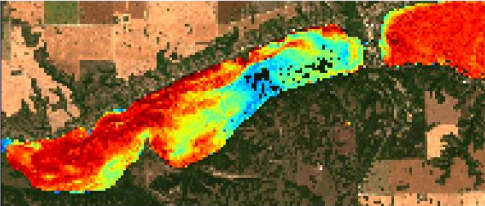
**Figure A.5. Fraction of the surface area of Pasqua Lake (central and eastern basins only) with reflectance ratio (Ref620 nm/Ref709 nm) less than critical value on X axis. Effects of fresh snow identified from RGB images are seen as sharp declines in the proportion of lake area with a high reflectance ratio as day of year (DOY) increases (see also Figure A.4). Values for Ref620 nm/Ref709 nm = 0.9 were stable at 4.25 ± 1.5% of Pasqua Lake area and were used to map potential locations of blue ice and water. Maximum potential extent of blue ice (0.68 ± 0.24 km<sup>2</sup>) was subtracted from total area analyzed (16.02 km<sup>2</sup>) and both entire and blue-free values were used to estimate the radius of the lake, if it were round. Differences between the two radius estimates was 48.5 m, suggesting that blue ice was located mainly close to the shore (see Figure A.4).**

Analysis of Chl a maps derived from Sentinel 2 MSI images also suggested that the blue-ice phenomenon may have arisen because late fall blooms of cyanobacteria were located mainly in nearshore regions (Figures A.3.b, Figure A.6). Time series of satellite images showed that intense blooms of phytoplankton (up to 100 µg Chl a L<sup>-1</sup>) arose in the shallower central basin before moving into the deep eastern basin along either the north or south shore (Figure A.6). As in other years, spring blooms of diatoms and cryptophytes (McGowan et al. 2005) declined during the June clearwater phase (Dröscher et al. 2009) before leading to late summer cyanobacteria maxima (Hayes et al. 2019) that were sustained into September (Figure A.2.e, f). In general, mean satellite-inferred Chl levels in the eastern basin (~40 - 60 µg Chl a L<sup>-1</sup>) during August and September were similar to those recorded by coeval sampling by WSA (~50 µg Chl a L<sup>-1</sup>) (Figure A.6.1). However, satellite images also revealed that blooms continued during October after *in situ* monitoring had concluded and that, just prior to ice formation in early November, elevated concentrations of chlorophyll (~20 µg Chl a L<sup>-1</sup>) were recorded throughout the littoral zone of Pasqua Lake (Figure A.6.i-k).

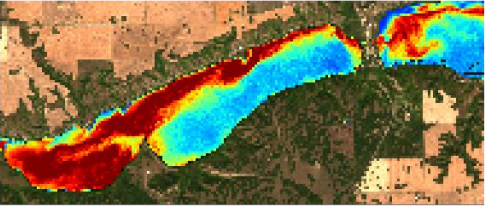
a. 19 Aug 2020 (DOY 232)



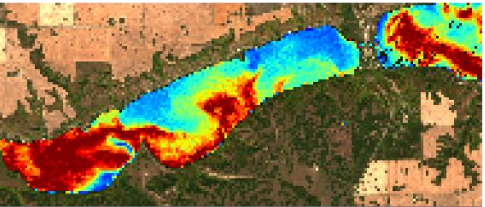
b. 27 Aug 2020 (DOY 240)



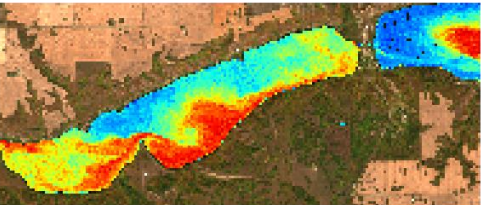
c. 11 Sep 2020 (DOY 255)



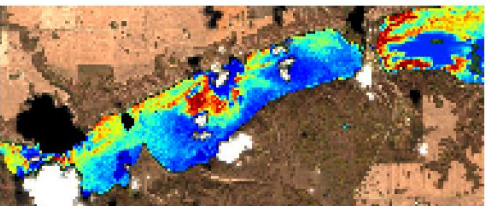
d. 16 Sep 2020 (DOY 260)



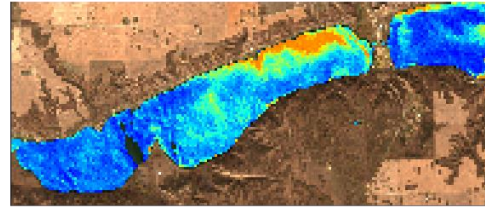
e. 21 Sep 2020 (DOY 265)



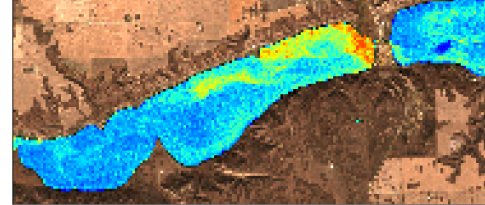
f. 03 Oct 2020 (DOY 277)



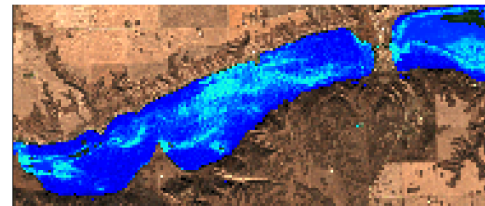
g. 08 Oct 2020 (DOY 282)



h. 13 Oct 2020 (DOY 287)



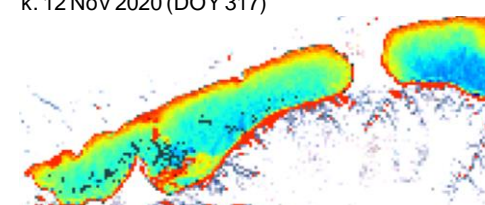
i. 02 Nov 2020 (DOY 307)



j. 10 Nov 2020 (DOY 315)



k. 12 Nov 2020 (DOY 317)



l. Mean Chl-a

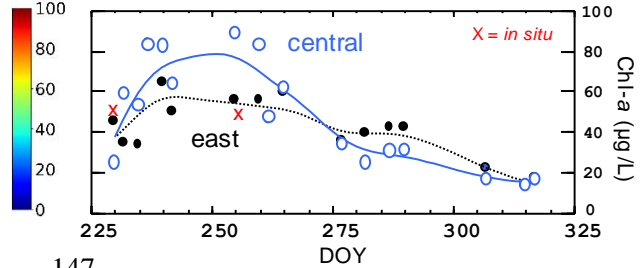


**Figure A.6. Heat map of surface water Chl-a concentrations ( $\mu\text{g/L}$ ) in Pasqua Lake as detected by Sentinel-2A/2B MSI sensors deployed 19 August to 12 November 2020. Hot (red) colors indicate elevated concentrations of Chl-a, whereas cool (blue) colors indicated low chlorophyll content. Note change in color scale after 10 November 2020. Panel I represents the mean Chl-a concentration recorded by satellite for central (blue) and eastern (black) basins, as well as by in situ measures from the eastern basin (red) measured by the Saskatchewan Water Security Agency.**

## **A.5 Conclusions**

Interactions between unprecedented rates of atmospheric warming and excessive nutrient influx have created conditions in which surface waters may experience novel conditions that cannot be anticipated from extrapolation of antecedent environments, a phenomenon known as ‘ecological surprises’ (Christensen et al. 2006, Filbee-Dexter et al. 2017). Here we used analysis of *in situ* pigmentation from phytoplankton and remote sensing to document the first widespread and marked blue discolouration of nearshore ice and lake water in late winter and early spring. Analyses suggest that this new phenomenon arose when exceptional late-fall blooms of *Aphanizomenon flos-aquae* were trapped in rapidly forming littoral ice, frozen and released water-soluble C-phycoerythrin. Such late blooms of *Aphanizomenon* spp. are becoming more common in highly eutrophic lakes (e.g., Wejnerowski et al. 2018, Shcherbak et al. 2019), possibly reflecting changes in fall heatwaves in lakes (Woolway et al. 2021) which favour continued growth of warm-water taxa (Hayes et al. 2019). Further, as late fall littoral blooms had high levels of *Aphanizomenon* akinetes (Figure A.3.d), and this species colonizes the water column from littoral deposits of akinetes, this warming may initiate a feedback loop to favour earlier and more profound cyanobacterial outbreaks, as has been documented recently for these lakes (Hayes et al 2019). Given that toxic blooms are common in the Canadian Prairies (Orihel et al. 2012, Hayes et al. 2019) and regional climate is forecast to warm by  $\sim 5$  °C by 2050, particularly during the colder seasons (Sauchyn et al. 2020), autumnal blooms and late winter blue discolouration may become much more common.

Fortunately blue-ice events did not coincide with greatly increased levels of common cyanobacterial toxins. Concentrations of cyanobacterial pigments in blue-ice fields (Figure A.2.e, f) were up to 10-fold greater than those observed during previous summer blooms when Chl was  $\sim 50$   $\mu\text{g}$

L<sup>-1</sup> (Figure A.3.b). Long-term monitoring of Pasqua Lake demonstrates that concentrations of the hepatotoxin microcystin can exceed 20 µg L<sup>-1</sup> during summer bloom events (Table A.1), values nearly twice the Health Canada proposed recreational contact advisory (Hayes et al. 2019). Together, these observations suggest that toxin content of blue waters could have been as high as 200 µg microcystin L<sup>-1</sup>, levels higher than seen elsewhere in Canada and well above acute health advisory thresholds (Orhiel et al. 2012). Instead, observed concentrations of microcystin (~0.2 µg L<sup>-1</sup>) were well below drinking-water advisories for the USA (1.0 µg L<sup>-1</sup>) and Canada (1.5 µg L<sup>-1</sup>). Low microcystin content in blue-ice samples may arise because *Aphanizomenon* species can have lower microcystin content than other cyanobacteria (Hayes et al. 2019), cellular quotas of toxin are normally highest in actively-growing populations and decline with bloom senescence (Finlay et al. 2010b), and C-phycoerythrin is known to catalyze photodegradation of microcystins (Song et al. 2007). Although further research is required, it appears initially as if there is no acute health threat associated with lake discolouration.

Further research is also needed to determine the extent of lake discolouration by C-phycoerythrin. Although Sentinel 3A/B with OLCI sensors provide approximations of C-phycoerythrin and cyanobacterial abundance during summer (Mishra et al. 2019, Ogashawara 2019), ours was the first attempt to use remote-sensed images to document the presence of the pigment under late-winter conditions. Here we found that intense blue discolouration at three field sites corresponded well to  $R_{rs620\text{ nm}}/R_{rs709\text{ nm}}$  ratios  $\leq 0.9$ , but also noted that the presence of fresh snow introduced bias and over-estimated of the extent of blue discolouration (Figure A.4). Employing a simple band ratio to qualitatively capture PC concentration can be justified in this study given the low contribution of other optically-active constituents. However, it should be treated cautiously in turbid waters where suspended minerals or phytoplankton biomass may interfere with PC absorption (Matthews 2011, Stumpf et al. 2016). Thus, Much more extensive ground validation will be required to refine the use of satellite imagery to detect the blue-ice phenomenon, as seasonal changes in snow cover, adjacency effect, spectral characteristics of lake water, and the distribution, composition and cause of blooms all need to be further constrained. Nonetheless, this promising first report suggests that some future ecological surprises may be detectable in near real time using the next generation of orbital platforms.

Ecological surprises, such as marked blue discolouration of lake ice and water, may be particularly challenging for lake managers. Although research on early-warming indicators is on-going

(Carpenter 2003), forecasts are usually not available for novel events, even when there exist extensive real-time monitoring programs (e.g., Meyers et al. 1997). This issue is likely to become more pronounced in the coming decades, as human population, resource use, atmospheric temperatures, and nutrient fluxes move beyond their historical ranges and appear to change without precedent (Magnuson et al. 1990). In our experience, rapid governmental and academic response to public concerns (< 1 week from first report to identified cause), including use of traditional and social media platforms, reduced public anxiety over potential proximate causes of the discolouration (septic leaks, anti-freeze spills, cryptic urban pollution, waste dumping, etc.) and improved institutional trust by the public. In particular, we note that coordinated collaboration between governmental and academic agencies may provide a valuable model for addressing future sudden environmental challenges.